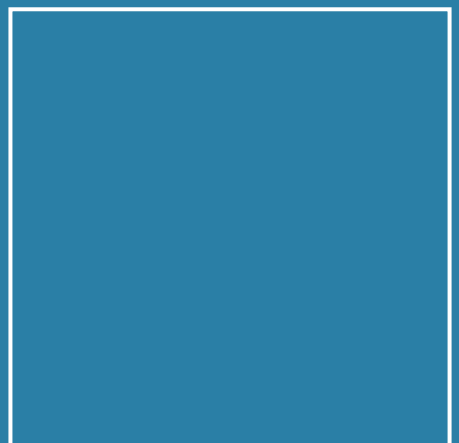
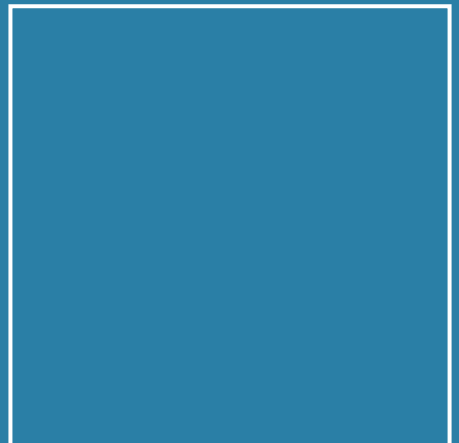




Dissertation

Jonas Constantin Gienger

Determination of optical and geometrical properties of blood cells and microparticles from light scattering measurements



ISSN 0341-6712
ISBN 978-3-95606-467-8

Physikalisch-Technische Bundesanstalt

Optik

PTB-Opt-85

Braunschweig, April 2019

Jonas Constantin Gienger

**Determination of optical and geometrical properties
of blood cells and microparticles from light scattering
measurements**

ISSN 0341-6712

ISBN 978-3-95606-467-8

Herausgeber:

Physikalisch-Technische Bundesanstalt

ISNI: 0000 0001 2186 1887

Presse und Öffentlichkeitsarbeit

Bundesallee 100

38116 Braunschweig

Telefon: (05 31) 592-93 21

Telefax: (05 31) 592-92 92

www.ptb.de

Zugl.: Berlin, Technische Universität, Diss., 2019

Determination of optical and geometrical properties of blood cells and microparticles from light scattering measurements

vorgelegt von
M. Sc.
Jonas Constantin Gienger
geb. in Darmstadt

von der Fakultät II – Mathematik und Naturwissenschaften
der Technischen Universität Berlin
zur Erlangung des akademischen Grades

Doktor der Naturwissenschaften
– Dr. rer. nat. –

genehmigte Dissertation

Promotionsausschuss:

Vorsitzender: Prof. Dr. Dieter Breitschwerdt
Gutachter: Prof. Dr. Markus Bär
Gutachter: Prof. Dr. Harald Engel
Gutachter: Prof. Dr. Christian Wagner

Tag der wissenschaftlichen Aussprache: 21. Januar 2019

Berlin 2019

Zusammenfassung

Diese Dissertation behandelt die Analyse von Messungen der Lichtstreuung an roten Blutzellen (RBZs) und künstlichen Mikropartikeln um ihre optischen und geometrischen Eigenschaften zu bestimmen. Die Lichtstreuungseigenschaften von Partikeln und Zellen werden durch deren Form und komplexen Brechungsindex (BI) bestimmt. RBZs haben minimale innere Struktur und sind ein beliebter Gegenstand der Grundlagenforschung, sie werden aber auch routinemäßig mit optischen Methoden in der Laboratoriumsmedizin untersucht. Literaturwerte für den Realteil des BI („reeller BI“) von RBZs und des sauerstofftransportierenden Blutfarbstoffes Hämoglobin (Hb) streuen stark, was eine quantitative Analyse von Lichtstreuendaten behindert.

Hier werden zwei komplementäre Ansätze zur Bestimmung des reellen BI von RBZs und Hb-Lösungen präsentiert: Zuerst wird der reelle BI im nahen Ultraviolett (UV), Sichtbaren und nahen Infrarot aus dem bekannten Absorptionsspektrum von Hb-Lösungen mittels Kramers-Kronig-Beziehungen (KK) bestimmt. Dazu wird das Absorptionsspektrum im tiefen UV mit einem Modell für das Peptid-Rückgrat des Metalloproteins Hb ergänzt. Man erhält so eine genaue Beschreibung der Dispersionsmerkmale, aber zur Festlegung der absoluten Skala werden zusätzliche Daten für den reellen BI benötigt, z. B. aus der Literatur. Der zweite Ansatz besteht in einer indirekten, gleichzeitigen Bestimmung von Größe und BI von intakten aufgekugelten RBZs in Suspension aus Messungen ihrer Extinktionsspektren. Diese Spektren beschreiben, wie viel Licht eine Partikel- oder Zellsuspension aus einem einfallenden Strahl durch Streuung und Absorption entfernt. Sie werden durch die Lösung eines inversen Problems analysiert, wobei das direkte Problem darin besteht, den mittleren Extinktionsschnitt eines Zellensembles mit bekannter Größenverteilung und optischen Eigenschaften mittels der Mie-Lösung für die Streuung an einer Kugel zu berechnen. Das inverse Problem wird durch eine geeignete Darstellung des reellen BI mit wenigen Parametern und nichtlinearer Optimierung gelöst. Nach Demonstration der Methode mit synthetischen Polystyrol-Mikrokugeln wird das konzentrationspezifische Inkrement des reellen BI von oxygenierten aufgekugelten RBZs für Wellenlängen zwischen 290 nm und 1100 nm bestimmt. Der BI anderer Hb-Varianten kann nun in Kombination mit den o. g. KK-Beziehungen genau bestimmt werden.

Die so erhaltenen BI-Daten werden verwendet um die Zusammensetzung von künstlichen Hämoglobin-Mikropartikeln (HbMP) zu beurteilen, die möglicherweise RBZ-Konzentrate in der Transfusionsmedizin ersetzen könnten. Die Zulassung zu klinischen Studien erfordert eine Charakterisierung des Gehalts an verschiedenen Hb-Varianten, insbesondere von oxygeniertem Hb, desoxygeniertem Hb und nichtfunktionalem Methämoglobin. Dies wird durch Vergleich zwischen gemessenen und berechneten Extinktionsspektren für variable Zusammensetzung erreicht.

Abschließend wird ein Lichtstreuproblem für RBZs in der optischen Durchflusszytometrie behandelt. Zur Interpretation gemessener ein- und zweidimensionaler Histogramme des Vorwärtsstreuquerschnitts (VSQ) von einzelnen nativen RBZs wird die Lichtstreuung mittels diskreter Dipolapproximation numerisch simuliert. Ein einfaches, gedehntes RBZ-Formmodell wird aufgestellt und durch Vergleich mit Messdaten wird demonstriert, dass bimodale VSQ-Histogramme aufgrund einer Kombination von zufälliger Orientierung der RBZs zum Laser und Deformation durch die starken Geschwindigkeitsgradienten im Hüllstrom des Zytometers auftreten.

Abstract

This thesis deals with the analysis of measurements of the scattering of light by red blood cells (RBCs) and artificial microparticles in order to determine their optical and geometrical properties. The light scattering properties of a particle or cell are determined by its shape and its complex refractive index (RI). RBCs have minimal internal structure and are a popular subject of fundamental research, but are also routinely examined with optical methods in laboratory medicine. Literature values for the real part of the RI (“real RI”) of RBCs and the oxygen-transport blood pigment hemoglobin (Hb) scatter widely, which hampers the quantitative analysis of light scattering data.

In this thesis, two complementary approaches are presented to determine the real RI of RBCs and Hb solutions: Firstly, the real RI in the near ultraviolet (UV), visible and near infrared region is determined from the well-known absorption spectrum of Hb solutions by Kramers-Kronig (KK) relations. To this end, the absorption spectrum is supplemented by a deep UV model for the peptide backbone of the metalloprotein Hb. This yields an accurate description of the dispersion features, but requires additional data for the real RI, e. g., from literature, to set the absolute scale. The second approach consists in an indirect, simultaneous determination of the size and RI of intact sphered RBCs in suspension from measurements of extinction spectra. These spectra describe how much light a particle or cell suspension removes from an incident beam due to scattering and absorption. They are analyzed by solving an inverse problem, where the direct problem consists in computing the average extinction cross section of a cell ensemble with known size distribution and optical properties using the Mie solution for light scattering by a sphere. The inverse problem is solved by a suitable few-parameter representation of the real RI and nonlinear optimization. After a demonstration of the method with synthetic polystyrene microbeads, it is applied to determine the Hb-concentration-specific increment of the real RI of oxygenated sphered RBCs for wavelengths between 290 nm and 1100 nm. The RI of other Hb variants can then be accurately determined in combination with the above-mentioned KK relations.

The RI data thus obtained are employed to assess the composition of artificial hemoglobin microparticles (HbMP), which might replace RBC concentrates in transfusion medicine. For the approval of clinical studies, characterization of their content of different Hb variants is required, in particular of oxygenated Hb, deoxygenated Hb and non-functional methemoglobin. This is achieved by a comparison between measured and computed extinction spectra for variable composition

Lastly, a light scattering problem for RBCs in optical flow cytometry is considered. To interpret measured one- and two-dimensional histograms of the forward scattering cross section (FSC) of single native RBCs, the light scattering processes is numerically simulated with the discrete dipole approximation. A simple elongated RBC shape model is proposed and by comparison with measurement data, it is demonstrated that bimodal histograms FSC occur because of a combination of random orientation of the RBCs to the laser and deformation due to strong velocity gradients of the sheath flow in the flow cytometer.

Contents

1	Introduction	1
1.1	Blood and red blood cells	1
1.2	Blood cell analysis and flow cytometry	2
1.3	Complex refractive index	3
1.4	Refractive index of RBCs and Hb	5
1.5	Outline of this thesis	6
2	Theoretical background: Light scattering problems	9
2.1	Maxwell's equations	9
2.2	Light scattering	11
2.2.1	Scattering problems in spherical coordinates: Mie scattering and the T -matrix method	12
2.2.2	Discrete dipole approximation	16
3	Calculation of optical properties of hemoglobin solutions with Kramers- Kronig relations	21
3.1	Introduction	21
3.2	Introduction to Kramers-Kronig relations	23
3.2.1	Simple derivation of Kramers-Kronig relations	23
3.2.2	Some analytical examples	25
3.3	Application to hemoglobin solutions	28
3.3.1	General considerations	28
3.3.2	Formal Kramers-Kronig transform of the spectrum of hemo- globin solutions and erythrocytes	29
3.3.3	UV absorption model	30
3.3.4	Fitting to measurement data	32
3.3.5	Hemoglobin variants	33
3.4	Results and discussion	34
3.4.1	Real refractive index increment for oxyHb, deoxyHb and metHb	34
3.4.2	Comparison to previous Kramers-Kronig analyses	36
3.4.3	Uncertainty analysis	38
3.5	Summary	40
	Appendices	41
3.A	Numerical integration scheme for Kramers-Kronig relations	41
4	Modeling and analysis of microparticle and red blood cell extinction spectra	43
4.1	Introduction	43
4.2	Theoretical background	45

4.3	Measurement of extinction cross sections	48
4.4	Data analysis	50
4.4.1	Forward model	50
4.4.2	Sensitivity of the forward model	54
4.4.3	Inverse problem	58
4.5	Application to polystyrene microbeads	68
4.5.1	Measurement data	68
4.5.2	Inverse problem settings	69
4.5.3	Optimization results and discussion	70
4.5.4	Modification: inference of the refractive index of the host medium	74
4.6	Application to sphered red blood cells	80
4.6.1	Experiment	81
4.6.2	Inverse problem	82
4.6.3	Comparison to literature data	85
4.7	Summary and outlook	87
Appendices		90
4.A	Effect of absorbing host medium	90
4.B	Details of nonlinear least-squares optimization	92
4.B.1	Brief overview of least-squares algorithms	93
4.B.2	Expressions for the numerical implementation of the model	94
4.C	Uncertainty analysis	96
5	Extinction spectra of artificial hemoglobin microparticles	98
5.1	Introduction	98
5.2	Mathematical modeling of HbMP	100
5.3	Results	103
5.3.1	Sensitivity to particle shape	103
5.3.2	Comparison to experiments	106
5.4	Summary and outlook	109
6	Modeling and simulation of light scattering by red blood cells in flow cytometry	113
6.1	Introduction	113
6.2	Experiment	115
6.2.1	Optical setup	115
6.2.2	Flow setup	116
6.2.3	Blood preparation	117
6.3	Hydrodynamics	118
6.3.1	Estimate of velocity gradients	118
6.3.2	Comparison to microfluidic flows	121
6.4	Optical modeling and simulation	123
6.4.1	Scattering problem and FSC	123
6.4.2	Shape model	124
6.4.3	Refractive index	126
6.4.4	DDA simulations	126
6.4.5	Propagation of probability distributions	127
6.4.6	Axes calibration	128
6.5	Results	130

6.5.1	Comparison between measurements and simulations	130
6.5.2	Influence of laser beam shape	134
6.6	Summary and Discussion	135
	Summary	138
	Own Publications	144
	References	145
	Abbreviations	156

List of Figures

1.1	(a) SEM image of a RBC, a platelet and a WBC; (b) Structure of a mature RBC	2
3.1	Three different absorption peaks (δ , rectangle and Lorentzian) and their Kramers-Kronig transforms	26
3.2	Complex refractive index of water	28
3.3	Imaginary refractive index increment of human hemoglobin variants in aqueous solutions	31
3.4	Real refractive index increment of oxyhemoglobin solutions computed with Kramers-Kronig relations	34
3.5	Kramers-Kronig results for the real refractive index increment of human hemoglobin variants	35
3.6	Comparison of refractive index of hemoglobin solutions between different Kramers-Kronig analyses and measurement	37
4.1	Extinction by a suspension of particles or cells (schematic)	47
4.2	Optical layout to measure extinction spectra	48
4.3	Example for measurement data: raw spectra, transmittance, extinction cross section and its uncertainty for 2.539 μm PS beads in water	49
4.4	Extinction cross sections $C_{\text{ext}}(\lambda)$ of single microspheres computed with wavelength-independent RIs for a wide spectral range	54
4.5	Influence of parameters on extinction cross section for 2.5 μm polystyrene spheres in water	55
4.6	Influence of size distribution on extinction cross section for 86 fL sphered RBCs in water	56
4.7	Influence of optical properties on extinction cross section for 86 fL sphered RBCs in water	57
4.8	RI of water at 20°C and polystyrene	58
4.9	Graphical solution of the pointwise RI inference problem for monodisperse PS spheres of known size without measurement noise	59
4.10	Illustration of the dependence of the pointwise RI inference problem in Fig. 4.9 on the knowledge of the particle radius R	60
4.11	An example for the LTRs used to represent the RI	63
4.12	An example for the cubic B-splines used to represent the RI increment	65
4.13	RI of PS retrieved from extinction measurements of 2.5 μm beads in water	72
4.14	Difference of the particle RI found by optimization to reference values	73
4.15	Measured extinction cross sections of 2.5 μm beads suspended in water and different glucose solutions	76

4.16	Inferred RI of water and different glucose solutions from extinction measurements of 2.5 μm beads suspended in them	77
4.17	Difference of inferred water and glucose RI to reference values	77
4.18	Measured extinction cross sections of 2.5 μm polystyrene beads suspended in a sphering reagent for RBCs in comparison to water and glucose solutions	78
4.20	Measured extinction cross sections of sphered RBCs suspended in sphering reagent and imaginary RI increment of oxyHb used in the forward model	82
4.21	Real RI increment of oxygenated human RBCs obtained from the measured extinction cross sections	83
4.22	Real RI of oxygenated RBCs computed with the RI increment determined in this chapter for three different Hb concentrations	84
4.23	Real RI increment of oxygenated human RBCs: Present result and various literature values	85
4.A.1	Measured imaginary RI of the Abbott sphering reagent for RBCs compared with literature values for water	91
5.1	Schematic of a HbMP made from cross-linked bovine Hb and HSA; Idealized “peanut shape” of a HbMP	98
5.2	Reversible binding of oxygen (O_2) to a prosthetic heme group of a Hb subunit	99
5.3	Complex RIs of human Hb solutions assumed for the simulations of HbMP extinction spectra	100
5.4	Orientation-averaged extinction and absorption cross sections of prolate spheroids in comparison to Mie and Rayleigh scattering	104
5.5	Deviation of the orientation-averaged extinction cross section of prolate spheroids from that of a sphere	105
5.6	Relative deviation of the cross sections of spheroids from those of a sphere in dependence on the spheroids’ aspect ration h	106
5.7	Simulated extinction spectra of HbMP modeled as polydisperse spheres	107
5.8	Measurements and simulations of HbMP converted to metHb	108
5.9	Measurements and simulations of HbMP in atmospheres of air and argon	109
6.1	Schematic of an optical flow cytometer	114
6.2	Optical layout of the flow cytometer for the simultaneous 2-direction FSC measurement	115
6.3	Surface triangulation of a discocyte shape model	115
6.4	Measurements of the 2-direction forward-scattered intensity of a blood sample at 632.8 nm	116
6.5	RBC in the flow channel of the cytometer (to scale)	118
6.6	Shape of a RBC in a microcapillary compared to the shape and orientation expected in the flow channel of the cytometer	122
6.7	Cross section through the center of the shape model and surface triangulation of the stretched model	125
6.8	Far-field intensity distributions $I^s(\vartheta, \varphi)$ at $\lambda = 632.8 \text{ nm}$ for the stretched RBC shape model	127
6.9	Dependence of the simulated FSC on orientation angle and elongation factor for fixed volume and Hb concentration	128

6.10	Calibration of FSC axes using spheroid RBCs and Mie theory	130
6.11	Comparison between measurements and simulations of the FSC at four different laser vacuum wavelengths	131
6.12	Measurement data and simulation of the 2-direction FSC for native RBCs	132
6.13	Simulation of the 2-direction FSC using the axisymmetric shape model	132
6.14	Measurement data and simulation of the 2-direction FSC for native RBCs injected through a flattened capillary	133
6.15	Dependence of the FSC of the stretched shape model on the waist diameter of a Gaussian beam	135

List of Tables

4.1	Calculated dilutions of examined suspension of PS beads with 2.539 μm nominal diameter in water made from 2% w/v basic material and resulting measured average transmittance \bar{T}	69
4.2	Optimization result for scalar parameters for PS beads in water	72
4.3	Sellmeier coefficients for the RI of PS microbeads determined in this chapter	73
4.4	Hematological parameters of RBC samples obtained from the CBC in comparison to the optimization results	82
4.A.1	Relative and absolute deviation of the extinction cross section of particles in an absorbing host medium from that in a non-absorbing host medium	92
6.1	Hematological parameters for the concentration distribution and size distribution of the RBC sample	117
6.2	Parameters of the shape models used	125
6.3	RI of water and RBCs (at $c_{\text{Hb}} = 344 \text{ g L}^{-1} = \text{MCHC}$) assumed for simulation	126

Chapter 1

Introduction

Optical methods for the examination of biological cells and tissues play a major role in both, fundamental research and medical diagnostics. These methods include various microscopy techniques, optical flow cytometry [1,2] and spectroscopic measurements [3] but also techniques for single cell manipulation like optical trapping and stretching [4]. Many modern optical measurement and imaging methods, including super-resolution microscopy [5,6] and many applications of optical flow cytometry [2], rely on fluorescence for a biomolecular analysis of cells, which in most cases requires genetic encoding of fluorescent proteins in organisms or labeling of cells with fluorescent dyes [5,6]. On the other hand, *label-free* methods are being developed which aim to eliminate the need for such manipulations of the cells or tissues at least for some applications in research and diagnostics by using the physical properties of the cells for contrast instead. These include Raman spectroscopy [3,7], holographic microscopy [8,9] quantitative phase microscopy [10–12] and optical tomography [13–15] as well as label-free flow cytometry based on light scattering [1,2]. Of these optical measurement methods, many fall within the framework of linear optics and elastic light scattering, in which case they rely on the *complex refractive index* (RI) of the cells and tissues as their source of contrast. This thesis is concerned with the light scattering properties of red blood cells (RBCs), which are among the simplest of animal cells with regard to their structure [16]. These oxygen-transporting cells make up the majority of blood cells in mammals, including humans [16], and are thus relatively easily available for fundamental research in biophysics. But they are also very important for medical diagnostics and are routinely examined as part of the complete blood count in laboratory medicine [17]. This thesis deals with the determination of the spectral RI of RBCs and the analysis of measurements of light scattering by RBCs as well as artificial microparticles.

1.1 Blood and red blood cells

Blood is composed of cells suspended in a liquid. In humans, the cellular constituents typically make up about 45% of the blood volume and the liquid, called *blood plasma* makes up the remaining 55%. The cellular portion of the blood is composed of erythrocytes or *red blood cells* (RBCs), leukocytes or *white blood cells* (WBCs) and thrombocytes or *platelets*. To give an impression, Fig. 1.1 (a) shows a scanning electron microscope (SEM) image of three different blood cells. WBCs can be further differentiated into monocytes, lymphocytes and different types of granulocytes. RBCs are the most numerous type of blood cell, 100 to 200 times as

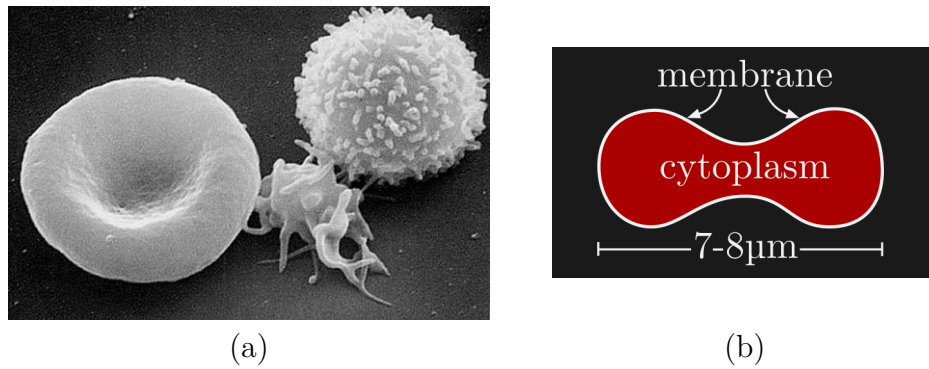


Figure 1.1: (a) SEM image of a RBC (left), a platelet (middle) and a WBC (right).[†] (b) Structure of a mature RBC.

[†] https://commons.wikimedia.org/wiki/File:Red_White_Blood_cells.jpg

By Electron Microscopy Facility at The National Cancer Institute at Frederick (NCI-Frederick) [Public domain], via Wikimedia Commons.

numerous as platelets and 500 to 1000 times as numerous as WBCs. [16]

Compared to other animal cells, mammalian RBCs have a particularly simple structure: They consist of a thin elastic membrane enclosing a liquid cytoplasm as illustrated in Fig. 1.1 (b). The membrane is composed of a lipid bilayer (outer membrane) with a thickness of the order of 10 nm [18], which on its inside is connected to a network of spectrin filaments forming the inner membrane [19]. In total, the membrane is not thicker than 100 nm [20]. In contrast to most other cells, mature erythrocytes have no cytoplasmic structures or organelles, i. e., they have neither a nucleus nor mitochondria [16, 17]. Their cytoplasm consists solely of a highly concentrated solution of the oxygen-transport metalloprotein hemoglobin (Hb) which dominates their optical properties because it amounts to about 98% of the RBCs' solids [21]. Typical mean intracellular Hb concentrations for healthy persons are 320 g L^{-1} to 360 g L^{-1} [17]. In the absence of external forces, RBCs have a biconcave-disc-like shape (*discocytes*) with $7 \mu\text{m}$ – $8 \mu\text{m}$ diameter [17] and $2.5 \mu\text{m}$ typical thickness [16]. Typical mean volumes of RBCs range between 80 fL and 100 fL ($1 \text{ fL} = 1 \mu\text{m}^3$) [17]. Like their Hb content, the unique shape of RBCs and their high deformability are related to their function of transporting oxygen to tissues by passing through small capillaries. [17]

1.2 Blood cell analysis and flow cytometry

Analysis of blood samples for medical diagnostics includes the determination of the parameters of the so called *complete blood count* (CBC), one of the most frequently performed measurements in laboratory medicine. Besides the concentrations of RBCs, WBCs and platelets, clinical parameters of the CBC include the mean corpuscular Hb concentration (MCHC), mean corpuscular volume (MCV) and the red cell distribution width (RDW) of a blood sample, that is, the coefficient of variation (relative standard deviation) of the volume of RBCs. Today, the method routinely used for automated analysis of blood cells and determination of CBCs is *flow cytometry* [17]. In a flow cytometer, cells or particles pass through the measuring apparatus in a fluid stream. Most modern devices make use of *hydrodynamic focusing* by means of a *sheath flow* to confine the sample fluid containing the cells near

the centerline of a laminarly flowing stream of cell-free sheath fluid. Thus cells or particles move downstream in a single file, where they are measured one by one [2]. Commonly used measurement principles include *optical flow cytometry*, based on light scattering and fluorescence emissions of (chemically stained) cells as well as *impedance-based* flow cytometers where cell sizes are determined based on changes of the electrical impedance as single cells pass a narrow orifice between two electrodes. Compared to the analysis of cells under a light microscope, flow cytometers allow for much higher throughput in the range of 1000 events per second. Their use is by far not restricted to hematology for the analysis of blood cells, but also widespread in other fields like immunology, cancer research, marine biology or even food science [2].

In automated hematology analyzers, light scattering by single RBCs is used to determine their volume and hemoglobin content. To allow for a relatively simple data analysis, the RBCs are *isovolumetrically sphered* by means of a special sheath fluid containing a chemical reagent— a method that was established more than three decades ago [22,23]. Of course, a detailed knowledge of the optical properties of the cells is required to analyze such measurements.

1.3 Complex refractive index

As discussed above, optical measurement techniques for biological cells and tissues besides optical flow cytometry include microscopy and spectroscopic techniques. In most label-free measurement methods, such as holographic microscopy [8,9] quantitative phase microscopy [10–12], optical tomography [13–15] or absorption spectroscopy [3] the contrast is provided by the complex RI of the cells, which describes their interaction with light. The complex RI of a cell depends on the concentrations and spatial distribution of a variety of intracellular molecules, correlated to the corresponding biological function. For RBCs, precise knowledge of the dependence between RI and intracellular Hb concentration is required for simulations [24–26] and analysis [22,27–29] of light scattering by single RBCs. Furthermore it is required to determine the intracellular Hb concentration from phase and holographic microscopy [8,30,31], to understand the interaction of light with whole blood or blood-perfused tissues for purposes of clinical diagnostics [32,33], or to visualize the appearance of tissues in computer graphics [34]. In this section, we will briefly outline the concept of a complex RI and its significance for light scattering problems.

Consider a homogeneous medium with complex refractive index (RI)

$$\mathbf{n} = n + i\kappa. \quad (1.1)$$

Throughout this thesis, we will use the term “real RI” equivalent to “real part of the RI” to refer to n , and likewise the term “imaginary RI” to refer to the imaginary part κ . A plane electromagnetic wave with an angular frequency ω propagating along the z direction through this medium is given by

$$\mathbf{E}(z, t) = \mathbf{E}_0 e^{iknz - i\omega t} = \mathbf{E}_0 e^{i\frac{2\pi}{\lambda}nz - i\omega t} e^{-\frac{2\pi}{\lambda}\kappa z}, \quad (1.2)$$

where t is the time and \mathbf{E} is the amplitude of the electric field. \mathbf{E}_0 is the amplitude for $t = 0$ at $z = 0$, $k = \omega/c_0$ is the vacuum wavevector and $\lambda = 2\pi c_0/\omega$ the vacuum wavelength with c_0 the speed of light in vacuum. I. e., the real RI n describes the change of phase velocity of the wave compared to vacuum. For sufficiently

transparent media, for which $\kappa \ll n$, the real RI is thus the cause of refraction of light waves at macroscopic interfaces. For example, if a plane wave propagating from medium 1 with RI n_1 into medium 2 with RI n_2 through a plane interface at an angle ϑ_1 , the wave is refracted and exits the interface at an angle ϑ_2 , where the relation between the two is given by the well-known *Snell's law*

$$n_1 \sin \vartheta_1 = n_2 \sin \vartheta_2. \quad (1.3)$$

As is evident from Eq. (1.2), the imaginary part of the RI κ describes an exponential decay of a plane wave propagating through a homogeneous medium. Instead of the electric field \mathbf{E} , this attenuation can be expressed in terms of the intensity of light $I \propto |\mathbf{E}|^2$ as

$$I(z) = I_0 e^{-\mu_a z} \quad (1.4)$$

with μ_a being the absorption coefficient and I_0 the intensity at $z = 0$. For a solution of an absorbing solute of molar concentration c_M (mass concentration c) one also often writes

$$I(z) = I_0 10^{-\varepsilon_M c_M z} = I_0 10^{-\varepsilon c z}, \quad (1.5)$$

which is the *Beer-Lambert law* with the molar attenuation coefficient ε_M (mass attenuation coefficient ε). Here, one usually thinks of z being the thickness of a plane-parallel sample (e. g., a cuvette filled with liquid) and I_0 is the intensity transmitted through the sample in the absence of the solute. Hence for a solution in a non-absorbing solvent, the conversion rule between the quantities is

$$\kappa = \frac{\mu_a \lambda}{4\pi} = \frac{\ln 10 \varepsilon_M c \lambda}{4\pi M}, \quad (1.6)$$

where M is the molar mass of the solute.

As outlined above, the complex RI determines the behavior of light at macroscopic interfaces between any two materials as well as its propagation in bulk media. Consequently, a variety of experimental methods exist for measuring the real RI of a material based on the refraction or reflection of light at a planar interface between the sample and some other known material, such as air, water or an optical glass. Transmittance measurements are used for the determination of the imaginary RI. Such approaches are feasible for materials that can exhibit macroscopically large defined interfaces, such as bulk liquids, homogeneous solids or thin films and permit RI measurements with high accuracy. For example, RI data for optical glasses are routinely specified to five decimal places [35]. Obviously such measurement techniques cannot be applied to biological cells or microparticles that have a size of just a couple of wavelengths (of visible light). One may even wonder, whether the concept of refractive index makes sense for such small particles at all. For RBCs, this question is particularly easy to answer, as each individual cell can be described by a single complex RI: The thickness of its membrane, at least for the lipid bilayer part, is very small compared to the vacuum wavelength of visible light (400 nm–800 nm) and the optical contrast of the membrane's material is moderate if the RBC is suspended in an aqueous solution. Thus one can usually neglect the membrane entirely in optical modeling. Even large biomolecules, such as Hb or other proteins, have sizes that are rather small (around 5 nm for a Hb molecule) on the scale of the light wavelength. Hence the liquid cytoplasm of RBCs, consisting mainly of a Hb solution can be assumed to be optically homogeneous and the RBC can be described as a dielectric particle defined by its shape and complex RI. The interaction with light

(or scattering thereof) of such a homogeneous microparticle with complex RI \mathbf{n}_s , embedded in a host medium with RI n_m is governed by the Helmholtz equation for the electric field \mathbf{E}

$$\Delta \mathbf{E}(\mathbf{r}) + \mathbf{n}^2(\mathbf{r}) k^2 \mathbf{E}(\mathbf{r}) = 0 \quad (1.7)$$

with a piecewise constant RI

$$\mathbf{n}(\mathbf{r}) = \begin{cases} \mathbf{n}_s & \text{for } \mathbf{r} \text{ inside the particle,} \\ n_m & \text{outside} \end{cases} \quad (1.8)$$

and appropriate boundary conditions on the particle surface. For a scattering problem, the total electric field is the sum of the incident beam \mathbf{E}^i and the scattered field \mathbf{E}^s . In combination with physically motivated radiation conditions for the asymptotic behavior of $\mathbf{E}^s(\mathbf{r})$ at $|\mathbf{r}| \rightarrow \infty$, this defines the scattering problem. For more complex cells, which exhibit internal structure, a spatial distribution of the complex RI $\mathbf{n}(\mathbf{r})$ has to be considered that corresponds to the different constituents of the cell. In any case, the electromagnetic field scattered off a cell or microparticle carries information about it and can thus be used for inferring some of its properties, i. e., for measurements such as microscopy or flow cytometry.

The complex RI of any material depends on the frequency or, equivalently, the vacuum wavelength of the light. Hence one is dealing with a function $\mathbf{n}(\lambda) = n(\lambda) + i\kappa(\lambda)$. This dependence on the wavelength, especially for the real part $n(\lambda)$ is usually called “dispersion”. For example, if the (real) RI decays monotonically with wavelength λ , this is referred to as *normal dispersion*, otherwise as *anomalous dispersion*. In the context of microparticles, this terminology is somewhat ambiguous, because the term “dispersion” is also used in colloidal and polymer science to describe the (non-)uniformity of an ensemble of particles. For example, a suspension of microspheres with identical sizes is called *monodisperse* and one with a size distribution of finite width is called *polydisperse*. In this thesis, we will encounter dispersion in both senses and use standard terminology, but it should always be clear which one is meant.

1.4 Refractive index of RBCs and Hb

Refractive index determination of RBCs and Hb solutions has been carried out already for many decades. Homogeneous solutions of Hb can be obtained from RBCs by breaking open the cell membranes (hemolysis) and it is known that their complex RI depends on the hemoglobin concentration c_{Hb} according to [36–38]

$$\mathbf{n}(\lambda, c_{\text{Hb}}) = \mathbf{n}_{\text{H}_2\text{O}}(\lambda) + c_{\text{Hb}}[\alpha(\lambda) + i\gamma(\lambda)], \quad (1.9)$$

where $\alpha(\lambda)$ is the increment of the real part of the RI or *real RI increment* and $\gamma(\lambda)$ is the increment of the imaginary part of the RI or *imaginary RI increment*. As discussed above, the latter quantity is directly related to the molar attenuation coefficient ε_M , which is well known in the visible, near infrared (IR) and in the near ultraviolet (UV) [37, 39] as is the RI of water $\mathbf{n}_{\text{H}_2\text{O}}(\lambda)$ [40, 41]. On the other hand measurements of $\alpha(\lambda)$, even for a homogeneous bulk liquid are challenging with problems arising from the strong absorbance in this spectral range and from sample preparation at physiological concentrations exceeding $c_{\text{Hb}} = 300 \text{ g L}^{-1}$, due

to high viscosity or incomplete dissolution of Hb [36]. As a result the values reported for $\alpha(\lambda)$ by various researchers differ by more than 30%. In the 1950s Barer and Joseph [36, 42] compiled and reported values of $\alpha \approx 0.19 \text{ mL g}^{-1}$ for Hb solutions in the visible range, without resolving the wavelength dependence. These values have been widely used in simulation and analysis of light scattering and microscopic data [8, 10, 22, 43]. Some more recent experiments confirmed these values in the visible and near IR [44], whereas deviating results were obtained by other authors. Two recent studies [45, 46] found values of $\alpha \approx 0.15 \text{ mL g}^{-1}$ in the visible range. In contrast, significantly higher values of $\alpha \approx 0.26 \text{ mL g}^{-1}$ were reported by Friebel and Meinke [37, 38] in a wider spectral range from 250 nm to 1100 nm. These values have been widely used in application-oriented investigations [13, 29, 30, 32, 47]. Recent studies employing microscopic techniques on Hb solutions in the visible [48] and single RBCs in the UV [49] reported values of $\alpha \approx 0.23 \text{ mL g}^{-1}$.

For practical applications, such as light scattering techniques and microscopy, the optical properties of interest are those of intact RBCs and usually not those of artificially produced Hb solutions. The two need not necessarily coincide quantitatively, even if similar features have been found for their wavelength dependence [15, 49]. As discussed above, the membrane of RBCs can be neglected in optical modeling, hence Eq. (1.9) is believed to provide a suitable model for the RI of intact RBCs, too. In addition to the intrinsic complexity of measuring the optical properties of single microscopic cells compared to bulk liquids, the task is further complicated by the fact that the intracellular concentration c_{Hb} is a priori unknown, since it varies by about 6–8% [22, 50] between the cells of a healthy individual. In studies where the RI of single intact RBCs was measured, data analysis either required a priori knowledge about $\alpha(\lambda)$ [8, 30, 31, 48, 50] or the concentration was eliminated by considering relative RI changes [15]. A very recent study presented spectral microscopic measurements of the complex RI of single cells [49], thus enabling the determination of α using the known γ .

1.5 Outline of this thesis

This thesis is concerned with the quantitative modeling of light scattering by RBCs for the analysis of optical measurements. As outlined above, this comprises two sub-problems: (1) An adequate description of the shapes of RBCs and (2) a knowledge of the complex RI of the cells. Because of the strong discrepancies in the literature values for the real part of the RI increment of RBCs and Hb solutions, much of this thesis is devoted to an accurate determination of this quantity. In combination with light scattering simulations, the results are then used for the interpretation of measurement data from extinction spectroscopy as well as flow cytometry.

The structure of this thesis is as follows: In chapter 2, we briefly discuss some theoretical background of light scattering problems. Chapters 3 and 4 deal with the determination of the (real part of) the RI increment of Hb solutions and RBCs with two complementary approaches. Chapters 5 and 6 present applications of the results of the previous two chapters and finally, the results of this thesis are summarized. Where required, appendices at the end of the respective chapters present additional technical information.

Chapter 2 discusses the governing equations for light scattering problems, derived from the Maxwell equations. A separation of variables for the Helmholtz equation

in spherical coordinates is outlined, which forms the foundation for the (numerical) T -matrix method as well as for the analytical solution of the scattering problem for a sphere (Mie scattering). Furthermore, the basic principles of the discrete dipole approximation (DDA) are discussed, which is a numerical solution method for scatterers with more general shapes.

Chapter 3 presents a theoretical approach that makes use of literature absorption spectra of Hb solutions in order to determine their real RI using Kramers-Kronig (KK) relations. These relations express the relation of the real and imaginary RI as functions of frequency. However, for their practical application, the existing data need to be supplemented in the deep UV by an absorption model that accounts for the peptide backbone of the protein complex Hb. The method is dependent on real RI data for fitting the free parameters of the deep UV model and two different options are discussed for this. As a consequence, the KK approach does not resolve the discrepancies between the existing measurement data for the real RI increment of Hb and RBCs with respect to their absolute value. It does, however, serve to smooth and interpolate or extrapolate (noisy) real RI data and as a consistency check. In addition, KK relations are used in this chapter to compute the RI of three different variants of Hb from their respective spectra, namely besides oxygenated Hb (oxyHb) also deoxygenated Hb (deoxyHb) and the non-functional methemoglobin (metHb) variant.

Chapter 4 discusses the analysis of extinction spectra of intact but sphered RBCs in order to determine their RI by solving an inverse problem. This approach is complementary to the analysis of chapter 3 in that it yields the absolute value of the real RI increment of intact RBCs, but only for the oxygenated case. Similar to the attenuation coefficient of a homogeneous solution, the ensemble-averaged extinction cross section of a dilute cell suspension describes the portion of a beam of light transmitted in the forward direction. It is determined by the cellular concentration in the suspension and by the properties of the cells (size and RI) via a scattering problem. Spectral extinction cross sections are mathematically modeled using the Mie solution for scattering by a homogeneous sphere and the sensitivity to the model parameters is discussed. For analysis of experimentally measured spectra, numerical optimization is employed in combination with a low-dimensional representation of the wavelength-dependence of the real RI. The method is evaluated using suspensions of microscopic synthetic polystyrene (PS) beads that are, e. g., commonly used as a calibration material in flow cytometry. Besides the determination of the size distribution and RI of the suspended particles in a known host medium (water), we discuss the determination of the RI of the suspending fluid using particles with known properties as a probe. Lastly, the method is applied to isovolumetrically sphered RBCs and the results are compared with the KK approach and literature data.

Chapter 5 is about the analysis of extinction spectra of artificially made hemoglobin microparticles (HbMP) [51–53] with respect to their composition of different Hb variants. These particles might serve as a replacement for RBC concentrates in transfusion medicine, but first, their function and safety has to be evaluated. We discuss the influence of the non-spherical “peanut shape” of these HbMP on their

spectral extinction cross sections by means of a spheroidal model and T -matrix computations. Simulations using variable Hb composition are compared to experimental spectra in order to assess the content of oxyHb, deoxyHb and metHb.

Chapter 6 deals with the light scattering by native RBCs in an optical flow cytometer and the interpretation of the corresponding measurement data. The hydrodynamic forces experienced by RBCs in the cytometer due to velocity gradients in the sheath flow are estimated and compared to RBC shapes reported in the literature for different flow conditions. Based on this, an elongated shape model is introduced that accounts for the deformation in flow. The scattering problem is solved numerically using the DDA for undeformed biconcave RBC shapes as well as for the elongated shape model. Measurements at different wavelengths are simulated using the RI dispersion determined in the previous chapters. The effects of random orientation of the RBCs in the flow channel and of their frequency distributions of volume and intracellular Hb concentration are taken into account by Monte Carlo sampling. This allows for a comparison with experimentally determined histograms of the forward scattering cross sections of spheroid RBCs and native RBCs and thus to interpret the data regarding the orientation of the RBCs and their deformation in flow.

Chapter 2

Theoretical background: Light scattering problems

In this chapter, we will outline the theoretical background of light scattering problems for small particles. The governing equations of light scattering problems will be given as well the analytical solution for a homogeneous sphere – *Mie scattering*. Furthermore, the basic principles of the *T-matrix method*, which can be seen as a generalization of Mie scattering and the *discrete dipole approximation* (DDA) are discussed, which are used in chapters 5 and 6 to solve the light scattering problem for artificial hemoglobin microparticles and for native RBCs in a flow cytometer, respectively.

2.1 Maxwell's equations

As we are dealing with problems of classical electrodynamics, the fundamental equations to consider are the Maxwell equations. In their general form, they read

$$\nabla \cdot \mathcal{B} = 0, \quad (2.1)$$

$$\nabla \times \mathcal{E} + \dot{\mathcal{B}} = 0, \quad (2.2)$$

$$\nabla \cdot \mathcal{D} = \rho, \quad (2.3)$$

$$\nabla \times \mathcal{H} - \dot{\mathcal{D}} = \mathbf{j}, \quad (2.4)$$

where \mathcal{B} is the magnetic flux density, \mathcal{E} is the electric field, \mathcal{D} is the displacement field, \mathcal{H} is the magnetic field and \mathbf{j} is the current density. All of these are vector-valued functions of space and time. The charge density ρ is scalar. In linear media and in the absence of external charges and currents, as is the case for the problems considered here, we have

$$\mathcal{B} = \mu \mathcal{H}, \quad (2.5)$$

$$\mathcal{D} = \varepsilon \mathcal{E}, \quad (2.6)$$

$$\rho = 0, \quad (2.7)$$

$$\mathbf{j} = \sigma \mathcal{E}. \quad (2.8)$$

Generally, the magnetic permeability $\mu := \mu_r \mu_0$, the electric permittivity $\varepsilon := \varepsilon_r \varepsilon_0$ and the electric conductivity σ are tensors. Here we assume isotropic media (e. g., the liquid cytoplasm of a RBC), such that μ , ε and σ are scalar quantities. For time

harmonic fields of the form

$$\mathcal{E}(\mathbf{r}, t) = \Re \left\{ \mathbf{E}(\mathbf{r}) e^{-i\omega t} \right\}, \quad (2.9)$$

$$\mathcal{H}(\mathbf{r}, t) = \Re \left\{ \mathbf{H}(\mathbf{r}) e^{-i\omega t} \right\} \quad (2.10)$$

we find the reduced Maxwell equations

$$\nabla \times \mathbf{E} - i\omega \mu \mathbf{H} = 0, \quad (2.11)$$

$$\nabla \times \mathbf{H} + i\omega \hat{\varepsilon} \mathbf{E} = 0 \quad (2.12)$$

with the complex permittivity $\hat{\varepsilon} := \varepsilon + i\sigma/\omega$. Note that in contrast to \mathcal{E} and \mathcal{H} , the amplitudes \mathbf{E} and \mathbf{H} are complex-valued. In physics textbooks, one then usually applies the curl ($\nabla \times$) operator once more to the equations and inserts them into each other. This yields expressions like

$$\begin{aligned} -\nabla \times \nabla \times \mathbf{E} + \mathbf{n}^2 \frac{\omega^2}{c_0^2} \mathbf{E} = \\ -\frac{1}{\mu} (\nabla \mu) \times (\nabla \times \mathbf{E}) \end{aligned} \quad (2.13)$$

where $c_0 = 1/\sqrt{\varepsilon_0 \mu_0}$ is the speed of light in vacuo and $\mathbf{n} = n + i\kappa := c_0 \sqrt{\hat{\varepsilon} \mu}$ is the (complex) RI. One can further use the identity

$$\nabla \times (\nabla \times \mathbf{E}) = -\Delta \mathbf{E} + \nabla (\nabla \cdot \mathbf{E}) \quad (2.14)$$

and exploit the divergence equations in the form $\nabla \cdot \mathbf{H} = 0 = \nabla \cdot \mathbf{E}$, in order to obtain homogeneous wave equations. This works, however, only for cases where the medium is (piecewise) homogeneous, i. e., ε, σ and μ are (piecewise) constant, or where the gradients of the material properties can be neglected. Otherwise, with $\nabla \cdot (\mu \mathbf{H}) = 0 = \nabla \cdot (\varepsilon \mathbf{E})$ one finds

$$\begin{aligned} \Delta \mathbf{E} + \mathbf{n}^2 \frac{\omega^2}{c_0^2} \mathbf{E} = -\nabla \left[\frac{1}{\varepsilon} (\nabla \varepsilon) \cdot \mathbf{E} \right] \\ -\frac{1}{\mu} (\nabla \mu) \times (\nabla \times \mathbf{E}), \end{aligned} \quad (2.15)$$

$$\begin{aligned} \Delta \mathbf{H} + \mathbf{n}^2 \frac{\omega^2}{c_0^2} \mathbf{H} = -\nabla \left[\frac{1}{\mu} (\nabla \mu) \cdot \mathbf{H} \right] \\ -\frac{1}{\hat{\varepsilon}} (\nabla \hat{\varepsilon}) \times (\nabla \times \mathbf{H}). \end{aligned} \quad (2.16)$$

While it is possible, also in this general case to decouple the equations for \mathbf{E} and \mathbf{H} , it is evident from this, that only for the special case of $\nabla \varepsilon = \nabla \sigma = \nabla \mu = 0$, they reduce to the Helmholtz equations

$$\Delta \mathbf{E} + \mathbf{n}^2 k^2 \mathbf{E} = 0, \quad (2.17)$$

$$\Delta \mathbf{H} + \mathbf{n}^2 k^2 \mathbf{H} = 0 \quad (2.18)$$

with the wavevector (in vacuo) $k = \omega/c_0$. In the optical frequency range, one can safely assume that in this high-frequency limit $\mu_r \equiv 1$, such that $\nabla \mu = \nabla \mu_0 = 0$, i. e., optical magnetism is assumed not to exist in any material. This simplifies equations (2.13), (2.15) and (2.16) somewhat. But, even with this reasonable assumption,

Eq. (2.15) becomes Eq. (2.17) only in the limiting case of $|\nabla\varepsilon|/\varepsilon$ small compared to the wavenumber k .

As already discussed in chapter 1, RBCs can be modeled as homogeneous dielectric particles, because of their liquid interior and the negligible thickness of their membrane. Hence, the Helmholtz equations (2.17), (2.18) for divergence-free fields provide a suitable framework to describe their interaction with light. However, some recent reports of the RI distribution inside individual RBCs, measured with optical tomographic methods suggest an inhomogeneous RI distribution with considerable gradients [14, 30, 50, 54, 55]. However, these findings may well be artifacts of the mathematical evaluation of the measurement data in such tomographic techniques. Instead of using the full Maxwell equations or equations derived from them for the general case of time-harmonic fields, like Eq. (2.13), the algorithms used in these tomographies rely either on effective equations for intensities instead of field vectors [30] or on approximations to the scalar Helmholtz equations (2.17), (2.18) for the Cartesian field components of \mathbf{E} and \mathbf{H} [14, 50, 54, 55], such as the Born approximation and Rytov approximation. However, the results thus obtained, i. e., a non-vanishing gradient for the complex RI \mathbf{n} and hence the permittivity ε is outside the range of validity of the scalar Helmholtz equations, let alone approximations thereof. Hence, throughout this thesis, we will model RBCs as optically homogeneous scatterers, which are described by a piecewise-constant RI distribution.

For the case of piecewise-constant material properties, e. g., material 1 in domain Ω (the scatterer) and material 2 outside Ω (the surrounding medium), the boundary conditions

$$[\boldsymbol{\nu} \times \mathbf{E}] = 0 \text{ and } [\boldsymbol{\nu} \times \mathbf{H}] = 0 \text{ on } \partial\Omega \quad (2.19)$$

need to be satisfied. Here, $[f]$ denotes the jump of function f , i. e., the difference between the limit values coming from inside and outside at a given point on the boundary $\partial\Omega$ of Ω and $\boldsymbol{\nu}$ is the outer normal to $\partial\Omega$. In words: The tangential components of vector fields \mathbf{E} and \mathbf{H} are continuous across the interface between two homogeneous media.

2.2 Light scattering

Equations (2.17) and (2.18), or in the more general case (2.15) and (2.16) describe the propagation of a time-harmonic field in a source-free medium in the general case. In microscopy, optical tomography, optical cytometry and many other applications, the setting for the electromagnetic waves is as follows: The sample (e. g., cell or particle), characterized by a complex RI distribution $\mathbf{n}(\mathbf{r})$ is illuminated by an incident electromagnetic field, described by $\mathbf{E}^i(\mathbf{r})$ and $\mathbf{H}^i(\mathbf{r})$. Often times the incident field can be described as a plane wave or a Gaussian beam. In the absence of the sample (e. g., in plain air or water), the incident field would be a solution to the Maxwell equations. In the presence of the sample, one seeks solutions in the form

$$\mathbf{E}(\mathbf{r}) = \mathbf{E}^i(\mathbf{r}) + \mathbf{E}^s(\mathbf{r}), \quad (2.20)$$

where \mathbf{E}^s is the scattered field, and analogously for the magnetic field $\mathbf{H} = \mathbf{H}^i + \mathbf{H}^s$. For a finite scatterer, the RI contrast $\mathbf{n}(\mathbf{r}) - n_m$ has compact support, i. e., is nonzero only on a finite domain Ω . Here n_m denotes the RI of the surrounding medium (e. g., water). In this case the scattered fields \mathbf{E}^s and \mathbf{H}^s must decay with distance from

the scatterer in a spherical-wave-like fashion. This is usually expressed in *Silver-Müller radiation conditions*

$$\begin{aligned}\lim_{r \rightarrow \infty} \left\{ \sqrt{\hat{\epsilon}} \mathbf{E}^s \times \mathbf{r} + \sqrt{\mu} r \mathbf{H}^s \right\} &= 0, \\ \lim_{r \rightarrow \infty} \left\{ \sqrt{\mu} \mathbf{H}^s \times \mathbf{r} - \sqrt{\hat{\epsilon}} r \mathbf{E}^s \right\} &= 0.\end{aligned}\tag{2.21}$$

2.2.1 Scattering problems in spherical coordinates: Mie scattering and the T -matrix method

Analytical solutions of the electromagnetic scattering problem exist for certain special cases, where the boundary of the (homogeneous) scatterer coincides with a coordinate iso-surface in coordinates where the Helmholtz operator is separable. This includes infinitely long cylinders and spheroids [56, 57]. However, probably the most well-known and widely used analytical solution is the one for homogeneous spheres, which is often referred to as “Mie theory”, “Mie scattering” or the “Mie solution”, named after Gustav Mie, who presented it in his famous 1908 paper on “the optics of turbid media, especially colloidal metal solutions”, Ref. [58]. The term “Lorenz-Mie theory” is also widely used, giving credit to Ludvig Lorenz, who reported on the topic in his 1890 paper, Ref. [59]. Of course, derivations of this solution and a detailed discussion of its historical background can be found in textbooks and review articles on light scattering [60–63]. Nevertheless, the basic steps in deriving the Mie solution are outlined in this section. As an excursus, we briefly discuss the T -matrix method for homogeneous scatterers of general shape, which can be seen as a generalization of Mie scattering in so far as both are based on expansions of the electromagnetic fields in vector spherical wavefunctions.

Vector spherical wavefunctions

As discussed above, the scattering by a homogeneous particle, represented by a piecewise-constant RI distribution is described by the Helmholtz equations for \mathbf{E} and \mathbf{H} . It suffices to consider the Helmholtz equation for the electric field [Eq. (2.17)], because the magnetic field follows according to Eq. (2.11), i. e., $\nabla \times \mathbf{E} = i\omega \mu_0 \mu_r \mathbf{H}$. Furthermore the electric field has to be divergence-free, i. e., $\nabla \cdot \mathbf{E} = 0$. Let us, however, first consider the *scalar* Helmholtz equation for some function ψ :

$$\Delta \psi + \mathbf{n}^2 k^2 \psi = 0.\tag{2.22}$$

To simplify notation, we will set $\mathbf{n} = 1$ for the time being. The complex RI can be added back in later, simply by replacing $k \rightarrow \mathbf{n} k$. With the expression for the Laplace operator in spherical coordinates, the Helmholtz equation becomes

$$\frac{1}{r^2} \frac{\partial}{\partial r} \left(r^2 \frac{\partial \psi}{\partial r} \right) + \frac{1}{r^2 \sin \vartheta} \frac{\partial}{\partial \vartheta} \left(\sin \vartheta \frac{\partial \psi}{\partial \vartheta} \right) + \frac{1}{r^2 \sin^2(\vartheta)} \frac{\partial^2 \psi}{\partial \varphi^2} + k^2 \psi = 0,\tag{2.23}$$

which can be solved by separation of variables, i. e., by the ansatz $\psi(r, \vartheta, \varphi) = R(r) \Theta(\vartheta) \Phi(\varphi)$. If this ansatz is put into the Helmholtz equation, the left hand side can be rearranged as the sum of three terms, each of which depends only on one variable. Because the equation holds for all r, ϑ and φ , each of the terms must be constant individually and one obtains ordinary differential equations for R, Θ and Φ . Because of the boundary conditions for the angle-dependent parts Θ and Φ , the

separation constants are integers and the solutions to the scalar Helmholtz equation read

$$\psi_{\mu\nu}^{(\iota)}(k r, \vartheta, \varphi) = z_{\nu}^{(\iota)}(k r) P_{\nu}^{\mu}(\cos \vartheta) e^{i\mu\varphi}, \quad (2.24)$$

where $\nu \in \mathbb{N}$ and $\mu = -\nu, -\nu + 1, \dots, \nu$. The functions P_{ν}^{μ} are associated Legendre polynomials and the four possible solutions for the radial component are

$$z_n^{(\iota)}(x) = \begin{cases} j_{\nu}(x) & \text{for } \iota = 1 \\ y_{\nu}(x) & \text{for } \iota = 2 \\ h_{\nu}^{(1)}(x) = j_{\nu}(x) + iy_{\nu}(x) & \text{for } \iota = 3 \\ h_{\nu}^{(2)}(x) = j_{\nu}(x) - iy_{\nu}(x) & \text{for } \iota = 4 \end{cases}. \quad (2.25)$$

Here j_{ν} and y_{ν} are the *spherical Bessel functions* of the first and second kind, respectively. The functions $h_{\nu}^{(1)}$ and $h_{\nu}^{(2)}$ are the *spherical Hankel functions* of the first and second kind, respectively. Obviously, the two latter functions are just a linear combination of the former two and thus not independent solutions. However, Eq. (2.25) provides two particularly handy solutions of the Helmholtz equation to use in a scattering problem: $j_{\nu}(k r)$ is regular at the origin ($r \rightarrow 0$), where all the other solutions have a singularity and $h_{\nu}^{(1)}(k r)$ decays like an outgoing spherical wave at $r \rightarrow \infty$. From these scalar spherical wavefunctions, we can now construct *vector spherical wavefunctions* (VSWFs) according to

$$\mathbf{M}_{\mu\nu}^{(\iota)}(k r, \vartheta, \varphi) := \nabla \times \left(\mathbf{r} \psi_{\mu\nu}^{(\iota)}(k r, \vartheta, \varphi) \right), \quad (2.26)$$

$$\mathbf{N}_{\mu\nu}^{(\iota)}(k r, \vartheta, \varphi) := \frac{1}{k} \nabla \times \mathbf{M}_{\mu\nu}^{(\iota)}(k r, \vartheta, \varphi) \quad (2.27)$$

for $\iota = 1, \dots, 4$. Due to the curl operator ($\nabla \times$), these are divergence-free. Using some vector-identities, it is relatively easy to show that functions generated in this way are solutions to the vector Helmholtz equations Eq. (2.17), (2.18) if the generating functions $\psi_{\mu\nu}^{(\iota)}$ are solutions to the scalar Helmholtz equation [62, 63]. Because for a divergence-free field that solves the Helmholtz equation, one has $\nabla \times \nabla \mathbf{M} = -\Delta \mathbf{M} = k^2 \mathbf{M}$, these functions furthermore satisfy

$$\mathbf{M}_{\mu\nu}^{(\iota)}(k r, \vartheta, \varphi) = \frac{1}{k} \nabla \times \mathbf{N}_{\mu\nu}^{(\iota)}(k r, \vartheta, \varphi). \quad (2.28)$$

Excursus: *T*-matrix method

The VSWFs defined above can now be used to express any solution to the vector Helmholtz equation in a medium with constant RI and hence for homogeneous scatterers of arbitrary shape. Let us, for the moment assume a general scatterer with RI $\mathbf{n}_s \in \mathbb{C}$ in a medium of RI $n_m \in \mathbb{R}$, defined by the domain Ω . Hence, the incident field, which is regular at the origin, can be formally expanded as

$$\mathbf{E}^i(\mathbf{r}) = \sum_{\nu=1}^{\infty} \sum_{\mu=-\nu}^{\nu} A_{\mu\nu} \mathbf{M}_{\mu\nu}^{(1)}(k_m \mathbf{r}) + B_{\mu\nu} \mathbf{N}_{\mu\nu}^{(1)}(k_m \mathbf{r}), \quad (2.29)$$

where $k_m := n_m k$ is the wavevector in the surrounding medium. Because the incident field is a solution in the absence of the scatterer (i. e., the RI is n_m everywhere), this expansion holds for all $\mathbf{r} \in \mathbb{R}^3$. In the presence of the scatterer, one has to distinguish between the inside and outside of the scatterer. The scattered field outside

the particle is expanded in irregular VSWFs which fulfill the radiation conditions Eq. (2.21)

$$\mathbf{E}^s(\mathbf{r}) = \sum_{\nu=1}^{\infty} \sum_{\mu=-\nu}^{\nu} P_{\mu\nu} \mathbf{M}_{\mu\nu}^{(3)}(k_m \mathbf{r}) + Q_{\mu\nu} \mathbf{N}_{\mu\nu}^{(3)}(k_m \mathbf{r}), \quad \text{for } \mathbf{r} \notin \Omega. \quad (2.30)$$

The *total* electric field inside the scatterer is expressed in regular VSWFs,

$$\mathbf{E}^{\text{int}}(\mathbf{r}) = \sum_{\nu=1}^{\infty} \sum_{\mu=-\nu}^{\nu} C_{\mu\nu} \mathbf{M}_{\mu\nu}^{(1)}(k_s \mathbf{r}) + D_{\mu\nu} \mathbf{N}_{\mu\nu}^{(1)}(k_s \mathbf{r}), \quad \text{for } \mathbf{r} \in \Omega. \quad (2.31)$$

where $k_s := k \mathbf{n}_s$ is the (complex) wavevector inside the scatterer. Formally, the solution approach is as follows: (1) determine the expansion coefficients $A_{\mu\nu}$ and $B_{\mu\nu}$ of the (known) incident wave in VSWFs, (2) determine the expansion coefficients $C_{\mu\nu}$ and $D_{\mu\nu}$ of the internal field as well as $P_{\mu\nu}$ and $Q_{\mu\nu}$ of the scattered field from matching at the boundary according to the boundary conditions Eq. (2.19), i. e.,

$$\lim_{\epsilon \searrow R} \boldsymbol{\nu} \times \left[\mathbf{E}^i(\mathbf{r} + \epsilon \boldsymbol{\nu}) + \mathbf{E}^s(\mathbf{r} + \epsilon \boldsymbol{\nu}) - \mathbf{E}^{\text{int}}(\mathbf{r} - \epsilon \boldsymbol{\nu}) \right] \stackrel{!}{=} 0 \quad \text{and} \quad (2.32)$$

$$\lim_{\epsilon \searrow R} \boldsymbol{\nu} \times \left[\mathbf{H}^i(\mathbf{r} + \epsilon \boldsymbol{\nu}) + \mathbf{H}^s(\mathbf{r} + \epsilon \boldsymbol{\nu}) - \mathbf{H}^{\text{int}}(\mathbf{r} - \epsilon \boldsymbol{\nu}) \right] \stackrel{!}{=} 0 \quad \forall \mathbf{r} \in \partial\Omega, \quad (2.33)$$

where the series expansions of the \mathbf{H} field is obtained using $\nabla \times \mathbf{E} = i\omega\mu_0 \mu_r \mathbf{H}$ and the curl of the series expansions is easily taken using Eqs. (2.27), (2.28). Formally, this leads to (infinite-dimensional) systems of equations like

$$\begin{pmatrix} \mathbf{P} \\ \mathbf{Q} \end{pmatrix} = \mathbb{T} \begin{pmatrix} \mathbf{A} \\ \mathbf{B} \end{pmatrix} \quad (2.34)$$

with \mathbf{A} being a vector containing the expansion coefficients $A_{\mu\nu}$ arranged in series and likewise for \mathbf{B} , \mathbf{P} and \mathbf{Q} . I. e., the coefficient vector of the scattered field can be computed from that of the incident field by means of a matrix \mathbb{T} , whose entries depend on the shape of the boundary of the scatterer. Likewise one finds a matrix that maps $(\mathbf{A}^T, \mathbf{B}^T)^T$ to the coefficients of the internal field $(\mathbf{C}^T, \mathbf{D}^T)^T$. This formalism is known as the *T-matrix method*. Of course, for scatterers with a general shape, computing the *T*-matrix is no trivial task and usually requires approximate numerical methods. A detailed description of this method is given in the book of Mishchenko [63]. We will use a numerical implementation of this method for spheroids to compute the scattering properties of artificial hemoglobin microparticles in chapter 5.

Mie scattering

After these general considerations let us return to the scattering of a plane wave by a homogeneous sphere. Without loss of generality, we can assume the spherical scatterer of radius R to be located at the origin of a spherical coordinate system r, φ, ϑ , i. e., defined by the RI distribution

$$\mathbf{n}(\mathbf{r}) = \begin{cases} \mathbf{n}_s \in \mathbb{C} & \text{for } r < R, \\ n_m \in \mathbb{R} & \text{otherwise.} \end{cases} \quad (2.35)$$

Due to symmetry of the scatterer, we can assume the incident plane wave \mathbf{E}^i to propagate in the z direction and be x -polarized, i. e.,

$$\mathbf{E}^i(\mathbf{r}) = E_0 \mathbf{e}_x e^{i k_m r \cos \vartheta}. \quad (2.36)$$

The expansion of this field in VSWFs can be found by “a lengthy, although straightforward procedure” [61] and reads

$$\mathbf{E}^i(\mathbf{r}) = \sum_{\nu=1}^{\infty} E_{\nu} \left(\mathbf{M}_{o1\nu}^{(1)}(k_m \mathbf{r}) - i \mathbf{N}_{e1\nu}^{(1)}(k_m \mathbf{r}) \right), \quad (2.37)$$

$$\text{with } E_{\nu} = E_0 i^{\nu} \frac{2\nu + 1}{\nu(\nu + 1)}, \quad (2.38)$$

where $\mathbf{M}_{o\mu\nu}^{(\iota)}$ and $\mathbf{N}_{o\mu\nu}^{(\iota)}$ are the VSWFs generated according to Eq. (2.26), (2.27) from the scalar spherical wave functions

$$\psi_{e\mu\nu}^{(\iota)}(k r, \vartheta, \varphi) = z_{\nu}^{(\iota)}(k r) P_{\nu}^{\mu}(\cos \vartheta) \cos(\mu \varphi), \quad (2.39)$$

$$\psi_{o\mu\nu}^{(\iota)}(k r, \vartheta, \varphi) = z_{\nu}^{(\iota)}(k r) P_{\nu}^{\mu}(\cos \vartheta) \sin(\mu \varphi) \quad \text{for } \iota = 1, \dots, 4. \quad (2.40)$$

I. e., for plane wave incidence, the symmetry of the problem causes all coefficients with $\mu \neq \pm 1$ to be zero. In this particular case, the internal and scattered fields are represented by [61]

$$\mathbf{E}^{\text{int}}(\mathbf{r}) = \sum_{\nu=1}^{\infty} E_{\nu} \left(c_{\nu} \mathbf{M}_{o1\nu}^{(1)}(k_s \mathbf{r}) - i d_{\nu} \mathbf{N}_{e1\nu}^{(1)}(k_s \mathbf{r}) \right), \quad (2.41)$$

$$\mathbf{E}^s(\mathbf{r}) = \sum_{\nu=1}^{\infty} E_{\nu} \left(-b_{\nu} \mathbf{M}_{o1\nu}^{(3)}(k_m \mathbf{r}) + i a_{\nu} \mathbf{N}_{e1\nu}^{(3)}(k_m \mathbf{r}) \right). \quad (2.42)$$

As evident, for each index ν , there are four coefficients to be determined. Four equations are defined from the boundary conditions at $r = R$ for the tangential components of (ϑ - and φ -components) of \mathbf{E} and \mathbf{H} . After some more lengthy calculus, this yields (assuming a relative permeability $\mu_r \equiv 1$) [61]

$$a_{\nu} = \frac{\mathbf{m}^2 j_{\nu}(\mathbf{m} X) [X j_{\nu}(X)]' - j_{\nu}(X) [\mathbf{m} X j_n(\mathbf{m} X)]'}{\mathbf{m}^2 j_{\nu}(\mathbf{m} X) [X h_{\nu}^{(1)}(X)]' - h_{\nu}^{(1)}(X) [\mathbf{m} X j_n(\mathbf{m} X)]'}, \quad (2.43)$$

$$b_{\nu} = \frac{j_{\nu}(\mathbf{m} X) [X j_{\nu}(X)]' - j_{\nu}(X) [\mathbf{m} X j_n(\mathbf{m} X)]'}{j_{\nu}(\mathbf{m} X) [X h_{\nu}^{(1)}(X)]' - h_{\nu}^{(1)}(X) [\mathbf{m} X j_n(\mathbf{m} X)]'}, \quad (2.44)$$

for the coefficients of the scattered field, where X is the dimensionless *size parameter* and \mathbf{m} is the *relative refractive index*:

$$X = k_m R = \frac{2\pi n_m R}{\lambda}, \quad \mathbf{m} = \frac{k_s}{k_m} = \frac{n_s}{n_m}. \quad (2.45)$$

For the coefficients of the internal field one obtains

$$c_{\nu} = \frac{j_{\nu}(X) [X h_{\nu}^{(1)}(X)]' - h_{\nu}^{(1)}(X) [X j_n(X)]'}{j_{\nu}(\mathbf{m} X) [X h_{\nu}^{(1)}(X)]' - h_{\nu}^{(1)}(X) [\mathbf{m} X j_n(\mathbf{m} X)]'}, \quad (2.46)$$

$$d_{\nu} = \frac{\mathbf{m} j_{\nu}(X) [X h_{\nu}^{(1)}(X)]' - \mathbf{m} h_{\nu}^{(1)}(X) [X j_n(X)]'}{\mathbf{m}^2 j_{\nu}(\mathbf{m} X) [X h_{\nu}^{(1)}(X)]' - h_{\nu}^{(1)}(X) [\mathbf{m} X j_n(\mathbf{m} X)]'}. \quad (2.47)$$

These coefficients define the electric field everywhere and the magnetic field follows using $\nabla \times \mathbf{E} = i\omega\mu_0\mu_r\mathbf{H}$. In particular, the coefficients a_{ν} and b_{ν} contain all the information about the far field, i. e., the asymptotic behavior at $r \rightarrow \infty$. For

example, the relation between the scattered field amplitudes and the incident field is given by

$$\begin{pmatrix} E_{\parallel}^s \\ E_{\perp}^s \end{pmatrix} = \frac{e^{ik_m(r-z)}}{-ik_m r} \underbrace{\begin{pmatrix} S_2 & 0 \\ 0 & S_1 \end{pmatrix}}_{=S} \begin{pmatrix} E_{\parallel}^i \\ E_{\perp}^i \end{pmatrix}. \quad (2.48)$$

Here E_{\parallel} and E_{\perp} denote the component of \mathbf{E} parallel and perpendicular to the scattering plane, respectively. The scattering plane is spanned by the direction of incidence, i. e., the z -axis and the direction of observation defined by the unit vector $\mathbf{e}_r(\vartheta, \varphi) = \mathbf{r}/r$. For Mie scattering, the elements of the *amplitude scattering matrix* S are given by

$$\begin{aligned} S_1(\vartheta) &= \sum_{\nu=1}^{\infty} \frac{2\nu+1}{\nu(\nu+1)} [a_{\nu}\pi_{\nu}(\vartheta) + b_{\nu}\tau(\vartheta)], \\ S_2(\vartheta) &= \sum_{\nu=1}^{\infty} \frac{2\nu+1}{\nu(\nu+1)} [a_{\nu}\tau_{\nu}(\vartheta) + b_{\nu}\pi(\vartheta)] \end{aligned} \quad (2.49)$$

with angle-dependent functions

$$\pi_{\nu}(\vartheta) = \frac{P_{\nu}^1(\cos \vartheta)}{\sin \vartheta}, \quad \tau_{\nu}(\vartheta) = \frac{dP_{\nu}^1(\cos \vartheta)}{d\vartheta}. \quad (2.50)$$

Obviously, a variety of quantities can be derived from this solution, such as the scattered intensity distribution in the far field or the various optical cross sections of the particle. Most importantly for this thesis, we will make use of the *extinction cross section* in chapters 4 and 5, which describes how much light a scatterer removes from the incident beam due to scattering and absorption.

For computations, one has to truncate the series at some ν_{\max} , which can be quite large (in the thousands) depending on the values of \mathbf{m} and X and the desired accuracy. Hence, an efficient evaluation is required of the special functions defining the coefficients a_{ν} and b_{ν} and the angle-dependent functions π_{ν} and τ_{ν} . For both cases, computation with downward recurrence schemes is possible [61] and has been implemented in various programming languages over the last decades [64].

2.2.2 Discrete dipole approximation

As evident from the discussion of Mie scattering above, obtaining an analytical solution for electromagnetic scattering problems is difficult enough even in the simplest cases. For general shapes, or inhomogeneous scatterers one usually has to use numerical methods. The numerical method that will be used to solve the scattering problem for native RBCs in chapter 6 of this thesis is the *discrete dipole approximation* (DDA). While the Mie solution and the T -matrix method are based on the separation of variables for the Helmholtz equation, the DDA is based on the use of the *Green's function* of the corresponding differential operator.

Let us, again, consider the Helmholtz equations Eq. (2.17) and (2.18). As long as we are using Cartesian coordinates, instead of \mathbf{E} or \mathbf{H} we can consider a scalar field ψ , corresponding, e. g., to one of the Cartesian components of the vector fields. We can then re-write the Helmholtz equation for ψ as

$$\Delta\psi + k_m^2 \psi = -k_m^2 (\mathbf{m}^2 - 1) \psi, \quad (2.51)$$

where, as before, $k_m = k n_m$ and $\mathbf{m} = \mathbf{n}/n_m$. The contrast or *object function*

$$f := \mathbf{m}^2 - 1 \quad (2.52)$$

then has compact support, i. e., it is zero outside the scatterer. Note that we do not restrict the RI distribution \mathbf{n} to be piecewise constant, but only require $\mathbf{n}(\mathbf{r}) = n_m \forall \mathbf{r} \notin \Omega$. We also note that there exists a Green's function G for the outgoing wave propagation from a source g , i. e., the inhomogeneous equation

$$\Delta\psi(\mathbf{r}) + k_m^2 \psi(\mathbf{r}) = -\delta(\mathbf{r} - \mathbf{r}') \quad (2.53)$$

is solved by

$$\psi(\mathbf{r}) = G(\mathbf{r}, \mathbf{r}'). \quad (2.54)$$

Equivalently, the equation

$$\Delta\psi(\mathbf{r}) + k_m^2 \psi(\mathbf{r}) = -g(\mathbf{r}) \quad (2.55)$$

is solved by

$$\psi(\mathbf{r}) = \int_{\mathbf{R}^3} G(\mathbf{r}, \mathbf{r}') g(\mathbf{r}') d\mathbf{r}', \quad (2.56)$$

for all (appropriately defined) source functions g . The Green's function of the three-dimensional (scalar) Helmholtz operator is

$$G(\mathbf{r}, \mathbf{r}') = \frac{1}{4\pi} \frac{e^{ik_m |\mathbf{r} - \mathbf{r}'|}}{|\mathbf{r} - \mathbf{r}'|}. \quad (2.57)$$

Note that this function describes radiating solutions caused by some source term g which is nonzero only on a finite domain. I. e., for scattering problems, it does not describe the incident field, which can be thought of as being caused by sources at infinity. Hence, if we formally solve Eq. (2.51), the result is

$$\psi(\mathbf{r}) = \psi^i(\mathbf{r}) + k_m^2 \int_{\Omega} G(\mathbf{r}, \mathbf{r}') f(\mathbf{r}') \psi(\mathbf{r}') d\mathbf{r}'. \quad (2.58)$$

Because the unknown ψ field appears on both sides of the equation, this does not solve the scattering problem, but is a *volume-integral* formulation thereof. Note that the integration domain is the volume of the scatterer Ω because f is equal to zero outside.

In the derivation of $\Delta\mathbf{E} + \mathbf{n}^2 k^2 \mathbf{E} = 0$, which is a scalar wave equation for the Cartesian components of \mathbf{E} , we had to assume a piecewise constant permittivity, i. e., $\nabla\varepsilon(\mathbf{r}) = 0$ almost everywhere or at least require that the gradients $\nabla\varepsilon$ are sufficiently small. For the volume-integral formulation one can, however, drop this restriction without adding much complexity to the problem. If we instead consider Eq. (2.13) with the only assumption that $\mu_r \equiv 1$ (no materials exhibiting optical magnetism have been found yet), we have

$$-\nabla \times \nabla \times \mathbf{E} + \mathbf{n}^2 k^2 \mathbf{E} = 0, \quad (2.59)$$

which is also known as the *vector Helmholtz equation* [62] or *vector wave equation* [63]. Like before for the (scalar) Helmholtz equation, it suffices to consider \mathbf{E} , because \mathbf{H} follows from $\nabla \times \mathbf{E} = i\omega \mu_0 \mathbf{H}$. As before, this vector equation can be

re-written with constant coefficients on the left hand side and a source term on the right hand side:

$$-\nabla \times \nabla \times \mathbf{E} + k_m^2 \mathbf{E} = -k_m^2 (\mathbf{m}^2 - 1) \mathbf{E} \quad (2.60)$$

$$\iff (\nabla \times \nabla \times \mathbb{1} - k_m^2) \mathbf{E} = i\omega \mu_0 \mathbf{J}, \quad (2.61)$$

where $\mathbb{1}$ denotes the 3×3 identity matrix and the current density \mathbf{J} is defined as

$$\mathbf{J}(\mathbf{r}) := -i\omega \varepsilon_0 n_m^2 (\mathbf{m}^2(\mathbf{r}) - 1) \mathbf{E}. \quad (2.62)$$

Like the object function f before, this current density has compact support, i. e., $\mathbf{J}(\mathbf{r}) = 0 \forall \mathbf{r} \notin \Omega$. The (tensor-valued) Green's function for the vector Helmholtz operator $(\nabla \times \nabla \times \mathbb{1} - k_m^2)$ reads [62, 63]

$$\mathbf{G}(\mathbf{r}, \mathbf{r}') = \left(\mathbb{1} + \frac{1}{k_m^2} \nabla \otimes \nabla \right) \frac{1}{4\pi} \frac{e^{ik_m |\mathbf{r} - \mathbf{r}'|}}{|\mathbf{r} - \mathbf{r}'|}, \quad (2.63)$$

which is known as the *free-space dyadic Green's function*. Here $\mathbf{a} \otimes \mathbf{b}$ denote the dyadic product of two vectors with $(\mathbf{a} \otimes \mathbf{b})_{mn} = a_m b_n$. Hence, by integrating Eq. (2.61) using the Green's function, one finds a formal expression for the total electric field

$$\mathbf{E}(\mathbf{r}) = \mathbf{E}^i(\mathbf{r}) + i\omega \mu_0 \int_{\Omega} \mathbf{G}(\mathbf{r}, \mathbf{r}') \mathbf{J}(\mathbf{r}') d\mathbf{r}'. \quad (2.64)$$

The idea of the DDA is to use a volume discretization, i. e., a partitioning of the scatterer into a finite number of subvolumes such that – by approximating the integrand inside each grid cell by a constant – the above integral equation becomes a system of linear equations. This is, however, not a straightforward task due to the singularity of the Greens function, which becomes more clear when Eq. (2.63) is written out [65]

$$\mathbf{G}(\mathbf{r}, \mathbf{r}') = \frac{1}{4\pi} \frac{e^{ik_m R}}{R} \left[\mathbb{1} - \frac{\mathbf{R} \otimes \mathbf{R}}{R^2} - \frac{1 - ik_m R}{k_m^2 R^2} \left(\mathbb{1} - 3 \frac{\mathbf{R} \otimes \mathbf{R}}{R^2} \right) \right] \quad (2.65)$$

with $\mathbf{R} := \mathbf{r} - \mathbf{r}'$ and $R = |\mathbf{R}|$. I. e., for $R \rightarrow 0$, the Green's function behaves like $1/R^3$. This singularity makes it necessary to perform the integration with utmost care when $\mathbf{r} \in \Omega$ in Eq. (2.64), i. e., when the field inside the scatterer is to be computed.

If we divide the volume of the scatterer into N disjoint subvolumes, i. e., $\Omega = \bigcup_{i=1}^N V_i$ and $V_i \cap V_j = \emptyset$ for $i \neq j$, then the volume integral equation can be written as

$$\mathbf{E}(\mathbf{r}) - i\omega \mu_0 \int_{V_i} \mathbf{G}(\mathbf{r}, \mathbf{r}') \mathbf{J}(\mathbf{r}') d\mathbf{r}' = \mathbf{E}^i(\mathbf{r}) + i\omega \mu_0 \sum_{\substack{j=1 \\ j \neq i}}^N \int_{V_j} \mathbf{G}(\mathbf{r}, \mathbf{r}') \mathbf{J}(\mathbf{r}') d\mathbf{r}', \quad (2.66)$$

where we are thinking of V_i being the subvolume containing \mathbf{r} . In this case, the integrals on the right hand side are regular and if the subvolumes V_j are sufficiently small, they can be approximated by assuming a constant current density

$$\mathbf{J}(\mathbf{r}') \approx \mathbf{J}(\mathbf{r}_j) \quad \forall \mathbf{r}' \in V_j, \quad (2.67)$$

where \mathbf{r}_j is a fixed point inside V_j for each $j = 1, \dots, N$. This constant term can be taken in front of the integral. The remaining integral $\int_{V_j} \mathbf{G}(\mathbf{r}, \mathbf{r}') d\mathbf{r}'$ then depends

only on the shape of the subvolume V_j and on the position vector \mathbf{r} relative to it. Usually one further approximates [65]

$$\int_{V_j} \mathbf{G}(\mathbf{r}_i, \mathbf{r}') d\mathbf{r}' \approx |V_j| \mathbf{G}(\mathbf{r}_i, \mathbf{r}_j) \quad \text{for } i \neq j. \quad (2.68)$$

For the integral in the left hand side of Eq. (2.66), the singularity of the Green's function can be formally separated out [62] using

$$\begin{aligned} \int_{V_i} \mathbf{G}(\mathbf{r}, \mathbf{r}') \mathbf{J}(\mathbf{r}') d\mathbf{r}' &= \int_{V_i} \left[\mathbf{G}(\mathbf{r}, \mathbf{r}') \mathbf{J}(\mathbf{r}') - \mathbf{G}^{\text{sta}}(\mathbf{r}, \mathbf{r}') \mathbf{J}(\mathbf{r}') \right] d\mathbf{r}' \\ &+ \frac{1}{k_m^2} \oint_{\partial V_i} \left[-\frac{\mathbf{r}' - \mathbf{r}}{4\pi |\mathbf{r}' - \mathbf{r}|^3} \mathbf{J}(\mathbf{r}') \right] \boldsymbol{\nu}(\mathbf{r}') dS(\mathbf{r}'), \end{aligned} \quad (2.69)$$

where $\boldsymbol{\nu}$ denotes the outer normal of V_i and

$$\mathbf{G}^{\text{sta}}(\mathbf{r}, \mathbf{r}') = \frac{1}{k_m^2} \nabla \otimes \nabla \frac{1}{4\pi |\mathbf{r}' - \mathbf{r}|} = -\frac{1}{4\pi k_m^2 R^3} \left(\mathbb{1} - 3 \frac{\mathbf{R} \otimes \mathbf{R}}{R^2} \right) \quad (2.70)$$

is the *static limit* of the free space dyadic Green's function, i. e., the limit for $k_m \rightarrow 0$. The term $\mathbf{G}^{\text{sta}}(\mathbf{r}, \mathbf{r}') \mathbf{J}(\mathbf{r}')$ was formally subtracted and added back in in Eq. (2.69). The surface integral in Eq. (2.69) results from application of the divergence theorem. Again using the approximation that for sufficiently small subvolumes the current density is constant, i. e., $\mathbf{J}(\mathbf{r}') \approx \mathbf{J}(\mathbf{r}_i)$ for all $\mathbf{r}' \in V_i$, one obtains

$$\int_{V_i} \mathbf{G}(\mathbf{r}_i, \mathbf{r}') \mathbf{J}(\mathbf{r}') d\mathbf{r}' \approx \left[\mathbf{M}_i - \frac{1}{k_m^2} \mathbf{L}_i \right] \mathbf{J}(\mathbf{r}_i) \quad (2.71)$$

$$\text{with} \quad \mathbf{M}_i := \int_{V_i} \left[\mathbf{G}(\mathbf{r}_i, \mathbf{r}') - \mathbf{G}^{\text{sta}}(\mathbf{r}_i, \mathbf{r}') \right] d\mathbf{r}' \quad (2.72)$$

$$\text{and} \quad \mathbf{L}_i := \oint_{\partial V_i} \left[\frac{\boldsymbol{\nu}(\mathbf{r}') \otimes (\mathbf{r}' - \mathbf{r}_i)}{4\pi |\mathbf{r}' - \mathbf{r}_i|^3} \right] dS(\mathbf{r}'). \quad (2.73)$$

Note that the integrals in \mathbf{M}_i and \mathbf{L}_i are regular and that they only depend on the geometry of the subvolume V_i .

With the volume of the scatterer discretized and the singularity of the Green's function explicitly treated, one now obtains for Eq. (2.66)

$$\mathbf{E}(\mathbf{r}_i) - i\omega \mu_0 \left[\mathbf{M}_i - \frac{1}{k_m^2} \mathbf{L}_i \right] \mathbf{J}(\mathbf{r}_i) \approx \mathbf{E}^i(\mathbf{r}_i) + i\omega \mu_0 \sum_{\substack{j=1 \\ j \neq i}}^N |V_j| \mathbf{G}(\mathbf{r}_i, \mathbf{r}_j) \mathbf{J}(\mathbf{r}_j), \quad (2.74)$$

which is a set of algebraic equations for the electric field \mathbf{E} and the current density \mathbf{J} at the fixed inner points \mathbf{r}_i of the grid cells V_i . Instead of the total field \mathbf{E} , this is the usually re-written [62] in terms of the *exciting field* \mathbf{E}^{exc} as

$$\mathbf{E}_i^{\text{exc}} = \mathbf{E}_i^i + i\omega \mu_0 \sum_{\substack{j=1 \\ j \neq i}}^N |V_j| \mathbf{G}_{ij} \mathbf{J}_j \quad (2.75)$$

where $\mathbf{E}_i := \mathbf{E}(\mathbf{r}_i)$ etc. and the exciting field is defined as

$$\mathbf{E}_i^{\text{exc}} := \mathbf{E}_i - i\omega \mu_0 \left[\mathbf{M}_i - \frac{1}{k_m^2} \mathbf{L}_i \right] \mathbf{J}_i. \quad (2.76)$$

By substituting the definition of the current density [Eq. (2.62)] back in, one has

$$\mathbf{E}_i^{\text{exc}} = \mathbf{E}_i - \left(k_m^2 \mathbf{M}_i - \mathbf{L}_i\right) \left(\mathbf{m}_i^2 - 1\right) \mathbf{E}_i = \underbrace{\left[\mathbb{1} - \left(k_m^2 \mathbf{M}_i - \mathbf{L}_i\right) \left(\mathbf{m}_i^2 - 1\right)\right]}_{=: \mathbf{A}_{ii}} \mathbf{E}_i, \quad (2.77)$$

$$\mathbf{J}_i = -i\omega\varepsilon_0 n_m^2 \left(\mathbf{m}_i^2 - 1\right) \mathbf{A}_{ii}^{-1} \mathbf{E}_i^{\text{exc}}. \quad (2.78)$$

This leads to the $3N \times 3N$ linear system of equations

$$\mathbf{E}_i^{\text{exc}} = \mathbf{E}_i^i + k_m^2 \sum_{\substack{j=1 \\ j \neq i}}^N |V_j| \mathbf{G}_{ij} \left(\mathbf{m}_j^2 - 1\right) \mathbf{A}_{jj}^{-1} \mathbf{E}_j^{\text{exc}} \quad (2.79)$$

which can be solved numerically for all inner grid cells (“dipoles”) \mathbf{r}_i , $i = 1, \dots, N$ of the scatterer for a known incident field \mathbf{E}^i and thus forms the basis of the DDA [62]. The result of this procedure, i. e., the exciting field $\mathbf{E}_i^{\text{exc}}$ (or the total field \mathbf{E}_i) inside the scatterer can then be used to compute all kinds of resulting quantities. For example the far field, i. e., the $|\mathbf{r}| \rightarrow \infty$ limit of $\mathbf{E}^s(\mathbf{r})$ is easily computed using the far-field limit of the Green’s function [63]

$$\mathbf{G}(\mathbf{r}, \mathbf{r}') \sim \frac{1}{4\pi} \frac{e^{ik_m r}}{r} e^{-ik_m \mathbf{e}_r \cdot \mathbf{r}'} \left[\mathbb{1} - \frac{\mathbf{e}_r \otimes \mathbf{e}_r}{r^2}\right] \quad \text{at } r \rightarrow \infty \text{ with } r' \text{ finite}, \quad (2.80)$$

where $\mathbf{e}_r = \mathbf{r}/r$. One finds

$$\mathbf{E}^s(\mathbf{r}) \sim \frac{e^{ik_m r}}{-ik_m r} \mathbf{F}(\mathbf{e}_r) \quad \text{at } r \rightarrow \infty \quad (2.81)$$

$$\text{with } \mathbf{F}(\mathbf{e}_r) \approx \frac{-ik_m^3}{4\pi} \left[\mathbb{1} - \frac{\mathbf{e}_r \otimes \mathbf{e}_r}{r^2}\right] \sum_{j=1}^N |V_j| \left(\mathbf{m}_j^2 - 1\right) \mathbf{A}_{jj}^{-1} \mathbf{E}_j^{\text{exc}} e^{-ik_m \mathbf{e}_r \cdot \mathbf{r}_j}. \quad (2.82)$$

Other far field properties of the scatterer, such as the scattering cross section can be computed from the scattering amplitude \mathbf{F} in a straightforward manner.

So far, we have not specified the shape of the subvolumes V_j , $j = 1, \dots, N$ used for discretization. Typically one uses a cubic grid, which is also the case for the ADDA 1.2 implementation [66] used in the computations presented in this thesis. The coefficient matrix defining the system of equations (2.79) can be quite large: If, for example, a scatterer with 100 fL volume (e. g., a typical RBC) is to be discretized with 50 nm cubes (about one tenth the vacuum wavelength of visible light), one has

$$N = \frac{100 \text{ fL}}{50 \text{ nm}^3} = 8 \times 10^5 \quad (2.83)$$

grid cells. Hence systems of more than a million equations ($3N$) are easily encountered and suitable methods of numerical linear algebra that exploit the special structure of the matrices occurring in this particular problem have to be used for efficiently solving light scattering problems in the DDA framework [62, 65]. The implementation of the DDA employed in this thesis (chapter 6) is the ADDA 1.2 code. More details on the ADDA code are found in Ref. [66]. A more detailed discussion of the theoretical aspects of the DDA and its different formulations (which, e. g., use different degrees of approximation) can be found in Refs. [62, 65].

Chapter 3

Calculation of optical properties of hemoglobin solutions with Kramers-Kronig relations*

3.1 Introduction

As discussed in chapter 1, the absorption spectra of hemoglobin (Hb) solutions have been measured with high accuracy over a wide range of wavelengths and are known since several decades. In contrast, measurements of their refractive index (RI), or rather, the real part thereof, especially at physiologically relevant high concentrations, are challenging and have only been presented as late as 2005 for a wide spectral range [37]. However, these data have much larger measurement uncertainties than the corresponding absorption spectra, such that the real part of the complex refractive index is less accurately known than its imaginary part, the absorbance.

As it turns out, the real and imaginary part of the complex RI as a function of frequency or vacuum wavelength are not independent, but they are connected through integral transformations, the *Kramers-Kronig* (KK) relations. Knowledge of the wavelength dependence of either the real or imaginary part of the RI allows for computing the respective other quantity. First described in 1926 by Ralph Kronig and in 1927 by Hendrik Anthony Kramers for specific models of an atomic gas (see, e.g., Ref. 67) these relations state that the real part of the RI can be computed from an integral transform of the absorption coefficient in the frequency domain (Kronig, Kramers) and vice versa (Kramers). It was later shown, that these relations are a general property of certain linear response functions, which stems from the fact that a physical system is subject to the causality principle: No response can occur before the excitation. If this simple restriction in the time domain is taken to the frequency domain (or wavelength domain), KK relations arise for any linear response function of a physical system, such as the electric permittivity or magnetic permeability of a material, relating its real and imaginary part by integral transforms. Consequently such relations also hold for the complex RI, which is an analytical function of permittivity and permeability. This has motivated researchers

* This chapter is based on
J. Gienger, H. Groß, J. Neukammer, and M. Bär. Determining the refractive index of human hemoglobin solutions by Kramers-Kronig relations with an improved absorption model. *Appl. Opt.*, 55(31):8951–8961, 2016.

to use KK relations to obtain the real part of the RI of different materials directly from accurate measurements of absorption spectra, i. e., the imaginary part of the RI as a function of wavelength. In particular, this has been applied to aqueous Hb solutions, with the aim to describe the optical properties of RBCs [68, 69].

In this chapter, first a short introduction is given to the physical and mathematical origin of the KK relations along with some examples of the dispersion properties of the RI they imply. We discuss why it is a non-trivial task to extract any meaningful wavelength-dependence of the real RI from absorption spectra, due to the finite wavelength range of the measured spectra and the global, long-ranged character of the KK relations. The KK relations are then applied to Hb solutions, making up the interior of RBCs. As mentioned above, this is not a new idea. However, previous theoretical studies of these solutions have missed important contributions of the real RI because they ignored the effects of the absorbance of water [68] or Hb itself [68, 69] outside the spectral range under consideration. To overcome these issues, the contribution of water can be separated in the equations as was presented by Sydoruk et al. [69]. Additionally an absorption model for proteins at low wavelengths can be constructed based on the scarce reports of deep UV protein spectra in the literature, which is presented in this chapter. A limitation of all KK analyses is the following: The dispersion features of the real RI can be accurately determined from the absorption spectra, whereas the wavelength-independent (or weakly wavelength-dependent) background to which these features are added is not accessible. Hence, any KK computation of the real RI from the imaginary RI has to be substituted by measurements of the real RI for at least one wavelength. For the approach presented here, this means that the free parameters of the deep UV model have to be determined by comparing to experimental data, which is achieved by non-local fitting. As discussed in chapter 1, literature data for the real RI (increment) of Hb solution scatter widely, hence the result of the KK analysis depends on the dataset used. Here, the model parameters will be fitted to the measurements of the real RI increment of oxygenated Hb (oxyHb) solutions presented by Friebel and Meinke [38], which were the best data available by the time the work described in this chapter was originally done. This case is published in the author's own article Ref. 47. More recent measurements on intact RBCs that are presented in chapter 4 of this thesis suggest that these literature data may have been off by 20% due to concentration errors of the Hb solutions. Hence the KK analysis is repeated with these data and the results are compared.

The result of the KK analysis is a curve for the real RI increment of oxyHb solutions, which may be smoothed significantly compared to the noisy literature data the model was fitted to [38]. We compare it to the results of previous studies that missed significant contributions of deep UV absorption [68, 69]. The main advantage of the KK analysis, however, is that besides oxyHb the real RI increment is easily computed for other Hb variants for which no measurement data exist, since the absorption spectra are known for a variety of Hb variants [39] and the deep UV absorbance is not expected to differ between them. This is demonstrated for deoxygenated Hb (deoxyHb) and the non-functional methemoglobin (metHb).

3.2 Introduction to Kramers-Kronig relations

3.2.1 Simple derivation of Kramers-Kronig relations

If a system is subject to a time-dependent perturbation $v(t)$ to which it reacts linearly, the time-dependent response $u(t)$ is given by convolution

$$u(t) = \int_{-\infty}^{\infty} f(\tau) v(t - \tau) d\tau = (f * v)(t), \quad (3.1)$$

where $f(t)$ is the response function of the system. All three functions f, u and v are real-valued. A physical example for such a system would be an electric field $\mathcal{E} \hat{=} v$ causing a polarization $\mathcal{P} \hat{=} u$ in a material. If the above equation is Fourier-transformed to the frequency domain, one obtains by the convolution theorem:

$$U(\omega) := \mathcal{F}[u](\omega) = \frac{1}{\sqrt{2\pi}} \int_{-\infty}^{\infty} u(t) e^{-i\omega t} dt = \sqrt{2\pi} F(\omega) V(\omega), \quad (3.2)$$

with the Fourier transforms of the individual functions $F(\omega) := \mathcal{F}[f](\omega)$ and $V(\omega) := \mathcal{F}[v](\omega)$. In the case of an electrically polarized material, one typically writes

$$\mathbf{P}(\omega) = \varepsilon_0 \chi(\omega) \mathbf{E}(\omega) \quad (3.3)$$

$$\mathbf{D}(\omega) = \varepsilon_0 [1 + \chi(\omega)] \mathbf{E}(\omega), \quad (3.4)$$

where $\mathbf{D}(\omega) := \mathbf{P}(\omega) + \varepsilon_0 \mathbf{E}(\omega)$ is the displacement field, $\chi(\omega)$ is the electric susceptibility of the material and $\varepsilon_0 = 8.854 \dots \times 10^{-12} \text{ F m}^{-1}$ is the vacuum permittivity. The relative permittivity is then defined as $\varepsilon_r := 1 + \chi(\omega)$. Hence $F(\omega) \hat{=} \varepsilon_0 \chi(\omega) / \sqrt{2\pi}$.

If the system exhibits *causality*, this requires that no response occurs before the system is excited. Hence the response function $f(t)$ in Eq. (3.1) can only be non-zero for positive times, i. e.,

$$f(t) = 0 \quad \forall t < 0. \quad (3.5)$$

Decomposing the function into an even and an odd part, this can also be written as

$$f(t) = f_{\text{odd}}(t) + f_{\text{even}}(t) = f_{\text{odd}}(t) + \text{sgn}(t) f_{\text{odd}}(t), \quad (3.6)$$

where $f_{\text{odd}}(-t) = -f_{\text{odd}}(t)$ and $f_{\text{even}}(-t) = f_{\text{even}}(t)$ and $\text{sgn}(t)$ denotes the sign of t . If this is transformed to the frequency domain, the product in the last term becomes a convolution

$$F(\omega) = \underbrace{\mathcal{F}[f_{\text{odd}}](\omega)}_{=: F_{\text{odd}}(\omega)} + \underbrace{\mathcal{F}[f_{\text{even}}](\omega)}_{=: F_{\text{even}}(\omega)} = F_{\text{odd}}(\omega) + \frac{1}{\sqrt{2\pi}} (F_{\text{odd}} * \text{SGN})(\omega), \quad (3.7)$$

where the Fourier transform of the sign function is

$$\text{SGN}(\omega) = \frac{1}{\sqrt{2\pi}} \int_{-\infty}^{\infty} \text{sgn}(t) e^{-i\omega t} dt = -\frac{1}{\sqrt{2\pi}} \frac{2i}{\omega}. \quad (3.8)$$

From the properties of the Fourier transform, it follows that the F_{odd} , being the transform of a real, odd function is an imaginary-valued function, whereas F_{even} is real-valued. Or in other words $F(\omega) = F_{\text{real}}(\omega) + i F_{\text{imag}}(\omega)$ with

$$F_{\text{odd}}(\omega) = i F_{\text{imag}}(\omega) \quad \text{and} \quad F_{\text{even}}(\omega) = F_{\text{real}}(\omega). \quad (3.9)$$

Hence, according to Eq. (3.7)

$$F_{\text{real}}(\omega) = \frac{1}{\sqrt{2\pi}} (i F_{\text{imag}} * \text{SGN})(\omega) = \frac{1}{\pi} \int_{-\infty}^{\infty} F_{\text{imag}}(\Omega) \frac{1}{\Omega - \omega} d\Omega. \quad (3.10)$$

The sign f denotes the Cauchy principal value integral. It has to be used since the kernel is singular at $\omega = \Omega$. For a function $x \mapsto f(x)$ that has a singularity at $x_0 \in [a, b]$, the principal value integral is defined as

$$\int_a^b f(x) dx := \lim_{\varepsilon \searrow 0} \left[\int_a^{x_0 - \varepsilon} f(x) dx + \int_{x_0 + \varepsilon}^b f(x) dx \right] \quad (3.11)$$

and likewise for multiple singularities.

Eq. (3.10) is the Kramers-Kronig relation in the most general form. Starting from a linear response of a system, described by the function real-valued $f(t)$ and the assumption that causality applies to the system, one finds that the real and imaginary parts of the Fourier transform $F(\omega)$ of the response function are connected by a *Hilbert transform*, i. e., a convolution with a $1/\omega$ kernel. One could also have expressed Eq. (3.6) in terms of f_{even} and obtained the complementary relations to Eq. (3.10), expressing F_{imag} as an integral transform of F_{real} .

The electric susceptibility $\chi(\omega)$ of a material was given as an example for such a linear response function. Because the Kramers-Kronig relations are linear, such relations also hold for the relative permittivity $\varepsilon_r(\omega) := 1 + \chi(\omega)$. Equivalently one finds these relations for the magnetic susceptibility and the relative permeability $\mu_r(\omega)$. Because the complex refractive index is an analytic function of the two

$$\mathbf{n}(\omega) = n(\omega) + i\kappa(\omega) = \sqrt{\varepsilon_r(\omega) \mu_r(\omega)}, \quad (3.12)$$

one finds KK relations of the same form [67]. They read

$$n(\omega) - 1 = + \frac{1}{\pi} \int_{-\infty}^{\infty} \frac{1}{\Omega - \omega} \kappa(\Omega) d\Omega, \quad (3.13)$$

$$\kappa(\omega) = - \frac{1}{\pi} \int_{-\infty}^{\infty} \frac{1}{\Omega - \omega} n(\Omega) d\Omega. \quad (3.14)$$

The first relation is written for $n(\omega) - 1$ instead of $n(\omega)$ since this function tends to 0 as $\omega \rightarrow \pm\infty$ and the Hilbert transform of a constant is zero for all finite ω . The real and imaginary parts of the RI fulfill an additional symmetry property: Upon time reversal (a wave propagating “backwards”), the refraction of an electromagnetic wave at an interface, described by the real part of the RI n does not change, whereas the absorption coefficient, proportional to the imaginary part of the RI κ , changes sign. Since time reversal ($t \leftrightarrow -t$) of the phase factor $e^{\pm i\omega t}$ is equivalent to $\omega \leftrightarrow -\omega$, one has

$$n(-\omega) = n(\omega) \quad \text{and} \quad \kappa(-\omega) = -\kappa(\omega). \quad (3.15)$$

Using this, the KK relations take their most common form

$$n(\omega) - 1 = + \frac{2}{\pi} \int_0^{\infty} \frac{\Omega}{\Omega^2 - \omega^2} \kappa(\Omega) d\Omega, \quad (3.16)$$

$$\kappa(\omega) = - \frac{2}{\pi} \int_0^{\infty} \frac{\omega}{\Omega^2 - \omega^2} n(\Omega) d\Omega, \quad (3.17)$$

which can be found in many optics textbooks, e. g., Ref. 61. The symmetry properties implied by these equations have to be borne in mind when modeling the absorption spectra outside the measured region.

It will also be useful to write the KK relations in terms of vacuum wavelength $\lambda = 2\pi c_0/\omega$, $c_0 = 2.99792458 \times 10^8 \text{ m s}^{-1}$. Without implied symmetry, they read

$$n(\lambda) - 1 = +\frac{1}{\pi} \mathcal{P} \int_{-\infty}^{\infty} \left(\frac{1}{\Lambda} - \frac{1}{\Lambda - \lambda} \right) \kappa(\Lambda) d\Lambda, \quad (3.18)$$

$$\kappa(\lambda) = -\frac{1}{\pi} \mathcal{P} \int_{-\infty}^{\infty} \left(\frac{1}{\Lambda} - \frac{1}{\Lambda - \lambda} \right) n(\Lambda) d\Lambda, \quad (3.19)$$

where n and κ were assumed to be bounded functions, such that the only singularities are due to the $1/(\Omega - \omega)$ or $1/(\Lambda - \lambda)$ terms. In this case, the change of variables in the principal value integrals works as for any other integral, which is however not generally the case. With the symmetry implications ($n(\lambda)$ is even, $\kappa(\lambda)$ is odd) they read

$$n(\lambda) - 1 = -\frac{2}{\pi} \mathcal{P} \int_0^{\infty} \frac{\lambda}{\Lambda} \frac{\lambda}{\Lambda^2 - \lambda^2} \kappa(\Lambda) d\Lambda =: \mathcal{K}[\kappa](\lambda), \quad (3.20)$$

$$\kappa(\lambda) = +\frac{2}{\pi} \mathcal{P} \int_0^{\infty} \frac{\lambda}{\Lambda^2 - \lambda^2} n(\Lambda) d\Lambda. \quad (3.21)$$

3.2.2 Some analytical examples

We will now illustrate the properties of the KK relations using some simple models for the imaginary RI that can be transformed analytically relatively easily. For this purpose, the representation in the wavelength domain is chosen, which is also used later for measurement data. The corresponding curves are shown in Fig. 3.1.

δ -Peak

A δ -function may be used to model spectral lines which are very far away from the observed wavelength range. The contribution from the δ -peak

$$\kappa_{\delta}(\lambda) = \frac{\pi}{2} a_{\delta} \lambda_{\delta} \delta(\lambda - \lambda_{\delta}) \quad \text{for } \lambda > 0, \lambda_{\delta} > 0 \quad (3.22)$$

with the dimensionless amplitude a_{δ} to the real part of the RI is

$$\mathcal{K}[\kappa_{\delta}](\lambda) = \frac{a_{\delta}}{\lambda_{\delta}^2} \left(\frac{1}{\lambda_{\delta}^2} - \frac{1}{\lambda^2} \right)^{-1}, \quad (3.23)$$

which for $\lambda \gg \lambda_{\delta}$ behaves like

$$\mathcal{K}[\kappa_{\delta}](\lambda) \sim a_{\delta} \left(1 + \frac{\lambda_{\delta}^2}{\lambda^2} \right) \quad (3.24)$$

and becomes a constant a_{δ} in the limit $\lambda_{\delta} \rightarrow 0^+$, hence for this model

$$\lim_{\lambda_{\delta} \rightarrow 0^+} n(\lambda) = 1 + a_{\delta}. \quad (3.25)$$

This simplistic model reveals an important consequence of the KK relations for the RI of basically any material in the visible range. Even if the material is non-absorbing in the visible spectral range, it usually exhibits strong absorbance at very

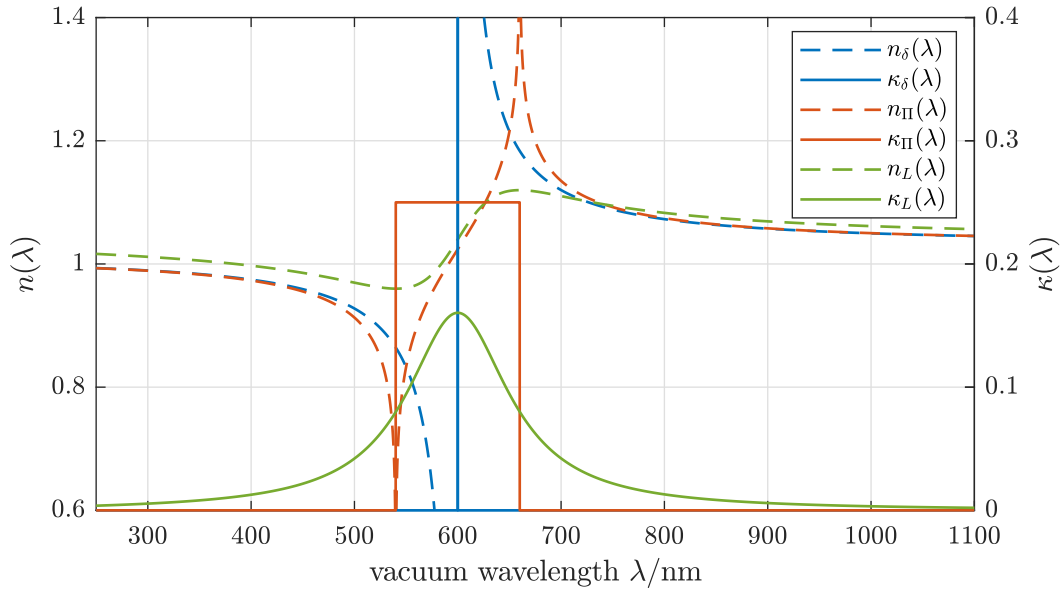


Figure 3.1: Three different absorption peaks (δ , rectangle and Lorentzian) and their KK transforms.

short wavelengths or high photon energies, such as the deep UV, since the inner electron shells of the atoms in the material will be excited. Thus, a variety of overlapping absorption lines is expected for any material at short wavelengths. If these lines are far away from the spectral region of interest, their contribution to the real RI reduces to that of a delta function. Hence a wavelength-independent background contribution of deep UV (or lower wavelength) absorption is a generic feature of real RIs in the visible spectral range, which are thus higher than 1.

Rectangle peak

A rectangle peak (or box function)

$$\kappa_{\Pi} = a_{\Pi} \frac{\lambda_{\Pi}}{\Gamma_{\Pi}} \begin{cases} 1 & \text{for } \lambda \in [\lambda_{\Pi} - \Gamma_{\Pi}, \lambda_{\Pi} + \Gamma_{\Pi}], \\ 0 & \text{otherwise for } \lambda > 0 \end{cases} \quad (3.26)$$

centered at λ_{Π} with dimensionless amplitude a_{Π} and half-width $\Gamma_{\Pi} > 0$ can serve as a very crude model for a finite-width absorption line. Its KK transform reads

$$\mathcal{K}[\kappa_{\Pi}](\lambda) = \frac{a_{\Pi}}{\pi} \frac{\lambda_{\Pi}}{\Gamma_{\Pi}} \left[2 \ln \left(\frac{\lambda_{\Pi} + \Gamma_{\Pi}}{\lambda_{\Pi} - \Gamma_{\Pi}} \right) + \ln \left| \frac{(\lambda_{\Pi} - \Gamma_{\Pi} - \lambda)(\lambda_{\Pi} - \Gamma_{\Pi} + \lambda)}{(\lambda_{\Pi} + \Gamma_{\Pi} - \lambda)(\lambda_{\Pi} + \Gamma_{\Pi} + \lambda)} \right| \right]. \quad (3.27)$$

I. e., the real part of the RI $n(\lambda) = 1 + \mathcal{K}[\kappa_{\Pi}](\lambda)$ diverges logarithmically at the edges of the rectangle at $\lambda_{\Pi} \pm \Gamma_{\Pi}$ (and, for $\lambda < 0$, their mirror images at $-\lambda_{\Pi} \mp \Gamma_{\Pi}$). This behavior indicates that one should preferably not compute $n(\lambda)$ from data for $\kappa(\lambda)$ on an incomplete spectral range that cuts off any absorption features, because this effectively means introducing such edges and divergences.

Lorentzian peak

The Lorentzian line

$$\kappa_L(\lambda) = a_L \frac{1}{\pi} \frac{\Gamma_L}{(\lambda - \lambda_L)^2 + \Gamma_L^2} \quad (3.28)$$

is a simple model for an absorption feature of finite width. Harmonic oscillator models for electrons yield this kind of functional dependence for the imaginary part of the susceptibility $\Im[\chi(\omega)]$, i. e., as a function of ω rather than λ . In the case of sufficiently narrow lines ($\Gamma_L \ll \lambda_L$) and low amplitude, the expression for $\Im[\chi(\omega)]$ can be approximated to yield the above equation. As written, $\kappa_L(\lambda)$ is neither an odd nor an even function of the wavelength λ . To model a physically plausible absorption, a second line with the peak at $\lambda = -\lambda_L$ has to be subtracted to fulfill $\kappa(-\lambda) = -\kappa(\lambda)$.¹ It is however easier to first transform the individual absorption lines with the KK relation for functions without defined parity functions [Eq. (3.18)] and later add/subtract the results. The Hilbert transform

$$\mathcal{H}[\kappa_L](\lambda) := \frac{1}{\pi} \int_{-\infty}^{\infty} \frac{1}{\Lambda - \lambda} \kappa_L(\Lambda) d\Lambda \quad (3.29)$$

can be computed either by complex integration with the residue theorem or by explicitly performing the real integration. It reads

$$\mathcal{H}[\kappa_L](\lambda) = -a_L \frac{1}{\pi} \frac{\lambda - \lambda_L}{(\lambda - \lambda_L)^2 + \Gamma_L^2}. \quad (3.30)$$

According to Eq. (3.18), the contribution to the real RI due to $\kappa_L(\lambda)$ is

$$n_L(\lambda) - 1 = \mathcal{H}[\kappa_L](0) - \mathcal{H}[\kappa_L](\lambda) = a_L \frac{1}{\pi} \left[\frac{\lambda_L}{\lambda_L^2 + \Gamma_L^2} + \frac{\lambda - \lambda_L}{(\lambda - \lambda_L)^2 + \Gamma_L^2} \right] \quad (3.31)$$

and accordingly for the mirrored Lorentzian line with $\lambda_L \leftrightarrow -\lambda_L$. The first term in the brackets is constant and the second term describes the shape of a typical dispersion feature at or around an absorption line, see Fig. 3.1.

Such a Lorentzian line will be used to substitute the literature spectra of Hb solutions in the deep UV. I. e., for some interval $\lambda \in [\lambda_a, \lambda_b]$ literature data is available and will be used to compute the KK transform. For $\lambda < \lambda_a$ a model function like above will be assumed for $\kappa(\lambda)$. When the KK transform of this model is computed, one needs to integrate only over the deep ultraviolet spectrum and not $\lambda \in] -\infty, \infty[$. The analytical expression for this reads

$$\begin{aligned} g_L(\lambda) &= \frac{1}{\pi} \int_{-\lambda_a}^{\lambda_a} \left(\frac{1}{\Lambda} - \frac{1}{\Lambda - \lambda} \right) \left[\kappa_L(\lambda) - \kappa_L(\lambda) \Big|_{\lambda_L \leftrightarrow -\lambda_L} \right] d\Lambda \\ &= \frac{a_L}{\pi^2} \left\{ \frac{1}{2} \ln \left(\frac{(\lambda_a - \lambda_L)^2 + \Gamma_L^2}{(\lambda_a + \lambda_L)^2 + \Gamma_L^2} \right) \times \left[\frac{\Gamma_L}{(\lambda - \lambda_L)^2 + \Gamma_L^2} + \frac{\Gamma_L}{(\lambda + \lambda_L)^2 + \Gamma_L^2} - \frac{2\Gamma_L}{\lambda_L^2 + \Gamma_L^2} \right] \right. \\ &\quad - \ln \left(\left| \frac{\lambda_a - \lambda}{\lambda_a + \lambda} \right| \right) \times \left[\frac{\Gamma_L}{(\lambda - \lambda_L)^2 + \Gamma_L^2} - \frac{\Gamma_L}{(\lambda + \lambda_L)^2 + \Gamma_L^2} \right] \\ &\quad + \left(\pi - \arctan \frac{\Gamma_L}{\lambda_a - \lambda_L} - \arctan \frac{\Gamma_L}{\lambda_a + \lambda_L} \right) \\ &\quad \left. \times \left[\frac{\lambda - \lambda_L}{(\lambda - \lambda_L)^2 + \Gamma_L^2} - \frac{\lambda + \lambda_L}{(\lambda + \lambda_L)^2 + \Gamma_L^2} + \frac{2\lambda_L}{\lambda_L^2 + \Gamma_L^2} \right] \right\} \quad (3.32) \end{aligned}$$

for $\lambda > \lambda_a$. Even though it looks somewhat involved, Eq. (3.32) is useful to describe the deep UV part of the absorption spectrum without the need for numerical integration. For later use, we also define the transformation for unit amplitude $\tilde{g}_L(\lambda)$, such that $g_L(\lambda) = a_L \tilde{g}_L(\lambda)$.

¹ This is also the case for the δ and rectangle peaks. Since they have finite support, this was taken into account automatically by using the KK relations in the form of Eq. (3.20) rather than Eq. (3.18).

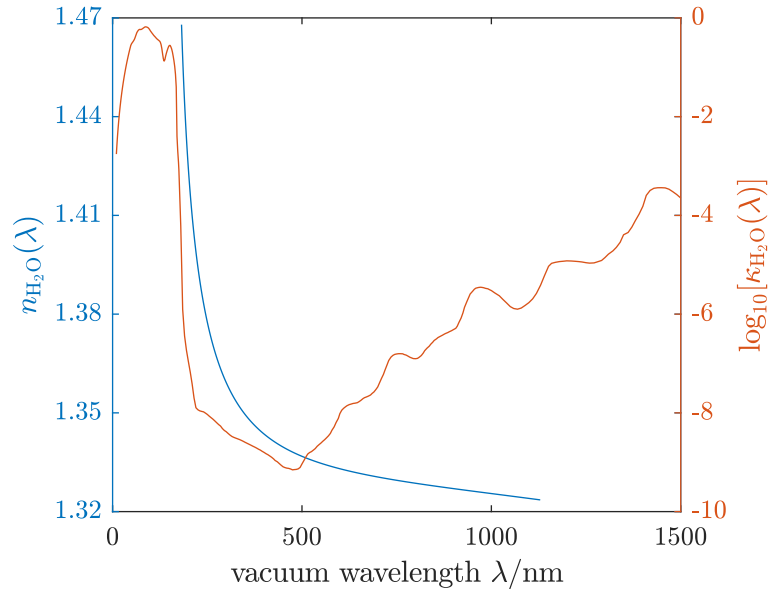


Figure 3.2: Complex RI of water. The real part $n_{\text{H}_2\text{O}}$ is from Ref. 41, the imaginary part $\kappa_{\text{H}_2\text{O}}$ from Ref. 40.

3.3 Application to hemoglobin solutions

3.3.1 General considerations

The KK relations Eq. (3.20) and (3.21) imply that knowledge of either the real part $n(\lambda)$ or the imaginary part $\kappa(\lambda)$ for all vacuum wavelengths $\lambda \in [0, \infty[$ fully determines the respective other function. However, the requirement $\lambda \in [0, \infty[$ can never be fulfilled in practice. This poses a problem in applying the KK relations to measurement data and one has to find ways to deal with the missing information outside the measured spectral domain. The most common application is to compute the real part $n(\lambda)$ from the imaginary part $\kappa(\lambda)$, where the latter is equivalent to the absorption spectrum. As already discussed above, basically every material exhibits strong absorbance at very short wavelengths (i. e., high energies), such as deep UV, causing a real RI significantly larger than 1 in the visible spectral range, even if the material is non-absorbing in this region. As an example (Fig. 3.2), water has very low $\kappa(\lambda) < 1 \times 10^{-5}$ for $\lambda \in [200, 1100]$ nm, but has an RI of $n(\lambda) > 1.3$. The cause for this is strong absorbance in the deep UV around $\lambda = 100$ nm and somewhat weaker absorbance in the IR for $\lambda > 1.5 \mu\text{m}$. While causing noticeable refraction in the visible, the wavelength dependence of $n(\lambda)$ is rather simple and monotonically decreasing, which is referred to as *normal dispersion*. This example shows that one cannot simply use finite-wavelength-range spectra without having at least an idea of what is happens outside this range. If one were to apply the KK relations to the spectrum of water restricted to the range $[200, 1100]$ nm (implying $\kappa_{\text{H}_2\text{O}}(\lambda) = 0$ outside this interval), the resulting real RI $n(\lambda)$ would differ from 1 on the 10^{-5} scale, which is obviously incorrect.

3.3.2 Formal Kramers-Kronig transform of the spectrum of hemoglobin solutions and erythrocytes

In the spectral range of $\lambda \in [250, 1100]$ nm the strongest absorption of light by RBCs and hence of blood is caused by Hb. Water has a fairly low absorption coefficient in this region (cf. Fig. 3.2) and other RBC components contained in the cytosol (e. g., other proteins, sugars, ions) exhibit rather low concentrations. Hence, it is not a strong simplification to consider a two-component system of water and hemoglobin.

Since the Beer-Lambert law is known to hold for Hb solutions at least up to physiological concentrations [37], the total imaginary RI of the solution is given by

$$\kappa(\lambda) = \frac{\ln 10 \lambda}{4\pi} \sum_{j=\text{Hb}, \text{H}_2\text{O}} \frac{\varepsilon_j^M(\lambda) c_j}{M_j} = \sum_{j=\text{Hb}, \text{H}_2\text{O}} \phi_j \kappa_j(\lambda), \quad (3.33)$$

where ε_j^M is the molar absorptivity, M_j the molar mass and κ_j is the imaginary RI of pure species j . The quantity

$$\phi_j := \frac{c_j}{\rho_j} \quad (3.34)$$

denotes the fraction between the respective mass concentration and the density of the pure species $j = \text{Hb}, \text{H}_2\text{O}$. As a side note, the density of the solution is given by

$$\rho = \sum_{j=\text{Hb}, \text{H}_2\text{O}} c_j = \sum_{j=\text{Hb}, \text{H}_2\text{O}} \phi_j \rho_j. \quad (3.35)$$

The density of Hb solutions is known to increase linearly with mass concentration up to at least 46% (mass/volume) [70] at a slope that corresponds to the relative density difference between a Hb crystal ($\rho_{\text{Hb}} \approx 1330 \text{ g L}^{-1}$ are given in [36] for proteins in general) and water ($\rho_{\text{H}_2\text{O}} \approx 1000 \text{ g L}^{-1}$). Under these circumstances, the fraction ϕ_j is also equal to the volume fraction of the constituents, i. e.,

$$\phi_j = \frac{V_j}{V_{\text{total}}} \quad (3.36)$$

and $\phi_{\text{Hb}} + \phi_{\text{H}_2\text{O}} = 1$, which is not generally the case for ϕ_j defined in Eq. (3.34). Hence, in the following we use $\phi_{\text{Hb}} \equiv \phi$ and $\phi_{\text{H}_2\text{O}} = 1 - \phi$.

The imaginary RI of the solution is

$$\kappa(\lambda) = \phi \kappa_{\text{Hb}}(\lambda) + (1 - \phi) \kappa_{\text{H}_2\text{O}}(\lambda), \quad (3.37)$$

where $\kappa_{\text{H}_2\text{O}}(\lambda)$ is the absorbance of pure water and $\kappa_{\text{Hb}}(\lambda)$ is the absorbance of “pure hemoglobin in aqueous solution”. It should be noted that κ_{Hb} is not equal to the imaginary RI of a crystal of pure hemoglobin as is revealed by comparison with data for the complex dielectric function of thin Hb films [71]. Eq. (3.37) is similar to the ansatz in [69], where, however, the authors did not include the prefactor $1 - \phi$ for the water absorbance, which results in a relevant difference: A normal physiological intra-erythrocyte Hb concentration of 340 g L^{-1} corresponds to a volume fraction of $\phi \approx 0.26$ or 26%. The term for the absorbance contribution of Hb, $\phi \kappa_{\text{Hb}}(\lambda)$, becomes

$$\phi \kappa_{\text{Hb}}(\lambda) = c_{\text{Hb}} \frac{\kappa_{\text{Hb}}(\lambda)}{\rho_{\text{Hb}}} \stackrel{\text{def.}}{=} \gamma(\lambda) c_{\text{Hb}} \gamma(\lambda), \quad (3.38)$$

where $\gamma(\lambda)$ is Hb’s concentration-specific increment of the imaginary RI, or the *imaginary RI increment*. Since the Hb concentration c_{Hb} is measured in g L^{-1} , the

unit for γ is L g^{-1} . Eq. (3.37) thus becomes

$$\kappa(\lambda) = c_{\text{Hb}} \gamma(\lambda) + \left(1 - \frac{c_{\text{Hb}}}{\rho_{\text{Hb}}}\right) \kappa_{\text{H}_2\text{O}}(\lambda). \quad (3.39)$$

Applying the KK relation Eq. (3.20) formally to the expression for the absorption of the Hb solution Eq. (3.39) for $\lambda \in [0, \infty[$, we obtain

$$n(\lambda) - 1 = c_{\text{Hb}} g(\lambda) + \left(1 - \frac{c_{\text{Hb}}}{\rho_{\text{Hb}}}\right) (n_{\text{H}_2\text{O}}(\lambda) - 1), \quad (3.40)$$

where $g(\lambda) := \mathcal{K}[\gamma](\lambda)$ is the transformed spectrum of Hb. This formal transformation of the absorption results in an equation for the real RI of the Hb solution and the real RI increment $\alpha(\lambda)$

$$\begin{aligned} n(\lambda) &= n_{\text{H}_2\text{O}}(\lambda) + c_{\text{Hb}} \left[g(\lambda) - \frac{n_{\text{H}_2\text{O}}(\lambda) - 1}{\rho_{\text{Hb}}} \right] \\ &\stackrel{\text{def. } \alpha(\lambda)}{=} n_{\text{H}_2\text{O}}(\lambda) + c_{\text{Hb}} \alpha(\lambda). \end{aligned} \quad (3.41)$$

The linear-affine dependence of $n(\lambda)$ on c_{Hb} in Eq. (3.41) is in agreement with experimental findings [38]. In Eq. (3.39), we have formally split off the water absorption. After KK transform, this term yields the real RI of water $n_{\text{H}_2\text{O}}(\lambda)$, which contributes to the background in the dispersion relations of the Hb solutions [cf. Eq. (3.41)]. Since the real RI of water – unlike the real RI of Hb – is known to high accuracy, this provides valuable additional information compared to the application of the KK-transform only to the measured absorption spectrum of a Hb solution in the visible and near UV/IR range. The latter approach was presented by Faber et al. [68] and the results later found to be in disagreement with measurements [37, 38].

The idea to separate the water contributions was already presented by Sydoruk et al. [69]. However, the prefactor $1 - \phi$ was missed in Eq. (3.37) and a different result obtained for $\alpha(\lambda)$. Compared to Sydoruk et al., we obtain an additional term $(n_{\text{H}_2\text{O}}(\lambda) - 1)/\rho_{\text{Hb}}$ for the real RI increment of Hb. We discuss the differences between the results obtained in [68], [69] and the present result with the improved model in section 3.4.2. For numerical values of $n_{\text{H}_2\text{O}}(\lambda)$, we use a four-term Sellmeier formula that is accurate to at least five decimal places [41].

3.3.3 UV absorption model

So far, we have used the KK relations to formally derive Eq. (3.41) and the fact that we are dealing with integrals over all wavelengths $\lambda \in [0, \infty[$ and slowly decaying integral kernels was not a problem. However, Eq. (3.41) still contains the term $g(\lambda) = \mathcal{K}[\gamma](\lambda)$ that is to be evaluated with experimental data for the imaginary RI increment $\gamma(\lambda)$ of Hb. Data are available only for finite wavelength ranges $\lambda \in [\lambda_a, \lambda_b] = [228, 1100] \text{ nm}$ [37, 39, 72]. Although the integral kernel in the KK relations [Eq. (3.20)] is decaying with increasing distance from the pole at $\Lambda = \lambda$, it is long-ranged. Hence, one cannot simply restrict the integration to $[\lambda_a, \lambda_b]$, as this would be equivalent to claiming $\gamma(\lambda) \equiv 0$ for $\lambda \notin [\lambda_a, \lambda_b]$. To deal with this, we can first formally split the absorption spectrum into three parts: (i) the ‘‘literature’’ range $\lambda \in [\lambda_a, \lambda_b] = [228, 1100] \text{ nm}$ where literature data is available, (ii) the deep UV $\lambda < \lambda_a$ with no quantitative spectra available and (iii) the far IR $\lambda > \lambda_b$ with no accurate quantitative spectra available.

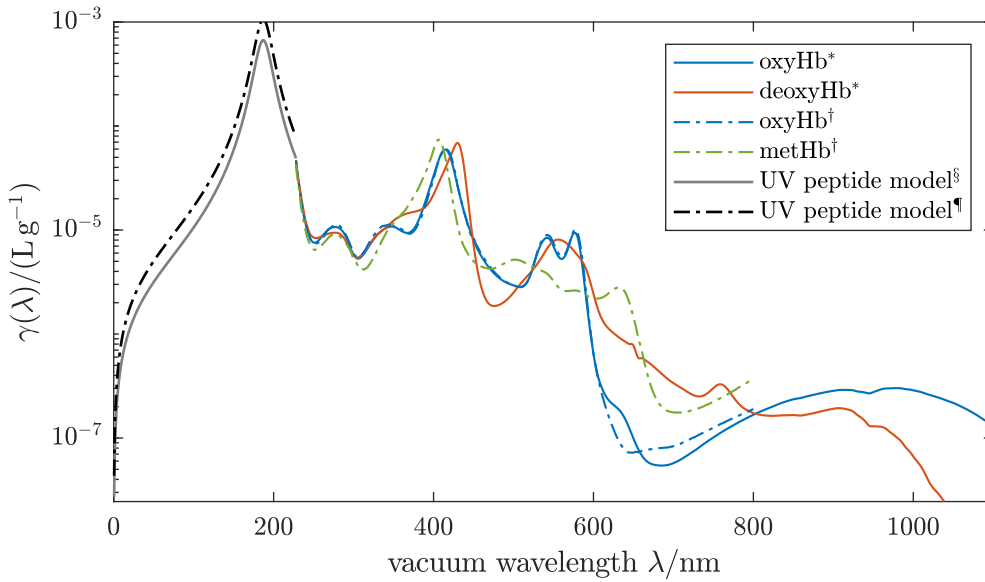


Figure 3.3: Imaginary RI increment $\gamma(\lambda)$ of human Hb variants in aqueous solutions. * denotes data for oxyHb and deoxyHb from Friebel and Meinke [37] for $\lambda \in [250, 1100]$ nm. † denotes data for oxyHb and deoxyHb from the book of Zijlstra, Buursma and van Assendelft [39] for $\lambda \in [450, 800]$ nm. Both sources were supplemented at the UV end ($\lambda > 228$ nm) with data from Sugita, Nagai and Yoneyama [72]. Cubic spline interpolation was applied to obtain a step width of 1 nm.

A Lorentzian peak models the deep UV absorbance of the peptide backbone. Parameter fits to two different datasets of the real RI increment are shown: § is fitted to measurements of Friebel and Meinke [38], ¶ is fitted to values determined from extinction spectra of RBCs in chapter 4 of this thesis.

In addition to the known absorption spectrum (Fig. 3.3) with strong absorption in the vicinity of the Soret band at 420 nm, the metalloprotein Hb has an even stronger absorption peak in the deep UV. This feature stems from the peptide bonds forming the backbone of any polypeptide or protein and is characteristic for this class of substances. The corresponding extinction coefficient curves $\varepsilon(\lambda)$ are similar among a variety of proteins and the absorbance maximum is typically located at $\lambda = 187$ nm [73, 74]. The similarity of the spectra between different proteins and peptides may be the reason for the scarcity of quantitative data in the literature: These deep UV spectra are not particularly helpful for the analysis of chemical composition or structure.

This peptide-peak must be accounted for to perform a proper KK analysis, but is, unfortunately, not resolved in the existing experimental Hb spectra. However, data were reported for human and bovine albumin [74] – a protein found in blood serum. Albumin is similar to hemoglobin in its molar mass and optical properties at wavelengths away from the characteristic Hb absorption band at 420 nm. The absorption maximum for human albumin is reported as $\varepsilon(187 \text{ nm}) = 86.0 \text{ L g}^{-1} \text{ cm}^{-1}$, corresponding to a value of $\gamma(187 \text{ nm}) = 2.95 \times 10^{-4} \text{ L g}^{-1}$, which is more than four times as high as the peak around 420 nm (Fig. 3.3).

This generic protein absorption is modeled as a Lorentzian curve

$$\gamma_L(\lambda) = a_L \frac{1}{\pi} \frac{\Gamma_L}{(\lambda - \lambda_L)^2 + \Gamma_L^2} - a_L \frac{1}{\pi} \frac{\Gamma_L}{(\lambda + \lambda_L)^2 + \Gamma_L^2}, \quad (3.42)$$

compare section 3.2.2 where the partial transform of this model curve, integrated over the deep UV only, was given. We set the central wavelength of the peak to $\lambda_L = 187$ nm. For the width of the curve, we note that for proteins in general, Woods and O'Bar report that “the increase in absorbance at 187 nm is threefold over that at 205 nm and fourfold over that at 210 nm” [74]. This description fits well to a half width of the curve of $\Gamma_L = 11.6$ nm. To account for the influence of extreme UV absorption at lower wavelengths, a constant offset in the real RI increment is added to the model. This can be interpreted as stemming from a delta-peak of unknown amplitude located at zero wavelength $\gamma_\delta(\lambda) = \lim_{\lambda_\delta \rightarrow 0^+} \frac{\pi}{2} a_\delta \lambda_\delta \delta(\lambda - \lambda_\delta)$.

The imaginary RI increment of Hb drops to below 10^{-7} L g^{-1} for $\lambda > 1100$ nm, and the imaginary RI of a 26.7 g L^{-1} Hb (oxyHb/deoxyHb) solution does not significantly exceed that of water at least up to $\lambda = 2.6 \mu\text{m}^2$. Hence, no significant contribution to the real RI increment is expected from $\lambda > \lambda_b$. The model used for the imaginary RI increment of Hb solutions is thus

$$\gamma(\lambda) = \begin{cases} \gamma_{\text{lit}}(\lambda) & \text{for } \lambda \in [\lambda_a, \lambda_b] \\ \gamma_L(\lambda) + \gamma_\delta(\lambda) & \text{for } \lambda \in [0, \lambda_a[\\ 0 & \text{for } \lambda > \lambda_b. \end{cases} \quad (3.43)$$

For metHb, the available high-quality spectra [39] end at $\lambda_b > 800$ nm. However, since the absorbance of metHb, oxyHb and deoxyHb is actually very low ($\gamma < 10^{-6} \text{ L g}^{-1}$) already for $\lambda > 700$ nm (see Fig. 3.3), the same model, i. e., zero absorbance above highest wavelength of literature spectra, is also used for metHb.

For the integral transform $g(\lambda) = \mathcal{K}[\kappa](\lambda)$, the contribution from the δ -peak $\gamma_\delta(\lambda)$ is $g_\delta(\lambda) = a_\delta$ and hence constant and the contribution $g_L(\lambda) = a_L \tilde{g}_L(\lambda)$ from the Lorentzian, integrated only over the deep UV part of the spectrum, can be obtained analytically (see section 3.2.2). Here $\tilde{g}_L(\lambda)$ is the contribution for a Lorentzian of unit amplitude. Thus, we are left with

$$g(\lambda) = g_{\text{lit}}(\lambda) + a_L \tilde{g}_L(\lambda) + a_\delta, \quad (3.44)$$

where only the first term $g_{\text{lit}}(\lambda) := \mathcal{K}[\gamma_{\text{lit}}](\lambda)$ needs to be evaluated numerically.

Numerical evaluation is straightforward. An integration scheme is used, which evaluates the KK relations as a Riemann sum with Taylor expansion at the singularities of the integrand as described, e. g., in [75]. The scheme used is described in Appendix 3.A.

3.3.4 Fitting to measurement data

There remain two free parameters in the expression for the real RI increment

$$\alpha(\lambda; a_L, a_\delta) = g_{\text{lit}}(\lambda) - \underbrace{\frac{n_{\text{H}_2\text{O}}(\lambda) - 1}{\rho_{\text{Hb}}}}_{=: g_{\text{H}_2\text{O}}(\lambda)} + a_L \tilde{g}_L(\lambda) + a_\delta. \quad (3.45)$$

Neither of the two free parameters, a_L and a_δ can be computed from literature absorption spectra a priori with satisfying accuracy. For the peptide absorption a_L , the order of magnitude can be estimated from the semi-quantitative data of

² An extended wavelength range of the data published in Ref. 37 was kindly provided by M. Friebe.

Ref. 74, where the absorbance maximum is given. It is important to keep in mind that, in the visible, the KK transform of the peptide-peak in the deep UV depends much stronger on the center position and the area under the peak than on its actual maximum. Since the peak shape is not quantitatively known, the peak height alone does not contain enough information to determine a_L . Thus we use a linear least squares approach to optimize the parameter values.

Measurement data for the real RI increment is given at N wavelengths λ_i , $i = 1, \dots, N$. The linear model in Eq. (3.45) for the vector with components $\alpha_i := \alpha(\lambda_i)$ can be written as

$$\boldsymbol{\alpha} = \mathbf{g}_{\text{lit}} + \mathbf{g}_{\text{H}_2\text{O}} + \underbrace{\mathbf{J}\mathbf{a}}_{=: \mathbf{f}(\mathbf{a})}. \quad (3.46)$$

Here the first two terms are the fixed part resulting from numerical KK transformation of the Hb spectrum and from the real RI of water, respectively and the $N \times 2$ matrix \mathbf{J} contains the contributions from the Lorentzian and δ -peak

$$\mathbf{g}_{\text{lit}} = \begin{pmatrix} g_{\text{lit}}(\lambda_1) \\ \vdots \\ g_{\text{lit}}(\lambda_N) \end{pmatrix}, \quad \mathbf{g}_{\text{H}_2\text{O}} = \begin{pmatrix} g_{\text{H}_2\text{O}}(\lambda_1) \\ \vdots \\ g_{\text{H}_2\text{O}}(\lambda_N) \end{pmatrix}, \quad \mathbf{J} = \begin{pmatrix} \tilde{g}_L(\lambda_1) & 1 \\ \vdots & \vdots \\ \tilde{g}_L(\lambda_N) & 1 \end{pmatrix}. \quad (3.47)$$

The parameter vector is $\mathbf{a} = (a_L, a_\delta)^T$. The vector of measurement data of the real RI increment at the N wavelengths is denoted as $\boldsymbol{\alpha}_{\text{meas}}$ and its difference to the fixed terms as $\mathbf{y} := \boldsymbol{\alpha}_{\text{meas}} - \mathbf{g}_{\text{lit}} - \mathbf{g}_{\text{H}_2\text{O}}$. The linear least squares problem is then $\chi^2(\mathbf{a}) \rightarrow \min$ with

$$\chi^2(\mathbf{a}) := [\mathbf{y} - \mathbf{f}(\mathbf{a})]^T \mathbf{W} [\mathbf{y} - \mathbf{f}(\mathbf{a})], \quad (3.48)$$

where $\mathbf{W} = \{w_{ij}\}_{i,j=1}^N$ is a weight matrix given by the inverse of the covariance matrix of the data vector. The conditions for minimal $\chi^2(\mathbf{a})$ are solved by standard linear algebra, which yields

$$\hat{\mathbf{a}} = \arg \min \chi^2(\mathbf{a}) = (\mathbf{J}^T \mathbf{W} \mathbf{J})^{-1} \mathbf{J}^T \mathbf{W} \mathbf{y}, \quad (3.49)$$

$$\hat{\mathbf{f}} = \mathbf{J} \hat{\mathbf{a}} = \underbrace{\mathbf{J} (\mathbf{J}^T \mathbf{W} \mathbf{J})^{-1} \mathbf{J}^T \mathbf{W} \mathbf{y}}_{=: \mathbf{F}} \quad (3.50)$$

for the parameter vector \mathbf{a} and the UV model $\mathbf{f}(\mathbf{a})$. The resulting amplitude of the Lorentzian is shown in Fig. 3.3 as generic peptide absorbance. As can be seen, the results depends on the real-RI-increment data used for fitting.

3.3.5 Hemoglobin variants

While the absorption spectra of different variants of Hb, including oxyHb, deoxyHb and metHb, are well known [39], measurements of the real RI increment $\alpha(\lambda)$ exist only for oxygenated Hb. Nevertheless, the KK analysis allows to derive a result for the real RI increment of other variants. To this end, we use the same model for the deep UV absorbance as above, Lorentzian and delta-peak, with the coefficients $\hat{a}_L, \hat{a}_\delta$ found by the least-squares fit for oxyhemoglobin. I. e., the optimal values of the UV model $\hat{\mathbf{f}}$ are determined from Eq. (3.50) with $\mathbf{y} = \boldsymbol{\alpha}_{\text{meas}}^{\text{oxy}} - \mathbf{g}_{\text{lit}}^{\text{oxy}} - \mathbf{g}_{\text{H}_2\text{O}}$. This result is then used for the other Hb variants, too, i. e.

$$\hat{\boldsymbol{\alpha}}^x = \mathbf{g}_{\text{lit}}^x + \mathbf{g}_{\text{H}_2\text{O}} + \hat{\mathbf{f}}, \quad x = \text{oxy, deoxy, met.} \quad (3.51)$$

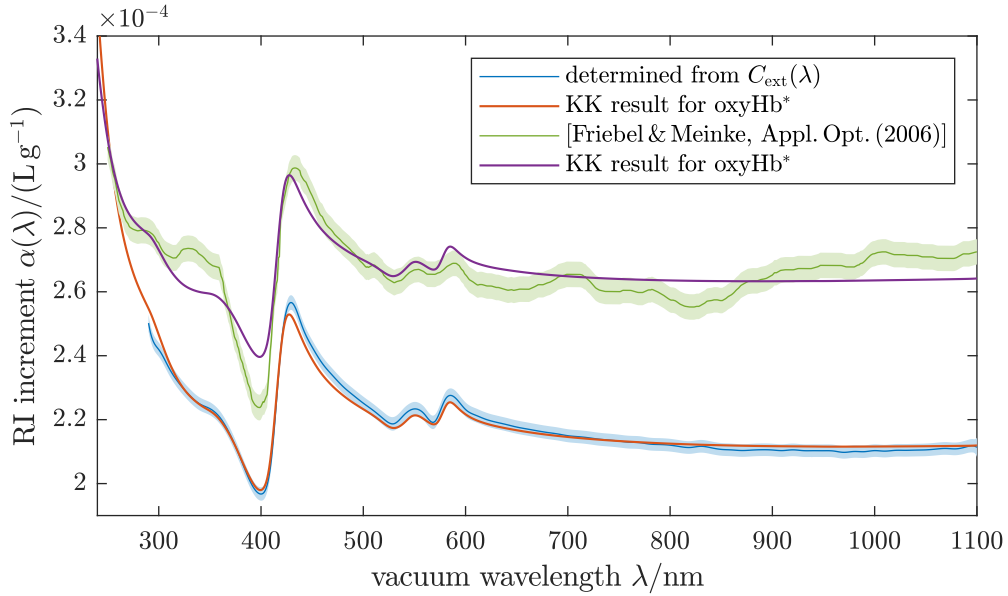


Figure 3.4: Real RI increment $\alpha(\lambda)$ of oxyhemoglobin solutions: The upper two curves are experimental data by Friebel and Meinke [38] and the KK result with free parameters of the deep UV model fitted to it. The lower two curves are results of chapter 4 and the corresponding KK results with fitted deep UV model. Shaded bands indicate ± 1 estimated standard uncertainty.

The reason to simply use the same deep UV model function for oxyHb as well as for other Hb variants is that it describes the absorption of light by the metalloprotein’s peptide backbone. The different Hb variants differ in the oxidization state of the iron ions in the prosthetic non-protein heme groups in the Hb molecules and also in the conformation of the protein chains [76], but not in the chemical structure of the peptide backbone.

3.4 Results and discussion

3.4.1 Real refractive index increment for oxyHb, deoxyHb and metHb

Fig. 3.4 shows the result of the presented KK computation for the real refractive increment $\hat{\alpha}(\lambda)$ for oxygenated Hb along with the experimental data of Friebel and Meinke [38] and values determined independently from RBC extinction spectra in chapter 4 of this thesis. While the overall shape is similar between the measurements of Friebel and Meinke [38] and the corresponding KK fit, deviations occur around the dispersion feature at 400 nm, exceeding the estimated measurement uncertainty provided in Ref. 38 combined with the estimated uncertainty of the KK result. The deviations between this chapter’s result $\hat{\alpha}(\lambda)$ and the data of Friebel and Meinke $\alpha^{\text{F\&M}}(\lambda)$ can not be attributed to unknown spectral absorptions outside the 250 nm–1100 nm range, since features producing such discrepancies would necessarily be inside this wavelength range. I. e., this is an actual inconsistency in the data, not a flaw of the theoretical model. Furthermore, we have modeled important spectral absorptions at the UV end of the spectrum. Concerning possible IR absorptions that are not considered in the proposed model, the following should be

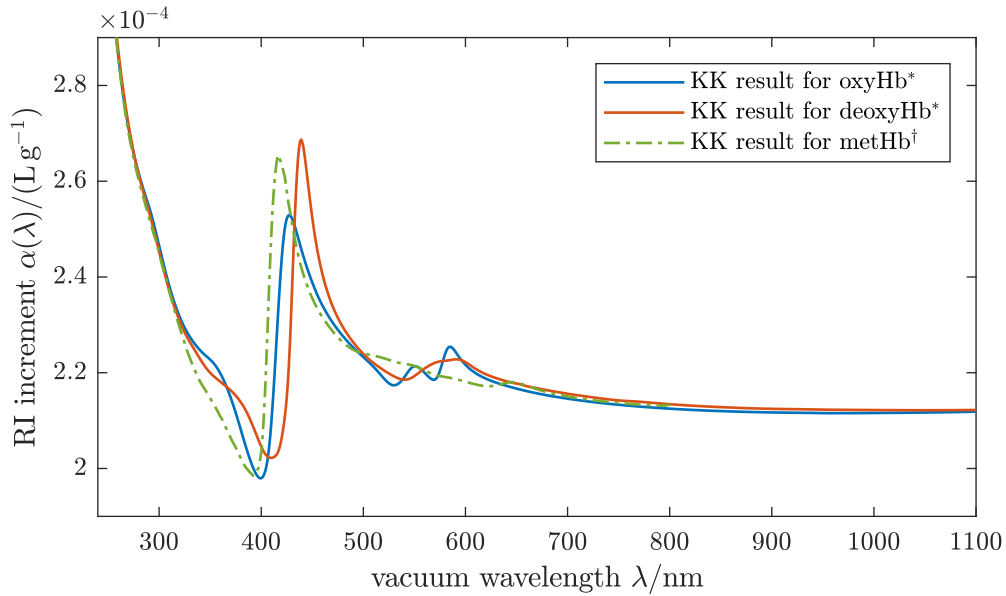


Figure 3.5: Real RI increment of aqueous hemoglobin solutions computed with KK relations: Result for deoxyHb and metHb obtained with the same model for deep UV absorbance as for oxyHb (¶ in Fig. 3.3 on 31), obtained by fitting to the results of chapter 4, compare Fig. 3.4.

noted: The absorption spectra of aqueous hemoglobin solutions in the IR between $1.1\ \mu\text{m}$ and $2.6\ \mu\text{m}$ are dominated by water [37] indicating that the imaginary RI increment of Hb is very low in this region. Hypothetical absorption lines due to Hb at even longer wavelengths would contribute to the real RI increment $\alpha(\lambda)$ in the form of constants or functions with a gentle negative slope. Any possible influence of the long-wavelength end of the spectrum of Hb would thus change the agreement between our result $\hat{\alpha}(\lambda)$ and the literature data $\alpha^{\text{F\&M}}(\lambda)$ for the worse. Thus we conclude that no important contribution to the absorption spectrum was missed at the long-wavelength end. The KK relations themselves are valid as long as the framework within which the data were measured holds, i. e., classical electrodynamics and linear, causal media. This implies that the absorption and refraction data presented in Refs. 37,38 are not self-consistent within the claimed measurement uncertainties for the real RI increment. In contrast, the RI increment determined from the extinction spectra of sphered RBC suspensions (chapter 4) is consistent with the KK result within the estimated uncertainties. This indicates that the RI increment data of Friebel and Meinke may be less reliable than the provided uncertainty estimates suggest.

When the work described in this chapter was first done, the data by Friebel and Meinke [38] were the best available, and were hence used for fitting in the corresponding publication, Ref. 47. Other measurements of the real RI increment of Hb solutions or intact RBCs have since become available. Besides the results of chapter 4 of this thesis, these are the measurements of Lazareva and Tuchin [44] performed with an Abbe refractometer for Hb solutions and the measurements of Ojaghi et al. [49] performed on a single RBC using UV spectral interferometric microscopy. The data of Lazareva and Tuchin are for eleven discrete wavelengths and the spectral dispersion is not resolved in detailed. This means that a KK fit can be performed but does not provide a consistency check as is does with the other datasets for quasi-continuous spectral ranges. Aside from that, the method

for obtaining the Hb solutions used by Lazareva and Tuchin [44] was identical to that of Friebel and Meinke [38], suggesting similar sources of error in both cases. The data of Ojaghi et al. [49] are consistent with the results of chapter 4, but cover a narrower wavelength range and exhibit higher noise levels. Hence, the results of chapter 4 of this thesis were selected for fitting the free parameters of the UV absorption model to.

The results for the real RI increment $\alpha(\lambda)$ of deoxyHb and metHb are shown in Fig. 3.5 in comparison to oxyHb. For $\lambda > 650$ nm, where the absorbance of either Hb variant is low, the real RI increments differ only little. Similarly, the difference becomes small for $\lambda < 250$ nm, where absorbance is strong, but spectra are almost identical for all Hb variants. Other spectral features such as the shift of the Soret band near 420 nm between the three variants and the transition of a double peak to a single peak around 560 nm upon deoxygenation are clearly reflected in the real RI increment $\alpha(\lambda)$.

The fact that results for other Hb variants can easily be obtained, too, once a reliable dataset for the real RI increment of oxyHb or oxygenated RBCs is available is the major benefit of the KK method. No data for the RI of other variants than oxyHb exist, but are required to model the interaction of light with blood cells, e. g., for deoxygenated venous blood. Another important application is the assessment of the functionality (i. e., capability to transport oxygen) of artificial Hb microparticles that are currently developed as a blood substitute and their content of non-functional metHb. This is discussed in chapter 5 where the KK results for the three Hb variants are used.

3.4.2 Comparison to previous Kramers-Kronig analyses

We will now briefly review two previous investigations on the refractive index of hemoglobin and red blood cells, that employed KK relations, namely Refs. 68, 69 and compare the methods. In their 2004 article, Faber et al. [68] started from Eq. (3.20) and applied it to the Hb absorption spectra in a finite spectral range, i. e., instead of Eq. (3.39) they assumed

$$\kappa_{\text{Faber et al.}}(\lambda) = c_{\text{Hb}} \gamma_{\text{lit}}(\lambda) = c_{\text{Hb}} \begin{cases} \gamma(\lambda) & \lambda \in [\lambda_a, \lambda_b] \\ 0 & \text{else} \end{cases}, \quad (3.52)$$

where $[\lambda_a, \lambda_b]$ is the spectral range of available literature data, which in their case was $[\lambda_a, \lambda_b] = [250, 1000]$ nm. For a comparison of the methods, we will assume the spectra in Fig. 3.3 covering a wider spectral range $[\lambda_a, \lambda_b] = [228, 1100]$ nm. Faber et al. then used a subtractive form of the KK relations, where the difference $n(\lambda) - n(\lambda_0)$ is considered which yields

$$n_{\text{Faber et al.}}(\lambda) = n(\lambda_0) + c_{\text{Hb}} [g_{\text{lit}}(\lambda) - g_{\text{lit}}(\lambda_0)] \quad (3.53)$$

with $g_{\text{lit}}(\lambda) = \mathcal{K}[\gamma_{\text{lit}}](\lambda)$. The free parameter $n(\lambda_0)$ is fixed by a refractometric measurement at wavelength $\lambda_0 = 800$ nm. If the non-subtractive KK relations had been used instead, the result would have been

$$n(\lambda) = 1 + c_{\text{Hb}} g_{\text{lit}}(\lambda), \quad (3.54)$$

which is off the true value by a significant amount, since it yields an RI near 1. One can remove this discrepancy by replacing the 1 in the above expression by a

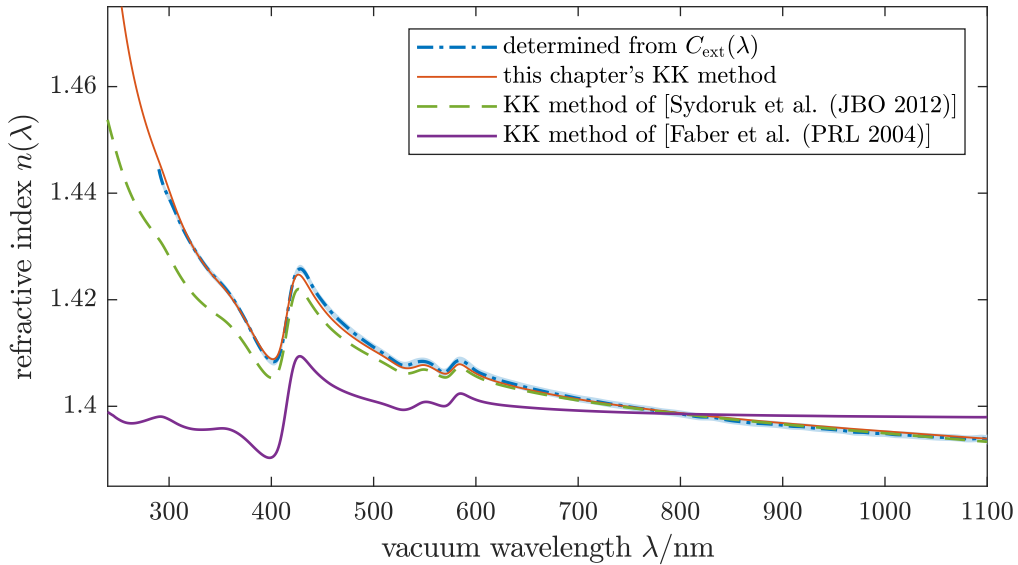


Figure 3.6: Comparison between the real RI of RBCs determined from $C_{\text{ext}}(\lambda)$ (chapter 4; measurement uncertainty indicated by shaded band) and different KK analyses. The Hb concentration is $c_{\text{Hb}} = 330 \text{ g L}^{-1}$. All KK methods were applied to the same spectrum (oxyHb* in Fig. 3.3). Curves calculated according to Faber et al. [68] and Sydoruk et al. [69] are matched to the blue reference curve at $n(\lambda_0 = 800 \text{ nm}) = 1.3986(7)$.

free parameter, which can be interpreted as deep UV absorption. Again, this free parameter can be fixed by a single measurement at λ_0 . The result is then the same as in Eq. (3.53). However, the subtractive KK transform $\mathcal{K}[\gamma](\lambda) - \mathcal{K}[\gamma](\lambda_0)$ can be re-written into a single integral where the kernel decays faster than in the standard KK relations, which is numerically favorable and thus given as an argument for the use of subtractive relations. When applying them, however, one must be certain not to have missed any important spectral features outside the measured range. E. g., a deep UV peak can only be represented by a constant if it is far away from the region of interest. If the location of the peak becomes important as is the case for water in the visible (see Fig. 3.2), this model is insufficient.

In their 2012 paper, Sydoruk et al. [69] made the ansatz

$$\kappa_{\text{Sydoruk et al.}}(\lambda) = \kappa_{\text{H}_2\text{O}}(\lambda) + c_{\text{Hb}} \gamma_{\text{lit}}(\lambda). \quad (3.55)$$

for the imaginary RI of the Hb solution. This takes the absorption due to water into account but neglects the finite volume fraction ϕ taken up by the Hb, i. e., a prefactor $(1 - \phi)$ is missing in front of $\kappa_{\text{H}_2\text{O}}(\lambda)$, in contrast to the approach presented in Eq. (3.39). Apart from this difference, the formal application of the KK relations in the present work is identical to that in [69]. The result was

$$n_{\text{Sydoruk et al.}}(\lambda) = n_{\text{H}_2\text{O}}(\lambda) + c_{\text{Hb}} g_{\text{lit}}(\lambda), \quad (3.56)$$

which also provides a theoretical derivation of the empirical finding $n(\lambda) = n_{\text{H}_2\text{O}}(\lambda)[1 + c_{\text{Hb}} \beta(\lambda)]$ reported in Ref. 38. However, the result that $\beta(\lambda) = g_{\text{lit}}(\lambda)/n_{\text{H}_2\text{O}}(\lambda)$ or $\alpha(\lambda) = g_{\text{lit}}(\lambda)$ is incomplete, as we have discussed. Subtractive KK relations were used as well to match the RI at $\lambda_0 = 800 \text{ nm}$.

To compare these two previously presented methods with the method developed here they are applied to the spectra of oxyhemoglobin presented shown in

Fig. 3.3. As an example, a concentration of $c_{\text{Hb}} = 330 \text{ g L}^{-1}$ was assumed and $n(\lambda_0 = 800 \text{ nm}) = 1.3986(7)$ was taken from the results of chapter 4 of this thesis. The comparison of the two methods applied by Faber et al. [68] and Sydoruk et al. [69] with the present method and the measurement results of chapter 4 is shown in Fig. 3.6. Neglecting the water background as in Ref. 68 yields a dispersion curve (purple line in Fig. 3.6) which substantially deviates from the measurement (dash-dotted blue line in Fig. 3.6) everywhere, except at λ_0 , where it was matched. With the water absorption and the resulting dispersion background taken into account [69] (dashed green line in Fig. 3.6) the agreement with the reference RI is already much better and almost perfect for $\lambda > 500 \text{ nm}$. However, increasing differences occur with decreasing wavelength, resulting from the influence of the peptide backbone. In contrast, almost perfect agreement is found for the full spectral range between the measurement results of chapter 4 and the KK approach presented in this chapter.

3.4.3 Uncertainty analysis

Both, the Kramers-Kronig transformation and the linear least-squares fit to the real RI data are linear transformations, which can formally be carried out by matrix multiplication. Hence, it is easy to perform the uncertainty propagation in terms of mean values and covariance matrices for the result of the KK analysis

$$\hat{\alpha}^x = \mathbf{g}_{\text{lit}}^x + \mathbf{g}_{\text{H}_2\text{O}} + \hat{\mathbf{f}}, \quad x = \text{oxy, deoxy, met.} \quad [\text{Eq. (3.51)}]$$

However, such an analysis relies on the availability of reliable uncertainty estimates of all the input quantities. The following is a brief outline of the important aspects of the uncertainty analysis.

Measurement uncertainties of the following quantities need to be taken into account:

1. The literature absorption spectra, expressed either in terms of imaginary RI increment $\gamma_{\text{lit}}(\lambda)$, the molar extinction coefficient $\varepsilon_M(\lambda)$ [72], or inverse absorption length $\mu_a(\lambda)$ [37].
2. The real RI increment $\alpha_{\text{meas}}(\lambda)$ of oxyHb used for fitting.
3. The hemoglobin density ρ_{Hb} relating mass concentration c_{Hb} and volume fraction ϕ . The uncertainty can be estimated with one digit, i. e., $u_{\rho_{\text{Hb}}} = 10 \text{ g L}^{-1} = 0.75\% \rho_{\text{Hb}}$.
4. The complex RI of water. Its uncertainty is $\leq 10^{-5}$, hence, the influence is negligible.

Combining the latter two uncertainties results in a relative uncertainty of $g_{\text{H}_2\text{O}}(\lambda)$ [see Eq. (3.45)] of 0.75%, which affects the absolute value, but not the wavelength dependence (uncertain prefactor). Compared to other influences, this effect is only minor. Points 1 and 2 have more influence. In the analysis process, both quantities, γ_{lit} and α_{meas} are transformed linearly

$$\gamma \mapsto \mathbf{g}_{\text{lit}} = \mathbf{K} \gamma_{\text{lit}}, \quad (3.57)$$

$$\alpha_{\text{meas}} \mapsto \hat{\mathbf{f}} = \mathbf{F} \alpha_{\text{meas}} - \mathbf{g}_{\text{lit}} - \mathbf{g}_{\text{H}_2\text{O}}, \quad (3.58)$$

where \mathbf{K} is the $N \times N$ matrix implementing the numerical KK transform (see appendix 3.A) and \mathbf{F} is the $N \times N$ matrix relating the wavelength dependence of the deep UV model to the input quantities [see Eq. (3.50)]. For the corresponding covariance matrices $[\Sigma(\mathbf{x})]_{ij} = \text{cov}(x_i, x_j)$ this means

$$\Sigma(\mathbf{g}_{\text{lit}}) = \mathbf{K} \Sigma(\boldsymbol{\gamma}_{\text{lit}}) \mathbf{K}^T, \quad (3.59)$$

$$\Sigma(\hat{\mathbf{f}}) = \mathbf{F} \Sigma(\boldsymbol{\alpha}_{\text{meas}}) \mathbf{F}^T + \text{contributions from } \mathbf{g}_{\text{lit}} \text{ and } \mathbf{g}_{\text{H}_2\text{O}}. \quad (3.60)$$

Both $\boldsymbol{\gamma}_{\text{lit}}$ and $\boldsymbol{\alpha}_{\text{meas}}$ are expected to have some contribution from detector noise, uncorrelated between different wavelengths or at least with correlations decaying relatively quickly over spectral distance. For these contributions, the covariance matrices are diagonal, such that their contributions to \mathbf{g}_{lit} and $\hat{\mathbf{f}}$ are suppressed. This is because the matrices \mathbf{K} and \mathbf{F} , representing non-local kernels, implement a kind of averaging of the elements of vectors \mathbf{g}_{lit} and $\hat{\mathbf{f}}$, respectively. On the other hand, $\boldsymbol{\gamma}_{\text{lit}}$ and $\boldsymbol{\alpha}_{\text{meas}}$ are also both affected by uncertainties of the (intracellular) Hb concentration c_{Hb} of the measured solution or RBC sample. Judging from the strong discrepancies between literature data for $\alpha(\lambda)$, this seems to be mainly a problem for RI measurements of highly concentrated solutions, not so much for the absorption spectra. If we assume a relative concentration error ξ in a measurement of the real RI increment, this can be expressed as

$$\boldsymbol{\alpha}_{\text{meas}} = (1 + \xi) \boldsymbol{\alpha}_{\text{true}}, \quad (3.61)$$

where ξ has expectation value $\mathbb{E}(\xi) = 0$ and variance $\text{var}(\xi) = \sigma_{\text{conc,rel}}^2$. The corresponding uncertainty contribution to the covariance matrix of $\boldsymbol{\alpha}_{\text{meas}}$ is

$$\Sigma^{\text{conc}}(\boldsymbol{\alpha}_{\text{meas}}) = \underbrace{\text{var}(\xi)}_{=\sigma_{\text{conc,rel}}^2} \boldsymbol{\alpha}_{\text{true}} \boldsymbol{\alpha}_{\text{true}}^T \approx \sigma_{\text{conc,rel}}^2 \boldsymbol{\alpha}_{\text{meas}} \boldsymbol{\alpha}_{\text{meas}}^T. \quad (3.62)$$

In contrast to spectral detector noise, this kind of covariance matrix has full positive correlation between all components, i. e., between all wavelengths. When propagated through the linear fit, the tensor-product structure (i. e., $\mathbf{x}\mathbf{x}^T$ with some column vector \mathbf{x}) is conserved

$$\Sigma^{\text{conc}}(\hat{\mathbf{f}}) = \mathbf{F} \Sigma^{\text{conc}}(\boldsymbol{\alpha}_{\text{meas}}) \mathbf{F}^T = \sigma_{\text{conc,rel}}^2 (\mathbf{F} \boldsymbol{\alpha}_{\text{meas}}) (\mathbf{F} \boldsymbol{\alpha}_{\text{meas}})^T, \quad (3.63)$$

i. e., this contribution to the total uncertainty of $\hat{\mathbf{f}}$ has full correlation between all wavelengths, too. This means that concentration errors and other systematic influences are not suppressed in the KK analysis and fitting procedure. Since this kind of error contributes the most significant source of uncertainty, the conclusion is: Concerning the absolute value of the real RI increment, the results of this chapter's analysis cannot be much more accurate than the reference curve $\boldsymbol{\alpha}_{\text{meas}}$ used to determine the free UV model parameters. Uncorrelated spectral noise in the input data is, however, suppressed. A detailed quantitative uncertainty analysis of the KK results $\hat{\boldsymbol{\alpha}}^x$ can be performed as outlined above. However, reliable uncertainty estimates of the literature data for the real RI increment $\boldsymbol{\alpha}_{\text{meas}}$ are mostly unavailable. As discussed in chapter 1, literature values for $\boldsymbol{\alpha}_{\text{meas}}$ differ by more than 30% between various sources, indicating that concentration errors may be in the same range for some of the reported data, but this is hard to quantify a posteriori. Hence, a quantitative uncertainty analysis as outlined above would be mainly based on guesswork.

3.5 Summary

The complex RI of a Hb solution, which forms the cytoplasm of erythrocytes and determines their optical properties can be computed as

$$\mathbf{n}(\lambda) = n_{\text{H}_2\text{O}}(\lambda) + i \kappa_{\text{H}_2\text{O}}(\lambda) + c_{\text{Hb}}[\alpha(\lambda) + i \gamma(\lambda)], \quad (3.64)$$

where the water absorbance $\kappa_{\text{H}_2\text{O}}(\lambda)$ is negligibly small for $\lambda \in [250, 1100]$ nm and physiological hemoglobin concentrations $c_{\text{Hb}} \geq 300 \text{ g L}^{-1}$. In this chapter, the real RI increment $\alpha(\lambda)$ of Hb was computed from literature spectra of the imaginary RI increment $\gamma(\lambda)$ for $\lambda \in [228, 1100]$ nm. We formally separated the solution's imaginary RI into a water and a hemoglobin part and then applied the Kramers-Kronig (KK) relations to obtain the real RI and thus an expression for $\alpha(\lambda)$, Eq. (3.41). The absorption spectra available in the literature [37, 39, 72] do not resolve the strong UV absorbance of hemoglobin's peptide-backbone. Hence, it was modeled by a Lorentzian line of unknown amplitude, located at 187 nm [74], which introduces a free parameter a_L (the amplitude of the absorption line) into the expression for $\alpha(\lambda)$. A second free parameter a_δ is introduced as a wavelength-independent term accounting for extreme UV absorbance, cf. Eq. (3.45). These two free parameters were determined by a linear least squares fit to an independently measured reference curve $\alpha_{\text{meas}}(\lambda)$, the result of the fit is denoted by $\hat{\alpha}(\lambda)$. We compared the measurements of Friebel and Meinke [38] with the values of $\alpha_{\text{meas}}(\lambda)$ determined in chapter 4 of this thesis from the extinction spectra of suspensions of sphered red blood cells. Fitting the parameters of the deep UV model to the real RI increment of Friebel and Meinke [38] results in significant discrepancies, indicating that these data may be incorrect. In contrast, the independent measurement results of chapter 4 are found to be in excellent agreement with the Kramers-Kronig results of this chapter, indicating that they are more reliable. Hence they were used in the following KK analysis of different Hb variants.

A comparison was made between the present KK analysis and previous investigations, that neglected a part [69] or all of the strong absorption features [68] outside the spectral range for which hemoglobin spectra are available. This comparison shows that the dispersion background of water is the most important contribution, but quantitative agreement with measurements can only be obtained if the deep-UV peptide absorbance is accounted for, too.

In addition to oxyHb, the KK analysis was applied to deoxyHb and metHb. For deoxyHb and metHb, no measurements of the real RI increment exist. Hence, the KK analysis provides an important tool to make such information available. The optical properties of different Hb variants are required, e. g., to analyze blood samples of varying oxygen saturation. Most importantly, the results for oxyHb, deoxyHb and metHb from this chapter are used in chapter 5 for the validation of the oxygen transport capability of artificial hemoglobin microparticles, intended for the use as a blood substitute in transfusion medicine.

Appendix

3.A Numerical integration scheme for Kramers-Kronig relations

For numerical integration of KK relations, we follow the concept described in Ref. 75: a Riemann sum with Taylor expansion at the singularities of the integrand. Numerical stability was tested by comparing to the analytical transformations of different Lorentzian and rectangular profiles.

For computing the transform in Eq. (3.20), we want to numerically evaluate the expression

$$\begin{aligned}\pi g(\lambda) &= -2 \int_{\lambda_a}^{\lambda_b} \frac{\lambda}{\Lambda} \frac{\lambda}{\Lambda^2 - \lambda^2} \gamma(\Lambda) d\Lambda \\ &= \int_{\lambda_a}^{\lambda_b} \left(\frac{2}{\Lambda} - \frac{1}{\Lambda + \lambda} - \frac{1}{\Lambda - \lambda} \right) \gamma(\Lambda) d\Lambda.\end{aligned}\quad (3.65)$$

The measurement data for κ are given on a uniform wavelength grid, or can be interpolated to uniform step width

$$\gamma_i := \gamma(\lambda_i), \quad (3.66)$$

$$\lambda_i := \lambda_a + t \left(i - \frac{1}{2} \right), \quad i = 1, \dots, N. \quad (3.67)$$

In the case of oxyHb and deoxyHb spectra, we have $\lambda_1 = 228$ nm, $\lambda_N = 1100$ nm and $t = 1$ nm. Hence $N = 873$. It suffices to evaluate the integral in Eq. (3.65) at the grid points $g_i := g(\lambda_i)$. The third term in the integral has a singularity at $\lambda = \Lambda$. The first two terms are not singular, hence no principal value integrals have to be used here. All integrals for non-singular integrands are approximated by Riemann sums, including the third term for $\Lambda \notin [\lambda_i - t/2, \lambda_i + t/2]$. The remaining principal value integral can be re-written by Taylor series expansion of the integrand. Using only the lowest non-vanishing order yields

$$\pi g_i \approx \sum_{j=1}^N \left(\frac{2}{\lambda_j} - \frac{1}{\lambda_j + \lambda_i} \right) \gamma_j t - \sum_{\substack{j \neq i \\ j=1}}^N \frac{1}{\lambda_j - \lambda_i} \gamma_j t - t \gamma'_i. \quad (3.68)$$

The last term stems from the singular integral over $\Lambda \in [\lambda_i - t/2, \lambda_i + t/2]$, the other terms stem from Riemann sums approximating the regular integrals. Numerically, we use the nearest-neighbor lattice-derivatives

$$t \gamma'_i = \begin{cases} (\gamma_{i+1} - \gamma_{i-1})/2 & 1 < i < N \\ \gamma_2 - \gamma_1 & i = 1 \\ \gamma_N - \gamma_{N-1} & i = N \end{cases}. \quad (3.69)$$

Note that Eq. (3.68) can also be written as $\mathbf{g} = \mathbf{K} \boldsymbol{\gamma}$, where \mathbf{K} is a $N \times N$ matrix.

Chapter 4

Modeling and analysis of microparticle and red blood cell extinction spectra*

4.1 Introduction

This chapter deals with the inference of the optical properties of microparticles and cells from their extinction spectra. Experimentally, the method is based on measurements of the collimated transmittance $T(\lambda)$ of a dilute suspension of cells or microparticles in dependence on the vacuum wavelength λ . Dilute suspensions are used, such that only single scattering occurs, i. e., the light scattered by a particle is most likely not scattered a second time before reaching the detector. From the transmittance spectrum of the suspension, one can compute *the ensemble-averaged extinction cross section* $\overline{C}_{\text{ext}}(\lambda)$ according to

$$\overline{C}_{\text{ext}}(\lambda) = -\ln [T(\lambda)] \frac{1}{dc}, \quad (4.1)$$

where c is the particle concentration (dimension $1/\text{length}^3$) and d is the optical path length of the sample. The extinction cross section $C_{\text{ext}}(\lambda)$ of a single scatterer describes how much light is removed from a beam of light by scattering and absorption processes. The measured quantity $\overline{C}_{\text{ext}}(\lambda)$ is the ensemble average over all particle parameters, such as varying size or – in the case of cells – intracellular protein concentration.

As already discussed in the previous chapters, the complex refractive index (RI) of the hemoglobin (Hb) solutions making up the interior of red blood cells (RBCs)

* This chapter is partly based on

J. Gienger, M. Bär, and J. Neukammer. Extinction spectra of suspensions of microspheres: determination of the spectral refractive index and particle size distribution with nanometer accuracy. *Appl. Opt.*, 57(2):344–355, 2018.

and

J. Gienger, K. Smuda, R. Müller, M. Bär, and J. Neukammer. Refractive index of human red blood cells between 290 nm and 1100 nm determined by optical extinction measurements. *Sci. Reports*, 9(1):4623, 2019.

The experimental data discussed and analyzed in this chapter were measured by Kathrin Smuda (Charité/PTB Berlin) with an optical measurement device designed and implemented by Jörg Neukammer and Ralph Müller (PTB Berlin).

is given by

$$\mathbf{n}(\lambda) = n(\lambda) + i\kappa(\lambda) = n_{\text{H}_2\text{O}}(\lambda) + c_{\text{Hb}} [\alpha(\lambda) + i\gamma(\lambda)]. \quad (4.2)$$

The approach to determine the optical properties of RBCs presented in this chapter is as follows: RBCs are isovolumetrically sphered by a reversible process that reduces their membrane surface area and the extinction spectra $\overline{C}_{\text{ext}}(\lambda)$ of RBC suspensions are measured over a wide wavelength range from 290 nm to 1100 nm. The extinction spectra are analyzed numerically by solving an *inverse problem*. The corresponding *direct problem* consists in computing the extinction spectra for given ensemble properties, such as complex RI increment $\alpha(\lambda) + i\gamma(\lambda)$, size distribution and distribution of intracellular Hb concentrations c_{Hb} using the Mie solution for scattering by spheres [58, 61]. From measurements of hemolyzed RBCs (as presented in the literature [37, 39]), the imaginary RI increment $\gamma(\lambda)$ of the RBCs is well known. The inverse problem is solved as a nonlinear least-squares problem using a series-expansion representation of the real RI increment $\alpha(\lambda)$ with a suitable set of basis function and numerical optimization. The parameter vector of the optimization problem is given by the expansion coefficients of the RI increment together with the parameters the distributions of cell size and Hb concentration, as well as a term accounting for the concentration of the cell suspension.

As an intermediate step, the method is applied to suspensions of microscopic polystyrene (PS) beads. These commercially available microspheres are widely used in colloidal and optical research, e. g., as a calibration material for cell measurements in optical and impedance flow cytometry [77] or attached as “handles” to optically manipulate biological cells [78]. Here, they serve as a test case to validate the method for measurement and analysis of extinction spectra. The wavelength dependence of the RI of PS is accurately known, at least for bulk material and wavelengths between 436 nm and 1052 nm [79]. The imaginary part of the RI is negligibly small in this spectral range [80]. In contrast to RBC suspensions, the RI of all particles in a suspension of PS microspheres is identical, which eliminates some parameters of the inverse problem. Also, the size distribution of the microspheres typically used for calibration is very narrow compared to RBCs and the mean particle size is accurately specified by the vendor. This allows to validate the method with respect to determination of the size distribution, too. Inferring the size distribution and/or RI of spherical or small particles from measurements of the scattering or extinction of light is not a new idea and many different approaches have been discussed in the literature [81–90]. These techniques can be divided into those relying on the angular scattering pattern at a single wavelength [81, 83–85], and into those techniques relying on spectra of extinction or diffuse transmittance [86–91]. Of course, a combination of these techniques is also possible [82]. Since here we are interested in the wavelength-dependent optical properties of particles and cells, only the second category is relevant. Of those, the particle sizing techniques [89, 91] typically rely on the RI to be known. Conversely, techniques for the RI determination usually require a knowledge of the particle size distribution [86, 88–90]. For a sample of RBCs, both, the RI (distribution) and the size distribution have to be determined, hence such techniques are not applicable.

In addition to determining the RI and size distribution of PS microspheres suspended in a fluid with known optical properties (e. g., water) from extinction measurements, the RI of the liquid surrounding the particles – the *matrix* – can be inferred, too, when the particle RI is known. This is demonstrated with glucose

solutions of different concentrations, for which the dependence between RI and concentration is well known [92] by suspending the same PS beads in them as used before. The approach is then applied to determine the RI of the chemical reagent used for sphering of the RBCs. In a second step the optical properties of the RBCs suspended in this reagent (with now known RI) are determined from their extinction spectra.

4.2 Theoretical background

Let us give a brief outline of the most important theoretical aspects of extinction cross sections in electromagnetic scattering. Detailed explanations are given in textbooks on light scattering. Here, we follow the derivations of Bohren and Huffman [61].

Let us consider the scattering and absorption of light by cells or particles suspended in a fluid. Firstly we consider a single particle surrounded by a quasi-infinite host medium (the matrix), which we assume to have refractive index $n_m \in \mathbb{R}$, i. e., to be non-absorbing. Let $\mathbf{E}^i(\mathbf{r})$ be the electric field of an incident electromagnetic time-harmonic wave which is assumed to be a plane wave propagating in the z -direction. The vacuum wavelength of the incident wave is λ , hence the wavevector within the matrix is given by $k_m = \frac{2\pi n_m}{\lambda}$. The intensity of the incident wave is given by

$$I_i = \frac{1}{2} \varepsilon_0 c_0 n_m |\mathbf{E}^i|^2, \quad (4.3)$$

where ε_0 is the dielectric constant, c_0 is the speed of light in vacuo. Note that the plane wave has infinite cross sectional area and hence the total power of the beam (intensity \times area) is infinite. In the absence of the particle, $\mathbf{E}^i(\mathbf{r})$ would be a solution to the Maxwell equations, but in the presence of the particle, an additional *scattered field* $\mathbf{E}^s(\mathbf{r})$ occurs. The particle is assumed to be located at the origin of coordinates and for sufficiently large distances from the particle ($k_m r \gg 1$) the scattered field behaves like a spherical wave with direction-dependent amplitude

$$\mathbf{E}^s(\mathbf{r}) \sim \frac{e^{ik_m(r-z)}}{-ik_m r} \mathbf{T}(\vartheta, \varphi), \quad (4.4)$$

where (ϑ, φ) is the angle of observation relative to the incident beam. A particularly handy quantity is the amplitude scattering matrix, a 2×2 complex matrix depending on (ϑ, φ) . The parallel and perpendicular components (relative to the scattering plane) of the scattered electric field are then

$$\begin{pmatrix} E_{\parallel}^s \\ E_{\perp}^s \end{pmatrix} = \frac{e^{ik_m(r-z)}}{-ik_m r} \mathbf{S}(\vartheta, \varphi) \begin{pmatrix} E_{\parallel}^i \\ E_{\perp}^i \end{pmatrix}. \quad (4.5)$$

The vector scattering amplitude \mathbf{T} and consequently the amplitude scattering matrix \mathbf{S} describes how much light is scattered in other directions by the particle, and also how much light is absorbed by it. For example, the rate W_{sca} at which light is scattered by the particle can be found by integrating the Poynting vector corresponding to \mathbf{E}^s over the surface of an imaginary sphere of arbitrary radius. The ratio of the scattered power (dimension energy/time) to the incident intensity [dimension energy/(time \times length²)]

$$C_{\text{sca}} := \frac{W_{\text{sca}}}{I_i} = \iint_{4\pi} \frac{|\mathbf{T}(\vartheta, \varphi)|^2}{k_m^2 |\mathbf{E}^i|^2} d\Omega(\vartheta, \varphi) \quad (4.6)$$

is called the *scattering cross section*. Similarly, one can define the rate at which light is absorbed W_{abs} . Consequently, the rate at which light is removed from the forward direction by either scattering or absorption is $W_{\text{ext}} = W_{\text{sca}} + W_{\text{abs}}$. For the corresponding *extinction cross section*, one finds the non-trivial result

$$C_{\text{ext}} := \frac{W_{\text{ext}}}{I_i} = \frac{4\pi}{k_m^2 |\mathbf{E}^i|^2} \Re\{\mathbf{E}^{i*} \cdot \mathbf{T}(0, \varphi)\}, \quad (4.7)$$

which is a form the *optical theorem*, stating that extinction depends only on the scattering amplitude in the forward direction [61]. The extinction cross section C_{ext} defined in this way can be measured in a transmittance measurement. If a detector D (sufficiently far away from the particle) has an area $A(D)$, it receives a power $U_0 = I_i A(D)$ in the absence of the particle and a power

$$U = I_i [A(D) - C_{\text{ext}}] \quad (4.8)$$

if the particle is interposed between the light source and the detector. I.e., C_{ext} , corresponds to the “size of the shadow” the particle casts onto the detector. The above equation, however, only holds if the solid angle $\Omega(D)$ covered by the detector is sufficiently small, because otherwise there will be a power contribution from non-forward scattered light falling onto the detector, increasing U . In this case the observed C_{ext} would be smaller than the actual value. This is why detector apertures in an extinction experiment need to be as small as possible.

For a spherically symmetric scatterer an plane wave incidence (and certain other cases) the solution of the scattering problem can be obtained analytically, which is known as *Mie theory* or *Mie scattering* [58,61]. Mie scattering yields the full electric field for the scattering problem as a series expansion in vector spherical harmonics. An outline is given in section 2.2.1 of chapter 2. For Mie scattering, the amplitude scattering matrix \mathbf{S} is diagonal and the extinction cross section reads

$$C_{\text{ext}} = \frac{4\pi}{k_m^2} \Re[S(0)] \quad (4.9)$$

with

$$S(0) := S_{11}(0, \varphi) = S_{22}(0, \varphi) = \frac{1}{2} \sum_{\nu=1}^{\infty} (2\nu + 1)(a_\nu + b_\nu), \quad (4.10)$$

where a_ν, b_ν are the expansion coefficients of the scattered field in vector spherical harmonics. They read

$$a_\nu = \frac{\mathbf{m} \psi_\nu(\mathbf{m}X) \psi'_\nu(X) - \psi_\nu(X) \psi'_\nu(\mathbf{m}X)}{\mathbf{m} \psi_\nu(\mathbf{m}X) \xi'_\nu(X) - \xi_\nu(X) \psi'_\nu(\mathbf{m}X)}, \quad (4.11)$$

$$b_\nu = \frac{\psi_\nu(\mathbf{m}X) \psi'_\nu(X) - \mathbf{m} \psi_\nu(X) \psi'_\nu(\mathbf{m}X)}{\psi_\nu(\mathbf{m}X) \xi'_\nu(X) - \mathbf{m} \xi_\nu(X) \psi'_\nu(\mathbf{m}X)} \quad (4.12)$$

for $\nu \in \mathbb{N}$ with

$$\psi_\nu(x) := x j_\nu(x), \quad \xi_\nu(x) := x h_\nu^{(1)}(x) \quad \forall x \in \mathbb{C}, \quad (4.13)$$

where $j_\nu(x)$ is a spherical Bessel function of the first kind and $h_\nu^{(1)}(x)$ is a spherical Hankel function of the first kind. Here

$$X := k_m R, \quad (4.14)$$

is the *size parameter*, where R is the radius of the sphere and

$$\mathbf{m} := \frac{\mathbf{n}}{n_m} \in \mathbb{C} \quad (4.15)$$

is the *relative refractive index* of the scatterer, where $\mathbf{n} = n + i\kappa \in \mathbb{C}$ is the complex RI of the sphere.

The above considerations are for a single particle. However, in a typical transmittance measurement like shown in Fig. 4.1 one does not measure the extinction of a single particle, but of a collection of particles that are randomly distributed within the volume of the sample. If there are N particles in the total volume V illuminated by the incident beam, one can write for the total electric field

$$\mathbf{E} = \mathbf{E}^i + \sum_{j=1}^N \mathbf{E}_j^s. \quad (4.16)$$

Under the assumption that the inter-particle distances are large enough, the scattered field for each particle j will be given by Eq. (4.4) with an additional phase factor $e^{ik^i \cdot \mathbf{R}_j}$ accounting for the position \mathbf{R}_j of the individual particles. Under the assumptions that the particle positions are uncorrelated, that the polarization of the light is not rotated by scattering with the particles (which is true for Mie scattering) and that summation over the particles can be replaced by integration over the (homogeneous) particle density, one finds for the transmitted electric field at some point r sufficiently far away from any of the particles

$$\mathbf{E}(\mathbf{r}) = \mathbf{E}^i(\mathbf{r}) \left\{ 1 - \frac{2\pi}{k_m^2 |\mathbf{E}^i|^2} [\mathbf{E}^{i*} \cdot \overline{\mathbf{T}}(0, \varphi)] c d \right\}, \quad (4.17)$$

where $c := N/V$ is the particle density or number concentration, d is the sample thickness and

$$\overline{\mathbf{T}} := \frac{1}{N} \sum_{j=1}^N \mathbf{T}_j \quad (4.18)$$

is the *ensemble average* of the vector scattering amplitude of the collection of particles. Under the assumption that the absolute value of the second term in the braces in Eq. (4.17) is small, one can make use of $1 - x \approx e^{-x}$ and write for the transmitted intensity $I \propto \|\mathbf{E}\|^2$

$$I = I_i \exp(-dc \overline{C}_{\text{ext}}), \quad (4.19)$$

compare Eq. (4.7), where $\overline{C}_{\text{ext}}$ is the ensemble-averaged extinction cross section. When written in terms of the transmittance $T = I/I_i$, this is identical to Eq. (4.1). As derived this equation strictly only holds for transmittances not much smaller than 1, or $dc \overline{C}_{\text{ext}} \ll 1$ in which case the exponential law is identical to a linear one. If, hypothetically, the particles did not scatter any light and all extinction were

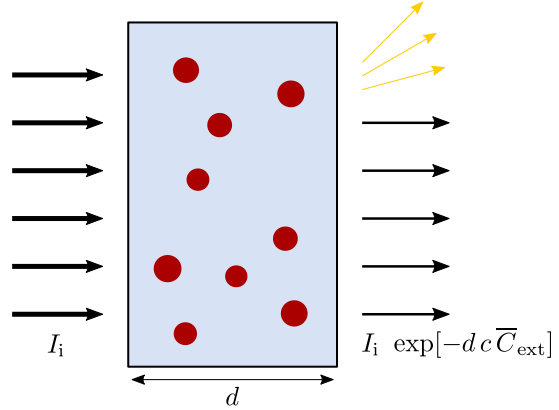


Figure 4.1: Extinction of a collimated incident beam (intensity I_i) by a suspension is the combined effect of scattering in other directions (yellow arrows) and absorption by the particles.

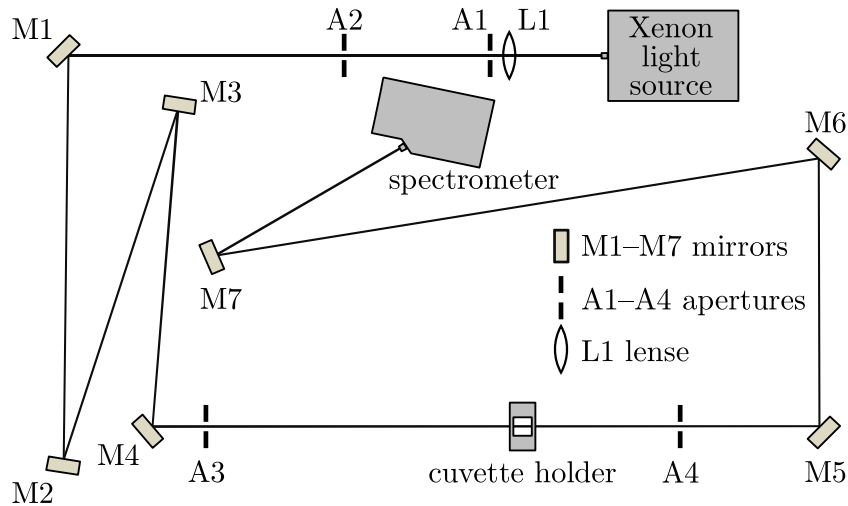


Figure 4.2: Optical layout to measure extinction spectra.

due to absorption, i. e., $C_{\text{sca}} = 0$ and $C_{\text{ext}} = C_{\text{abs}}$, then the exponential law could be easily derived in the same way as one usually derives the Beer-Lambert law: Consider the intensity absorbed by infinitesimally thin slabs, which is proportional to the incident intensity and the number of particles in the slab. Then integrate over thickness. If in addition scattering occurs, this derivation does not hold anymore, because scattered light may be scattered again and get back into the transmitted beam. As the complications with the derivation of the exponential law stem from scattering, the condition for the above equation (4.19) can be relaxed to $dc\bar{C}_{\text{sca}} \ll 1$, which is equally restrictive for non-absorbing particles. In any case, the validity of Eq. (4.19) and thus Eq. (4.1) can be experimentally assessed by varying either the sample thickness d or concentration c . As we will see, the exponential law is actually found to hold for experimental data even for non-absorbing particles at relatively low transmittances.

4.3 Measurement of extinction cross sections

As we have seen above, the extinction cross section of a single scatterer, or the ensemble-averaged extinction cross section of a collection of scatterers can be measured by transmission measurements of a collimated beam (mimicking a plane wave) using a detector sufficiently far away from the scatterer(s) and with sufficiently small aperture.

Here, we analyze data from a dedicated optical setup for measuring extinction spectra of suspensions of microparticles and cells, which was developed and built by Jörg Neukammer and Ralph Müller (PTB Berlin, AG 8.01/8.32). A schematic is shown in Fig. 4.2. A high-power Xenon light source (HPX-2000, Ocean Optics, Inc., USA) emits white light and irradiates the sample in the wavelength range between 185 nm to 2000 nm. For spectral analysis between 200 nm and 1100 nm, a Maya2000 Pro spectrometer was used (Ocean Optics, Inc., USA). With the help of 4 mirrors M1–M4 the folded light path features a length of approximately 2.5 m between the light source and the sample cuvette. The lens L1 is used as condenser to obtain an approximately parallel light beam. The apertures A1–A3 serve to reduce the size of the beam to a diameter of about 1 mm corresponding to a divergence of 0.2 mrad

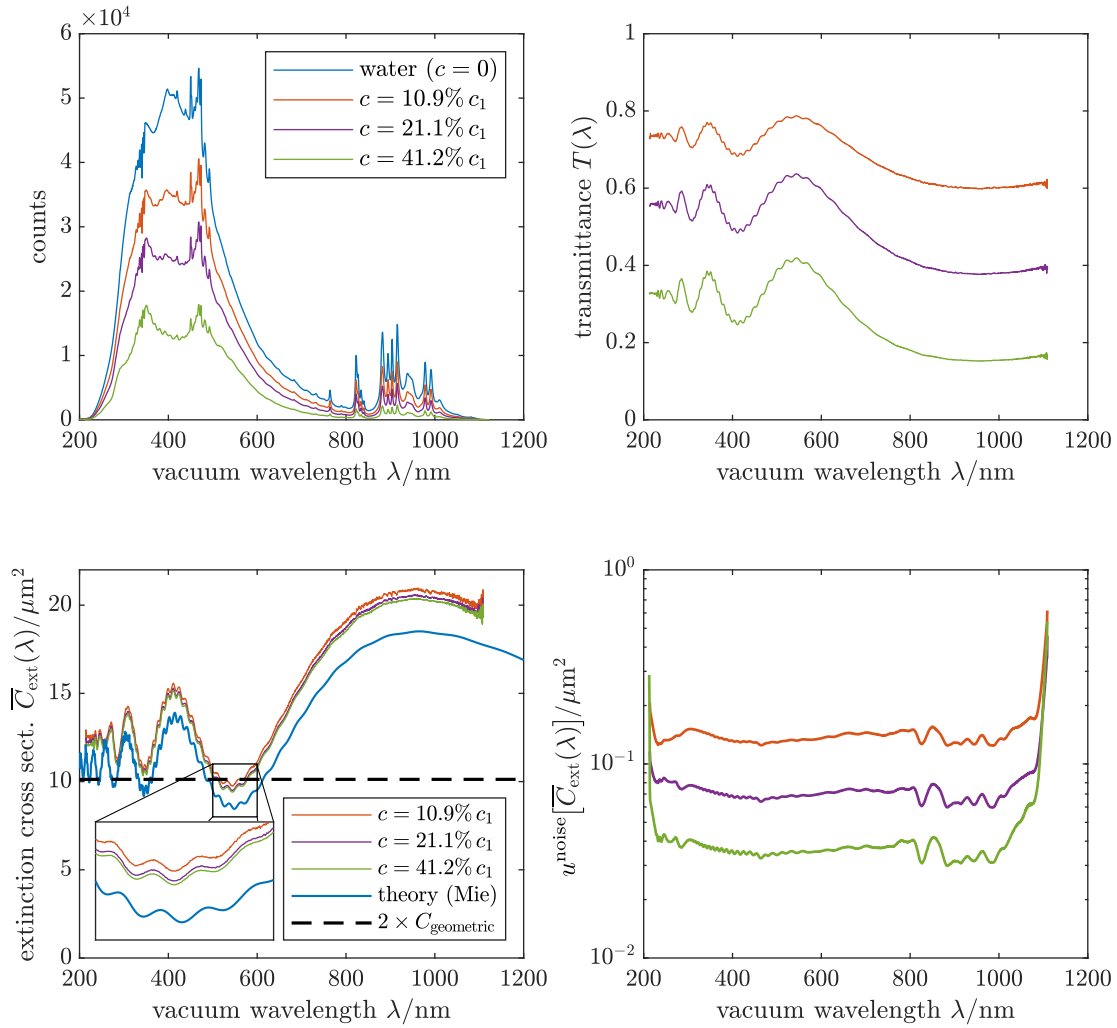


Figure 4.3: Example for measurement data for PS beads in water (top left to bottom right): (1) raw spectra [counts are $\propto I(\lambda)$] with and without samples, (2) corresponding transmittance $T(\lambda)$, (3) corresponding extinction cross section $\overline{C}_{\text{ext}}(\lambda)$ (with inset zooming in on the ripple structure) and (4) the estimated uncertainty due to spectral noise. The PS beads used here have a specified mean diameter of $\text{mean}(D) = 2.539 \mu\text{m} \pm 0.038 \mu\text{m}$ and a specified size distribution width (standard deviation) of $\text{std}(D) = 0.035 \mu\text{m}$. $C_{\text{geometric}} = \frac{\pi}{4} \text{mean}(D)^2$ is the geometric cross section. The stock solution had an estimated particle concentration of $c_1 = 22.4 \times 10^3 \mu\text{L}^{-1}$. Data for three different dilutions of the stock solution are shown.

or 0.01° (half angle). The samples are filled in a quartz cuvette (Hellma Analytics, Germany) with $d = (10 \pm 0.01) \text{mm}$ optical path length. Aperture A4 blocks the light scattered in the non-forward direction by the sample. The spectrometer is placed 1.5 m from the sample via mirrors M5–M7 and receives light from an observation angle of 0.3mrad or 0.02° (half angle). The long distance of 1.5 m between the cuvette and the detector serves to effectively suppress light scattered at small angles into the spectrometer’s aperture. This allows to neglect unwanted contributions to the directed transmittance when analyzing the measurements. The spectral resolution of the CCD is approximately 1 pixel = 0.45nm and one measurement of $I(\lambda)$ takes about 10 s.

An example for raw measurement data, i. e., the spectra $I(\lambda)$ are shown in Fig. 4.3

along with the transmittance $T(\lambda)$ and extinction cross section $\overline{C}_{\text{ext}}(\lambda)$ computed according to Eq. (4.1) for PS microspheres. To estimate the measurement uncertainty each spectrum was recorded $m = 5$ times and the uncertainty of the transmittance due to detector noise was computed as

$$u^{\text{noise}}[T(\lambda)] = \sqrt{\frac{m-1}{2} \frac{\Gamma\left(\frac{m-1}{2}\right)}{\Gamma\left(\frac{m}{2}\right)} \frac{\text{std}[T(\lambda)]}{\sqrt{m}}}, \quad (4.20)$$

where Γ is the gamma function and $\text{std}[T(\lambda)]$ is the sample standard deviation of the m measurements¹, which is made to an unbiased estimator of the standard deviation by the prefactor in the above equation under the assumption of normally distributed values. The estimated standard uncertainty of the transmittance $u^{\text{noise}}[T(\lambda)]$ was propagated accordingly to the extinction cross section to obtain $u^{\text{noise}}[\overline{C}_{\text{ext}}(\lambda)]$, i. e., the standard uncertainty due to measurement noise of the extinction cross section. For further analysis, white noise is assumed for $u^{\text{noise}}[\overline{C}_{\text{ext}}(\lambda)]$, i. e., the noise at different wavelengths $\lambda_i, \lambda_j, i \neq j$ is assumed to be uncorrelated and the corresponding covariance matrix $\Sigma^{\text{noise}}[\overline{C}_{\text{ext}}(\lambda_i)]$ is assumed to be diagonal. This assumption of white noise may not be perfectly adequate as the actual spectral resolution of the MAYA2000 spectrometer with the entrance slit used is specified to about 4 pixels of the detector, i. e., neighboring pixels of the CCD detector are correlated. To model this adequately would require to use a band-diagonal covariance matrix.

To assess the validity of the exponential dependence in Eq. (4.1) and Eq. (4.19), concentration series were recorded for all particles considered. The $\overline{C}_{\text{ext}}(\lambda)$ curves computed according to Eq. (4.1) from measurements at different dilutions agree with each other almost perfectly. The remaining deviations can be explained by errors in the assumed concentrations c when computing $\overline{C}_{\text{ext}}(\lambda)$ from the transmittance $T(\lambda)$. The curves can be brought into agreement by rescaling, which compensates for the concentration error. This validates the assumption of single scattering. More details in the sample measurements for PS beads are given in section 4.5. Measurements of sphered RBCs are discussed in section 4.6.

4.4 Data analysis

4.4.1 Forward model

Mie scattering

As discussed before, the elastic scattering of an incident electromagnetic time-harmonic wave $\mathbf{E}^i(\mathbf{r})$ by a dielectric sphere is fully characterized by the two dimensionless parameters X (the size parameter) and \mathbf{m} (the relative RI). The sphere's extinction cross section C_{ext} can be computed according to

$$C_{\text{ext}} = \frac{2\pi}{k_{\text{m}}^2} \sum_{\nu=1}^{\infty} (2\nu+1) \Re\{a_{\nu} + b_{\nu}\}, \quad (4.21)$$

where the expansion coefficients of the scattered field $a_{\nu}, b_{\nu}, \nu \in \mathbb{N}$ are rational functions of spherical Bessel and Hankel functions of the first kind of arguments

¹ $\text{std}[T(\lambda)]$ as a function of wavelength was smoothed by a Gaussian convolution filter of 15 grid points (approx. 7 nm) standard deviation.

X and $\mathbf{m}X$ (see Eq. (4.12)). For the problem at hand this means that besides the known quantities vacuum wavelength λ and RI of the matrix $n_m(\lambda)$, the two quantities sphere radius R and sphere's RI $\mathbf{n}(\lambda)$ are the two free parameters of the system. Using a numerical implementation of the above equation, which truncates the sum at some $\nu = \nu_{\max}$ and computes the required special functions recursively, [93,94], accurate values for the extinction cross section of a single particle are easily obtained for any given parameters $\mathbf{n}(\lambda)$ and R in the relevant range. We denote these numerically obtained values by the function

$$\mathcal{C}(\lambda; \mathbf{n}, R).$$

This notation shall indicate that we are considering a wavelength-dependent function with two parameters, one of which, the RI $\mathbf{n}(\lambda)$, is a function of the wavelength itself.

Polydispersity

The above scattering cross section is for a single sphere. In the experiment a large number of particles is measured simultaneously. The measured ensemble average $\bar{\mathcal{C}}_{\text{ext}}$ is modeled by integrating $\mathcal{C}(\lambda; \mathbf{n}, R)$ over the corresponding distribution of particle radii and particle refractive indices. In the case of PS spheres, which all have the same RI, one has

$$\bar{\mathcal{C}}(\lambda; \mathbf{n}|r) = \int_0^\infty \mathcal{C}(\lambda; \mathbf{n}, R) r(R) dR, \quad (4.22)$$

where $r(R)$ is the probability density function (pdf) of the radius R . A normal distribution

$$r(R) \propto \exp \left\{ -\frac{1}{2} \frac{[R/R_t - \mu_R]^2}{\sigma_R^2} \right\} \quad (4.23)$$

is known to describe the size distribution of polystyrene microspheres very well [95]. This distribution has two parameters: μ_R is the mean and σ_R the standard deviation of the distribution of radii, relative to a typical size R_t (e.g., a rough guess for the mean particle radius), by which the parameters are rescaled, resulting in dimensionless quantities of the order of 1. This rescaling is done in order to improve numerical stability in the optimization presented later in this chapter.

In the case of RBCs (and other cells) the cells' RI is not constant either, but depends linearly on the hemoglobin (more generally: protein) concentration within the cell according to Eq. (4.2). From measurements of the transmittance of a RBC suspension one obtains an average over both, radius and concentration,

$$\bar{\mathcal{C}}(\lambda; \alpha + i\gamma|p) = \int_0^\infty \int_0^\infty \mathcal{C}(\lambda; n_{\text{H}_2\text{O}} + c_{\text{Hb}}[\alpha + i\gamma], R) p(c_{\text{Hb}}, R) dR dc_{\text{Hb}}. \quad (4.24)$$

Measurements on single RBCs suggest that R and c_{Hb} are statistically independent [22,50], thus motivating a factorization of the joint probability density function p

$$p(c_{\text{Hb}}, R) = q(c_{\text{Hb}}) r(R), \quad (4.25)$$

where q is the pdf of the intracellular Hb concentration c_{Hb} . We model the concentration distribution by a normal distribution

$$q(c_{\text{Hb}}) \propto \exp \left[-\frac{1}{2} \frac{(c_{\text{Hb}}/c_t - \mu_c)^2}{\sigma_c^2} \right] \quad (4.26)$$

and the distribution of cell radii by a log-normal distribution

$$r(R) \propto \frac{1}{R} \exp \left\{ -\frac{1}{2} \frac{[\ln(R/R_t) - \mu_R]^2}{\sigma_R^2} \right\}. \quad (4.27)$$

Here, again, rescaling by a typical concentration c_t and RBC radius R_t is done in order to have dimensionless parameters $\mu_c, \sigma_c, \mu_R, \sigma_R$ of the order of 1 for the optimization problem. In the case of the normal concentration distribution, the mean and standard deviation are given by $\mathbb{E}(c_{\text{Hb}}) = \mu_c c_t$ and $\text{std}(c_{\text{Hb}}) = \sqrt{\text{var}(c_{\text{Hb}})} = \sqrt{\mathbb{E}(c_{\text{Hb}}^2) - \mathbb{E}(c_{\text{Hb}})^2} = \sigma_c c_t$. In physiology, one commonly uses the quantities *mean corpuscular hemoglobin concentration* (MCHC) and *hemoglobin distribution width* (HDW), i. e., the mean and coefficient of variation of c_{Hb} . These are given by

$$\text{MCHC} := \mathbb{E}(c_{\text{Hb}}) = \mu_c c_t \quad \text{and} \quad \text{HDW} := \frac{\text{std}(c_{\text{Hb}})}{\mathbb{E}(c_{\text{Hb}})} = \frac{\sigma_c}{\mu_c}. \quad (4.28)$$

Of course, a normal distribution (which has support $] -\infty, \infty[$) for a non-negative quantity, such as the Hb concentration, only makes sense if is sufficiently narrow. This is the case, since typically $\text{HDW} < 10\%$.

The log-normal size distribution has moments

$$\mathbb{E}(R^j) = R_t^j e^{j\mu_R + \frac{1}{2}j^2\sigma_R^2} \quad \text{for } j \in \mathbb{N}. \quad (4.29)$$

Consequently the mean and standard deviation of the radius are

$$\mathbb{E}(R) = R_t e^{\mu_R + \frac{1}{2}\sigma_R^2} \quad \text{and} \quad \text{std}(R) = \mathbb{E}(R) \sqrt{e^{\sigma_R^2} - 1}. \quad (4.30)$$

For the *mean corpuscular volume* (MCV) one finds

$$\text{MCV} := \mathbb{E} \left(\frac{4\pi}{3} R^3 \right) = \frac{4\pi}{3} R_t^3 e^{3\mu_R + \frac{9}{2}\sigma_R^2} \quad (4.31)$$

and for the *red cell distribution width* (RDW), i. e., the coefficient of variation of $V = \frac{4\pi}{3} R^3$, one finds

$$\text{RDW} := \frac{\text{std}(V)}{\mathbb{E}(V)} = \sqrt{\frac{\mathbb{E}(R^6)}{\mathbb{E}(R^3)^2} - 1} = \sqrt{e^{9\sigma_R^2} - 1}. \quad (4.32)$$

Like the MCHC, the MCV and the RDW are parameters measured in the complete blood count (CBC).

To implement the integrals in the ensemble average numerically, we replace the integration domain $[0, \infty[$ by a finite interval $[a, b]$ and we use finite sums over histograms, namely the trapezoidal rule on a uniform grid

$$\int_a^b f(x) dx \approx \frac{h}{2} \sum_{i=1}^{I-1} [f(x_{i+1}) + f(x_i)], \quad x_i = a + (i-1)h, \quad h = \frac{b-a}{I-1}. \quad (4.33)$$

Since the Mie computation is numerically rather cheap, the number of grid points required for numerical integration is not overly critical. However, it could possibly be reduced by using a more adapted integration scheme, like the Gauss-Hermite quadrature for integrals involving normal distributions. Consequently, the normalization factor of the analytical expressions for the pdfs (e. g., $1/\sqrt{2\pi}\sigma$ for a normal

distribution) is replaced by a normalization prefactor obtained by numerical integration such as

$$r(R) = \frac{\rho(R)}{\frac{h_R}{2} \sum_{i=1}^{I_R-1} [\rho(R_{i+1}) + \rho(R_i)]}, \quad \rho(R) = \exp \left\{ -\frac{1}{2} \frac{[R/R_t - \mu_R]^2}{\sigma_R^2} \right\} \quad (4.34)$$

for the normal size distribution. The size average for PS spheres is then computed as

$$\bar{\mathcal{C}}(\lambda; \mathbf{n}|r) = \frac{h_R}{2} \sum_{i=1}^{I_R-1} [\mathcal{C}(\lambda; \mathbf{n}, R_{i+1}) r(R_{i+1}) + \mathcal{C}(\lambda; \mathbf{n}, R_i) r(R_i)] \stackrel{\text{def. } \tilde{r}}{=} \sum_{i=1}^{I_R} \mathcal{C}(\lambda; \mathbf{n}, R_i) \tilde{r}_i \quad (4.35)$$

and accordingly the size and concentration average of RBCs is computed as

$$\bar{\mathcal{C}}(\lambda; \alpha + i\gamma|p) = \sum_{i=1}^{I_c} \sum_{j=1}^{I_R} \mathcal{C}(\lambda; n_{\text{H}_2\text{O}} + c_i [\alpha + i\gamma], R_j) \tilde{q}_i \tilde{r}_j \quad (4.36)$$

with analogous definitions of the discretized pdfs \tilde{q}_i and \tilde{r}_j .

In the inverse problem, grids with $I_c = I_R = 11$ points were used, spanning ± 4 standard deviations around the center of the respective distribution. The approximation error due to this integration scheme was found (by comparison with $I_c = I_R = 50$) to be well below 0.05% for RBCs with typical properties, which is less than the experimental measurement uncertainty of $> 0.1\%$. For PS beads grids with $I_R = 31$ were used, also spanning ± 4 standard deviations around the center of the size distribution.

Concentration error

As evident from Eq. (4.1) on page 43, the spectral extinction cross section $\bar{\mathcal{C}}_{\text{ext}}(\lambda)$ computed from the transmittance measurement is inversely proportional to both the sample thickness d , given by the optical path length of the cuvette, and the particle concentration in the sample c . Hence, using linearized uncertainty propagation, any relative error of c or d results in a contribution to the relative error of $\bar{\mathcal{C}}_{\text{ext}}(\lambda)$ of the same amplitude and opposite sign, i. e.,

$$\bar{\mathcal{C}}_{\text{ext}}^{\text{meas}}(\lambda) = -\ln [T(\lambda)] \frac{1}{(dc)^{\text{true}} [1 + \epsilon_{dc}^{\text{rel}}]} = [1 - \epsilon_{dc}^{\text{rel}}] \bar{\mathcal{C}}_{\text{ext}}^{\text{true}}(\lambda) + \mathcal{O}(\epsilon_{dc}^{\text{rel}2}), \quad (4.37)$$

where $\epsilon_{dc}^{\text{rel}}$ is the relative deviation of the term dc from its true value.

For the 10 mm cuvettes used, the path length d is known to a relative accuracy of 10^{-3} . In contrast, the particle concentration c has higher measurement uncertainty. For the PS spheres, the concentration of the sample material was estimated from the specified mass-in-volume concentration using the nominal particle volume and the density of PS. For the examined RBC samples, the cell concentrations of the undiluted RBC samples were measured using a hematology analyzer. These flow-cytometric devices have a relative measurement uncertainty of about 4%. Both, the PS and RBC samples were further diluted with multiple dilution steps. The volumetric dilution by adjustable pipettes contributes to the uncertainty of the concentration c of an estimated 2%–4%, depending on dilution. These effects accumulate to values of $|\epsilon_{dc}^{\text{rel}}| \approx 6\%$. This means that agreement between measured ensemble averages $\bar{\mathcal{C}}_{\text{ext}}^{\text{meas}}(\lambda)$ and simulated values computed according to Eqs. (4.22), (4.24)

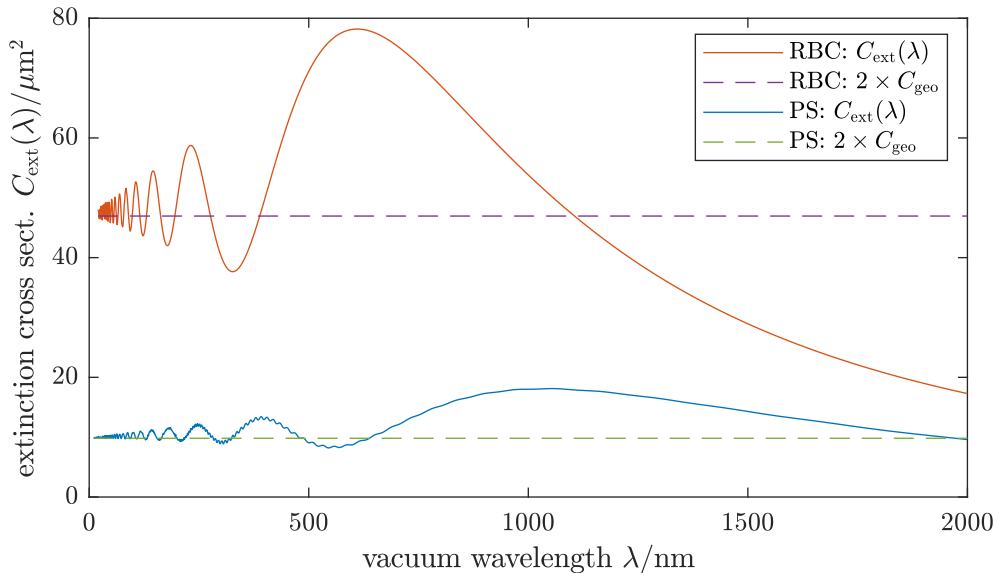


Figure 4.4: Extinction cross sections $C_{\text{ext}}(\lambda)$ of single microspheres computed with wavelength-independent RIs. Case “RBC” is for diameter $D = 2R = 5.47 \mu\text{m}$ (volume $V = 86 \text{ fL}$) and particle RI $n_s = 1.413$. Case “PS” is for diameter $D = 2R = 2.5 \mu\text{m}$ and particle RI $n_s = 1.61$. The surrounding medium has $n_m = 1.34$ in both cases.

is only expected up to this uncertain prefactor, even if the correct optical properties and sizes are fed into the simulation. Similarly, measurements of $\bar{C}_{\text{ext}}(\lambda)$ from dilution series only agree up to a scaling factor, see Fig. 4.3. This effect will be accounted for in the inverse problem in section 4.4.3.

4.4.2 Sensitivity of the forward model

Before approaching the inverse problem, the influence of parameters on the forward model shall be discussed. To demonstrate some generic features and to separate the effects of RI dispersion and absorption from those of the Mie scattering formulas on the wavelength-dependence of $\mathcal{C}(\lambda; \mathbf{n}, R)$, wavelength-independent and real-valued RIs were assumed. To mimic PS beads, the particle RI was set to $n_s(\lambda) = 1.61$. To mimic RBCs, the RI was set to $\mathbf{n}_s(\lambda) = 1.413$, which corresponds to $\mathbf{n}_s(\lambda) = n_{\text{H}_2\text{O}}(\lambda) + c_{\text{Hb}}[\alpha(\lambda) + i\gamma(\lambda)]$ with $n_{\text{H}_2\text{O}}(\lambda) = 1.34$, $\alpha(\lambda) = 0.22 \text{ mL g}^{-1}$, $\gamma(\lambda) = 0$ and $c_{\text{Hb}} = 330 \text{ g/L}$. These over-simplified optical properties are only used for the demonstrations in this subsection. Throughout the rest of this chapter, dispersion and absorption are accounted for. Fig. 4.4 shows the computed extinction cross section of a single microsphere $\mathcal{C}(\lambda; \mathbf{n}, R)$ for two exemplary cases and a wide wavelength range and demonstrates some generic features of the extinction cross section. Firstly oscillations, called *Mie resonances* or *interference structure* are visible for both cases. For longer wavelengths, the spacing between these resonances grows large and eventually the extinction cross section decays asymptotically to zero for $\lambda \rightarrow \infty$ or size parameter $X = 2\pi n_m R/\lambda \rightarrow 0$. On the other end of the spectrum, as $\lambda \rightarrow 0$ or $X \rightarrow \infty$ the Mie resonances become attenuated and the extinction cross section approaches the limit of geometrical optics $C_{\text{ext}}(\lambda) \rightarrow 2C_{\text{geo}}$, where $C_{\text{geo}} = \pi R^2$ is the geometrical cross section of the sphere. In addition to the Mie resonances, a fine *ripple structure* may appear on top of the long-ranged Mie

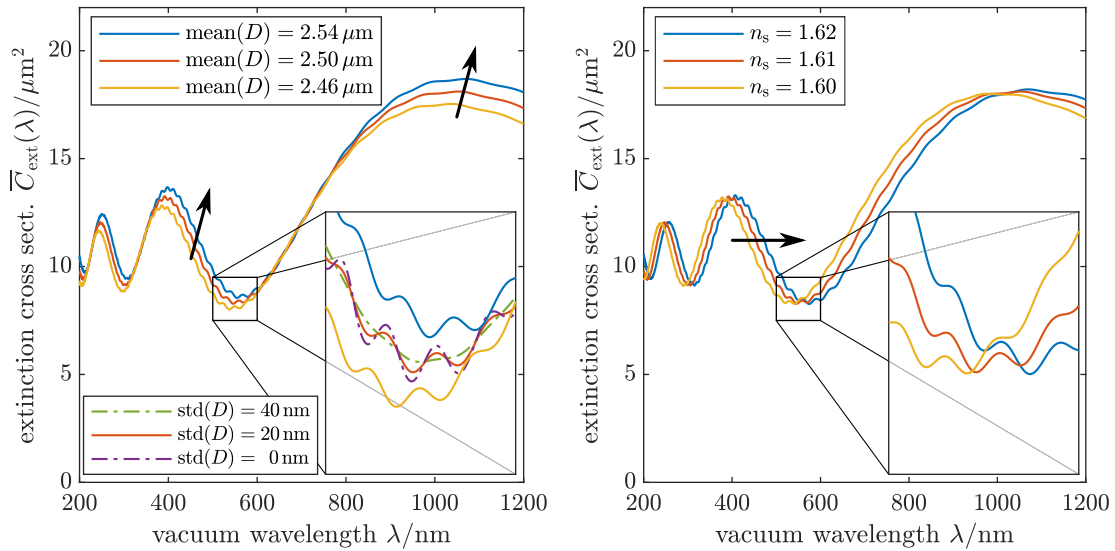


Figure 4.5: Influence of parameters on extinction cross section for $2.5\ \mu\text{m}$ spheres with wavelength-independent RIs $n_s(\lambda) = 1.61$ and $n_m(\lambda) = 1.34$. This corresponds roughly to PS in water for visible light. A normal size distribution with $\text{std}(D) = 20\ \text{nm}$ was used unless otherwise stated. The left panel shows the influence of the mean diameter. The inset shows the ripple structure in detail, also for different size distribution widths. The right panel shows the influence of the particle RI. Arrows indicate the direction of change with the respective parameter.

resonances. In the examples shown, these are only visible for the particle with higher relative RI (PS), since these ripples become more pronounced for high relative RI contrast $|\mathbf{m} - 1| = |n_s/n_m - 1|$ and vanish for $\mathbf{m} \rightarrow 1$. The influence of the different parameters on the ensemble-averaged cross sections are discussed in the following.

Polystyrene The influence of size and RI on the ensemble average $\bar{C}(\lambda; \mathbf{n}|r)$ [see Eq. (4.22)] is depicted in Fig. 4.5 for spheres of mean particle diameter $\text{mean}(D) = 2\mathbb{E}(R) = 2.5\ \mu\text{m}$. To demonstrate the effect of particle size, $\text{mean}(D)$ is varied by $\pm 40\ \text{nm}$ or $\pm 1.6\%$ in the left panel of Fig. 4.5. A larger diameter leads to overall higher cross sections and a shift of the Mie resonances (of which three minima and three maxima are visible in the main plots of Fig. 4.5) to larger wavelengths. Furthermore, the fine ripple structure (inset in the left panel of Fig. 4.5) reacts sensitively to changes in size. Consequently, the ripple structure is smoothed out if the ensemble average is taken for a wider size distribution, which is demonstrated using three different distribution widths $\text{std}(D) = 0\ \text{nm}$, $20\ \text{nm}$, $40\ \text{nm}$. In particular, a distribution width of $\text{std}(D) = 40\ \text{nm} = 1.6\% \text{mean}(D)$ leaves hardly any noticeable ripple structure. However, this ripple structure is clearly visible in the experimental data in Fig. 4.3 on page 49 measured for spheres with a manufacturer-specified $\text{std}(D) = 35\ \text{nm}$. This indicates that the size distribution of the examined PS microbeads is indeed narrower than the specification.

The influence of optical properties is demonstrated in the right panel of Fig. 4.5 by changing the particle RI by ± 0.01 . Similar to particle size, increasing RI shifts the resonances to longer wavelengths, too, but in contrast to particle size it hardly changes the overall cross section. Furthermore the position of the ripples remains largely unaffected by these changes of the RI (inset in the right panel of Fig. 4.5). This is an important observation, as it demonstrates that the effects of RI and size

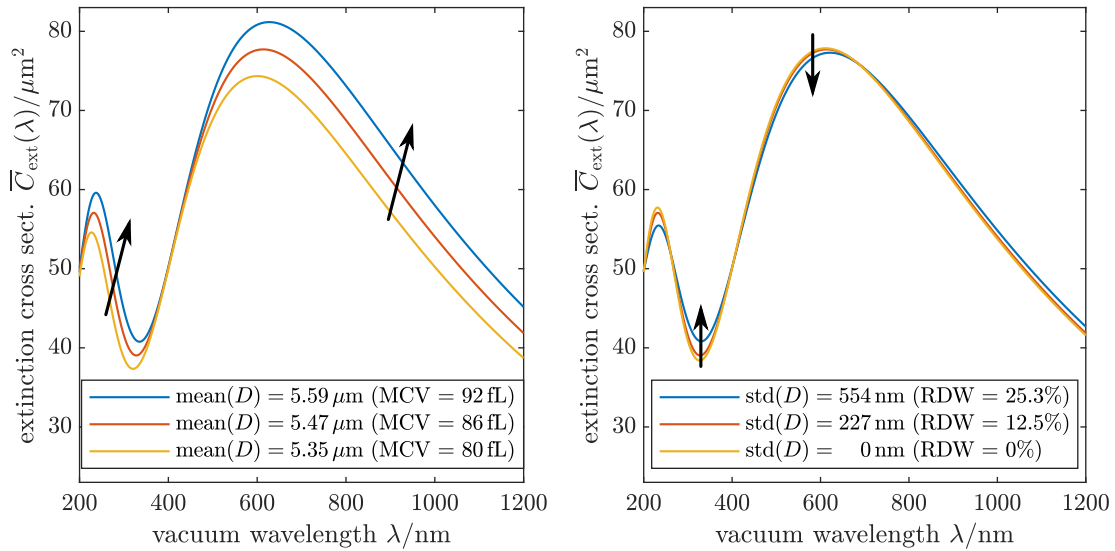


Figure 4.6: Influence of size distribution on extinction cross section for a simplified model of sphered RBCs in water, using wavelength-independent RIs: $n_m(\lambda) = n_{\text{H}_2\text{O}}(\lambda) = 1.34$ and $\alpha(\lambda) = 0.22 \text{ mL g}^{-1}$, $\gamma(\lambda) = 0$. Intracellular Hb concentration is normally distributed with $\text{MCHC} = \text{mean}(c_{\text{Hb}}) = 330 \text{ g/L}$, $\text{std}(c_{\text{Hb}}) = 15 \text{ g/L}$ [$\text{HDW} = \text{std}(c_{\text{Hb}})/\text{mean}(c_{\text{Hb}}) = 4.5\%$]. Size is log-normally distributed with $\text{mean}(D) = 5.47 \mu\text{m}$, $\text{std}(D) = 227 \text{ nm}$ [$\text{MCV} = \text{mean}(V) = 86 \text{ fL}$, $\text{RDW} = \text{std}(V)/\text{mean}(V) = 12.5\%$], unless otherwise stated. The left panel shows the influence of mean size, the right panel the influence of size distribution width. Arrows indicate the direction of change with the respective parameter.

distribution can be told apart, even in the presence of additional degrees of freedom like the concentration error discussed in the previous section. That is, however, only for narrow distributions where ripples occur.

Red blood cells The influences of size distribution and optical properties on the extinction cross section of sphered RBCs are depicted in Figs. 4.6 and 4.7. The log-normal size distribution has a mean diameter of $5.47 \mu\text{m}$ and a standard deviation of 227 nm . Converted to hematological parameters [Eq. (4.31) and (4.32)], this corresponds to $\text{MCV} = \text{mean}(V) = 86 \text{ fL}$, $\text{RDW} = \text{std}(V)/\text{mean}(V) = 12.5\%$, which represents a typical RBC size distribution of a healthy person. The mean intracellular hemoglobin concentration was set to $\text{MCHC} = \text{mean}(c_{\text{Hb}}) = 330 \text{ g/L}$, which represents a typical physiological value, too. Like for PS particles, larger diameter shifts the extinction cross section to higher values and the Mie resonances to longer wavelengths (see left panel of Fig. 4.6). However, since no ripple structure is present for the RBCs, there is nothing to be smoothed out for wider size distributions. Consequently, the size distribution width has little effects for moderate values of $\text{RDW} \leq 12.5\%$. For wider distributions, damping of the Mie resonances themselves occurs. Fig. 4.7 illustrates the effect of the RBCs' RI. Like increasing the real RI for PS spheres, increasing the real RI increment of RBCs shifts the Mie resonances to the right (top left panel). In this simplified model, the mean Hb concentration would have the same effect (at fixed HDW), since only the product $c_{\text{Hb}} \alpha(\lambda)$ appears in Eq. (4.2). Note, however, that if, like in reality, absorption is present, i. e., $\gamma(\lambda) \neq 0$, the effects of $\alpha(\lambda)$ and the MCHC are somewhat different. The effect of the concentration distribution width $\text{std}(c_{\text{Hb}})$ (top right panel of Fig. 4.7) is very

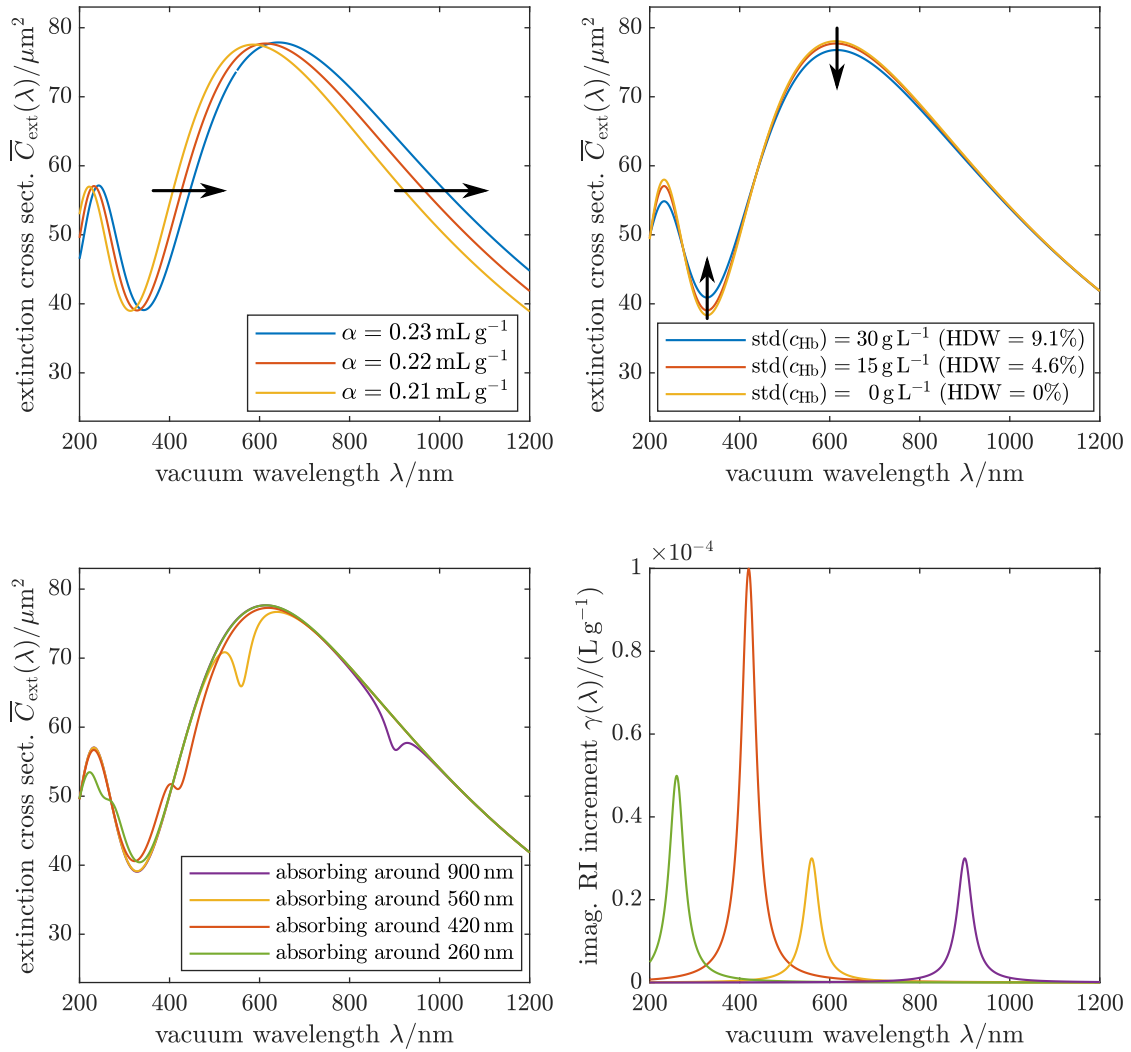


Figure 4.7: Influence of optical properties on extinction cross section for a simplified model of spheroid RBCs in water. Unless otherwise stated, parameters are those used in Fig. 4.6. Top row: Influence of the real RI increment α (left) and hemoglobin concentration distribution width (HDW). Arrows indicate the direction of change with the respective parameter. Bottom row: Influence of the imaginary RI increment $\gamma(\lambda)$ exemplified using different Lorentzian lines.

similar to that of $\text{std}(D)$, i. e., to dampen the Mie resonances. This indicates that an unambiguous simultaneous determination of both parameters from extinction measurements may be difficult. But, again, this simplified model assumes non-absorbing spheres. The effect of a nonzero imaginary RI increment $\gamma(\lambda)$ is demonstrated in the bottom row of Fig. 4.7 where the right panel shows different curves for $\gamma(\lambda)$ and the left panel show the resulting extinction cross sections. The effect of absorption is to attenuate the extinction cross section $\overline{C}_{\text{ext}}(\lambda)$ towards average values, i. e., roughly in the direction of the limit of geometrical optics $2C_{\text{geo}} = 47 \mu\text{m}^2$ (for the mean diameter).

4.4.3 Inverse problem

Optical properties for synthetic data

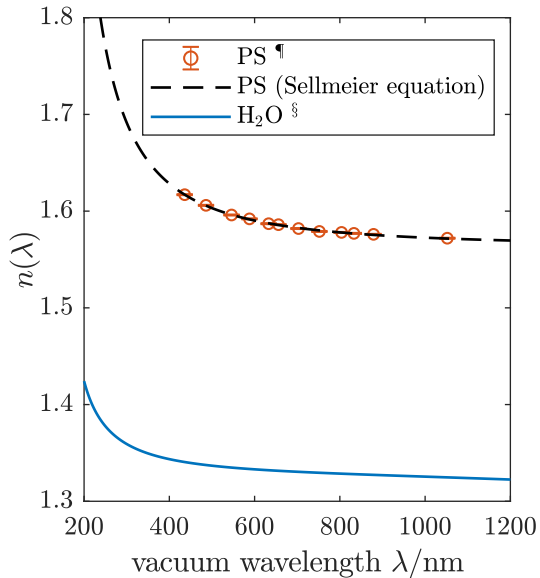


Figure 4.8: RI of water at 20°C and polystyrene. § Sellmeier curve of Daimon and Masamura [41], ¶ values of Nikolov and Ivanov [79]. The one-term Sellmeier equation (black dashed line) extrapolates the literature data to the near UV and was used to create synthetic extinction data.

For the wavelength-dependent RI of pure water a four-term Sellmeier equation was used with coefficients determined by Daimon and Masamura [41] from measurements in the wavelength range 182 nm–1129 nm. The absorbance of water in the wavelength range under consideration is low ($\kappa_m < 10^{-5}$) and can thus be neglected. This is quantified in detail in Appendix 4.A. PS is quasi-nonabsorbing ($\kappa < 10^{-5}$) for most part of the considered wavelength range. However, the assumption of a real-valued RI does not hold in the UV for photon energies above 4.5 eV (i. e., wavelengths below 270 nm), where absorption bands ($\kappa > 10^{-2}$) occur [80]. The RI of PS will be treated as real-valued nevertheless, since this wavelength range is excluded from the analysis of any measurement data.

Pointwise reconstruction of the RI

We now approach the inverse problem of inferring the RI of microparticles from their extinction spectra. For sake of simplicity, let us first consider a monodisperse system or, equivalently, extinction by a single sphere. A synthetic data set for 2.5 μm PS spheres in water was created using RIs in Fig. 4.8. Measurement data (or synthetic data) will be denoted by an asterisk. Under the assumption of additive noise, the components of the measurement data vector are $C_i^* = C_{\text{ext}}^*(\lambda_i) + \xi_i$, where $\lambda_i, i = 1, \dots, N$ are the discrete wavelengths, $C_{\text{ext}}^*(\lambda_i)$ are the underlying true (generally unknown) values and ξ_i is measurement noise on the data. For the time

² The one-term Sellmeier equation reads $n(\lambda)^2 = 1 + \frac{B\lambda^2}{\lambda^2 - \lambda_{\text{res}}^2}$ and fits the literature data for PS [79] with $B = 1.4432$ and $\lambda_{\text{res}} = 142.1$ nm.

After this discussion of some generic features, realistic synthetic datasets need to be generated for the examination of some of the aspects of the inverse problem. This will be exemplified for extinction spectra of PS beads suspended in water. The literature values for the wavelength-dependent RI of bulk PS and water used for synthetic data are shown in Fig. 4.8. The data for the RI of PS by Nikolov and Ivanov [79] were measured at discrete wavelengths between 436 nm and 1052 nm and can be fitted very well using a one-term Sellmeier equation containing a single absorption pole.² This Sellmeier curve was also used to extrapolate the RI at lower and higher wavelengths to generate synthetic data for the spectral range [200, 1200] nm like the theoretical curve in Fig. 4.3. Note however, that it does not necessarily correspond to the actual RI of PS in the UV. For the wavelength-

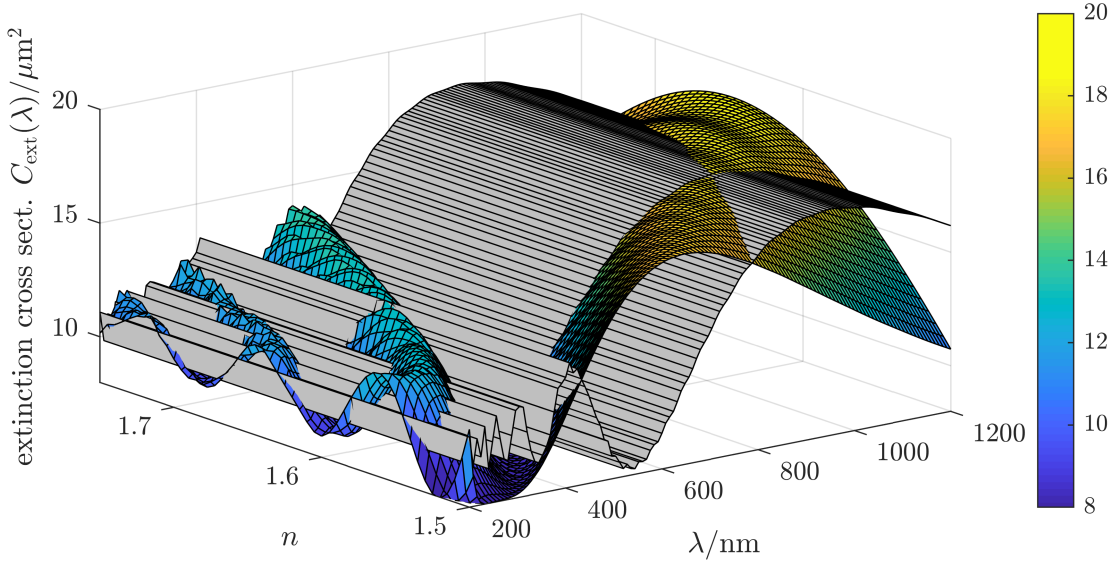


Figure 4.9: Graphical solution of the pointwise RI inference problem for monodisperse PS spheres of known size ($R_{\text{test}} = R_{\text{target}} = 1250$ nm) without measurement noise. The forward model for the Mie extinction cross section $\mathcal{C}(\lambda; n, R_{\text{test}})$ is shown as a curved colored surface in dependence on vacuum wavelength λ and RI n . A synthetic dataset $C_i^* := \mathcal{C}(\lambda_i; n_{\text{target}}(\lambda), R_{\text{target}})$ (no dependence on n) is shown in gray and “extruded” into the n direction, hence it is only curved into the λ direction. The necessary condition $\mathcal{C}(\lambda_i; n, R_{\text{test}}) \stackrel{!}{=} C_i^*$ is fulfilled where the two surfaces intersect.

being, we ignore the effects of noise, i. e., $\xi_i = 0$. Hence, the synthetic dataset is given by $C_i^* = \mathcal{C}(\lambda_i; n_{\text{target}}(\lambda), R_{\text{target}})$, where $n_{\text{target}}(\lambda)$ is the literature RI of PS [79] and $R_{\text{target}} = 1250$ nm.

For a suspension with known particle radius $R_{\text{test}} = R_{\text{target}}$, one could now try to obtain the RI from the target data by solving the following problem: Find an N -vector with entries n_i such that

$$\mathcal{C}(\lambda_i; n_i, R_{\text{test}}) = C_i^* \quad \forall i = 1, \dots, N, \quad (4.38)$$

which are N independent nonlinear equations. Hence, this is a *pointwise* approach to infer the particle RI and the above set of equations is the necessary condition for the inference problem. The roots of these equations can be used by standard numerical techniques like the bisection method or Newton’s method. The graphical solution of this problem for the noiseless synthetic data of monodisperse PS spheres is illustrated in Fig. 4.9. Lines of intersection between the two surfaces are the solutions of the necessary condition. As can be seen from this figure, the solution is not unique, as there are multiple such intersection lines. An even more serious problem than this non-uniqueness is illustrated in Fig. 4.10, where the square of the residuals $F(\lambda_i, n, R_{\text{test}}) := \mathcal{C}(\lambda_i; n, R_{\text{test}}) - C_i^*$ is plotted. The necessary condition Eq. (4.38) is fulfilled where $F(\lambda_i, n, R_{\text{test}}) = 0$. From the upper panel of Fig. 4.10 one can see the solutions form multiple branches, only one of which corresponds to the physical solution, i. e., the target RI $n(\lambda) = n_{\text{target}}(\lambda)$. The other branches are “false solutions” that intersect the true solutions at certain wavelengths. The lower panel shows the case where the radius assumed for reconstruction R_{test} is smaller

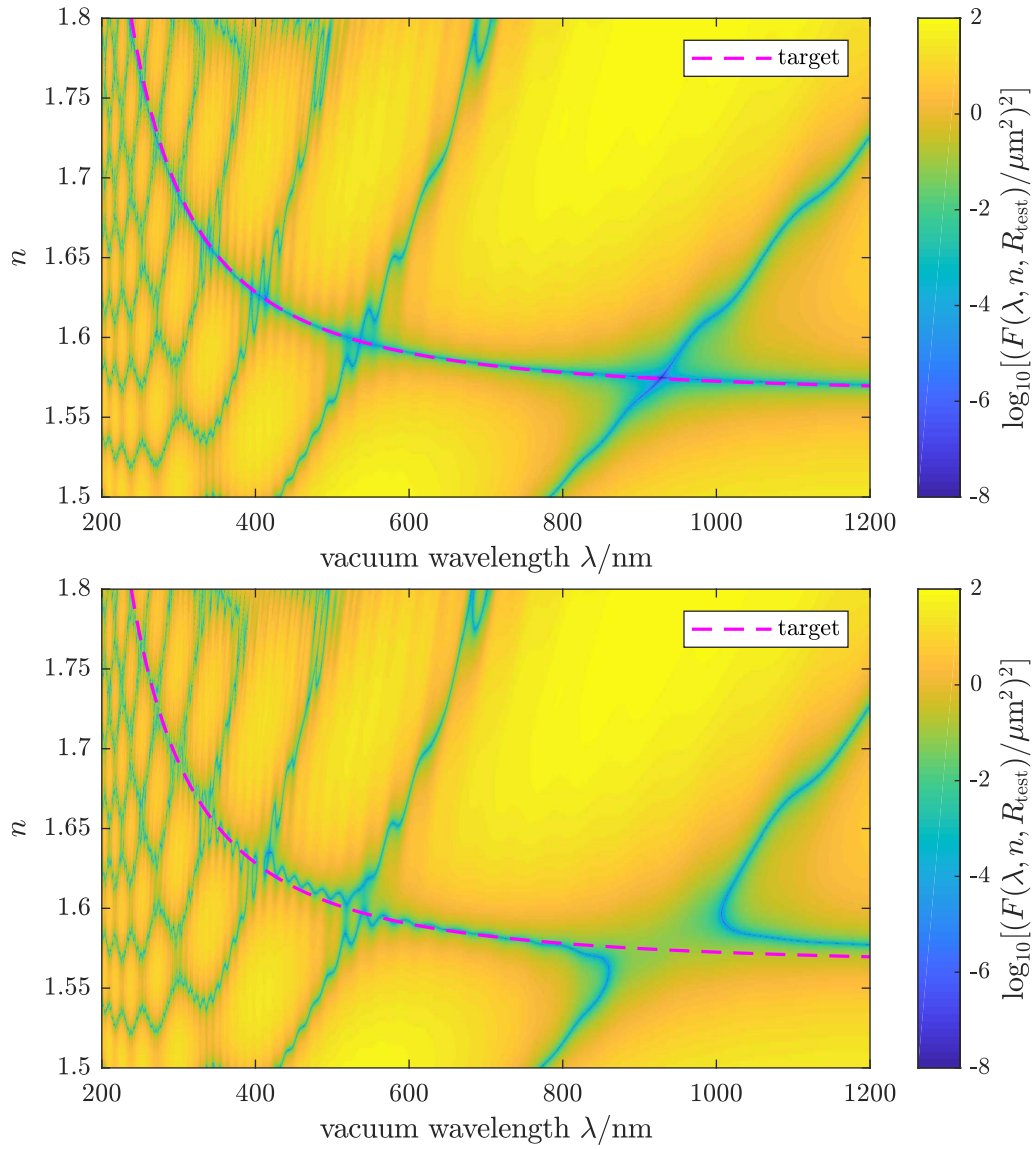


Figure 4.10: Illustration of the dependence of the pointwise RI inference problem in Fig. 4.9 on the knowledge of the particle radius R . Logarithmic density plot of the square of the residual $F(\lambda_i, n_j, R_{\text{test}}) := \mathcal{C}(\lambda_i; n_j, R_{\text{test}}) - C_i^*$ for a fine grid $\lambda \in \{\lambda_1, \dots, \lambda_N\}$, $n \in \{n_1, \dots, n_L\}$. Solutions of the necessary condition (4.38) for RI reconstruction are visible as dark lines. The target RI is marked by a dashed line. Upper panel: $R_{\text{test}} = R_{\text{target}} = 1.25 \mu\text{m}$. Lower panel: $R_{\text{test}} = 1.24 \mu\text{m}$.

than the true value by 10 nm, i.e., $R_{\text{test}} = 1.24 \mu\text{m}$. To put this in perspective, this small error is well within the specified uncertainty of the mean particle radius of the sample material measured in the experiment. Even though the radius is only changed by 0.8%, the effect on the inference problem is drastic: The solution branches to Eq. (4.38) form “avoided crossings” leading to non-solvability near the former crossings. For example, no RI value fulfills the necessary condition near 950 nm. These (avoided) crossing points coincide with the minima and maxima of the target data C_i^* , because here the two surfaces in Fig. 4.9 intersect tangentially. If the assumed particle radius R_{test} is changed, the model function $\mathcal{C}(\lambda_i; n, R_{\text{test}})$ shifts to higher values (compare Fig. 4.5), which leads to these avoided crossings. This means that for certain wavelengths, small errors in R_{test} lead to the necessary

condition Eq. (4.38) not having solutions. Hence, the inference problem is unstable with respect to the particle radius. A similar problem occurs with the scaling error due to concentration error, see Eq (4.37).

It follows that besides the particle RI, the particle radius R and the concentration error have to be reconstructed from the data as well, which makes the pointwise inference problem underdetermined: One would try to obtain at least $N + 2$ parameters from N measurement data. For polydisperse systems, the parameters of the size distribution need to be inferred, too. If measurement noise is present in the data, even more instabilities may arise for the reconstruction. At first glance, this leaves one with more parameters to be reconstructed than data points. But the problem can be restated in a non-pointwise sense as a least-squares optimization problem if the number of parameters used to represent the RI is reduced. This can be achieved because the spectral resolution of the measurement is higher than the width of typical features of the RI to be inferred.

Restatement of the inverse problem

Under realistic circumstances, for the kinds of particles and cells discussed above, the RI cannot be inferred from the measured extinction cross section by wavelength-wise matching of the model RI to the data. To make the problem solvable, a constraint is applied on the admissible functions $n(\lambda)$, namely that they can be expressed as a finite sum of smooth basis functions, i. e.,

$$n(\lambda) = \sum_{j=1}^M a_j g_j(\lambda) \quad (4.39)$$

for an optically monodisperse ensemble like PS spheres, where $a_j \in \mathbb{R}$, and the g_j are real valued functions, e. g., $g_j \in C^\infty(\mathbb{R}) \forall j = 1, \dots, M$. I. e., we are working in the subspace spanned by the M basis functions. $M < N$ has to be chosen and typically $M \ll N$ can be achieved. For the Hb solutions making up the interior of RBCs we have used the same kind of representation for the real RI increment $\alpha(\lambda)$

$$\begin{aligned} \mathbf{n}(\lambda) &= n(\lambda) + i\kappa(\lambda) = n_{\text{H}_2\text{O}}(\lambda) + c_{\text{Hb}} [\alpha(\lambda) + i\gamma(\lambda)], \\ \text{where } \alpha(\lambda) &= \sum_{j=1}^M a_j g_j(\lambda). \end{aligned} \quad (4.40)$$

By defining the matrix of all basis functions $\mathbf{G} := \{g_j(\lambda_i)\}_{i,j} \in \mathbb{R}^{N \times M}$ and the vectors of RI (increments) at all wavelengths $\mathbf{n} = (n(\lambda_1), \dots, n(\lambda_N))^T$ and $\boldsymbol{\alpha} = (\alpha(\lambda_1), \dots, \alpha(\lambda_N))^T$ this can also be written as matrix-vector products

$$\text{polystyrene: } \mathbf{n} = \mathbf{G} \mathbf{a}, \quad \text{RBCs: } \boldsymbol{\alpha} = \mathbf{G} \mathbf{a}. \quad (4.41)$$

Choice of basis functions

The representations of RI and RI increment in Eq. (4.39) and Eq. (4.40) are useful only if a suitable set of basis functions is found that represents typical features of the functions $n(\lambda)$ and $\alpha(\lambda)$ with a rather small number of parameters. Often-used basis functions like polynomials or trigonometric functions prove unsuitable for this task, because they do not describe the generic behavior of a RI. One possible choice

for basis functions is given by the Cauchy equation

$$n(\lambda) = \sum_{j=1}^M b_j \left(\frac{1}{\lambda^2} \right)^j, \quad (4.42)$$

which can be used to represent real RI in the regime of normal dispersion with rather few terms, i. e., $M \leq 3$. However this approximate expression is only valid far away from any absorbing regions in the spectrum. Another widely-used expression for the real RI in the non-absorbing regime is the Sellmeier equation

$$n(\lambda)^2 = 1 + \sum_{j=1}^M b_j \frac{\lambda^2}{\lambda^2 - C_j}, \quad (4.43)$$

which describes the RI of water [41], optical glasses [35] and optical plastics [79] well in the UV, visible and near IR range. While this extended wavelength range is an advantage over the Cauchy equation, this expression has a mathematical disadvantage: The RI $n(\lambda)$ (and also its square $n(\lambda)^2$) depend on the coefficients nonlinearly. Furthermore, the “basis functions” $\frac{\lambda^2}{\lambda^2 - C_j}$ are formally identical for all j . This may cause instabilities if this expression is used in a complicated nonlinear optimization problem, because there is the possibility of two terms becoming identical by having $C_j = C_k$ for some index pair (j, k) , or because this expression has singularities at wavelengths $\lambda = \sqrt{C_j}$, $j = 1, \dots, M$, i. e., the parameters C_j need to be restricted to outside $[\lambda_1^2, \lambda_N^2]$. Finally, while better agreement to measurement data is obtained near absorption bands than with the Cauchy equation, also the Sellmeier equation is only valid sufficiently far away from these absorption bands. Thus it cannot be applied to Hb solutions in the spectral range under consideration (near UV, visible and near IR).

Lorentz-type resonances Hence, we will use a different set of functions to represent the RI and RI increment. These functions are physically motivated as follows: A typical absorption spectrum of a material is made up of absorption lines, that can often be described (at least approximately) by a function like

$$\kappa(\lambda) = \tilde{a} \frac{\gamma}{(\lambda - y)^2 + \gamma^2}, \quad (4.44)$$

i. e., the full spectrum is the sum of many such lines with different amplitudes \tilde{a} , central wavelengths y and characteristic widths γ . As discussed in chapter 3, real and imaginary part of the RI are connected through Kramers-Kronig (KK) relations [see Eq. (3.18) on page 25]. For a single absorption line described above, the KK relations yield

$$n(\lambda) = \underbrace{1 + \tilde{a} \frac{y}{y^2 + \gamma^2}}_{\text{constant}} + \underbrace{\tilde{a} \frac{\lambda - y}{(\lambda - y)^2 + \gamma^2}}_{\text{wavelength-dependent}}. \quad (4.45)$$

Hence, it seems a very natural choice to use functions

$$\begin{aligned} f_1(\lambda) &= 1, \\ f_j(\lambda) &= \frac{\lambda - y_j}{(\lambda - y_j)^2 + \gamma_j^2}, \quad j = 2, \dots, M \end{aligned} \quad (4.46)$$

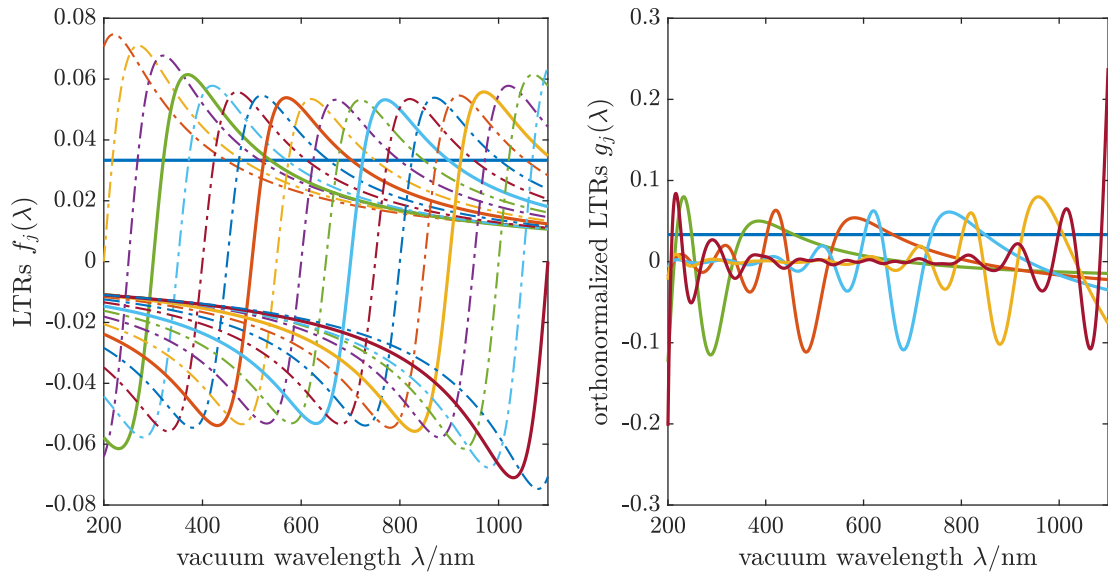


Figure 4.11: An example for the LTRs used to represent the RI. $M = 22$ functions of width $\gamma = 70$ nm were distributed on the interval $[200, 1100]$ nm with a spacing of $\Delta_y = 50$ nm. The left panel shows the functions before orthogonalization, but already normalized. The right panel shows the set of functions after orthonormalization, with only every fourth curve shown for readability.

to describe the wavelength-dependence of $n(\lambda)$. These functions will be referred to as *Lorentz-type resonances* (LTRs) in the following. To avoid the problems discussed already for the Sellmeier equation above (nonlinear parameter dependence and formal identity of all terms), the width of all functions is chosen constant $\gamma_j = \gamma \forall j = 2, \dots, M$ and a uniform grid is used for the central wavelengths y_j , i.e., $y_j - y_{j-1} = \Delta_y \forall j = 3, \dots, M$. In contrast to the Sellmeier equation, the resonance wavelengths y_j of this set of functions are allowed to be within the measured spectral range. The LTRs f_i are linearly independent, but they are not useful for a practical implementation, since they are far from being orthogonal, i.e., the scalar products between them (i.e., the integrals over the product of two functions) are not close to zero, which would lead to problems in the numerics. To avoid this problem, the set of functions $\{f_1, \dots, f_{M-1}\}$, or rather the set the values of these functions at $(\lambda_1, \dots, \lambda_N)$, is orthonormalized using the (modified) Gram-Schmidt process, in which the projections onto all preceding functions $k = 1, \dots, j - 1$ are subtracted from f_j with subsequent normalization, i.e.,

$$\begin{aligned}
 g_1 &:= \frac{f_1}{\|f_1\|}, \\
 g_j &:= \frac{\tilde{g}_j}{\|\tilde{g}_j\|}, \quad \text{where} \quad \tilde{g}_j := f_j - \sum_{k=1}^{j-1} \langle f_j, g_k \rangle g_k \quad \text{for } j = 2, \dots, M,
 \end{aligned} \tag{4.47}$$

where $\langle \cdot, \cdot \rangle$ denotes the standard inner product in \mathbb{R}^N . This yields an orthonormal set $\{g_1, \dots, g_M\}$ with

$$\langle g_i, g_j \rangle = \delta_{ij} \quad \forall j = 1, \dots, N. \tag{4.48}$$

An example is shown in Fig. 4.11. This set of functions can then be used for the RI representation in Eq. (4.39). To give an example for the number of basis functions needed, a set of $M = 22$ LTRs on the interval $[200, 1100]$ nm, ($\Delta_y = 50$ nm) with

$\gamma = 70$ nm approximate the RI of water [41] with a maximum error of 10^{-4} and an RMS error of 2.7×10^{-5} . For comparison, the underlying Sellmeier equation of the water RI has 8 free parameters.

B-splines The functions described in Eq. (4.48) and Eq. (4.46) are able to approximate literature data for the real RI of polystyrene and the real RI increment of Hb solutions [38] very well, if a suitable width γ and grid spacing Δ_y is used. However, when used in the inverse problem for extinction cross sections there is one disadvantage, which they also share with the Cauchy and Sellmeier equations: The functions f_j , $j = 2, \dots, M$ are long-ranged, i. e., they decay like $1/(\lambda - y_j)$ for λ away from y_j . The result of this nonlocal behavior is that a coefficient a_j in Eq. (4.39) affects the RI non-locally. For the rather simple wavelength dependence of a non-absorbing substance like PS, this poses no problem, since only few terms are needed. For the feature rich RI increment of RBCs and Hb solutions, this can lead to oscillatory behavior of the optimized function $\alpha(\lambda)$. Orthonormalization (functions g_j) does not improve this behavior in any way. Hence, a set of localized basis functions is desirable to describe the RI increment of RBCs. Even though the many spectral features add complexity to the problem, an upside of the behavior of the RI increment of RBCs compared to the RI of PS is that it has only moderate slopes and mostly fluctuates around a mean value. Hence, cardinal B-splines provide a suitable means to represent the optical properties of RBCs.

Cardinal B-splines are piecewise polynomials of finite support, i. e., they are nonzero only on a finite interval. The cardinal B-spline of zero degree is defined as [96]

$$\varphi_0(x) := \begin{cases} 1, & x \in [0, 1[\\ 0, & \text{otherwise} \end{cases}, \quad (4.49)$$

which is the characteristic function of the interval $[0, 1[$ and a piecewise polynomial of degree 0. The higher-degree cardinal B-splines are defined recursively by a convolution [96]

$$\varphi_p(x) := [\varphi_{p-1} * \varphi_0](x) = \int_{\mathbb{R}} \varphi_{p-1}(x-y)\varphi_0(y) dy \quad (4.50)$$

for $p \in \mathbb{N}$. Written explicitly, the lowest-order cardinal B-splines are [97]

$$\varphi_1(x) = \begin{cases} x, & x \in [0, 1[\\ 2-x, & x \in [1, 2[\\ 0 & \text{otherwise} \end{cases}, \quad (4.51)$$

$$\varphi_2(x) = \begin{cases} \frac{1}{2}x^2, & x \in [0, 1[\\ -x^2 + 3x - \frac{3}{2}, & x \in [1, 2[\\ \frac{1}{2}x^2 - 3x + \frac{9}{2}, & x \in [2, 3[\\ 0 & \text{otherwise} \end{cases}, \quad (4.52)$$

$$\varphi_3(x) = \begin{cases} \frac{1}{6}x^3, & x \in [0, 1[\\ -\frac{1}{2}x^3 + 2x^2 - 2x + \frac{2}{3}, & x \in [1, 2[\\ \frac{1}{2}x^3 - 4x^2 + 10x - \frac{22}{3}, & x \in [2, 3[\\ -\frac{1}{6}x^3 + 2x^2 - 8x + \frac{32}{3}, & x \in [3, 4[\\ 0 & \text{otherwise} \end{cases}. \quad (4.53)$$

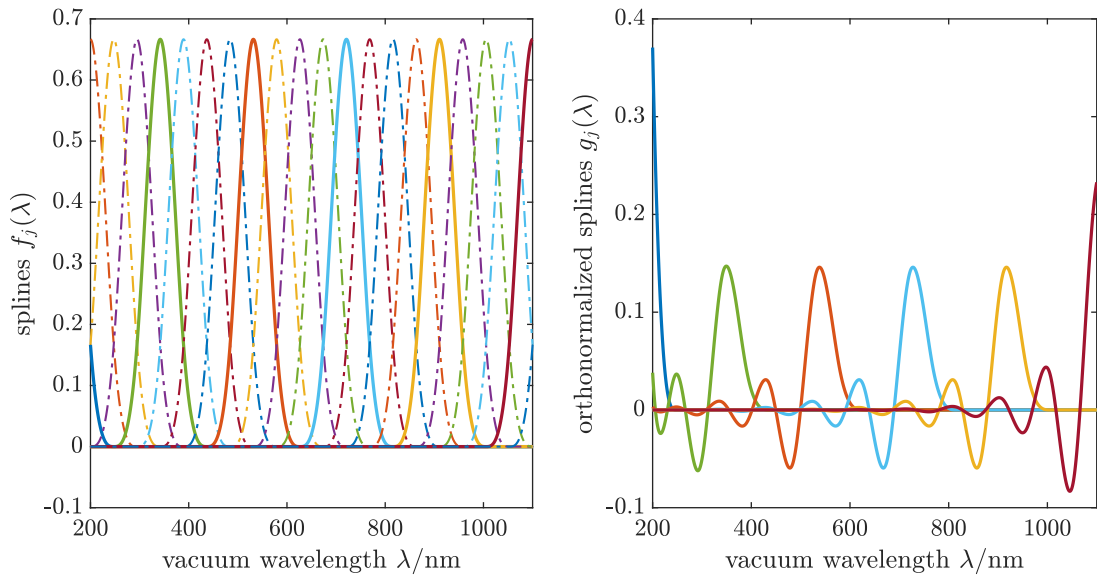


Figure 4.12: An example for the cubic B-splines used to represent the RI increment. $M = 22$ function were distributed on the interval $[200, 1100]$ nm, resulting in a spacing of $\Delta_y = 47.4$ nm. The left panel shows the functions before orthonormalization. The right panel after orthonormalization, with only every fourth curve shown for readability.

As one can see, the support of φ_p is the interval $[0, p + 1[$ and φ_p is symmetric about the center of the interval $\frac{p+1}{2}$. To represent the real RI increment on the interval $\lambda \in [\lambda_1, \lambda_N]$, we use the functions

$$f_j(\lambda) := \varphi_p \left(\frac{\lambda - y_j}{\Delta_y} \right) \quad \text{for } j = 1, \dots, M \quad (4.54)$$

with $y_j = \lambda_1 + (j - p) \Delta_y$ and $\Delta_y = \frac{\lambda_N - \lambda_1}{M - p}$

with the polynomial degree set to $p = 3$. As before, the set of functions $\{f_1, \dots, f_M\}$ is orthonormalized by the Gram-Schmidt method to yield the set $\{g_1, \dots, g_M\}$. An example is shown in Fig. 4.12. In contrast to the f_j , which have a finite support of fixed size $\Delta_y(p + 1)$, the support of the g_j grows with increasing j , in the Gram-Schmidt algorithm, the projections onto all preceding functions are subtracted. However, this does not lead to long-ranged functions $\{g_1, \dots, g_M\}$ but to tails that decay exponentially on the length scale of the grid spacing. Hence, the splines keep their local character, even after orthonormalization. With the same number of basis functions M , the B-splines and LTRs yield about the same approximation error for literature values of the RI increment of Hb solutions [38].

Solution of inverse problem by nonlinear optimization

With this representation of the real part of the RI (for PS spheres) or the real RI increment (for RBCs), we now have a mathematical forward model for the spectral extinction cross section which reads

$$\mathcal{M}(\lambda; \boldsymbol{\psi}) := (1 + \eta) \bar{\mathcal{C}}(\lambda; \mathbf{a}, \boldsymbol{\theta}). \quad (4.55)$$

Here the parameter η corresponds to the (negative) relative concentration error of the suspension to lowest order, i. e., $\eta = -\epsilon_{dc}^{\text{rel}}$ in Eq. (4.37). Including this parameter

allows the model to compensate for concentration errors. The full parameter vector that characterizes the particle suspension is given by

$$\boldsymbol{\psi} := \begin{pmatrix} \mathbf{a} \\ \boldsymbol{\theta} \\ \eta \end{pmatrix} \in \mathbb{R}^L, \quad (4.56)$$

where \mathbf{a} are the expansion coefficients of the RI (increment) in Eq. (4.41). The vector $\boldsymbol{\theta}$ contains the parameters of size and concentration distributions, i. e.,

$$\boldsymbol{\theta} = \begin{pmatrix} \mu_c \\ \sigma_c \\ \mu_R \\ \sigma_R \end{pmatrix} \text{ for RBCs} \quad \text{and} \quad \boldsymbol{\theta} = \begin{pmatrix} \mu_R \\ \sigma_R \end{pmatrix} \text{ for PS beads}, \quad (4.57)$$

see equations (4.23), (4.26) and (4.27). The expression $\bar{\mathcal{C}}(\lambda; \mathbf{a}, \boldsymbol{\theta})$ is shorthand for the corresponding ensemble-averaged Mie extinction cross sections [see Eq. (4.22) and Eq. (4.24)] with the RI (or RI increment) represented by \mathbf{a} and the size (and Hb concentration) distribution characterized by $\boldsymbol{\theta}$. If M basis functions are used to represent $n(\lambda)$ or $\alpha(\lambda)$, the parameter vector has $L = M + 3$ components for PS beads and $L = M + 5$ components for RBCs.

The inverse problem is then solved by minimizing the cost functional consisting of the summed squared residuals

$$F_i := \mathcal{M}(\lambda_i; \boldsymbol{\psi}) - \bar{\mathcal{C}}_i^*, \quad (4.58)$$

$$\chi^2(\boldsymbol{\psi}) := \sum_{i,j=1}^N w_{ij} F_i F_j = \mathbf{F}^T \mathbf{W} \mathbf{F}, \quad (4.59)$$

where \mathbf{W} is a symmetric weight matrix and $\bar{\mathcal{C}}_i^*$ are the measurement data. The weight matrix is set to the inverse covariance matrix of the data, i. e., $\mathbf{W} = \boldsymbol{\Sigma}^{\text{noise}}(\bar{\mathbf{C}}^*)^{-1}$, which is diagonal for the noise model used. The necessary condition for optimal parameters that minimize χ^2 is then

$$0 = \nabla_{\boldsymbol{\psi}} \chi^2(\boldsymbol{\psi}) = \mathbf{J}^T \nabla_{\mathbf{F}} \chi^2(\boldsymbol{\psi}) = 2 \mathbf{J}^T \mathbf{W} \mathbf{F}, \quad (4.60)$$

where we have introduced the Jacobian matrix

$$\mathbf{J} := \left\{ \frac{\partial F_i}{\partial \psi_j} \right\}_{ij} = \left\{ \frac{\partial \mathcal{M}(\lambda_i; \boldsymbol{\psi})}{\partial \psi_j} \right\}_{ij} \in \mathbb{R}^{N \times L}. \quad (4.61)$$

Numerically, the minimization can be done using standard optimization algorithms. The results in this thesis were obtained using the trust-region algorithm implemented in the Matlab (Matlab R2018a, The MathWorks Inc.) function `lsqnonlin`. An outline of some algorithms commonly used for least-squares problems is given in Appendix 4.B.1.

When converged, the numerical routine yields an optimal parameter set $\hat{\boldsymbol{\psi}}$ corresponding to a local minimum and χ^2 normalized to the degrees of freedom

$$\chi_{\text{dof}}^2 := \frac{\chi^2(\hat{\boldsymbol{\psi}})}{N - L + 1} \quad (4.62)$$

provides a measure for the quality of the fit and should be near 1.

Using additional information for regularization To invert the extinction cross sections of PS beads, the optimization problem as stated above is sufficient to extract the RI of the particles from the measurement data, provided a sufficiently wide range of initial values is used for the parameter in the iterative, local optimization. This is achieved by multiple optimization runs from random initial values.

For the case of RBC suspensions, it is found that unambiguous parameter retrieval is not possible with the stated minimization problem. This affects mainly the average value of $\alpha(\lambda)$ and the model parameters of polydispersity $\boldsymbol{\theta}$, that correspond to the hematological parameters MCHC, HDW, MCV and RDW. This unambiguity arises not because the model $\mathcal{M}(\lambda_i; \boldsymbol{\psi})$ is insensitive to these parameters individually, but because they have similar effects on the measured spectrum, e. g., a too high MCHC or MCV may compensate for a too low $\alpha(\lambda)$, as discussed in subsection 4.4.2 above. On the other hand, complementary information to the extinction spectrum is available in the form of hematological parameters from the complete blood counts (CBCs) measured for the individual samples. Hence this complementary information can be used to regularize the optimization problem. To this end, a *regularization term* is added to the cost functional which penalizes deviations from the CBC measurements

$$\chi^2(\boldsymbol{\psi}) = \mathbf{F}^T \mathbf{W} \mathbf{F} + [\mathcal{R}(\boldsymbol{\theta}) - \mathbf{z}]^T \mathbf{W}^{\mathcal{R}} [\mathcal{R}(\boldsymbol{\theta}) - \mathbf{z}]. \quad (4.63)$$

The secondary model $\mathcal{R}(\boldsymbol{\theta})$ computes the vector of hematological parameters $\mathbf{z} = (\text{MCHC}, \text{MCV}, \text{RDW})^T$ from $\boldsymbol{\theta}$ according to equations (4.28), (4.31) and (4.32). Weights are set to $w_{jj}^{\mathcal{R}} = 1/u(z_j)^2$, where the uncertainties are given by the estimated accuracy of the hematology analyzer used. The above expression is formally identical to Eq. (4.59), if the residual vector \mathbf{F} is extended by the three components of $\mathcal{R}(\boldsymbol{\theta}) - \mathbf{z}$ and the weight matrix is adapted accordingly. Hence the same methods can be applied for minimization.

Sampling of initial values

The local optimization algorithm employed finds minima by starting from an initial parameter vector and iteratively minimizing $\chi^2(\boldsymbol{\psi})$. Hence, a found minimum is local and not necessarily a global one, because usually $\chi^2(\boldsymbol{\psi})$ has a number of minima for the problem at hand. The quality of the fit thus depends on a reasonable choice of initial values for $\boldsymbol{\psi}$. To make sure that the deepest minimum is found, initial values of the parameter vector were sampled randomly around a given mean with a sufficiently broad distribution and the local optimization was repeated several times. The parameter vector with the lowest χ^2 was used as the result $\hat{\boldsymbol{\psi}}$. The details of this procedure are given in sections 4.5 and 4.6 where the applications to PS beads and RBCs are discussed, respectively.

Propagation of measurement uncertainties

The contribution to the uncertainty of the found minimum $\hat{\boldsymbol{\psi}}$ due to measurement noise is estimated by linearized covariance matrix propagation according to

$$\Sigma^{\text{noise}}(\hat{\boldsymbol{\psi}}) = [\mathbf{J}^T \Sigma^{\text{noise}}(\overline{\mathbf{C}}^*)^{-1} \mathbf{J}]^{-1} = (\mathbf{J}^T \mathbf{W} \mathbf{J})^{-1}. \quad (4.64)$$

Similarly, if the regularization term [Eq. (4.63)] is used

$$\Sigma^{\text{noise}}(\hat{\boldsymbol{\psi}}) = [\mathbf{J}^T \mathbf{W} \mathbf{J} + \mathbf{J}^{\mathcal{R}T} \mathbf{W}^{\mathcal{R}} \mathbf{J}^{\mathcal{R}}]^{-1}, \quad (4.65)$$

where

$$J_{ij}^{\mathcal{R}} = \frac{\partial \mathcal{R}_i(\boldsymbol{\psi})}{\partial \psi_j} \quad (4.66)$$

is the Jacobi matrix of the secondary model with respect to the full parameter vector. I. e., $J_{ij}^{\mathcal{R}} = 0$ for all components ψ_j to which no regularization is applied. In case of the RBCs these are the coefficients of the real RI increment \boldsymbol{a} ($j = 1, \dots, M = L-5$) and the concentration error η ($j = L$). Note that even if \mathbf{W} is diagonal, $\Sigma^{\text{noise}}(\hat{\boldsymbol{\psi}})$ is generally not, i. e., parameter uncertainties are correlated.

From the parameter covariance matrix $\Sigma^{\text{noise}}(\hat{\boldsymbol{\psi}})$ thus estimated we can easily extract the covariance matrix of the spectral refractive index of PS beads ($\boldsymbol{n} = \mathbf{G} \boldsymbol{a}$) or the RI increment of RBCs ($\boldsymbol{\alpha} = \mathbf{G} \boldsymbol{a}$) as

$$\Sigma^{\text{noise}}(\boldsymbol{n}) = \mathbf{G} \Sigma^{\text{noise}}(\hat{\boldsymbol{a}}) \mathbf{G}^T \quad \text{or} \quad \Sigma^{\text{noise}}(\boldsymbol{\alpha}) = \mathbf{G} \Sigma^{\text{noise}}(\hat{\boldsymbol{a}}) \mathbf{G}^T, \quad (4.67)$$

where $\Sigma^{\text{noise}}(\hat{\boldsymbol{a}})$ corresponds to the first $M \times M$ entries of $\Sigma^{\text{noise}}(\hat{\boldsymbol{\psi}})$. Analogously one can propagate the uncertainty to any other resulting observables (e. g., the mean particle volume) using the respective Jacobi matrices in place of \mathbf{G} .

The corresponding standard uncertainty is computed as the square-root of the diagonal elements of the covariance matrix, e. g., for the particle RI

$$u^{\text{noise}}[n(\lambda_i)] = \sqrt{\Sigma_{ii}^{\text{noise}}(\boldsymbol{n})}. \quad (4.68)$$

This estimated uncertainty accounts for the effects of noise in the measured spectra (contained in \mathbf{W}) and – if regularization is employed – the uncertainty of the complementary information used for regularization (contained in $\mathbf{W}^{\mathcal{R}}$). It does not account for other sources of error such as model errors or measurement uncertainties not included in the noise model employed. This is discussed in the next section.

4.5 Application to polystyrene microbeads

4.5.1 Measurement data

Note: The preparation of RBC samples and the extinction measurements were performed by Kathrin Smuda (Charité and PTB Berlin).

The PS beads used are a commercially available “NIST-traceable particle size standard” (PS-ST-L2552, Microparticles GmbH, Berlin, Germany) with a specified mean diameter of $\text{mean}(D) = 2.539 \mu\text{m} \pm 0.038 \mu\text{m}$ and a specified size distribution width (standard deviation) of $\text{std}(D) = 0.035 \mu\text{m}$. They come in a 2% weight-in volume (w/v) aqueous particle suspensions, where the fluid contains surfactants and antimicrobial agents to ensure colloidal stability during storage. For transmission measurements, they were further diluted with pure water, or the respective fluid in question (e. g., glucose solution) and the spectral intensity $I_{\text{sample},j}(\lambda)$ was measured for 6 different dilutions per sample. Due to this strong dilution, the added surfactants and antimicrobial agents do not cause any noticeable changes of the RI of the matrix compared to, e. g., water.

The dilutions of the PS suspension were selected such that the transmittance $T_j(\lambda) = I_{\text{sample},j}(\lambda)/I_0(\lambda)$ ranged from roughly 95% down to 25% (see wavelength average \bar{T} in Tab. 4.1). $I_0(\lambda)$ is the null measurement where the cuvette is filled with the fluid (water) only. The offset due to dark counts and read out procedure of the diode array were subtracted from all spectra.

The particle volume fraction in the undiluted sample material was computed by dividing the concentration of 2% w/v by the density of PS of 1.04 g mL^{-1} . From this, the particle concentration is estimated by division with the nominal particle volume of 8.570 fL of the $2.539 \mu\text{m}$ spheres. The concentrations c_j of the measured samples were computed according to the respective dilution factor ϕ_j , see Tab. 4.1.

The concentration series were recorded such that the cuvette was not moved between measurements: Increasing volumes of the particle suspension were added to the fluid-filled 10 mm cuvette (starting with 2.2 mL of water) and mixed by pipetting back and forth and using the magnetic stir bar. Care was taken not to touch the cuvette walls in the process, as not to change the angle relative to the incident beam. This minimizes errors from light reflected at the cuvette and avoids artifacts due to displacement of the transmitted light when tilting the cuvette.

The ensemble-averaged extinction cross sections were computed according to Eq. (4.1). Up to a scaling factor, the $\overline{C}_{\text{ext},j}(\lambda)$ curves thus computed lie on top of each other inside the measurement accuracy, hence multiple scattering can be excluded.

Three spectra of a dilution series of PS beads in water are shown in Fig. 4.3 which correspond to dilutions #3, #4 and #6 in Tab. 4.1. The raw spectra have a wavelength range of approximately 200 nm to 1120 nm. However, due to low signal-to-noise ratio near the ends of the spectral range and possibly other artifacts the usable wavelength range was found to be 270 nm to 1100 nm. This wavelength range also excludes any relevant absorbance of the PS beads.

The experimental setup does not feature a temperature control for the samples. However, the experiments were conducted in an air-conditioned laboratory and a thermometer was attached to the cuvette holder (Fig. 4.2) of which a reading was taken for every measured spectrum. For all the measurements of PS beads shown in this chapter, the temperature was between 16.8°C and 18.5°C . Since the RI of a material is in general also a function of temperature, the temperature-dependence of the water RI (which ‘‘sets the scale’’ for determining the particle RI) was taken into account by interpolating the Sellmeier coefficients given by Daimon and Masumura [41] as a function of temperature with second-order polynomials. However, due to the small temperature changes, the RI of water didn’t change by more than 1.5×10^{-4} during the experiments.

4.5.2 Inverse problem settings

As mentioned before, initial values of the parameter vector $\boldsymbol{\psi} = (\mathbf{a}^T, \boldsymbol{\theta}^T, \eta)^T$ were sampled randomly around a given mean and the local optimization was repeated several times. For the inference of the RI of $2.5 \mu\text{m}$ PS particles, the initial values sampled from the following distributions [$\mathcal{N}(\mu, \sigma)$ denotes normally distributed random numbers of mean μ and standard deviation σ]:

1. The RI was initialized as a piecewise-linear function spanned over the points

Table 4.1: Calculated dilutions of examined suspension of PS beads with $2.539 \mu\text{m}$ nominal diameter in water made from 2% w/v basic material and resulting measured average transmittance \overline{T}

#j	dilution ϕ_j	\overline{T}_j
#1	5600	93%
#2	2850	88%
#3	915	68%
#4	473	48%
#5	277	30%
#6	243	25%

$n[(225, 300, 575, 1200) \text{ nm}] = (1.93, 1.69, 1.59, 1.57)$ (or rather, its projection to the space of basis function $\{g_1(\lambda), \dots, g_M(\lambda)\}$), which is a crude approximation of the Sellmeier curve (Fig. 4.8). To generate random initial values, a constant $\text{const} \in \mathcal{N}(0, 10^{-2})$ was added and then additional normally distributed independent random numbers were added to the coefficients a_j individually, resulting in random dispersion features of 10^{-2} standard deviation for $n(\lambda)$.

2. The mean radius was sampled from $\text{mean}(R) \in \mathcal{N}(1269.5 \text{ nm}, 38 \text{ nm})$ corresponding to the manufacturer-specified mean and twice its specified uncertainty. The distribution width was sampled from $\text{std}(R) \in \mathcal{N}(3 \text{ nm}, 2 \text{ nm})$, which deviates from the specified value of $\text{std}(R) = 17.5 \text{ nm}$ (no uncertainty given). This was done because, given the clearly visible ripple structure of the measurement data, the specified value (possibly defining an upper bound, or a “tolerance for monodispersity”) is implausible. Once the ripple structure is smeared out [e. g., by setting a too high $\text{std}(R)$ initially], it is very difficult for the local optimization algorithm to reduce the width of the size distribution again because in the absence of ripples the sensitivity to the distribution width is low. Hence, it was found to work best to start from a narrow distribution and let it become broader during the course of optimization.
3. The relative particle concentration error was sampled from $\eta \in \mathcal{N}(0, 3\%)$.

25 random initial conditions were sampled and the optimization was run for 15 iterations. Afterwards the six parameter vectors with the lowest χ^2 were further optimized until a given tolerance was met, which in most cases didn’t take more than an additional 10 iterations. The parameter vector with the lowest χ^2 was used as the result $\hat{\psi}$. Typically several initial conditions ended up in the same minimum, but other less deep local minima were found as well.

To represent the RI of PS, LTRs [Eq. (4.46)] with a spacing of $\Delta_y = 50 \text{ nm}$ and a width of $\gamma = 80 \text{ nm}$ were used. The first (last) grid point was set to be one grid spacing Δ_y smaller (larger) than the lowest (highest) wavelength.

4.5.3 Optimization results and discussion

Synthetic data results

Synthetic datasets for polystyrene particles suspended in pure water were used to test the analysis method. The mean radius of the spheres was set to $\text{mean}(R) = 1250 \text{ nm}$ and different values were tested for the coefficient of variation $\text{CV}(R) = \text{std}(R)/\text{mean}(R)$. Additive Gaussian white noise according to the lowest estimated $u^{\text{noise}}[\overline{C}_{\text{ext}}(\lambda)]$ in Fig. 4.3 on page 49 was added to the synthetic data and the numerical optimization for the inverse problem was performed as described. For each set of size distribution parameters, three different noise realizations for \overline{C}_i^* were analyzed. In all cases χ_{dof}^2 of the deepest minimum was near 1, it ranged between 0.95 and 1.10. For $\text{CV}(R) = 0.5\%$ ($\text{std}(R) = 6.25 \text{ nm}$), which corresponds to the experimental data analyzed below, the mean and standard deviation of the radius were found correctly within the estimated standard uncertainties of $u^{\text{noise}}[\text{mean}(R)] = 0.12 \text{ nm}$ and $u^{\text{noise}}[\text{std}(R)] = 0.10 \text{ nm}$. The estimated standard uncertainty of the particle RI ranged between 4×10^{-5} and 7×10^{-3} , depending on wavelength, and was very similar to the result for experimental data shown below in the right panel of Fig. 4.13.

This estimated standard uncertainty reflected the fluctuations of the inverse problem results for the particle RI around the true value (Fig. 4.8) well. Similar results were found for $CV(R) = 1.0\%$ ($std(R) = 12.5$ nm), where the uncertainties of the size distribution increased to $u^{\text{noise}}[\text{mean}(R)] = 0.34$ nm and $u^{\text{noise}}[std(R)] = 0.19$ nm and also the uncertainty of the RI increased slightly. Beginning at $CV(R) = 1.5\%$ ($std(R) = 18.75$ nm) the results obtained from different noise realizations started to diverge. While results for some datasets were on the target within their estimated uncertainties, deviations occurred for other noise realizations in the form of too high (too low) RI accompanied by a too small (too large) particle size. At $CV(R) = 2.0\%$ ($std(R) = 25.0$ nm) these deviations occurred for all noise realizations, where the deviations amounted to about $\pm 3 \times 10^{-4}$ for the RI (mostly independent of wavelength) and ∓ 15 nm for $\text{mean}(R)$. Here, opposite signs (\pm vs. \mp) denote negative correlation. At $CV(R) = 3.0\%$ ($std(R) = 37.5$ nm) the deviations amounted to about $\pm 4 \times 10^{-4}$ for the RI and ∓ 20 nm for $\text{mean}(R)$. In contrast, the distribution width $std(R)$ was still within ± 1 nm of the true value. Several minima with χ^2 close to each other were found in these cases.

These findings indicate that in the case of narrow size distributions, where the ripple structure is visible in $\overline{C}_{\text{ext}}(\lambda)$ and one unique deepest minimum is found, the linearized uncertainty estimate [Eq. (4.67) and Eq.(4.64)] for both, the RI and the size distribution is reliable as long as the model for the measurement uncertainty is appropriate. For wider distributions where the ripple structure is attenuated and does not exceed the noise level anymore, the inverse problem result may acquire systematic errors which are not covered by the uncertainty estimate and multiple minima may occur.

Measurement data results

Results for the inference of the particle RI $n_s(\lambda)$ from the measured extinction cross sections of $2.5 \mu\text{m}$ PS beads in water (Fig. 4.3) are shown in Fig. 4.13. The three curves shown here correspond to the three lowest dilutions (Tab. 4.1) and hence the lowest estimated measurement noise. The corresponding size distribution parameters and concentration errors η are shown in Tab. 4.2. A regularization of the least-squares problem according to Eq. (4.63) was tested using the manufacturer specification for the size distribution and its uncertainty. The convergence behavior with and without the regularization term was equally good and the found deepest minima, which were used as the result, did not show any appreciable difference (i. e., the differences were not significant with the estimated uncertainties). This relative uselessness of the regularization in the present scenario (i. e., determining the RI of quasi-monodisperse PS particles) is due to the high sensitivity of the model to the parameters of the size distribution at this particular point in the parameter space in combination with the rather high uncertainties of the manufacturer specification.

The left panel in Fig. 4.13 shows the results for the RI of PS in comparison with the curve around which random initial values were sampled (piecewise linear, projected onto the space of LTR basis function used) and with literature values for the RI of bulk PS in the range 436 nm to 1052 nm [79]. Also shown is the one-term Sellmeier curve fitting and interpolating the literature data, which was also used to generate synthetic datasets earlier in this chapter (see Fig. 4.8 and footnote 2 on page 58). The right panel in Fig. 4.13 shows the estimated uncertainties of the inferred RI stemming from measurement noise and propagated linearly through the forward

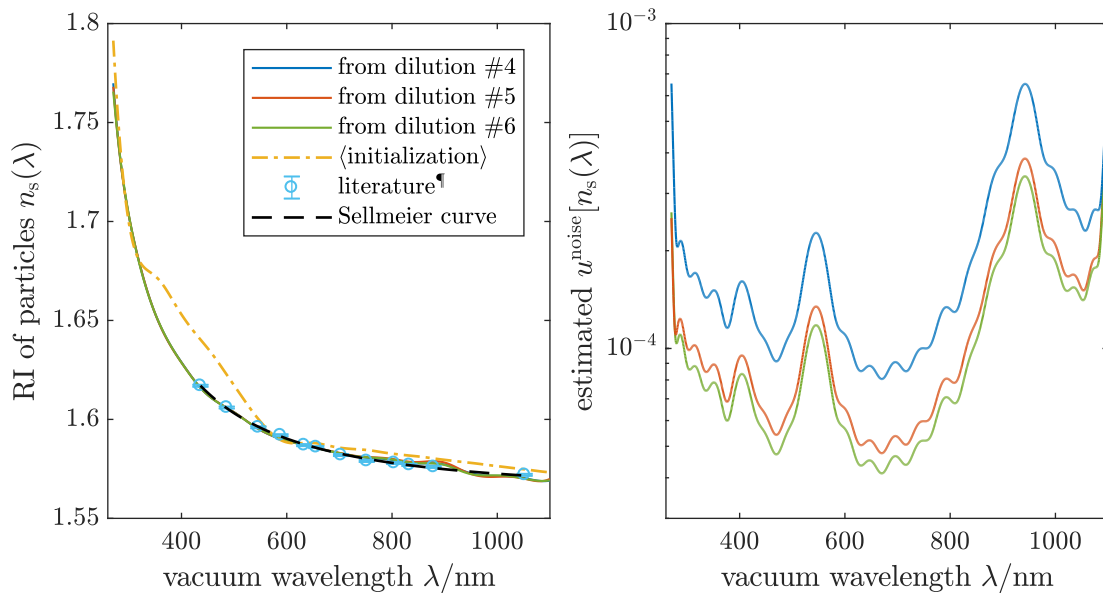


Figure 4.13: RI of PS retrieved from extinction measurements of $2.5\ \mu\text{m}$ beads in water. Results from measurements of $\overline{C}_{\text{ext}}(\lambda)$ at three different dilutions of the stock solution. The right panel shows the estimated uncertainty due to measurement noise [Eq. (4.64) and Eq. (4.68)].

¶ values of Nikolov and Ivanov for bulk PS [79]. The black dashed line is the best fit of a one-term Sellmeier equation to these data and is used as a reference.

model according to Eq. (4.67) and Eq.(4.64). The overall agreement of the inverse problem result with the literature RI is good and the estimated uncertainties suggest that their accuracy is between 5×10^{-5} and 8×10^{-4} depending on wavelength and the dataset analyzed. Thus they would be far more accurate (at least for most wavelengths) than the literature values for bulk PS featuring uncertainties of 10^{-3} [79]. However, looking at the difference of the result to the literature values

$$\Delta n_s(\lambda) = n_s(\lambda) - n_{\text{lit}}(\lambda) \quad (4.69)$$

in Fig. 4.14 it becomes evident that the differences $\Delta n_s(\lambda)$ cannot be explained by the combined uncertainties of the literature values and the estimate $u^{\text{noise}}[n_s(\lambda)]$ made here, which would not exceed 1.2×10^{-3} . The differences $|\Delta n_s(\lambda)|$ are highest near the extrema of $\overline{C}_{\text{ext}}(\lambda)$ at 540 nm and 950 nm, which is consistent with the observations made for synthetic data, see Fig. 4.10. On the other hand, the deviations between the RI curves #4, #5 and #6 are compatible with the uncertainty $u^{\text{noise}}[n_s(\lambda)]$, which also holds true for the scalar quantities in Tab. 4.2.

Table 4.2: Optimization result for scalar parameters for PS beads in water. The numbers in parentheses are the estimated standard uncertainties due to noise referred to the last digits of the respective results.

	χ_{dof}^2	mean(R)/nm	std(R)/nm	η
specification		1267(19)	17.5	–
#4	0.325	1259.17(20)	6.23(18)	12.93(5)%
#5	0.889	1259.16(12)	6.28(11)	12.29(3)%
#6	0.837	1259.09(10)	6.18(09)	11.91(3)%

This makes sense, as the uncertainty of the measurement data that was used to compute $u^{\text{noise}}[n_s(\lambda)]$ was estimated from repeated measurements in the same setup. Hence this uncertainty estimate does not account for any systematic measurement errors that may still be present in the experimental setup, even after careful adjustment. In particular these errors may include artifacts in the spectra due to the strong atomic lines of the Xenon lamp, which significantly exceed the black-body background for $\lambda \geq 800$ nm (see upper left panel of Fig. 4.3 on page 49). With a suitable error model accounting for all these sources of measurement uncertainty, the propagation through the model according to Eq. (4.64) may yield reliable uncertainty estimates. Another way would be a statistical approach with the measurement of many different samples (e. g., different particle diameters). However, this would be time-consuming and since the PS beads examined here merely serve to demonstrate the method in general, this was not pursued any further.

Judging from the differences $\Delta n_s(\lambda)$, the RI can be determined with an accuracy of 3×10^{-3} or better for $\lambda \geq 436$ nm. Below 436 nm, literature values exist for the optical properties of thin PS films [80] and PS microspheres [86]. These data indicate a monotonous increase of the RI with decreasing wavelength in the UV, just as do the results found here. These literature values were determined only indirectly and are less accurate than those for bulk material [79] with which they don't agree well, such that no quantitative comparison is attempted here. Unfortunately, in contrast to the RI no such comparison is possible for the size distribution, as the manufacturer specification of the microparticles (sold as a particle size standard) is not nearly accurate enough. In any case, the results found here for the mean particle size are well within the manufacturer specified uncertainty.

Table 4.3: Sellmeier coefficients [Eq. (4.70)] for the RI of PS microbeads determined in this chapter

j	B_j	$C_j/\mu\text{m}^2$	$\sqrt{C_j}/\text{nm}$
1	0.2010	0.0479	218.8
2	1.2473	0.0137	117.1

In contrast to the literature data used to generate synthetic data [79] that were measured between 436 nm and 1052 nm, the results obtained here cover a wider wavelength range of [270 nm, 1100 nm] and thus require a second term for a good fit. The nonlinear fit of the four parameters B_1, B_2, C_1, C_2 was weighted with the estimated $1/u^{\text{noise}}[n_s(\lambda)]^2$. The resulting χ_{dof}^2 for measurements #4, #5 and #6

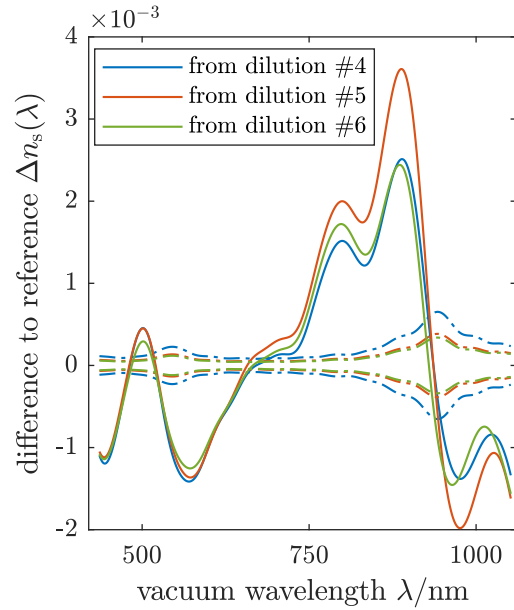


Figure 4.14: Difference of the particle RI found by optimization to the one-term Sellmeier curve in Fig. 4.13. Dash-dotted lines indicate $\pm u^{\text{noise}}[n_s(\lambda)]$ for the respective curves.

As a final result for later use and to smooth out most of the wavelength-dependent errors of the RI curves, they were fitted with a two-term Sellmeier equation, i. e.,

$$n_s^2(\lambda) = 1 + B_1 \frac{\lambda^2}{\lambda^2 - C_1} + B_2 \frac{\lambda^2}{\lambda^2 - C_2}. \quad (4.70)$$

were 26.6, 102 and 89, respectively. Assuming that the Sellmeier equation is a physically adequate model, this indicates that the uncertainty estimates made for the particle RI are approximately 5 to 10 times too small (square root of χ_{dof}^2), which is also consistent with the finding from comparison with literature data ($\Delta n_s(\lambda)$ in Fig. 4.14 above). The root-mean-square deviation between inverse problem results and Sellmeier fits does not exceed 1.5×10^{-3} for the three curves, which can also serve as a (wavelength-averaged) measure of the accuracy of the RI determination presented here. The Sellmeier coefficients for the average of the three datasets are given in Tab. 4.3. The corresponding $n_s(\lambda)$ curve agrees with the one-term Sellmeier fit to literature data used above as a reference [79] within 6×10^{-4} , i. e., within the uncertainty of the literature data.

4.5.4 Modification: inference of the refractive index of the host medium

The measurement setup and data analysis discussed in this chapter can not only be used to determine the RI of microparticles suspended in a known fluid such as water. Complementarily, the roles of surrounding medium (or “matrix”) and particle RI can be interchanged in the optimization. In this way, the spectral RI of the matrix, can be deduced using (quasi-monodisperse) micro-spheres with known optical properties (and size) as a probe. To demonstrate this, the same datasets used before can be analyzed with respect to the matrix RI, while keeping the, now known, particle RI constant. The modifications to the forward model $\mathcal{M}(\lambda; \boldsymbol{\psi})$ and its derivatives are quite straight forward. The coefficient vector \boldsymbol{a} now represents the matrix RI in a set of suitable basis functions instead of the particle RI. The parameters of the particle size distribution $\boldsymbol{\theta}$ and the relative concentration error η have the exact same meaning as before. Depending in the sensitivity, regularization with previous results for the particle size distribution may be applied, or certain parameters may be held fixed at their initial values.

Of course, inverting the same datasets used to determine the RI of the PS microbeads to now determine the RI of the matrix (i. e., water) using the results for the PS RI may not be a suitable test scenario. This is because certain errors could cancel out in this exact configuration, that might otherwise not. One example for this effect is the following thought experiment: We have seen that certain deviations occur between the retrieved RI of PS beads and literature values. However, in the forward model, these retrieved RI curves explain the measured spectral extinction cross sections optimally, given the accurate RI data for water. Hence, if one tries to determine the RI of water using these results for the RI of the PS beads, it is expected that the RI of water is retrieved closely to its true value. On the other hand, much larger deviations might occur if instead the literature RI data for PS are used in the forward model, which do not explain the measured extinction spectra optimally in combination with the literature RI data for water. Similar effects can be thought of for the other model parameters. To avoid these problems, firstly, instead of using the exact output of the optimization for the particle RI $n_s(\lambda)$, we use the two-term Sellmeier fit obtained above. Secondly, in addition to analyzing only pure water, measurements with PS particles (from the same vial) suspended in solutions of D-glucose were taken. The RI of glucose solutions in dependence on wavelength and concentration is known for the wavelength range 320 nm to 1000 nm [92] for concentrations up to 50 g L^{-1} . In this range a linear concentration dependence is found.

For higher concentrations, measurements at single wavelengths [98] indicate that the concentration dependence does not deviate from a linear relationship by more than a few percent. Hence, the wavelength-dependent RI is assumed to be known also at higher concentrations. Because the RI of a highly concentrated glucose solution may be higher than that of water by 0.05 in the visible, glucose solutions of different concentrations provide a suitable test case for determining the matrix RI over a relatively wide RI range.

The roles of matrix and particle RI in Mie scattering are, however, not perfectly interchangeable. From equations (4.14) and (4.15) on page 46, we see that the particle RI n only appears in the parameter \mathbf{m} , while the matrix RI n_m appears in both parameters, \mathbf{m} and X defining the Mie scattering problem. This means that the sensitivity to n (or n_s as denoted in the previous section) and n_m is generally different. For the parameters considered here, however, the quality of the reconstruction of either the particle or matrix RI is relatively similar. When inferring the RI of water (for which some sources of error are expected to cancel) and with smoothing of the results for the RI of PS using a Sellmeier curve in order to prevent accumulation of errors during the two-step inverse problem solution the differences between the inferred RI of water and the reference curve [41] oscillates on the scale of 3×10^{-3} , similar to the findings for PS (Fig. 4.14). This accuracy of the inferred RI may not be satisfactory when a low-concentration aqueous solution is examined, where the quantity of interest is the change in RI caused by the solute which may range between 10^{-3} and 10^{-2} . For simple, non-absorbing solutions, the accuracy of the RI inference can be somewhat improved by using a different set of basis functions to represent $n_m(\lambda)$ than the Lorentz-type resonances (LTRs) used before for PS. These LTRs provide a relatively flexible model for the wavelength-dependence of the real part of the RI, also near or at absorption lines, while at the same time using relatively many parameters ($M = 20$ in the results shown for PS above). The real RI of an aqueous solution can be expressed as

$$n_m(\lambda) = n_{\text{H}_2\text{O}}(\lambda) + \delta n(\lambda) \quad (4.71)$$

and sufficiently far away from any strong absorption lines the RI difference $\delta n(\lambda)$ has only a weak wavelength-dependence. Hence, one can express $\delta n(\lambda)$ with few basis functions. Since for glucose solutions, Sobral and Peña-Gomar [92] successfully used a three-term Cauchy equation

$$\delta n(\lambda) = b_1 + \frac{b_2}{\lambda^2} + \frac{b_3}{\lambda^4} \quad (4.72)$$

to express the RI increment, we will use the same basis functions, i. e.,

$$f_1(\lambda) = 1, f_2(\lambda) = \frac{1}{\lambda^2}, f_3(\lambda) = \frac{1}{\lambda^4}, \quad (4.73)$$

to represent the RI difference $\delta n(\lambda)$ with only three parameters and using the known RI of water [41]. This suppresses the tendency of unphysical oscillations in $n_m(\lambda)$ that occurs when using LTRs.

The method will also be applied to determine the RI of a commercially available spherizing reagent for RBCs used for the measurements in section 4.6 below, for which no RI information is available.

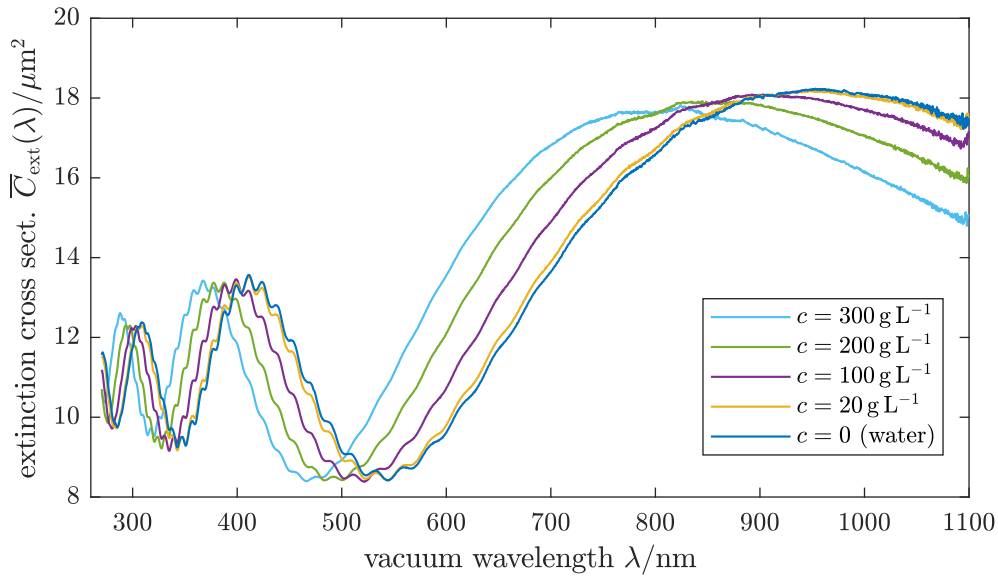


Figure 4.15: Measured extinction cross sections of $2.5 \mu\text{m}$ beads suspended in water and different glucose solutions. The curves shown are rescaled according to the optimization results to eliminate the effect of particle concentration errors [rescaled by $1/(1 + \eta)$, cf. Eq. (4.55)].

Results for D-glucose

The measurements of the spectral extinction were repeated in the same way as before, but instead of pure water using 5 different glucose solutions with concentrations $c \in \{10, 20, 100, 200, 300\} \text{ g L}^{-1}$ corresponding to $\{1\%, 2\%, 10\%, 20\%, 30\%\}$ weight-in-volume. The resulting extinction cross sections are shown in Fig. 4.15, where the particle concentration corresponds to dilution #6 in Tab. 4.1, which has the lowest measurement noise of the concentration series and was thus analyzed. The curve for $c = 10 \text{ g L}^{-1}$ is not shown in Fig. 4.15 for readability, because it would almost overlap the curves for water and $c = 20 \text{ g L}^{-1}$. One can clearly see the shift of the Mie resonances to lower wavelengths as the matrix RI increases and consequently the relative RI of the particles decreases. At the same time, the positions of the fine ripples remain almost unchanged. In this sense, the effect of increasing the matrix RI is very similar to decreasing the particle RI, see Fig. 4.5 on page 55.

For the inverse problem, the RI was initialized to a piecewise linear function $n_m(250 \text{ nm}, 460 \text{ nm}, 800 \text{ nm}, 1200 \text{ nm}) = (1.38, 1.34, 1.33, 1.32)$, which is a rough approximation of the RI of water. For the 10%, 20% and 30% glucose solutions, the initial RI was increased by 0.015, 0.030 and 0.045, respectively. Apart from that and the switched roles of matrix RI and particle RI, the parameter vector was initialized randomly in the same way as discussed before when inferring the RI of PS. For the 30% glucose solution, the minima thus found all corresponded to a size distribution with mean radius at least 80 nm too big and a much too high distribution width. To prevent the optimization algorithm from running into these unphysical minima, the size least-squares problem was regularized [Eq. (4.63)] with the previous findings for the size distribution, i. e., $\text{mean}(R) = 1259.09(10) \text{ nm}$ and $\text{std}(R) = 6.18(09) \text{ nm}$. The measurements from the lower-concentration solutions were analyzed without regularization.

The RIs of the glucose solutions, inferred with the difference to water $\delta n_m(\lambda)$ parametrized by a three-term Cauchy equation, are shown in Fig. 4.16 along with

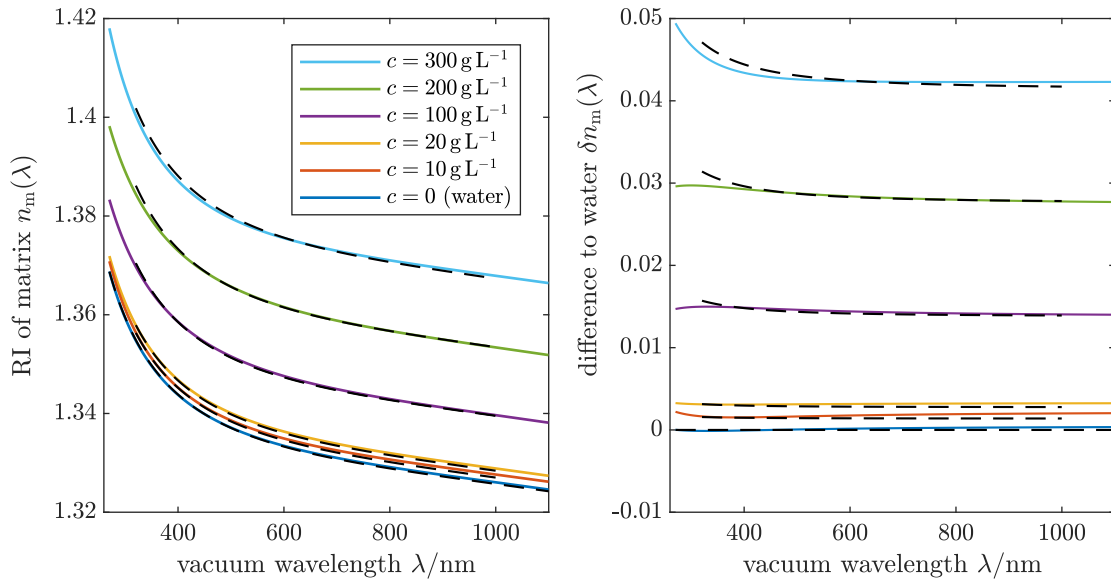


Figure 4.16: Inferred RI of water and different glucose solutions from extinction measurements of $2.5 \mu\text{m}$ beads suspended in them. The left panel shows the total real RI. The right panel shows the real RI difference to water $\delta n_m(\lambda) = n_m(\lambda) - n_{\text{H}_2\text{O}}(\lambda)$.

the literature values (also expressed by Cauchy equations). The results for the mean particle radius $\text{mean}(R)$ ranged between 1258.9 nm and 1259.2 nm and those for the distribution width $\text{std}(R)$ between 6.1 nm and 6.6 nm , which is highly consistent with the previous findings. The overall increase of the RI with glucose concentration is reproduced very well by the inverse problem results, and possible deviations from a linear concentration dependence (which is known to hold at least up to 50 g L^{-1} [92]) are apparently not too strong. However, even smaller than before for the PS RI, the estimated uncertainties $u^{\text{noise}}[n_m(\lambda)]$ range from 6×10^{-6} to 1×10^{-4} depending on concentration and wavelength and do not explain the deviations from the reference values [41], even for water or at low glucose concentrations $c_{\text{glucose}} \leq 50 \text{ g L}^{-1}$, where they are known to be reliable. These differences $\Delta n_m(\lambda)$ are shown in Fig. 4.17 and exceed 5×10^{-4} for low concentrations ($c_{\text{glucose}} \leq 20 \text{ g L}^{-1}$). For higher concentrations, they do exceed 10^{-3} , but this might in part be attributed to violations of the linear concentration-dependence of the RI assumed for the reference values.

Results for sphering reagent

The application of the inverse problem for the RI of the matrix surrounding the microparticles to glucose solutions (for which literature data exists) served as a proof

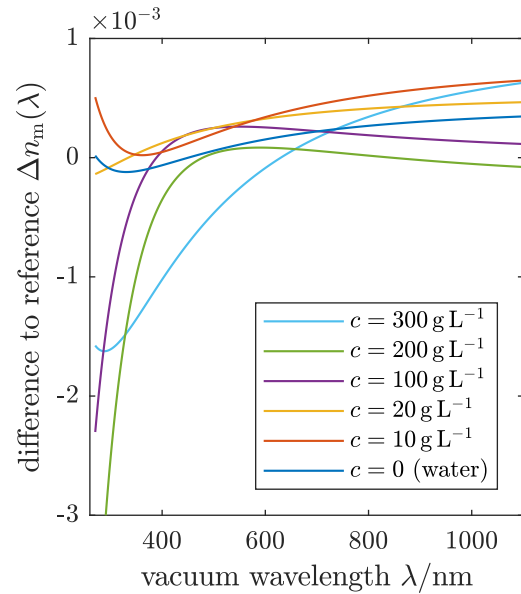


Figure 4.17: Difference of inferred water and glucose RI (see Fig. 4.16) to reference values [41, 92]

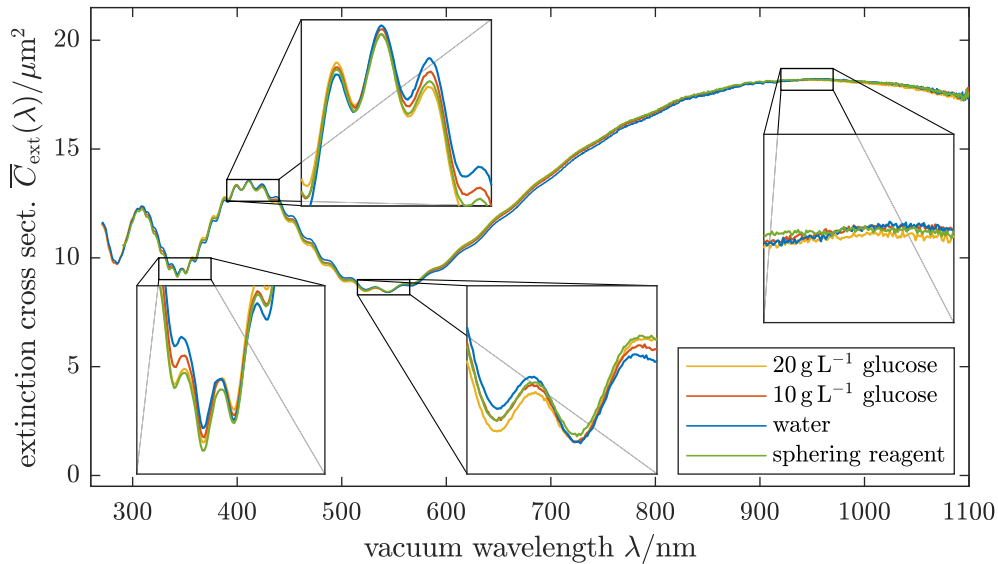


Figure 4.18: Measured extinction cross sections of $2.5 \mu\text{m}$ PS beads suspended in a sphering reagent for RBCs in comparison to water and glucose solutions. The curves shown are rescaled according to the optimization results to eliminate the effect of particle concentration errors [rescaled by $1/(1 + \eta)$, cf. Eq. (4.55)].

of concept and to estimate the accuracy of the method. A question of actual importance for the basic research problem presented in the next section – to determine the optical properties of RBCs from their extinction spectra – is the application of the method to a sphering reagent for RBCs. This sphering reagent is a commercially available substance (CELL-DYN diluent/sheath reagent, Abbott GmbH & Co. KG, Diagnostik, Germany) normally used for the isovolumetric sphering of RBCs in hematology analyzers. It was used in the experiments discussed in the next section of this chapter to render RBCs spherical for extinction measurements, in order to analyze data with Mie theory. The sphering occurs only as long as the cells are suspended the reagent and is reversed when it is replaced by isotonic saline. Hence the measurements have to be performed with RBCs suspended in the sphering reagent rather than a fluid with well-known optical properties like water or isotonic saline. The basic concept of isovolumetric sphering of RBCs by chemical treatment of the membrane was published by Kim and Ornstein [99] and Tycko et al. [22] in the 1980s. The ingredients of their sphering solutions were isotonic saline, sodium dodecyl sulfate (SDS; a surfactant) and the bovine serum albumin (BSA; a plasma protein). However, neither are the wavelength-dependent RIs of SDS and BSA known, nor is the exact composition of the commercial product, which likely contains additional substances like preservatives. This is unfortunate, as it means that the RI of the sphering reagent has to be determined before measured RBC extinction spectra can be analyzed.

In order to quantitatively infer the RI of the sphering reagent, $2.5 \mu\text{m}$ PS beads were suspended in it and the extinction measurements were repeated as before. Measurements were taken for the undiluted sphering reagent (as used for the RBCs) and dilutions of 25% and 50% with pure water. Furthermore, the absorption spectrum was recorded with the setup in Fig. 4.2. An absorption band was found between 220 nm and 300 nm with a peak in the imaginary part if the RI of 10^{-5} at 284 nm. This limits the lowest wavelength in our analysis to 290 nm since the transmittance in a 10 mm cuvette drops down to about 1.2% compared to water at the absorption

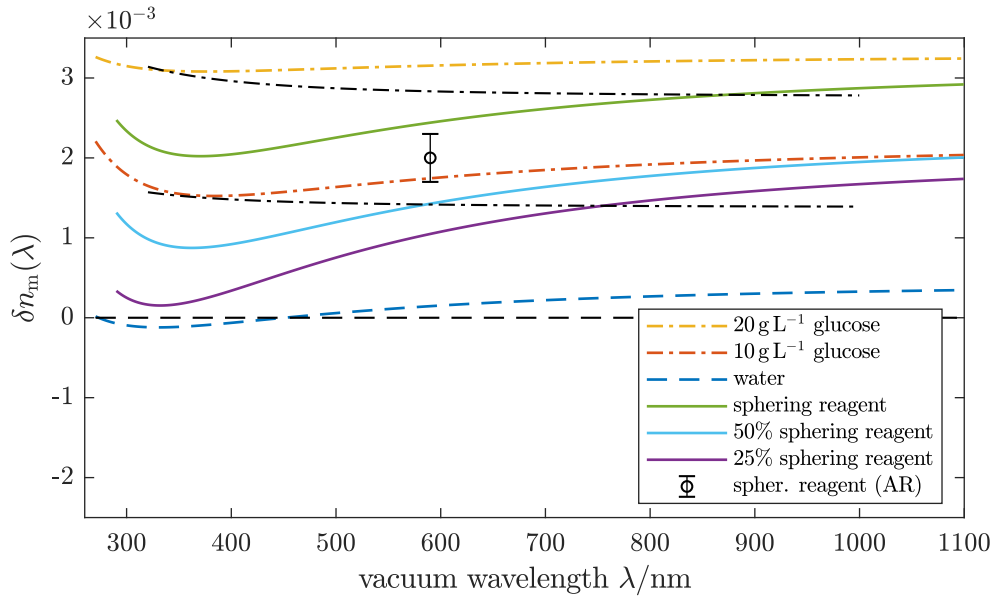


Figure 4.19: RI difference to water obtained for different fluid matrices (compare to Fig. 4.18). The black lines represent the respective reference curves for water [41] and the D-glucose solutions [92]. The errorbar indicates the measurement of the undiluted sphering reagent with an Abbe refractometer (AR).

peak, which results in a very low signal to noise ratio, i. e., the wavelength range in the analysis has to be reduced to [290, 1100] nm. From a theoretical point of view, the spectra could still be analyzed below 290 nm using standard Mie scattering, see Appendix 4.A. The analysis of the measured spectral extinction cross sections was performed like for low-concentration glucose solutions. For the 50% dilution, regularization of the size distribution became necessary like for the 30% glucose solution. The other two dilutions were analyzed without regularization.

The measured extinction cross sections $\overline{C}_{\text{ext}}(\lambda)$ of PS beads suspended in the sphering reagent are shown in Fig. 4.18 in comparison to measurements in 1% and 2% D-glucose solutions and water. The differences between the curves are subtle, but can be seen by comparing the ripple structure (insets in Fig. 4.18). The curve for the sphering reagent lies in between those of the two glucose solutions. Without solving any inverse problem, this already allows to conclude that the RI of the sphering reagent is different from water by a similar figure as the RI of a 1% or 2% glucose solution. Furthermore, this indicates that the RI of the unknown solution is in between those of the two glucose solutions.

The RI differences to pure water $\delta n_m(\lambda)$ found by optimization, with $\delta n_m(\lambda)$ expressed by a three-term Cauchy equation are shown in Fig. 4.19 for the three dilutions (25%, 50%, 100%) of the sphering reagent and the two glucose solutions. Also shown in this figure is the measurement of the RI of the (undiluted) sphering reagent with an Abbe refractometer (ORT 1RS, Kern Optics, Germany) at a single wavelength $\lambda = 590$ nm, which resulted in $\delta n = 0.0020(3)$. This direct measurement and the respective curve $\delta n_m(\lambda)$ are not quite in agreement with each other. If one accounts for the fact that at this wavelength the RIs of the glucose solutions are higher than the respective reference values (black lines in Fig. 4.19) by about 3.2×10^{-4} , and corrects the inverse problem result for the sphering reagent by this number, one obtains for the sphering reagent $\delta n^{\text{corr}} = 0.0021$, which is inside the uncertainty of the refractometer measurement. One can attempt to apply this correction (i. e.,

subtracting the differences between the glucose results and their reference curves from the sphering reagent result) to the full wavelength range. This results in a RI difference for the sphering reagent which is in between $0.0020 \leq \delta n^{\text{corr}}(\lambda) \leq 0.0023$ for the wavelength range considered. However, even with this correction attempt, the wavelength-dependence obtained from the analysis of the extinction spectra is most likely not reliable for the following reasons:

1. At least for $\lambda \geq 350$ nm, the inverse problem results in Fig. 4.19 all feature anomalous dispersion (i. e., $d\delta n_m/d\lambda < 0$), even though this is known not to be the case for water ($\delta n_m \equiv 0$) and glucose. For the sphering reagent, this remains the case even after a correction attempt (curves not shown). The anomalous dispersion obtained for the sphering reagent is most likely exaggerated as it is physically not plausible: There is only a weak absorption line around 270 nm that causes a dispersion feature, however since $\kappa(\lambda) \leq 10^{-5}$ for this line, one finds (KK transform, see chapter 3) and amplitude of the real RI feature of less than 10^{-5} . Also this absorption line would cause *normal dispersion* at higher wavelengths, not anomalous dispersion.
2. The anomalous dispersion of the 25% and 50% dilutions of the sphering reagent are more pronounced than for the undiluted solution. Since the solution has only low to moderate concentration of any solutes (reflected in a small δn), a linear relation between RI and concentration should be a reasonable assumption. The inverse problem results for the wavelength dependence violate this linear relationship, which indicates that the a large part of the wavelength-dependence consists of artifacts due to measurement and/or model errors.

Given the most-likely not significant wavelength-dependence, the inverse problem results can only confirm the conclusion drawn from looking at the ripple structure in the extinction spectra: The RI of the sphering reagent is in between those of a 1% and 2% glucose solution.

4.6 Application to sphered red blood cells

After the demonstration of the size and RI inference method for quasi-monodisperse PS beads for which accurate RI literature data exists, we will now apply it to sphered RBCs to obtain their optical properties. For the extinction measurements blood samples from three different volunteers were used. Unlike for PS beads which are commercially available in a wide range of sizes, the mean volume of RBCs (MCV) of most healthy persons falls within the reference range of 80 fL to 100 fL [17]. From a data analysis point of view this is unfortunate, since we have seen already for PS beads that the RI inference is most challenging at the minima and maxima of the Mie resonances in $\overline{C}_{\text{ext}}(\lambda)$. Since the wavelengths at which these resonances occur depend on particle size, it is favorable to collect data from blood samples with significantly different mean RBC volumes, rather than similar ones. In order to have at least some size variation one of the three healthy volunteers was selected for his/her MCV of approximately 63 fL, which is significantly outside of the reference range.

In order to apply the data analysis presented in the previous sections, the RBCs in suspension were sphered using a chemical treatment that reduces the membranes' area while leaving them intact and not affecting the inside of the cell [22, 99]. The

sphering occurs only as long as the cells are suspended in a specific reagent and is reversed when it is replaced by isotonic saline. Hence the measurements have to be performed with RBCs suspended in the sphering reagent rather than a fluid with well-known optical properties like water or isotonic saline. The determination of the RI of the sphering reagent was discussed in the previous section.

4.6.1 Experiment

Note: The preparation of RBC samples and the extinction measurements were performed by Kathrin Smuda (Charité and PTB Berlin).

Freshly withdrawn venous blood, anti-coagulated by ethylenediaminetetraacetic acid (EDTA, 1.8 g L^{-1}), was collected from 3 healthy volunteers (A, B and C) with the vacutainer system from BD (BD, Heidelberg, Germany) and immediately processed. Informed consent was obtained from all donors in written form. The blood samples were withdrawn in accordance with the transfusion law of Germany. The use of donor blood samples for scientific purposes was approved by the ethics committee of the Charité – Universitätsmedizin Berlin (# EA1/137/14). For leukocyte and thrombocyte depletion, 10 mL of whole blood were washed three times (150 g, 5 min) in 50 mL of phosphate buffered saline (PBS; sigma, Germany). Washed RBCs were re-suspended in PBS to a final volume of 10 mL. Complete blood counts (CBCs) were taken using a XS-800i analyzer (Sysmex Europe GmbH, Germany) for whole blood and an ABX Micros 60 analyzer (Axon Lab AG, Germany) before and after washing to ensure that leukocyte and thrombocyte concentrations are low and extinction spectra of RBCs are not distorted. For sphering, washed RBCs were diluted 1:100 in the sphering reagent (CELL-DYN diluent/sheath reagent, Abbott GmbH & Co. KG, Diagnostik, Germany). This pre-diluted suspension was used as stock solution for dilution series. For transmission measurements, pre-diluted sphered RBCs were further diluted with the sphering reagent. The concentration series for the spectral transmittance were recorded just like for the PS beads described in the previous section 4.5 with 6–8 dilutions measured per sample and transmittances ranging from roughly 10% to 95%. Extinction cross sections were computed according to Eq. (4.1) and examined for effects of multiple scattering, which can be excluded for the curves analyzed in the following.

Measured spectral extinction cross sections $\overline{C}_{\text{ext}}(\lambda)$ of sphered RBCs from three volunteers (A, B, C), recorded at room temperature are shown in Fig. 4.20 (left panel). Absorption spectra of lysed RBCs were measured for all the samples and found to agree with literature data for oxyHb [37, 39] up to the concentration error from volumetric dilution. Hence we can use the literature values [37] for $\gamma(\lambda)$ in the analysis (right panel of Fig. 4.20). This also confirms that the RBCs were fully oxygenated due to contact of the samples with air. Hematological parameters from the CBCs of the blood samples are shown in Tab. 4.4. In contrast to PS beads, no ripple structure is visible, which is a result of the lower relative RI of the RBCs. Due to the different MCVs of the sample the Mie resonances and overall magnitude of the $\overline{C}_{\text{ext}}(\lambda)$ are clearly shifted between the curves in Fig. 4.20. At the same time, the features stemming from the absorption bands of Hb, such as the double peak around 560 nm and the Soret band near 420 nm are shared between the three curves. Note that Fig. 4.7 on page 57 illustrates the general effect of the imaginary RI on $C_{\text{ext}}(\lambda)$.

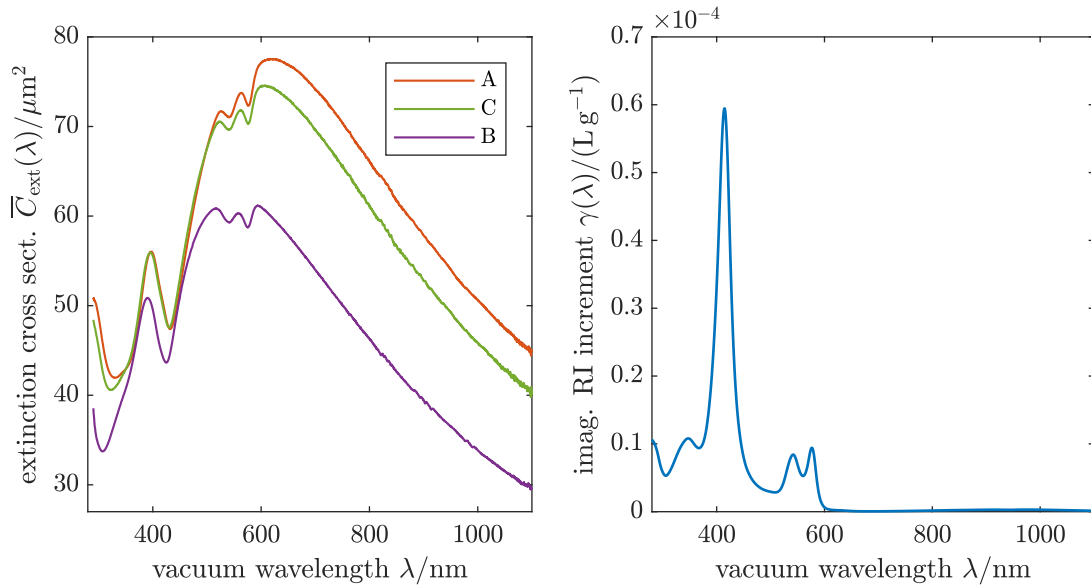


Figure 4.20: Measured extinction cross sections of sphered RBCs suspended in sphering reagent (left panel) and imaginary RI increment of oxyHb [38] used in the forward model (right panel). Samples from three volunteers A, B and C who exhibit significantly different MCV were investigated. The curves shown are rescaled according to the optimization results to eliminate the effect of particle concentration errors [rescaled by $1/(1 + \eta)$, cf. Eq. (4.55)].

4.6.2 Inverse problem

The wavelength dependence of the RI of the sphering reagent (in which the RBCs are suspended during measurement) could not be inferred with sufficient accuracy from extinction measurements with PS beads (see section 4.5.4) to be used for inverting the extinction spectra of RBCs. Due to the low absorbance of the solution in the measured range ($\kappa \leq 10^{-5}$) the presence of strong dispersion features of the real

Table 4.4: Hematological parameters of RBC samples obtained from the CBC of whole blood (top) and used for regularization in the optimization in comparison to the optimization results (bottom). c_{RBC} is the RBC concentration in the whole blood sample and ϕ the dilution factor applied for the extinction measurement. η is the (negative) relative concentration error found by optimization. The numbers in parentheses are the estimated standard uncertainties, referred to the last digit.

volunteer	CBC					ϕ
	$\frac{\text{MCHC}}{\text{g L}^{-1}}$	HDW	$\frac{\text{MCV}}{\text{fL}}$	RDW	$\frac{c_{\text{RBC}}}{10^{12} \text{ L}^{-1}}$	
A	329(6)	–	86.0(1.0)	12.7(1.0)%	4.6	1700
B	324(10)	–	63.0(2.2)	15.7(1.2)%	6.6	7300
C	331(6)	–	81.5(1.0)	15.2(1.0)%	4.5	3200
	optimization result					η
A	324(6)	3.9(5)%	85.7(1.0)	12.7(1.0)%	+1.9(8)%	
B	332(4)	6.4(3)%	62.3(2.0)	15.7(1.2)%	-13.1(1.9)%	
C	331(6)	4.6(5)%	81.5(1.1)	15.2(1.0)%	+2.4(9)%	

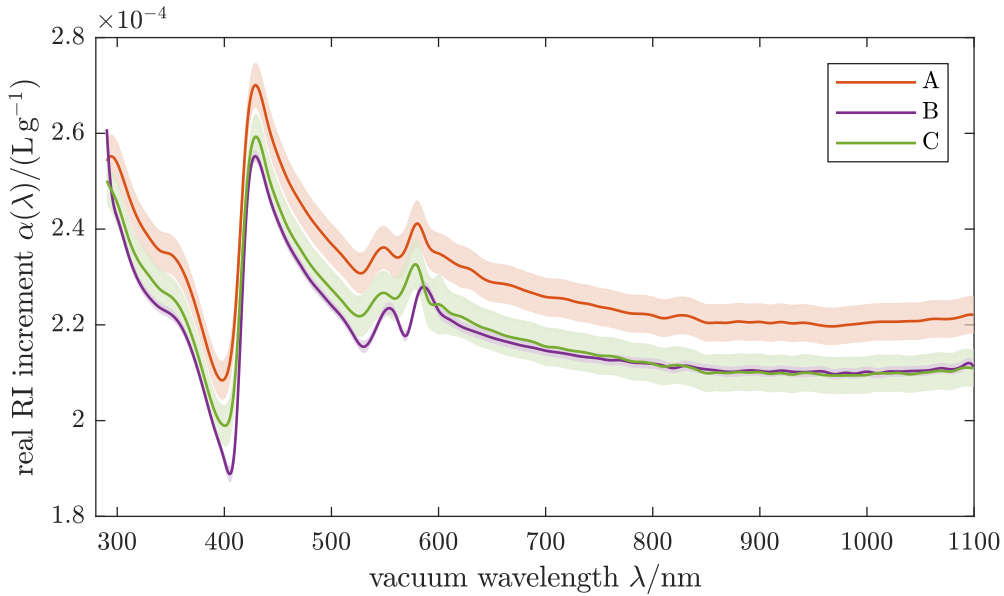


Figure 4.21: Real RI increment of oxygenated human RBCs obtained from the measured extinction cross sections in Fig. 4.20. Shaded bands indicate ± 1 estimated uncertainties $u^{\text{noise}}[\alpha(\lambda)]$, accounting for noise in the analyzed spectra and uncertainties of CBC parameters.

RI is unlikely. From the comparison between extinction spectra of $2.5\ \mu\text{m}$ PS beads suspended in 1% and 2% D-glucose solutions and of the same beads suspended in the sphering reagent, it becomes clear that the RI of the latter solution is somewhere between the RIs of the former two solutions, at least for the quasi-nonabsorbing range $\lambda \geq 290\ \text{nm}$. The RI increment of D-glucose in aqueous solution is known to have only a very weak wavelength-dependence in the 320 nm to 1000 nm range [92] (the RI difference to pure water of a 1.5% D-glucose solution changes by less than 3×10^{-4} over this wavelength range). Due to the similarity, we conclude that the RI difference of the sphering reagent compared to pure water also has negligible wavelength dependence. Hence, in the forward model for sphered RBCs we assume $n_{\text{m}}(\lambda) = n_{\text{H}_2\text{O}}(\lambda) + 0.0020(3)$ for all λ , as this RI difference was measured for the sphering reagent at 590 nm using a refractometer.

For the set of basis function $g_j(\lambda)$ used to represent the real RI increment $\alpha(\lambda)$, we use a set of orthonormalized third-order cardinal splines with a uniform grid spacing of $\Delta_y = 10\ \text{nm}$ on the measured interval [290, 1100] nm. In contrast to most datasets from PS beads, a regularization term according to Eq. (4.63) was employed in the analysis of all RBC extinction spectra that penalizes deviations from the CBC measurements, see Tab. 4.4.

Sampling of initial parameter values

As already mentioned, initial values of the parameter vector were sampled randomly around a given mean and the local optimization was repeated several times. More specifically, the coefficient vector \mathbf{a} of the real RI increment $\alpha(\lambda)$ was initialised in a two-step process: (i) $\alpha(\lambda)$ was set to a random constant $\text{const} \in \mathcal{N}(0.235\ \text{mL g}^{-1}, 0.04\ \text{mL g}^{-1})$ and (ii) additional normally distributed independent random numbers were added to the coefficients a_j , resulting in random dispersion features of $0.004\ \text{mL g}^{-1}$ standard deviation for $\alpha(\lambda)$. For the size and concentra-

tion distribution, the parameters θ were randomly initialized around those values obtained from the CBC. Standard deviations of the Gaussian random numbers were set to 30 g L^{-1} for $\text{mean}(c_{\text{Hb}})$, 120 nm for $\text{mean}(R)$ and 30 nm for $\text{std}(R)$. The width of the Hb concentration distribution and the particle concentration error were sampled from $\text{std}(c_{\text{Hb}}) \in \mathcal{N}(7\% \text{MCHC}, 10 \text{ g L}^{-1})$ and $\eta \in \mathcal{N}(0, 3\%)$, respectively.

25 random initial conditions were sampled and the optimization was run for 15 iterations. Afterwards the six parameter vectors with the lowest χ^2 were further optimized for up to 150 iterations or until a given tolerance was met. The parameter vector with the lowest χ^2 was used as the result $\hat{\psi}$. Like for PS beads, typically several initial conditions ended up in the same minimum, but other less deep local minima were found as well.

Optimization results

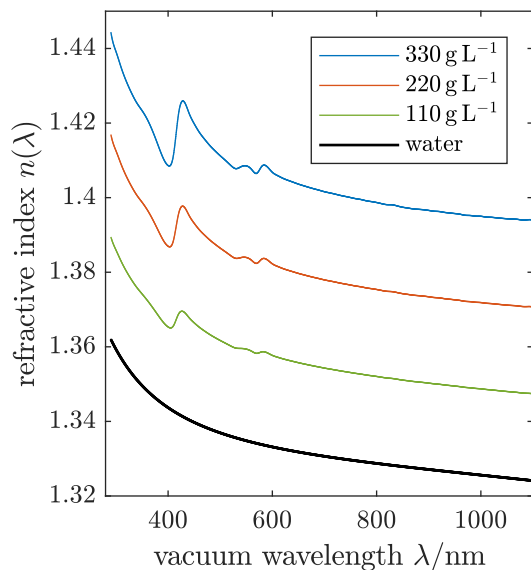


Figure 4.22: Real RI of oxygenated RBCs computed with the RI increment determined in this chapter for three different Hb concentrations

tions might be caused by possible scattering effects of residual WBCs or blood platelets in the washed RBC samples, by different concentrations of proteins other than Hb in the RBCs of the volunteers or by model errors due to the class of functions assumed for the distributions of size and Hb distribution. Lastly the fact that these deviations exceed the estimated uncertainties could simply be a result of the model employed for measurement noise, which was found to be insufficient for uncertainty propagation for the PS beads. In order to account for these influences at least to some extent, as a final result for the real RI increment of oxygenated RBCs the average of the three curves was taken, weighted with the respective uncertainties (inverse covariance matrices) of the individual curves, which is shown as the blue curve in Fig. 4.23. The uncertainties of the result are determined from the weighted sample variance, details are given in Appendix 4.C. The resulting total RI of RBCs at three different concentration computed with this result is shown in Fig. 4.22.

The optimization results for the hematological parameters are shown in Tab. 4.4. Because of the described effect of mutually compensating parameters in the forward model, the found MCHC, MCV and RDW mean values and uncertainties basically

The real RI increment $\alpha(\lambda)$ obtained by nonlinear optimization is shown in Fig. 4.21. Even though the underlying $\bar{C}_{\text{ext}}(\lambda)$ (Fig. 4.20) differ significantly, the $\alpha(\lambda)$ have almost the same wavelength dependence within their respective estimated uncertainties, except for a small offset. All three curves lie around $\alpha \approx 0.22 \text{ mL g}^{-1}$, with differences between 0.01 mL g^{-1} at the IR end and 0.013 mL g^{-1} at the UV end being present between the highest curve (volunteer A) and the lowest (volunteer B). This agreement is remarkably good, given that the estimated standard uncertainties (shaded bands in Fig. 4.21) account only for effects of noise in the measured extinction spectra and uncertainties of the parameters from the CBC. The observed systematic deviations

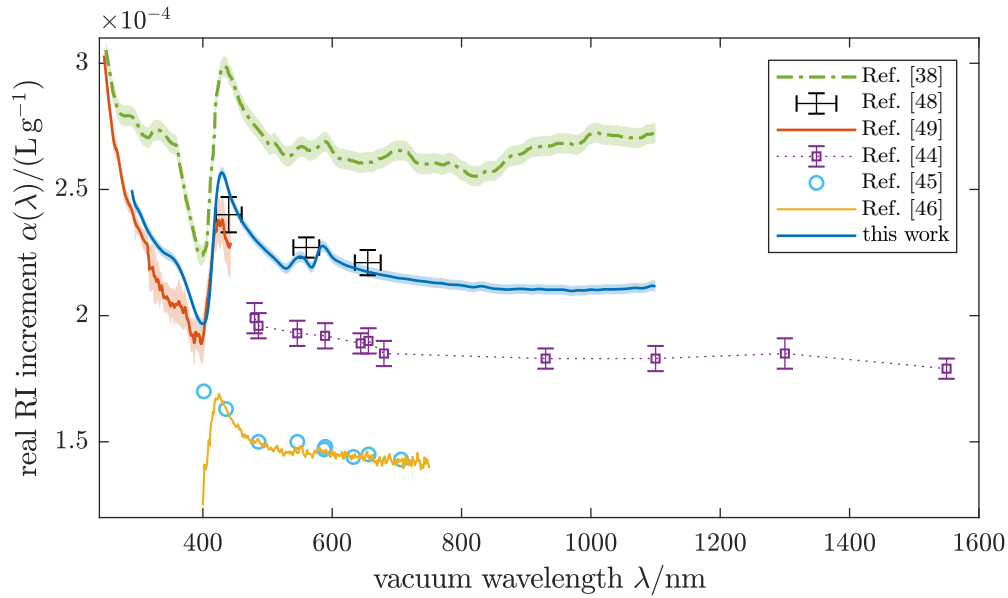


Figure 4.23: Real RI increment of oxygenated human RBCs. The blue line is the weighted average of the individual curves in Fig. 4.21. Various literature values for the RI increment of oxygenated Hb solutions and RBCs are shown for comparison. Samples for these measurements were: (i) Hb solutions from powder [45, 46, 48], (ii) Hb solutions from freshly hemolyzed RBCs [38, 44] and (iii) single native RBCs [49].

reflect the input CBC parameters and their respective uncertainties, which were used for regularization. In addition, the width of the intracellular Hb concentration distribution $\text{HDW} = \text{std}(c_{\text{Hb}})/\text{mean}(c_{\text{Hb}})$, which is not part of the standard CBC was also retrieved. Hence, there is no reference measurement to compare to, but the HDW values obtained appear at least plausible compared to typical physiological values [22, 50].

4.6.3 Comparison to literature data

Fig. 4.23 shows the final result obtained here for the real RI increment $\alpha(\lambda)$ of oxygenated RBCs along with various literature values of Hb solutions and intact RBCs. Compared to the widely used values reported by Barer and Joseph [36, 42] of $\alpha \approx 0.19 \text{ mL g}^{-1}$ for Hb in the visible range, the results for RBCs found in this chapter (blue curve in Fig. 4.23) of $\alpha(\lambda) \approx 0.22 \text{ mL g}^{-1}$ are significantly higher. On the other hand, the results found here are in good agreement with values measured from a single native RBC using hyperspectral microscopy by Ojaghi et al. [49] for wavelengths $\lambda \in [250, 440] \text{ nm}$ (red curve in Fig. 4.23) while exhibiting a less noisy profile with lower uncertainties and covering a wider wavelength range $\lambda \in [290, 1100] \text{ nm}$. Good agreement is also found for values measured for solutions prepared from Hb powder using spectroscopic phase microscopy by Park et al. [48] at discrete wavelengths $\lambda \in [440 \text{ nm}, 700 \text{ nm}]$ (black error crosses in Fig. 4.23). Note that Park et al. [48] also reported measurements of the RI increment of bovine serum albumin (BSA) of $\alpha_{\text{BSA}} = 0.18 \text{ mL g}^{-1}$, which is lower as their values of α_{Hb} and consistent with those values of Barer and Joseph [36, 42]. This makes it plausible that the RI increments reported for various proteins by Barer and Joseph are generally correct, but that the RI increment of Hb is too low.

The values obtained here for $\alpha(\lambda)$ are about 0.05 mL g^{-1} or 20% lower than

values measured by Friebel and Meinke for homogenized RBC cytoplasm, obtained by hemolysis [38] (green dash-dotted curve in Fig. 4.23). At the same time the peak-peak amplitude $\Delta_{pp}\alpha = 0.060 \text{ mL g}^{-1}$ of the dispersion feature around $\lambda \approx 420 \text{ nm}$ is lower by the same percentage. Comparing to the measurements of Lazareva and Tuchin [44] (purple dotted line in Fig. 4.23) for samples prepared from fresh RBCs in a similar way as those used by Friebel and Meinke [38], the present results for $\alpha(\lambda)$ are about 0.03 mL g^{-1} higher. As a hypothesis, these deviations in both directions can be explained by a scaling error of some of the curves, most likely stemming from the measurement of the Hb concentration. Another possible source for these discrepancies is the formation of Hb-enriched or depleted layers near interfaces, as these measurements were performed at solution-air interfaces [38] and solution-glass interfaces [44], respectively.

Comparing to other results for the RI increment of Hb solutions, the findings of this chapter are incompatible with the data presented by Zhernovaya et al. [45] and Wang et al. [46] (cyan circles and yellow line in Fig. 4.23), where values of $\alpha(\lambda) \approx 0.15 \text{ mL g}^{-1}$ for $\lambda \in [400 \text{ nm}, 750 \text{ nm}]$ were reported for solutions prepared from human and bovine Hb in dry form and concentrations determined from the weighed-in protein mass. The limitations of this method over spectroscopic concentration determination have been discussed [36]. Furthermore, the solutions created from dry Hb, being in the form of non-functional methemoglobin (metHb), require conversion to oxygenated Hb (oxyHb) using sodium bicarbonate. This may, at least in part, explain the discrepancies.

The overall wavelength-dependence of the presented result for $\alpha(\lambda)$ obtained from extinction cross sections of intact RBCs closely resembles the curves computed using the Kramers-Kronig (KK) transformation of the absorption spectrum of Hb solutions presented in chapter 3 of this thesis. However, the agreement between the two hinges on the real RI increment dataset used for fitting the unknown parameters of the deep UV absorbance model. This is because the parameters of this model, which contributes the background to $\alpha(\lambda)$ cannot be determined from the available absorption spectra alone. Fig. 3.4 on page 34 shows the KK fit to two different curves: the measurement results of Friebel and Meinke [38] and this chapter's result. The former is the case published in the author's own article Ref. [47], before the results of this chapter became available. However, only for the latter case does one find good agreement between the KK result and the curve it was fitted to within the estimated uncertainties. In particular, the peak-peak amplitude around $\lambda \approx 420 \text{ nm}$ differs by less than 5% between the KK result and this chapter's result. This observation indicates that the RI of RBCs is indeed practically identical to that of an aqueous Hb solution of equal concentration, for which the KK analysis was performed. It also justifies the use of imaginary RI increment data obtained from absorption spectra of bulk Hb solutions in the present analysis of RBC extinction spectra.

As errors of the Hb concentration pose a serious problem in RI measurements of RBCs and Hb solutions, and may have affected some of the measurements presented in the literature, we need to carefully estimate their potential influence on the present results. To determine the mean intracellular Hb concentration (MCHC) of the examined RBC samples, a hematology analyzer was employed. These devices are used in laboratory medicine and undergo frequent external controls and calibration in order to yield reliable values for medical diagnoses. Furthermore the RBCs remained intact over the course of the experiment. This means that errors

in the number concentration of the cells can occur during preparation, but are easily compensated during data analysis. On the other hand changes of the MCHC are unlikely, as this would require loss of cells of only a certain intracellular Hb concentration. This is in contrast to measurements employing Hb solutions, where adherence of the protein to container walls always goes along with Hb concentration errors. Thus an error of the MCHC (which would directly affect the result for α) of more than 2% is not expected for our findings, which was accounted for as uncertainty of the CBC measurements used for regularization in the least-squares parameter optimization.

4.7 Summary and outlook

In this chapter, we have considered the measurement of the spectral extinction cross sections of polystyrene microspheres and spheroided RBCs suspended in water and other liquids and developed an inverse-problem method to determine the optical properties of these particles, cells and liquids from their extinction spectra. The measurements $\overline{C}_{\text{ext}}^*(\lambda)$ represent averages over the size distribution and – in the case of RBCs – distribution of intracellular Hb concentration of the polydisperse ensemble. The sensitivity of numerically computed (Mie scattering) spectral extinction cross sections to size and optical properties of the particles and cells was discussed using simplified models for the RI, such that the effects of different parameters can be studied independently. The problems inherent to a pointwise (or wavelength-wise) inference of the particle RI under the assumption of a known size distribution were demonstrated for PS beads using synthetic data. To overcome these issues and reduce the number of parameters representing the scatterers, an expression of the real particle RI $n(\lambda)$ or the real RI increment of the RBCs $\alpha(\lambda)$ with a relatively small set of suitable basis functions was discussed. For the determination of the RI of PS beads $M = 20$ functions were found sufficient to analyze spectra containing roughly $N = 1800$ data points, using Lorentz-type resonances (LTRs). For the real RI increment of RBCs, $M = 84$ third-order cardinal splines were employed. A forward model $\mathcal{M}(\lambda; \boldsymbol{\psi})$ for the measured cross sections was developed, in which the size and concentration distributions are characterized by a mean and standard deviation, respectively. Additionally the forward model can compensate errors of the particle or cell concentration in the measured suspensions, that may occur due to volumetric dilution using adjustable pipettes. For the cases discussed, the parameter vector $\boldsymbol{\psi}$ of the forward model has dimension $L = 23$ (for PS) to $L = 89$ (for RBCs). Applying standard nonlinear least-squares optimization, these L model parameters were fitted to the measurement data.

The uncertainties of these results were estimated using linearized propagation of covariance matrices of the measurement data, which in turn were estimated from repeated spectral measurements of the same sample. For PS beads it was found that the uncertainties of the RI result thus obtained could not explain the differences to literature values for the RI of bulk PS. Rather than indicating that PS microbeads have a RI different from bulk material, this is an indicator of an insufficient model for the uncertainties of the measured spectra, which does not account for all sources of error. One likely source of error are artifacts of the spectral lines of the Xenon lamp in the measured transmittance spectra, which are visible mainly at the infrared end of the measured range. Besides nonlinearities of the detector of the spectrometer, these artifacts could be caused by changes in reflectance at the cuvette

walls, even though the cuvette was not actively moved between measurements. In this case a remedy could be to place the cuvette in a permanently-mounted container filled with immersion oil, as was used in a predecessor of the experimental setup used here and discussed in [100], which would minimize the reflections at the cuvette walls. However, the measurements taken with this predecessor setup had other drawbacks, like a smaller wavelength range, higher detector noise and the necessity to use an ad-hoc mathematical “compensation curve” in the forward model that was not motivated physically in order to obtain reasonable inverse problem results. On the data-analysis side, a remedy for the insufficient error model consists in analyzing multiple datasets of differently-sized particles or cells with the same optical properties to be inferred in the hope that the influence of these errors can be estimated statistically. This approach was taken for the RBCs where samples from three volunteers with significantly differing mean RBC volume (MCV) were examined. Of course, a reliable statistical analysis would require more samples, meaning more time spent on sample preparation and measurements. Model errors might have an additional effect not analyzed here, e. g., deviations from a spherical shape or *surface roughness*. However, for the case of PS beads, even the most intricate details of the extinction spectra, i. e., their ripple structure, can be fitted with the model. Hence, it seems unlikely that surface roughness is relevant for these artificial microspheres. For sphered RBCs on the other hand, which are subject to biological variation and imperfections and may acquire surface roughness due to the sphering process [99], this could be a more serious problem. The scattering properties from ensembles of rough spheres have been examined theoretically [101, 102] and it was found that the deviations between spheres and rough spheres are largest for side scattering and backscattering amplitudes, whereas forward and near-forward scattering is least sensitive to irregularities. Due to the optical theorem [61], which states that the extinction cross section of a particle is directly related the scattering amplitude in the forward direction, this means that the extinction cross section C_{ext} is very insensitive to irregularities of the particles’ surfaces. Hence the Mie scattering formulae may be used even for somewhat irregular particles or cells.

The mean diameter of 2.5 μm PS beads determined from extinction spectra was well within the uncertainty specified by the manufacturer of the material used. On the other hand, the width of the size distribution, expressed by the coefficient of variation of the diameter, was found to be about 0.5%, which is significantly lower than the specification of 1.4%. It follows that the particles are closer to monodispersity than declared, presumably since the specified distribution widths are estimates of the corresponding upper limit during production.

Even though estimating the uncertainties of the determined particle RI by propagation of the estimated spectral measurement noise proved to be insufficient, comparison with reference values indicates that the accuracy of the RI inference is not worse than 3×10^{-3} . A very similar figure was found for the case where the particle RI is assumed to be known and the RI of the fluid matrix surrounding the microparticles is the quantity determined by optimization, which was demonstrated using D-glucose solutions as a matrix. Unfortunately this RI accuracy was found to be insufficient to resolve the (weak) wavelength dependence of the RI increment of the sphering reagent in which RBCs were suspended during measurement. Hence, a wavelength-independent value with appropriate uncertainty was used in the following analysis.

The real RI increment $\alpha(\lambda)$ of sphered RBCs (oxygenated, room temperature)

was determined from blood samples from three different volunteers. The hematological parameters MCHC, MCV and RDW obtained from blood counts with hematology analyzers were used for regularization of the least-squares optimization problem, because otherwise an unambiguous determination of these parameters and the mean RI increment was not possible. The three curves for $\alpha(\lambda)$ thus obtained agree relatively well, given that the uncertainties estimated from measurement noise were found much too small for the case of PS beads, which indicates an insufficient uncertainty model for the extinction spectra in general. The results presented here speak in favor of the real RI increment of Hb solutions and RBCs being around $\alpha \approx 0.22 \text{ mL g}^{-1}$. This is in good agreement with some of the values reported in the literature (having higher uncertainties) [48, 49] and also in very good agreement with the Kramers-Kronig analysis of chapter 3. However, due to the literature data ranging from about $\alpha \approx 0.15 \text{ mL g}^{-1}$ to $\alpha \approx 0.27 \text{ mL g}^{-1}$, disagreement is found with many other sources. Possible explanations for these deviations and the advantages of the method employed here were discussed.

Perspectively, the measurement technique along with the data analysis method presented here provide a more precise approach for future determination of the optical properties of approximately spherical biological entities such as RBCs in different oxygenation states or chemical environments (e. g., incubated with glucose [103]), other animal cells [12], phytoplankton [104]. An application to artificial Hb based blood substitutes [52] is subject of the next chapter. Besides Mie scattering by homogeneous spheres, efficient numerical light scattering simulation tools exist for concentric spheres [61] (e. g., a model for lymphocytes) or spheroids [56, 105] (e. g., a simplified model for rod-shaped *E. coli* bacteria, blood platelets or native RBCs). For more general shapes, T -matrix methods [63] can be used to compute particle extinction cross sections averaged over orientation. Hence, the data analysis method presented here is, in principle, applicable to such objects, too. However, the computational cost is generally much higher for such methods. Hence the analysis might not be feasible on a desktop PC or notebook computer in a couple of seconds or minutes anymore. The method presented to infer the RI of the fluid surrounding the particles might be useful as an alternative to standard refractometry in some applications, e. g., to determine the wavelength-dependent optical properties of protein solutions or blood plasma.

Appendix

4.A Effect of absorbing host medium

In this chapter we have made extensive use of the analytical solution for the scattering of a plane electromagnetic wave from a single dielectric sphere of radius R embedded in an (infinite) dielectric matrix of refractive index $\mathbf{n}_m = n_m + i\kappa_m$. Classical textbooks on light scattering [60, 61] treat only the case of a non-absorbing medium surrounding the particles, i. e., $\mathbf{n}_m \in \mathbb{R}$ or $k_m = 2\pi \mathbf{n}_m/\lambda \in \mathbb{R}$ while the particle RI \mathbf{n} may be complex. This is the Mie solution used in the inverse problem analysis of the extinction spectra. However, the assumption of a non-absorbing fluid suspending the particles is only fulfilled to a certain degree. The imaginary RI of the sphering reagent used for RBCs was measured to peak at $\kappa_m = 10^{-5}$ in the near UV, see Fig. 4.A.1. However this wavelength range $\lambda < 290$ nm was excluded from the analysis due to high measurement noise. But even the imaginary RI of water amounts to a few 10^{-6} in the IR for $\lambda > 900$ nm. Hence the question arises, in how far the presence of a nonzero imaginary part \mathbf{n}_m affects the measurement and analysis of particle extinction cross sections discussed here. Firstly and most significantly, $\kappa_m > 0$ means that the incident beam is attenuated while passing through the cuvette, even in the absence of any scatterers. For example, for the sphering reagent with $\kappa_m(284\text{ nm}) \approx 10^{-5}$ this means that only about $\exp[-4\pi\kappa_m d/\lambda] \approx 1.2\%$ of the light is transmitted at $\lambda = 284$ nm through the $d = 10$ mm cuvettes used compared to a cuvette filled with water ($\kappa_m < 10^{-8}$). This decreases the measurable signal by the same factor, and makes the measurement prone to errors. But besides increased measurement noise this effect does not cause any problems and is corrected for in the analysis, since all spectra of particle suspensions are normalized to the spectrum of the matrix used. Furthermore, the signal-to-noise ratio could be reduced by using a thinner cuvette, e. g., $d = 1$ mm, which would still transmit 64% but prohibit the use of a magnetic stir bar for mixing the samples or by increasing the integration time of the spectrometer, which would saturate the detector at other wavelengths and thus complicate the measurements. In any case, even though these experimental issues need to be dealt with, there is no fundamental reason not to be able to measure extinction spectra of particles suspended in an absorbing matrix.

Hence the actual question is whether the extinction cross section of the particles itself changes due to the nonzero imaginary part of the matrix RI \mathbf{n}_m and whether the use of the Mie scattering formulae for non-absorbing surrounding media is appropriate. There is no debate about the fact that the Mie solution to the scattering of a plane wave by a sphere can be generalized to an absorbing host medium with formally identical expressions for the electromagnetic field. Also for a complex RI of the matrix $\mathbf{n}_m \in \mathbb{C}$, the expansion coefficients a_ν, b_ν of the scattered field are still given by Eq. (4.12) (page 46) and the amplitude scattering matrix in the forward

direction reads

$$S(0) = \frac{1}{2} \sum_{\nu=1}^{\infty} (2\nu + 1)(a_{\nu} + b_{\nu}). \quad (4.74)$$

The only difference for these expressions is that the wavevector $k_m = k'_m + ik''_m = 2\pi \mathbf{n}_m/\lambda$ and consequently the size parameter $X = k_m R$ now has a nonzero imaginary part and that the relative RI $\mathbf{m} = \mathbf{n}/\mathbf{n}_m$ has to be computed with the complex matrix RI.

In the case of a non-absorbing matrix ($k_m \in \mathbb{R}$) the optical theorem in the form

$$C_{\text{ext}}^{\text{nonabs}} = \frac{4\pi}{k_m^2} \Re[S(0)] \quad \text{for } k_m \in \mathbb{R} \quad (4.75)$$

is used to compute the particle's extinction cross section. Over the last decades, there has been some disagreement between researchers on how to generalize the observables “extinction cross section”, and – if possible – “scattering cross section” and “absorption cross section”. These should be properties of the particle alone, computed from the scattered far field, and not of the measurement setup, e.g., the exact distance to the detector or the exact finite (but large) extent of the absorbing matrix. However, this led to somewhat controversial results, partly because considerations of the energy flux through the surface of some arbitrary imaginary sphere around the scatterer

are not as easily interpreted since the energy is not conserved in the absorbing medium. Some expressions were proposed for the *extinction* (not *extinction cross section*), that still depend on the geometry of the measurement setup by Mundy, Roux and Smith [106] and by Chýlek [107]. It is rather unclear how to apply their equations to the measurement setup at hand. A very convincing concept for the generalization of C_{ext} based on what is measured in an extinction experiment was given by Bohren and Gilra in 1979 [108] and similarly by Videen and Sun in 2003 [109]. Their generalization of the optical theorem reads

$$C_{\text{ext}} = 4\pi \Re \left[\frac{S(0)}{k_m^2} \right] \quad \text{for } k_m \in \mathbb{C} \quad (4.76)$$

as opposed to Eq. (4.75).

However, only as late as 2007, it was pointed out by Mishchenko [110] that the derivation of Bohren and Gilra [108], and similarly that of Videen and Sun [109] contained an invalid mathematical step due to k_m being complex. Hence, according to Mischenko, the correct formula for a spherically symmetric particle should be

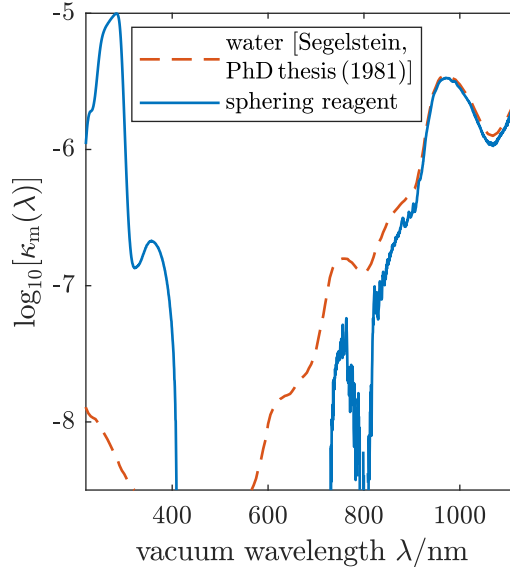


Figure 4.A.1: Measured imaginary RI of the Abbott sphering reagent for RBCs compared with literature values for water [40]. The measurement is not necessarily very accurate below 10^{-6} , because the cuvette had to be refilled (i. e., was moved) between sample and reference measurement.

(notation adapted to that of Bohren, Huffman and Gilra [61, 108])

$$C_{\text{ext}} = \frac{4\pi}{k'_m} \Re \left[\frac{S(0)}{k_m} \right] \quad \text{for } k_m \in \mathbb{C}. \quad (4.77)$$

To the author, this seems to be the correct expression to use for the optical theorem for a particle in an absorbing surrounding medium.

To quantify the sensitivity of this modified expression for the extinction cross section to the imaginary RI of the host medium, Mie computations were performed with both $\mathbf{n}_m \in \mathbb{R}$ and $\mathbf{n}_m \in \mathbb{C}$ comparing Eqs. (4.75) and (4.77) between 220 nm and 1100 nm. For the sake of completeness, the values computed according to (the most likely incorrect) Eq. (4.76) were compared as well. However it was found that values obtained for C_{ext} with Eq. 4.76 and Eq. 4.77 differ from each other at least one order of magnitude less than they do from Eq. 4.75 with the parameter values relevant here. Monodisperse 2.5 μm PS spheres and 86 fL (5.47 μm) sphered RBCs with 330 g L^{-1} Hb served as test cases. The real part of the matrix RI was that of water, the imaginary part was set to a wavelength-independent value which was varied between 10^{-6} and 10^{-2} . The results are summarized in Tab. 4.A.1, where the highest deviation $\Delta C_{\text{max}} := C_{\text{ext}}(\lambda_{\text{max}}) - C_{\text{ext}}^{\text{nonabs}}(\lambda_{\text{max}})$ between the extinction cross section including absorption [Eq. (4.77)] and without absorption [Eq. (4.75)] is listed. λ_{max} is the wavelength of the largest deviation. For the RBC test case this was $\lambda_{\text{max}} = 734 \text{ nm}$, except for κ_m where $\lambda_{\text{max}} = 300 \text{ nm}$. For the PS test case the largest deviation occurred around $\lambda_{\text{max}} \approx 278 \text{ nm}$ for all tested κ_m . Also shown is the relative deviation $\Delta C_{\text{rel}} = \Delta C_{\text{max}} / C_{\text{ext}}^{\text{nonabs}}(\lambda_{\text{max}})$. To put these values in perspective, the relative measurement uncertainty of $\overline{C}_{\text{ext}}(\lambda_{\text{max}})$ is at least 1.1×10^{-3} for RBCs and 3.2×10^{-3} for PS beads. This means that for a host medium with an absorption coefficient of $\kappa_m \geq 10^{-4}$ the effect would be comparable to or higher than the detector noise and should be included into the forward model. The imaginary RIs in the measurements analyzed in this chapter, however, are at least one order of magnitude below that. Hence, the classical Mie scattering formulae can safely be used.

Table 4.A.1: Relative and absolute deviation of the extinction cross section C_{ext} of particles in an absorbing host medium with imaginary RI κ_m from $C_{\text{ext}}^{\text{nonabs}}$ in a non-absorbing host medium.

	RBC		PS	
κ_m	$\Delta C_{\text{max}} / \mu\text{m}^2$	ΔC_{rel}	$\Delta C_{\text{max}} / \mu\text{m}^2$	ΔC_{rel}
10^{-6}	1.1×10^{-3}	1.4×10^{-5}	-1.2×10^{-4}	-1.2×10^{-5}
10^{-5}	1.1×10^{-2}	1.4×10^{-4}	-1.2×10^{-3}	-1.2×10^{-4}
10^{-4}	1.1×10^{-1}	1.4×10^{-3}	-1.2×10^{-2}	-1.2×10^{-3}
10^{-3}	1.2	1.5×10^{-2}	-1.2×10^{-1}	-1.1×10^{-2}
10^{-2}	1.6×10^1	2.8×10^{-1}	-1.1	-1.2×10^{-1}

4.B Details of nonlinear least-squares optimization

In this section, some more background is presented on the algorithm used to solve the least-squares problem introduced on page 66 and some details of the numerical

implementation of the forward model are given.

4.B.1 Brief overview of least-squares algorithms

Local optimization algorithms work iteratively and the most common algorithms employed for least-squares problems are based on an a low-order Taylor expansion of the objective function $\chi^2(\boldsymbol{\psi}) = \mathbf{F}^T \mathbf{W} \mathbf{F}$, or rather, its gradient $\nabla_{\boldsymbol{\psi}} \chi^2(\boldsymbol{\psi})$. This Taylor approximation involves the Hessian (i. e., the matrix of second partial derivatives)

$$H_{ij} := \frac{\partial^2 \chi^2}{\partial \psi_i \partial \psi_j} = 2 \left[\left(\mathbf{J}^T \mathbf{W} \mathbf{J} \right)_{ij} + \mathbf{F}^T \mathbf{W} \frac{\partial^2 \mathbf{F}}{\partial \psi_i \partial \psi_j} \right]. \quad (4.78)$$

The necessary condition for a minimizer of χ^2 is

$$0 \stackrel{!}{=} \nabla_{\boldsymbol{\psi}} \chi^2(\boldsymbol{\psi}) = 2 \mathbf{J}^T \mathbf{W} \mathbf{F}. \quad (4.79)$$

If this equation is expanded around a point $\boldsymbol{\psi}^k$ to linear order in $\Delta \boldsymbol{\psi}^k := \boldsymbol{\psi} - \boldsymbol{\psi}^k$, one obtains a linear system of equations

$$\nabla_{\boldsymbol{\psi}} \chi^2(\boldsymbol{\psi}) \approx 2 \mathbf{J}^{kT} \mathbf{W} \mathbf{F}^k + \mathbf{H}^k \Delta \boldsymbol{\psi}^k \stackrel{!}{=} 0 \quad (4.80)$$

that can be solved for $\Delta \boldsymbol{\psi}^k$ to iteratively optimize the parameters. Here \mathbf{F}^k , \mathbf{J}^k and \mathbf{H}^k , denote the residuals, Jacobian of the forward model and Hessian of χ^2 evaluated at $\boldsymbol{\psi}^k$, respectively. If one uses the full above equation for iteration, i. e., at step $k \in \mathbb{N}$ solves

$$\mathbf{H}^k \Delta \boldsymbol{\psi}^k = -2 \mathbf{J}^{kT} \mathbf{W} \mathbf{F}^k \quad (4.81)$$

for $\Delta \boldsymbol{\psi}^k$ and then updates $\boldsymbol{\psi}^{k+1} = \boldsymbol{\psi}^k + \Delta \boldsymbol{\psi}^k$, one has *Newton's method* or the *Newton-Raphson method* for finding the roots of Eq. (4.79). This method is a general root finding algorithm, not restricted to least-squares problems. If we make use of the fact that the objective function χ^2 is the sum of the squared residuals and neglect the term in the Hessian containing $\frac{\partial^2 \mathbf{F}}{\partial \psi_i \partial \psi_j}$, we can write Eq. (4.79) as

$$\mathbf{J}^{kT} \mathbf{W} \mathbf{J}^k \Delta \boldsymbol{\psi}^k = -\mathbf{J}^{kT} \mathbf{W} \mathbf{F}^k. \quad (4.82)$$

This system of linear equations is known as *normal equations* and, when solved for $\Delta \boldsymbol{\psi}^k$ forms the iterations of the *Gauß-Newton algorithm*. Compared to Newton's method, the advantage in numerical cost is that the second derivatives of the forward model $\frac{\partial^2 \mathbf{F}}{\partial \psi_i \partial \psi_j}$ do not need to be computed, which would generally have higher complexity than the first derivatives: If no analytical expression is available to compute $\frac{\partial \mathbf{F}}{\partial \psi_j}$, one can always approximately compute it from evaluations of $\mathbf{F}(\boldsymbol{\psi})$ at $\boldsymbol{\psi} \pm \Delta \boldsymbol{\psi} \mathbf{e}_j$ for $j = 1, \dots, L$. In total, this takes $\mathcal{O}(L)$ evaluations of the full forward model for the first derivatives. For the second derivatives $\frac{\partial^2 \mathbf{F}}{\partial \psi_i \partial \psi_j}$ the complexity is $\mathcal{O}(L^2)$. Hence, the Gauß-Newton algorithm is computationally cheaper. On the other hand, this algorithm may perform poorly if these second derivatives become important. To tackle this problem, the *Marquardt algorithm* and *Levenberg-Marquardt algorithm* were developed. For the Marquardt algorithm, one solves

$$\left[\mathbf{J}^{kT} \mathbf{W} \mathbf{J}^k + \Lambda_k \text{diag}(\mathbf{J}^{kT} \mathbf{W} \mathbf{J}^k) \right] \Delta \boldsymbol{\psi}^k = -\mathbf{J}^{kT} \mathbf{W} \mathbf{F}^k, \quad (4.83)$$

where $\text{diag}(\mathbf{A})$ denotes the diagonal matrix with the same diagonal elements as \mathbf{A} . Similarly, for the Levenberg-Marquardt algorithm, one solves

$$\left[\mathbf{J}^{kT} \mathbf{W} \mathbf{J}^k + \Lambda_k \mathbf{1}_L \right] \Delta \boldsymbol{\psi}^k = -\mathbf{J}^{kT} \mathbf{W} \mathbf{F}^k, \quad (4.84)$$

where $\mathbf{1}_L$ is the unit (or identity) matrix of size $L \times L$. The damping parameter Λ_k can be used to change from a pure Gauß-Newton behavior ($\Lambda_k = 0$) to a pure steepest-descent behavior ($\Lambda_k \rightarrow \infty$; the step size tends to 0). In these algorithms, at iteration k an update by the proposed step $\Delta \boldsymbol{\psi}^k$ is only carried out if it results in a lower objective function, i. e., if $\chi^2(\boldsymbol{\psi}^k + \Delta \boldsymbol{\psi}^k) < \chi^2(\boldsymbol{\psi}^k)$. If so, the damping Λ_k is decreased for the next iteration, otherwise it is increased.

All the above algorithms solve unconstrained subproblems for their iterations. Depending on the distance to the minimum, i. e., depending on the initial conditions, this may lead to non-convergence because the proposed step leaves the range of validity of the underlying Taylor approximation. At least for the problem at hand, i. e., the fitting of optical extinction cross sections, it was found that a *trust-region method* converged from a wider range of initial parameter values than the Marquardt or Levenberg-Marquardt algorithms as they are implemented in Matlab (Matlab R2018a, The MathWorks Inc.). The trust region is a neighborhood around the current parameter vector $\boldsymbol{\psi}^k$ inside which the Taylor approximation for the objective function, such as Eq. (4.80) is reasonable. Instead of solving Eq. (4.80), the trust-region subproblem for a least-squares problem is stated as

$$\min \left\{ \mathbf{J}^{kT} \mathbf{W} \mathbf{F}^k + \frac{1}{2} \mathbf{H}^k \Delta \boldsymbol{\psi}^k \quad \text{such that} \quad \|\mathbf{D} \Delta \boldsymbol{\psi}^k\| \leq \delta^k \right\}, \quad (4.85)$$

where \mathbf{D} is a diagonal scaling matrix and δ^k is a positive scalar, defining an ellipsoidal trust region. In analogy to the Gauß-Newton step, the second derivatives $\frac{\partial^2 \mathbf{F}}{\partial \psi_i \partial \psi_j}$ are usually dropped from the Hessian \mathbf{H} . Like in the Levenberg-Marquardt algorithm, a trial step is accepted if it reduces χ^2 , in which case the size of the trust-region δ^k is increased. Details of the algorithm used can be found in the Matlab documentation [111, 112].

4.B.2 Expressions for the numerical implementation of the model

As discussed in the previous subsection, it is advantageous if one provides not only an implementation of the model function $\mathcal{M}(\lambda; \boldsymbol{\psi})$ itself to local optimization algorithms but also (at least) the first partial derivatives with respect to the parameter vector. Due to the structure of the forward model, a more numerically efficient way to compute derivatives exists than explicit evaluations of $\mathcal{M}(\lambda; \boldsymbol{\psi})$ at various combinations of increased or decreased parameters $\boldsymbol{\psi} \pm \Delta \psi \mathbf{e}_j$, $j = 1, \dots, L$.

As a reminder, the forward model is [Eq. (4.55) on page 65]

$$\mathcal{M}(\lambda; \boldsymbol{\psi}) = (1 + \eta) \bar{\mathcal{C}}(\lambda; \mathbf{a}, \boldsymbol{\theta}).$$

For the Jacobian matrix one finds

$$J_{ij} = \frac{\partial F_i}{\partial \psi_j} = \frac{\partial \mathcal{M}(\lambda_i; \boldsymbol{\psi})}{\partial \psi_j} = \begin{cases} (1 + \eta) \frac{\partial \bar{\mathcal{C}}(\lambda_i; \mathbf{a}, \boldsymbol{\theta})}{\partial \psi_j}, & j = 1, \dots, L - 1 \\ \bar{\mathcal{C}}(\lambda_i; \mathbf{a}, \boldsymbol{\theta}), & j = L \end{cases}. \quad (4.86)$$

Similarly, the second derivatives read

$$\frac{\partial^2 F_i}{\partial \psi_j \partial \psi_l} = \begin{cases} (1 + \eta) \frac{\partial^2 \bar{\mathcal{C}}(\lambda_i; \mathbf{a}, \boldsymbol{\theta})}{\partial \psi_j \partial \psi_l}, & j, l = 1, \dots, L - 1 \\ \frac{\partial \bar{\mathcal{C}}(\lambda_i; \mathbf{a}, \boldsymbol{\theta})}{\partial \psi_j}, & j = 1, \dots, L - 1 \text{ and } l = L \\ 0, & j = l = L \end{cases} \quad (4.87)$$

For PS beads with the ensemble averages approximated by trapezoidal sums [see Eq. (4.35) on page 53] one has

$$\bar{\mathcal{C}}(\lambda_i; \mathbf{a}, \boldsymbol{\theta}) = \sum_{t=1}^{I_R} \mathcal{C}(\lambda_i; n_i(\mathbf{a}), R_t) \tilde{r}_t(\boldsymbol{\theta})$$

and hence

$$\begin{aligned} \frac{\partial \bar{\mathcal{C}}(\lambda_i; \mathbf{a}, \boldsymbol{\theta})}{\partial a_j} &= \sum_{t=1}^{I_R} \left[\frac{\partial}{\partial n_i} \mathcal{C}(\lambda_i; n_i, R_t) \right] \tilde{r}_t \frac{\partial n_i}{\partial a_j} \\ &= \sum_{t=1}^{I_R} \left[\frac{\partial}{\partial n_i} \mathcal{C}(\lambda_i; n_i, R_t) \right] \tilde{r}_t G_{ij}, \end{aligned} \quad (4.88)$$

$$\frac{\partial \bar{\mathcal{C}}(\lambda_i; \mathbf{a}, \boldsymbol{\theta})}{\partial \theta_j} = \sum_{t=1}^{I_R} \mathcal{C}(\lambda_i; n_i(\mathbf{a}), R_t) \frac{\partial}{\partial \theta_j} \tilde{r}_t(\boldsymbol{\theta}). \quad (4.89)$$

Similarly, for RBCs, where [see Eq. (4.36) on page 53]

$$\bar{\mathcal{C}}(\lambda_i; \mathbf{a}, \boldsymbol{\theta}) = \sum_{s=1}^{I_c} \sum_{t=1}^{I_R} \mathcal{C}(\lambda_i; \mathbf{n}_i(c_s; \mathbf{a}), R_t) \tilde{q}_s(\boldsymbol{\theta}) \tilde{r}_t(\boldsymbol{\theta})$$

$$\text{with } \mathbf{n}_i(c_{\text{Hb}}; \mathbf{a}) = n_{\text{H}_2\text{O}}(\lambda_i) + c_{\text{Hb}} \left[\sum_{j=1}^M G_{ij} a_j + i\gamma(\lambda_i) \right]$$

and hence

$$\frac{\partial \bar{\mathcal{C}}(\lambda_i; \mathbf{a}, \boldsymbol{\theta})}{\partial a_j} = \sum_{s=1}^{I_c} \sum_{t=1}^{I_R} \left[\frac{\partial}{\partial \mathbf{n}_i} \mathcal{C}(\lambda_i; \mathbf{n}_i, R_t) \right] \tilde{q}_s \tilde{r}_t c_s G_{ij}, \quad (4.90)$$

$$\frac{\partial \bar{\mathcal{C}}(\lambda_i; \mathbf{a}, \boldsymbol{\theta})}{\partial \theta_j} = \sum_{s=1}^{I_c} \sum_{t=1}^{I_R} \mathcal{C}(\lambda_i; \mathbf{n}_i(c_s; \mathbf{a}), R_t) \frac{\partial}{\partial \theta_j} [\tilde{q}_s(\boldsymbol{\theta}) \tilde{r}_t(\boldsymbol{\theta})]. \quad (4.91)$$

As one can see from the above equations, computing the elements of the Jacobian \mathbf{J} requires only the derivatives of the Mie cross section \mathcal{C} with respect to the RI \mathbf{n} and the derivatives of the size (and concentration) distributions with respect to its corresponding parameters $\boldsymbol{\theta}$. The latter are straightforward if the numerical normalization factor of the pdfs is treated correctly. Since evaluating the Mie extinction cross sections is the computationally most expensive contribution in this problem we focus on its derivatives. A partial derivative like $\frac{\partial}{\partial n_i} \mathcal{C}(\lambda_i; \mathbf{n}_i, R)$ can be computed numerically by finite differences, i. e., by the evaluation of $\mathcal{C}(\lambda_i; \mathbf{n}_i, R)$ not only at \mathbf{n}_i but also at $\mathbf{n}_i \pm \delta n$. This requires $2 - 3 \times$ the evaluations of the Mie cross section as compared to computing only $\mathcal{C}(\lambda_i; \mathbf{n}_i, R)$. I. e., computing the Jacobian has the same computational complexity (scaling behavior with N and L) as evaluating the forward model. Either the plus or minus sign in $\mathbf{n}_i \pm \delta n$ are sufficient to compute the first derivative. If both are evaluated, one can even compute the second partial

derivative $\frac{\partial^2}{\partial \mathbf{n}_i} \mathcal{C}(\lambda_i; \mathbf{n}_i, R)$, which occurs in $\frac{\partial^2 \mathbf{F}}{\partial \psi_i \partial \psi_j}$. Hence, we see that one can compute the matrix of second partial derivatives of \mathcal{M} with respect to the parameters $\boldsymbol{\psi}$ with the same complexity as the first derivatives. This actually makes it unnecessary to drop the $\frac{\partial^2 \mathbf{F}}{\partial \psi_i \partial \psi_j}$ -term in the Hessian of χ^2 . Thus, instead of Gauß-Newton-like steps in the trust-region algorithm one might just as well use steps according to the Newton algorithm – a fact that could be useful if the numerical methods used for the solution of the problem is to be improved. However, the available algorithms (not involving second derivatives) worked satisfactory for research purposes. Hence, this was not looked into any further. In any case, the above equations (4.86) through (4.91) were used to explicitly provide the Jacobian \mathbf{J} in the numerical optimization.

4.C Uncertainty analysis

The uncertainty estimated according the covariance matrices $\boldsymbol{\Sigma}^{\text{noise}}(\hat{\boldsymbol{\psi}})$ and $\boldsymbol{\Sigma}^{\text{noise}}(\hat{\boldsymbol{\alpha}})$ [Eq. (4.64) and Eq. (4.65) on page 67] accounts only for the effects of noise in the measured spectra (quantified from repeated measurements of the same sample) and, in the case of RBCs, the uncertainty of the hematological parameters from the CBC used for regularization. It does not account for other sources of error such as model errors, systematic errors in the measures spectra. To combine the results for the real RI increment of the $P = 3$ measurements for RBCs from volunteers A, B and C, we take the weighted average of the optimization results $\hat{\boldsymbol{\alpha}}^{(A)}, \hat{\boldsymbol{\alpha}}^{(B)}, \hat{\boldsymbol{\alpha}}^{(C)}$ where the weight matrices are given by $\boldsymbol{\Omega}^{(i)} = \boldsymbol{\Sigma}^{\text{noise}}(\hat{\boldsymbol{\alpha}}^{(i)})^{-1}$ for $i = A, B, C$.

$$\langle \hat{\boldsymbol{\alpha}} \rangle = \mathbf{V}_1^{-1} \sum_{i=A, B, C} \boldsymbol{\Omega}^{(i)} \hat{\boldsymbol{\alpha}}^{(i)} \quad \text{with} \quad \mathbf{V}_1 := \sum_{i=A, B, C} \boldsymbol{\Omega}^{(i)}. \quad (4.92)$$

The average of the vector of real RI increments at N wavelengths is computed as $\langle \hat{\boldsymbol{\alpha}} \rangle = \mathbf{G} \langle \hat{\boldsymbol{\alpha}} \rangle$, where \mathbf{G} is the $N \times M$ matrix of all basis functions. This is the blue curve shown Fig. 4.23 on page 85. The covariance matrix corresponding to the uncertainty of this weighted result was estimated as

$$\boldsymbol{\Sigma}(\langle \hat{\boldsymbol{\alpha}} \rangle) = \frac{\mathbf{V}_1^{-1}}{NP - 1} \sum_{i=A, B, C} (\hat{\boldsymbol{\alpha}}^{(i)} - \langle \hat{\boldsymbol{\alpha}} \rangle)^T \boldsymbol{\Omega}^{(i)} (\hat{\boldsymbol{\alpha}}^{(i)} - \langle \hat{\boldsymbol{\alpha}} \rangle) \quad (4.93)$$

which corresponds to the weighted sample covariance, thus also accounting for other sources of error than spectral noise and CBC measurement uncertainties as far as possible with the given data. The $N \times N$ covariance matrix $\boldsymbol{\Sigma}(\langle \hat{\boldsymbol{\alpha}} \rangle)$ of the real RI increments at all N wavelengths follows accordingly, by multiplying the $M \times M$ matrix $\boldsymbol{\Sigma}(\langle \hat{\boldsymbol{\alpha}} \rangle)$ from left and right with \mathbf{G} and its transpose, respectively (see Eq. (4.67) on page 68). This empirical estimate, which accounts at least for some of the influences not covered by the measurement noise model, could also be employed to PS beads, provided a sufficient number of different datasets (e. g., different particle sizes) had been measured.

To assess the influence of the RI of the sphering reagent and its uncertainty, an additional inverse problem analysis was performed assuming for the suspending fluid $n_m(\lambda) = n_{\text{H}_2\text{O}}(\lambda)$ instead of $n_m(\lambda) = n_{\text{H}_2\text{O}}(\lambda) + \delta n_m$ as done before with $\delta n_m = 0.002$. The resulting $\alpha(\lambda)$ is lower by $6 \times 10^{-3} \text{ mL g}^{-1}$ without any significant wavelength-dependence. Hence the sensitivity of the optimization result to the numerical value of the RI of $n_m(\lambda)$ is

$$\frac{\partial \alpha}{\partial n_m} \approx \frac{6 \times 10^{-3} \text{ mL g}^{-1}}{2 \times 10^{-3}} = 3 \text{ mL g}^{-1}. \quad (4.94)$$

To account for the uncertainty of the RI of the sphering reagent of $u[n_m(\lambda)] = 3 \times 10^{-4}$, stemming from the measurement of δn_m with an Abbe refractometer,³ an additional uncertainty term

$$u_{n_m}[\alpha(\lambda)] = \frac{\partial \alpha}{\partial n} u[n_m(\lambda)] = 9 \times 10^{-4} \text{ mL g}^{-1} \quad (4.95)$$

is included. The total estimated standard uncertainty of the result for the real RI increment of RBCs is thus

$$u[\alpha(\lambda_i)] = \sqrt{u_{n_m}[\alpha(\lambda_i)]^2 + \Sigma(\langle \hat{\alpha} \rangle)_{ii}}. \quad (4.96)$$

This is the half-width of the blue band shown in Fig. 4.23 on page 85.

³ The expected value and uncertainty of $\delta n_m = 0.0020(3)$ measured with the Abbe refractometer at $\lambda = 590 \text{ nm}$ also covers the range in which a wavelength dependence of $\delta n_m(\lambda)$ for $\lambda \in [290, 1100] \text{ nm}$ appears possible from the analysis of extinction spectra of PS beads suspended in the sphering reagent and D-glucose solutions if one takes into account the found $\Delta n_m(\lambda)$ (deviations of the determined RI from the reference values) for glucose solutions with RI similar to the sphering reagent.

Chapter 5

Extinction spectra of artificial hemoglobin microparticles*

5.1 Introduction

This chapter deals with the modeling and analysis of extinction spectra of suspensions of hemoglobin microparticles (HbMP) that might serve as a replacement for erythrocyte concentrates in transfusion medicine, i. e., be used as an oxygen-carrying “blood substitute”. For the approval of clinical studies and also for quality control of the production process, characterization of the composition of different Hb variants in these artificial particles is required. Most importantly, this includes the assessment of their content of oxygenated and deoxygenated hemoglobin (oxyHb and deoxyHb) as well as the non-functional methemoglobin (metHb) variant.

The HbMP discussed here are fabricated by the co-precipitation–cross-linking–dissolution technique [51–53, 113]. In this method a biopolymer is co-precipitated from solution in a template of inorganic salts. For the HbMP, one starts with bovine Hb in an aqueous solution of manganese chloride (MnCl_2) to which a solution of sodium carbonate (Na_2CO_3) is added. This forms insoluble manganese carbonate (MnCO_3) which precipitates (falls out of solution) forming clusters that entrap Hb molecules, hence “co-precipitation”. The result are aggregates of Hb molecules,

*As in chapter 4, the experimental data discussed and analyzed in this chapter were measured by Kathrin Smuda (Charité/PTB Berlin) with an optical measurement device designed and implemented by Jörg Neukammer and Ralph Müller (PTB Berlin).

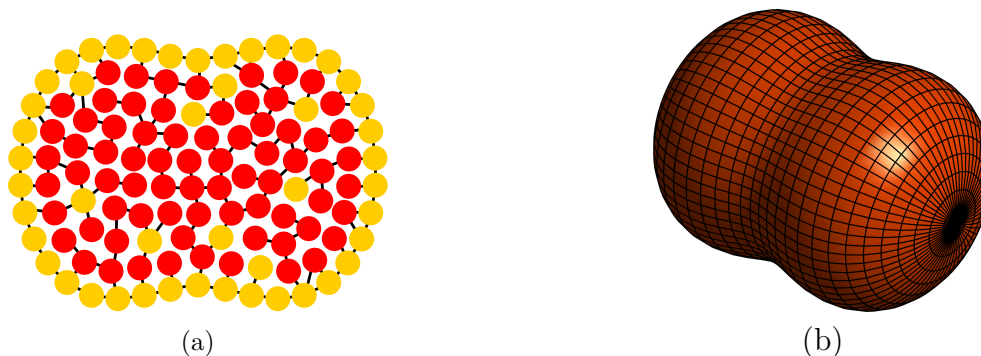


Figure 5.1: (a) Schematic of a HbMP made from cross-linked bovine Hb (red) and HSA (yellow) molecules. (b) Idealized “peanut shape” of a HbMP.

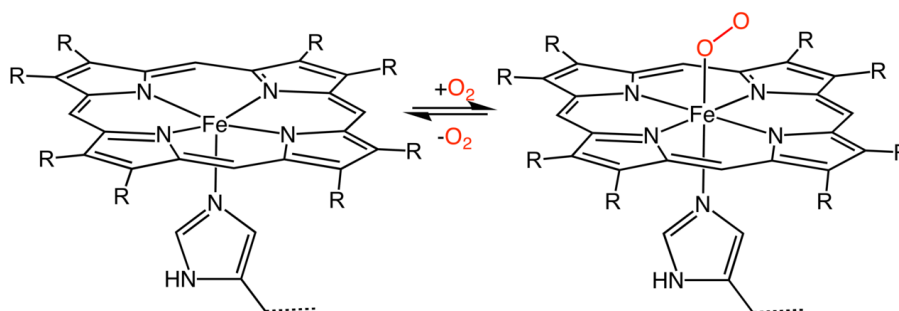


Figure 5.2: Reversible binding of oxygen (O_2) to a prosthetic heme group of a Hb subunit (protein chain not shown). On the left the iron ion is in the Fe^{2+} state, on the right in the Fe^{3+} state.

<https://commons.wikimedia.org/wiki/File:Mboxygenation.png>

By Smokefoot [CC BY-SA 4.0 (<https://creativecommons.org/licenses/by-sa/4.0>)], from Wikimedia Commons (no modifications made).

which are then covered with human serum albumin (HSA), serving to prevent the agglomeration of the HbMP. For the particles considered here, some HSA is also added to the initial bovine Hb solution, such that HSA is also found inside the particles. The Hb and HSA molecules are then cross-linked with glutaraldehyde ($\text{OCH}(\text{CH}_2)_3\text{CHO}$), i. e., covalent bonds are formed between the different protein chains and within the chains of individual proteins. Eventually the inorganic salt template is dissolved with EDTA, which results in the HbMP that are about 700 nm in size, i. e., much smaller than a RBC. The structure of the HbMP is illustrated in Fig. 5.1 (a). Their size distribution is relatively narrow, but wider than that of RBCs, and they have a nearly uniform morphology described as “peanut-shaped”, i. e., somewhat elongated aspherical particles with a slight contraction in the middle, see Fig. 5.1 (b). In contrast to RBCs, which have a liquid interior, held together by an elastic membrane, the HbMP are “sponge-like” elastic particles that are permeable for liquids. One consequence of this structure is that their volume is not well-defined but depends on the applied force. This makes it difficult to measure their volume fraction in suspension (hematocrit) by centrifugation.

As mentioned before, hemoglobin is a metalloprotein, which – in humans and most other vertebrates – is made up of four subunits [76]. Each subunit consists of a protein chain and a non-protein prosthetic heme group. Each heme group consists of an iron (Fe) ion held in a porphyrin ring, see Fig. 5.2. As a part of hemoglobin’s biological function as an oxygen carrier, oxygen molecules (O_2) can reversibly bind to the iron ions in the heme groups. If no oxygen is bound to a functional heme group, the iron ion is in the ferrous state (Fe^{2+}). When oxygen binds to this heme group, the iron ion is temporarily oxidized to the Fe^{3+} state and the oxygen molecule is temporarily reduced to the superoxide ion O_2^- [114]. If, without oxygen bound, the iron ion is in the ferric state (Fe^{3+}), the heme group cannot form a reversible complex with O_2 and one has *ferrihemoglobin* or *methemoglobin*. Hence metHb cannot transport oxygen [115]. Normally, within RBCs, Hb is oxidized to metHb at a certain rate, but is converted back by enzymes, thus metHb levels stay below 3% [115]. Obviously, it would be favorable for the artificial HbMP to exhibit similarly low metHb levels in order to function optimally as oxygen carriers.

As already discussed in previous chapters, the absorption spectra of Hb variants in the visible range are well known for humans and various other animals [39].

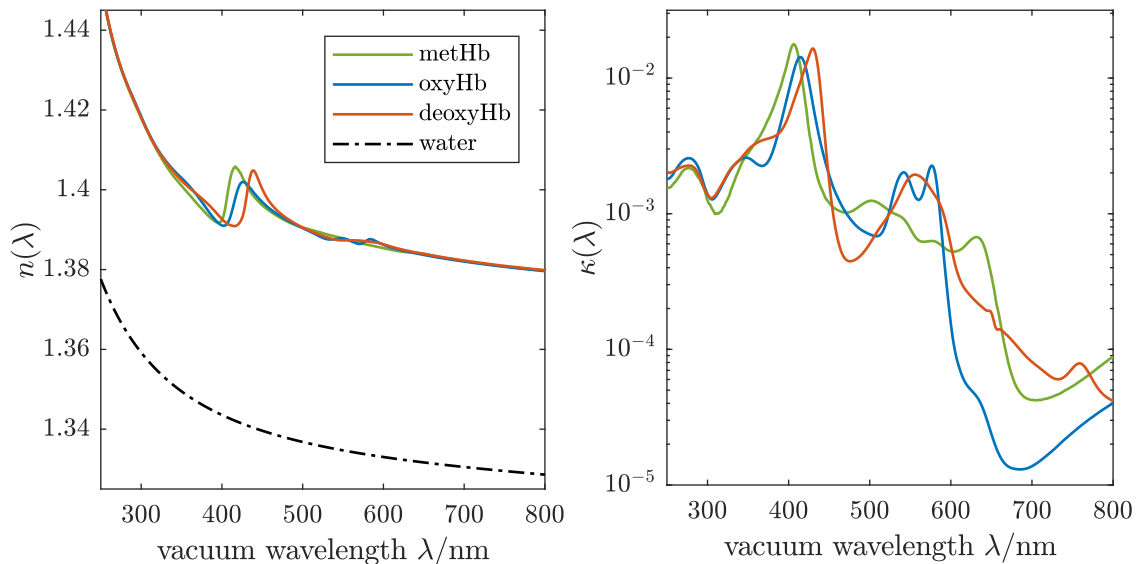


Figure 5.3: Complex RIs of human Hb solutions ($c_{\text{Hb}} = 240 \text{ g L}^{-1}$) of the pure variants assumed for the simulations of HbMP extinction spectra

These spectra can be used for differentiation of Hb variants. For example, if oxyHb is deoxygenated, the Soret band around 420 nm shifts to higher wavelengths and the double-peak around 560 nm becomes a single peak. If oxyHb is converted to metHb, the 420 nm and 560 nm peaks shift to lower wavelengths and the double-peak becomes a single peak as well. For RBCs, which can be lysed (i. e., their membrane broken open) to obtain a homogeneous Hb solution, an analysis of the absorption spectra suffices to accurately determine the levels of either Hb variant. Since the HbMP are held together by cross-linking of the proteins, not by a membrane, lysis is not possible. Hence, they have to either be further processed before analyzing them, which alters the chemical structure of the Hb or they have to be analyzed “as is” in the form of light-scattering microparticles. In this case, the analogue of absorption spectra are extinction spectra computed from the collimated transmittance as discussed before in chapter 4. The optical properties of human oxyHb, deoxyHb and metHb were determined in chapter 3 and chapter 4. These complex RI data will now be used in light scattering simulations in order to analyze extinction spectra of HbMP. The absorption spectra of human and bovine hemoglobins are known to differ very little in the visible and near IR [39] and consequently the RIs differ very little, too. Hence the error made by assuming the optical properties of human Hb even though the HbMP are made of bovine Hb is small.

5.2 Mathematical modeling of HbMP

Images of HbMP recorded with scanning electron microscopy (SEM; measured by Detlef Bergmann, PTB Braunschweig) reveal particle shapes like the idealized peanut shape in Fig. 5.1 (b), but with some additional roughness and asymmetries. A typical length and width are 700 nm and 400 nm, respectively. However, for SEM the samples need to be spread out on a surface and coated with platinum. This may cause shrinking due to drying-out of the particles and does not correspond to the situation during extinction measurements (suspension). Light microscopy with structured illumination (measured by Andreas Kummrow, PTB Berlin) of the suspended

particles reveals similar sizes of about $800 \text{ nm} \times 600 \text{ nm}$, but at a much lower spatial resolution. The light scattering by particles with shapes like in Fig. 5.1 (b) could in principle be computed using suitable numerical methods like the discrete dipole approximation (DDA). However, this can be computationally expensive, since we will need to average over particle orientations and sizes. Also, if one goes into such detail for the particle shape, one should possibly consider shape variations of the particles, too. On the other hand, the HbMP are not much larger than the vacuum wavelength of visible light. Hence, their detailed shape might not have a strong effect on the spectral extinction cross section, as we have already discussed with regard to surface roughness of RBCs in section 4.7 of chapter 4. In order to assess the effect of particle shape, we will model the HbMP as spheroids, which still matches the shapes observed with SEM relatively well. This simple model will be compared to an even more simplified model – a sphere. A spheroid is generated by rotating an ellipse around either its major or minor axis. It is defined by the semi-axis c along the axis of rotational symmetry and the semi-axis a perpendicular to that direction. For $c > a$ the spheroid is called *prolate* (i. e., it is “rugby ball-shaped”), for $c < a$ it is called *oblate* (i. e., it is “smarty-shaped”). The degenerate case of $c = a$ corresponds to a sphere. We define the *aspect ratio* as

$$h := \frac{c}{a} \quad (5.1)$$

and obviously $h > 1$ corresponds to prolate and $h < 1$ to oblate spheroids. HbMP are modeled as prolate spheroids. The volume of the spheroid is

$$V = \frac{4\pi}{3} a^2 c \quad (5.2)$$

and thus the radius of a volume-equivalent sphere is

$$R_V = \sqrt[3]{a^2 c}. \quad (5.3)$$

The spheroidal shape model can be seen as a lowest-order representation of the deviation of the shape of HbMPs from spheres in a series expansion of the particle radius as a function of solid angle $r(\vartheta, \varphi)$ in spherical harmonics. In this series expansion, the higher order terms that describe the deviation of the peanut-shape in Fig. 5.1 (b) from a sphere or spheroid are expected to have less effect than the leading term [101, 102]. Spheroids are a good means for examining the deviation from a spherical shape, since the light scattering simulations are computationally relatively cheap compared to more general irregular shapes.

As already mentioned, the HbMP feature a typical size of 700 nm. Hence we will assume an average volume equivalent radius $\mathbb{E}(R_V) = 350 \text{ nm}$ for the size distribution. The aspect ratio h is varied to estimate its influence on the spectra. Besides structured-illumination light microscopy and SEM, dynamic light scattering (DLS) measurements of the HbMP were taken (Kathrin Smuda, Charité and PTB Berlin). DLS measures the particles’ diffusion coefficient by means of Brownian motion, which can in turn be used to compute a sphere-equivalent hydrodynamic particle size. These measurements are consistent with a log-normal size distribution with a standard deviation of $\text{std}(R_V) = 20\% \mathbb{E}(R_V)$, which is thus assumed for the mathematical model. For mathematical details of the size distribution, see Eq. (4.27) in chapter 4 on page 52.

The optical properties of the HbMP are assumed to be those of RBCs and Hb solutions as determined in chapters 3 and 4. However, the particles are assumed to

be composed of a mixture of three Hb variants. I. e., the complex RI of a HbMP is given by

$$\mathbf{n}(\lambda; c_{\text{Hb}}, \boldsymbol{\phi}) = n(\lambda) + i\kappa(\lambda) = \mathbf{n}_{\text{H}_2\text{O}}(\lambda) + c_{\text{Hb}} \sum_{x=\text{oxy,deoxy,met}} \phi^x [\alpha^x(\lambda) + i\gamma^x(\lambda)], \quad (5.4)$$

where α^x and γ^x are the real and imaginary RI increments of the respective Hb variants and ϕ^x is their fraction of the total Hb (by mass), hence

$$\sum_{x=\text{oxy,deoxy,met}} \phi^x = 1. \quad (5.5)$$

As already mentioned, the error made using the complex RI of human Hb instead of bovine Hb (from which the HbMP are made) is small. But whether these optical properties of Hb solutions quantitatively agree with those of the Hb molecules in the fluid-perfused sponge-like HbMP that are chemically altered by the cross-linking process will have to be evaluated. Due to the lack of additional information, the intra-particle total Hb concentration c_{Hb} and the ratios ϕ^x are set to the same values for all particles in an ensemble. I. e., the HbMP in a sample are assumed to be optically monodisperse, like the polystyrene beads in the previous chapter. We will, however, change the ratios ϕ^x to simulate the effect of (de-)oxygenation and of samples with different metHb levels.

The question is, which value for the total intra-particle Hb concentration is realistic. The average hemoglobin concentration within the suspension (particles + liquid) can be determined by enzymatic digestion of the particles, followed by methods that are also used for RBCs. Such a measurements yields typical values of HGB $\approx 26 \text{ g L}^{-1}$ for samples with an estimated volume fraction HCT = 20%. This would correspond to an (average) intra-particle concentration of MCHC = HGB/HCT = 130 g L^{-1} , which only about 40% the Hb concentration within a typical RBC. However, the HbMP do not have a well-defined volume and the outcome of HCT measurements employing centrifugation depend on the measurement protocol (acceleration, time). This indicates that these MCHC estimates might not be very reliable. From comparison between simulations and measured extinction spectra it was found that values of $c_{\text{Hb}} = \text{MCHC} = 220 \text{ g L}^{-1} \dots 260 \text{ g L}^{-1}$ are more suitable for modeling the particles if average sizes between $2 R_V = 600 \text{ nm}$ and 900 nm are assumed. Hence the intra-particle Hb concentration of the particles was set to $c_{\text{Hb}} = 240 \text{ g L}^{-1}$ in the simulations and the corresponding RIs of the pure Hb variants are shown in Fig. 5.3.

During the optical measurements, the HbMP are in suspension with no preferred orientation. Hence, the quantity measured in an extinction experiment corresponds to the orientation and size average

$$\bar{\mathcal{C}}(\lambda; \boldsymbol{\phi}, h|r) = \int_0^{2\pi} \int_0^\pi \int_0^\infty \mathcal{C}(\lambda; \mathbf{n}(\lambda; c_{\text{Hb}}, \boldsymbol{\phi}), R_V, h, \boldsymbol{\nu}(\vartheta, \varphi)) r(R_V) dR_V \sin \vartheta d\vartheta d\varphi, \quad (5.6)$$

where $\mathcal{C}(\lambda; \mathbf{n}, R_V, h, \boldsymbol{\nu})$ is the extinction cross section of a single spheroidal particle with complex RI \mathbf{n} , equivalent radius R_V , aspect ratio h and a rotational axis defined by the unit vector $\boldsymbol{\nu}$ in the direction defined by angles ϑ, φ . $r(R_V)$ is the probability density function of the radius R_V .

It should be noted that due to the small size of the particles, no Mie resonances are recorded in the extinction spectra for $\lambda \in [250, 1100] \text{ nm}$ and – besides features

due to RI dispersion – the $\overline{C}_{\text{ext}}(\lambda)$ curves are monotonically decaying with wavelength. Thus, the effects of different parameters like mean particle volume, volume distribution width and intra-particle concentration are rather unspecific and mainly consist in increasing or decreasing the extinction cross section. Hence, their exact values chosen for the simulations should not be overly critical when comparing the positions of spectral lines as we will do in this chapter.

Numerical solver

Similar to spherical scatterers, there exists an analytical solution for the scattering of light by a spheroid [56,57] that is based on the expansion of the electromagnetic field in the eigenfunctions of the Helmholtz operator in the corresponding spheroidal coordinates. In principle, this solution could be used to compute the extinction spectra of the HbMP. However, for a numerical evaluation the infinite series of this analytical solution need to be truncated and it turns out that the convergence properties of these truncated series are unfavorable. Hence, a *T-matrix method* is used instead to solve the scattering problem. Like the analytical Mie solution, the *T-matrix method* is based on the expansion of the electromagnetic fields in vector spherical harmonics and the (infinite-dimensional) *T-matrix* is the matrix that describes the mapping from the expansion coefficients of the incident field to those of the scattered field. Unlike for a sphere, for which the *T-matrix* can be computed analytically because its boundary coincides with a coordinate isosurface, the equations for the boundary conditions have to be solved by numerical integration for a more general scatterer. Of course, the *T-matrix* has to be truncated to be finite-dimensional. The numerical solver employed here is the SMARTIES v1.01 [105] Matlab (Matlab 2018a, The MathWorks, Inc.) package, that makes use of the symmetries of the spheroidal scatterer to efficiently implement this numerical integration. Once the (approximate) *T-matrix* of a scatterer is determined, its scattered field can be computed for different incident beams by simply changing the vector of expansion coefficients to which the *T-matrix* is multiplied to yield the expansion coefficients of the scattered field. For incident beams with analytically known expansion coefficients, like the plane wave assumed here, this allows for computing orientation averages like in Eq. (5.6) with basically no additional computational cost and only the size average has to be computed by sampling and numerical integration. All results shown here correspond to an average over all possible orientations. In the case of spherical scatterers, Mie scattering computations are performed like in the previous chapter.

5.3 Results

5.3.1 Sensitivity to particle shape

We will now discuss the influence of the shape of the HbMP modeled as spheroids on the orientation-averaged spectral extinction cross section. For the sake of demonstration, monodisperse particles with a fixed size $R_V = 350$ nm are considered, made entirely of oxyHb (Fig. 5.3). In the next subsection, we will consider polydisperse particles of varying composition.

The spectral extinction cross section simulated with the SMARTIES package for prolate spheroids with an aspect ratio of $h = 1.4$ is shown in Fig. 5.4 in comparison with the result of a Mie computation for volume-equivalent spheres and of the ap-

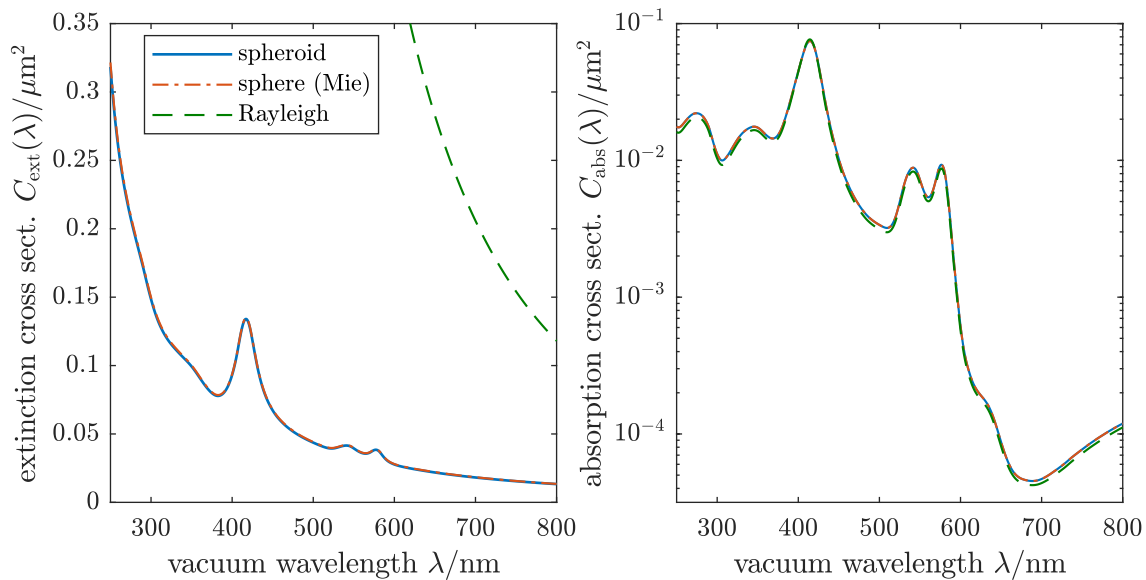


Figure 5.4: Simulated orientation-averaged extinction and absorption cross sections of prolate spheroids ($h = 1.4$) assuming oxyHb (Fig. 5.3) in comparison to Mie scattering for spheres and Rayleigh scattering for small particles.

proximations in the Rayleigh limit. The aspect ratio $h = 1.4$, i. e., semi-minor axis $a = 313$ nm and semi-major axis $c = 438$ nm corresponds to typical values observed for the HbMP by structured-illumination light microscopy and SEM. The Rayleigh limit is the limit for small (spherical) scatterers that fulfill $X \ll 1$ and $|\mathbf{m} X| \ll 1$. As in the previous chapter, $X = 2\pi n_m R_V/\lambda$ is the size parameter and $\mathbf{m} = \mathbf{n}/n_m$ is the particle RI relative to the host medium (water). In this limiting case the Mie formulae can be simplified and one finds for the scattering and absorption cross sections [61]

$$C_{\text{sca}} = \frac{8\pi R^2}{3} X^4 \Re \left\{ \left(\frac{\mathbf{m}^2 - 1}{\mathbf{m}^2 + 2} \right)^2 \right\}, \quad (5.7)$$

$$C_{\text{abs}} = 4\pi R^2 X \Im \left\{ \frac{\mathbf{m}^2 - 1}{\mathbf{m}^2 + 2} \right\}. \quad (5.8)$$

The extinction cross section follows according to $C_{\text{ext}} = C_{\text{sca}} + C_{\text{abs}}$. As evident from the left panel of Fig. 5.4, the difference between the extinction cross sections of spheres and spheroids is very small. In contrast, the extinction cross section computed in the Rayleigh approximation is completely off the correct curve. This was to be expected, since for the HbMP with a size comparable to the wavelength, i. e., with a size parameter X near unity, the assumption of small particles is not fulfilled. In view of this, it is all the more interesting to note that the spectral absorption cross section computed according to the Rayleigh limit [Eq. (5.8)] shown in the right panel of Fig. 5.4 agrees with the curves for spheres and spheroids almost perfectly. For the particles considered here, for which the imaginary part of the relative RI $\mathbf{m} = m' + im''$ is much smaller than the real part, i. e., $m'' \ll m'$, one can further approximate Eq. (5.8):

$$C_{\text{abs}} \approx 24\pi R^2 X \frac{m'm''}{(m'^2 + 2)^2}. \quad (5.9)$$

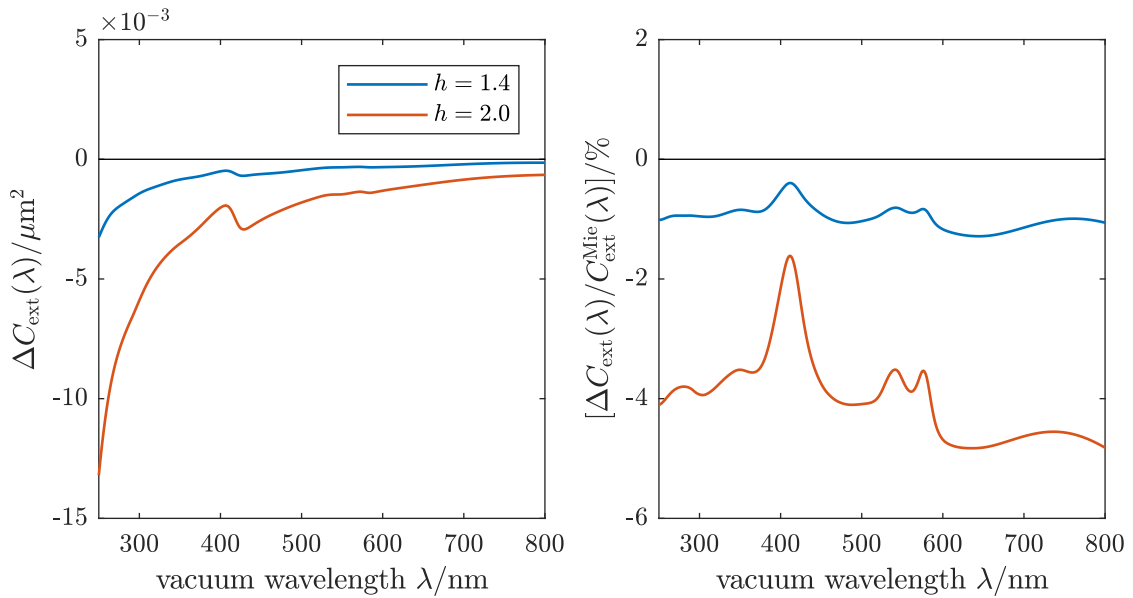


Figure 5.5: Relative and absolute deviation of the orientation-averaged extinction cross section of prolate spheroids ($h = 1.4$ and 2.0) from that of a sphere, assuming oxyHb (Fig. 5.3).

The wavelength dependence of the real relative RI $m'(\lambda)$ is much weaker than that of the imaginary relative RI $m''(\lambda)$ and of the size parameter X . Hence, the spectral absorption cross section $C_{\text{abs}}(\lambda)$ of the HbMP basically reflects the absorption spectrum $\kappa(\lambda)$ of Hb (compare oxyHb in Fig. 5.3 to Fig. 5.4), which is not generally the case, e.g., for larger particles. This resemblance of $C_{\text{abs}}(\lambda)$ and $\kappa(\lambda)$ means that if the absorption cross section $C_{\text{abs}}(\lambda)$ could be measured instead of the extinction cross section $C_{\text{ext}}(\lambda)$, or in addition to it, the analysis of the particles' chemical composition would be equally simple as analyzing an absorption spectrum of a homogeneous solution. This will be discussed in section 5.4.

The difference between the extinction cross section of HbMP modeled spheroids and of HbMP modeled as spheres

$$\Delta C_{\text{ext}}(\lambda) := C_{\text{ext}}^{\text{spheroid}}(\lambda) - C_{\text{ext}}^{\text{Mie}}(\lambda) \quad (5.10)$$

is small, but not zero. This is shown in Fig. 5.5 for spheroids of two different aspect ratios. For prolate spheroids with an aspect ratio $h = 1.4$, corresponding to a typical value for HbMP, the orientation-averaged extinction cross section is about 1% smaller than that of a volume equivalent sphere, almost independent of wavelength. An aspect ratio of $h = 2.0$ is already an extreme case that will – if at all – likely only be found for a small fraction of the HbMP. In this case there is some considerable wavelength dependence of $\Delta C_{\text{ext}}(\lambda)$, i.e., the deviation is smallest at the highest imaginary RI around 420 nm and deviations of up to 5% occur at the red end of the spectrum. The dependence of the relative deviation on the aspect ratio of the particles is resolved in more detail in the left panel of Fig. 5.6. Four different wavelengths are shown that correspond to the beginning and end of the considered spectral range and to the absorption bands of Hb at around 420 nm and 560 nm, respectively. The relative deviation of C_{ext} depends on the wavelength only weakly and C_{ext} generally decreases when h deviates from 1 in either direction. The relative deviation of the absorption cross section C_{sca} is shown in the right panel of Fig. 5.6. The deviations between spheroids and spheres are generally much smaller than for

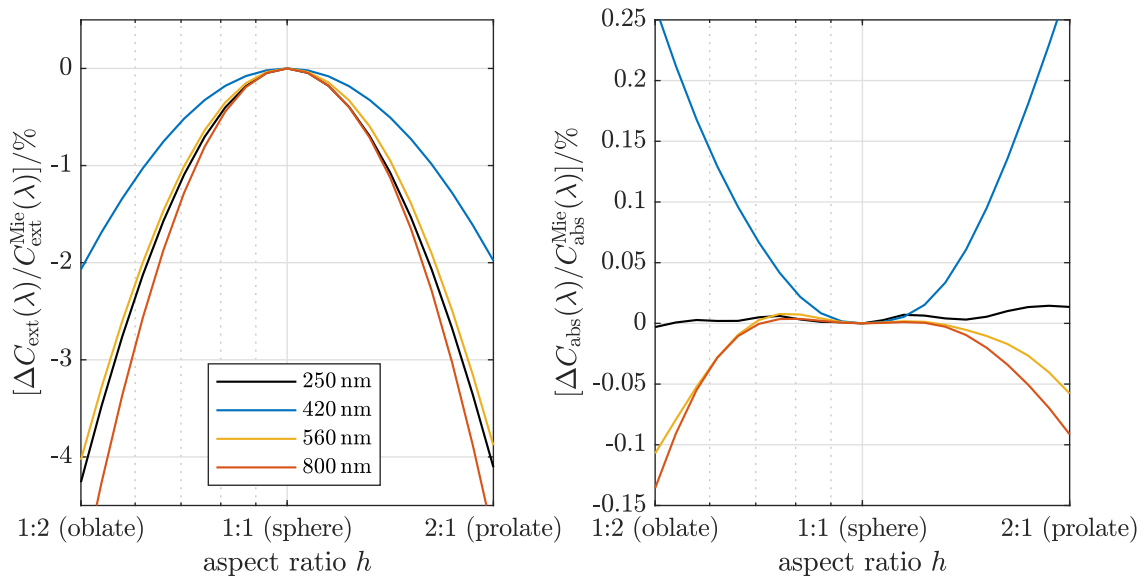


Figure 5.6: Relative deviation of the orientation averaged cross sections C_{ext} and C_{abs} of spheroids from those of a sphere at four selected wavelengths in dependence on the spheroids' aspect ratio h . Note the logarithmic scale for h .

C_{ext} , not exceeding 0.3% even for $h = 2$ prolate spheroids. While the extinction cross section C_{ext} generally decreases with deviation from the spherical shape, for $\lambda = 420$ nm the absorption cross section C_{abs} actually increases away from $h = 1$, which can be attributed to the strong absorption at this wavelength. Note that in the Rayleigh limit [Eq. (5.8)], there would be no change of C_{abs} with aspect ratio, because C_{abs} is proportional to the particle volume in this case.

The deviations of C_{ext} and C_{abs} when spherical scatterers are assumed instead of spheroids amount to at most 1% for aspect ratios $h \in [0.7, 1.4]$ and the wavelength-dependence of these deviations is even weaker than 1%. The deviations of the actual shape of the HbMP from a spheroid are higher-order terms in a perturbation series and are expected to cause even less effect on the cross sections [101, 102]. On the other hand, uncertainties of other parameters of the particles, such as their size distribution and intra-particle Hb concentration result in much higher uncertainties for the extinction cross section than 1%. For the purposes of this chapter, the error made in modeling the HbMP as spherical scatterers is negligible. Thus, Mie scattering computations are used in the following.

5.3.2 Comparison to experiments

We will now compare simulated spectral extinction cross sections of suspensions of HbMP to experimentally measured curves. The HbMP were fabricated by CC-Ery GmbH (Berlin, Germany) as briefly outlined in section 5.1 and described in detail in Ref. 52. Sample preparation and the extinction measurements were performed by Kathrin Smuda (Charité and PTB Berlin) in the same manner as described in chapter 4 for RBCs and PS beads and using the same optical setup (Fig. 4.2 on page 48). In contrast to spheroid RBCs, the HbMP were suspended in water for the measurements discussed here. Like in the previous chapter, spectra were recorded for a wavelength range of $\lambda \in [220, 1100]$ nm, but the differences between the Hb variants can mainly be seen between 350 nm and 600 nm (compare simulations in

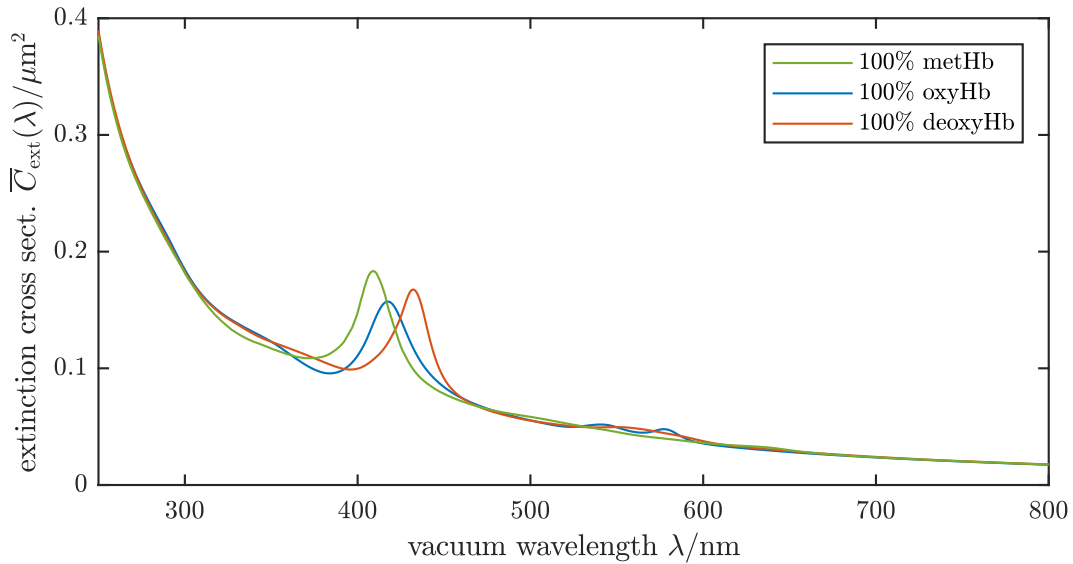


Figure 5.7: Simulated extinction spectra of HbMP modeled as spheres with $\text{mean}(2R) = 700 \text{ nm}$ and $\text{std}(R) = 20\% \text{ mean}(R)$. Particles are optically monodisperse, cross sections for the pure Hb variants (Fig. 5.3) are shown.

Fig. 5.7). Hence the discussion of the measured spectra is restricted to this range. Because of the uncertainty of the particle concentration in the suspensions, the $\overline{C}_{\text{ext}}(\lambda)$ curves of different measurements were rescaled to have minimal deviations before comparing them further, compare chapter 4, p. 53.

Throughout this subsection, HbMP are modeled as spheres with a log-normal size distribution with $\text{mean}(2R) = 700 \text{ nm}$ and $\text{std}(R) = 20\% \text{ mean}(R)$ and variable Hb composition. Simulation results for particles made from the pure Hb variants are shown in Fig. 5.7. The $\overline{C}_{\text{ext}}(\lambda)$ curves for the three cases differ from each other significantly, indicating that a differentiation of HbMP of different composition is in principle possible from their extinction spectra. Furthermore, the spectral extinction cross section $\overline{C}_{\text{ext}}(\lambda)$ exhibit similar shifts of spectral lines as the underlying complex RIs (Fig. 5.3). As expressed in Eq. (5.4), the complex RI of the particles is a weighted sum of the three curves in Fig. 5.3. In contrast, the spectral extinction cross sections of particles of arbitrary composition cannot be computed by such a linear combination of the three curves in Fig. 5.7, because of the nonlinear dependence of $\overline{C}_{\text{ext}}(\lambda)$ on the particle RI.

Fig. 5.8 shows measurements of two kinds of HbMP: (1) as fabricated and (2) treated with potassium ferricyanide ($\text{K}_3[\text{FeCN}_6]$). Potassium ferricyanide oxidizes the iron ion in the heme groups of the Hb molecules to the Fe^{3+} state and thus converts the molecules to metHb. I. e., the assumption is that the green curve in the left panel of Fig. 5.8 corresponds to particles made of 100% metHb, whereas the blue curve corresponds to particles with a lower metHb content, with the remainder of the Hb oxygenated, since the samples were in contact with air. If the untreated particles have a low metHb level below 5% (as desired) and are able to reversibly bind oxygen, the blue curve in Fig. 5.8 should correspond to (almost) 100% oxyHb. To test this, the right panel of Fig. 5.8 shows simulations where the the metHb level ϕ^{met} varied between 0% and 100% and the rest of the Hb was oxygenated, i. e., $\phi^{\text{oxy}} = 1 - \phi^{\text{met}}$ and $\phi^{\text{deoxy}} = 0$ in Eq. (5.4). First of all, we have to note that the peaks of $\overline{C}_{\text{ext}}(\lambda)$ between 400 nm and 450 nm due to the Soret band of Hb are more pronounced in the simulations than in the measurement. This may have several reasons, including the

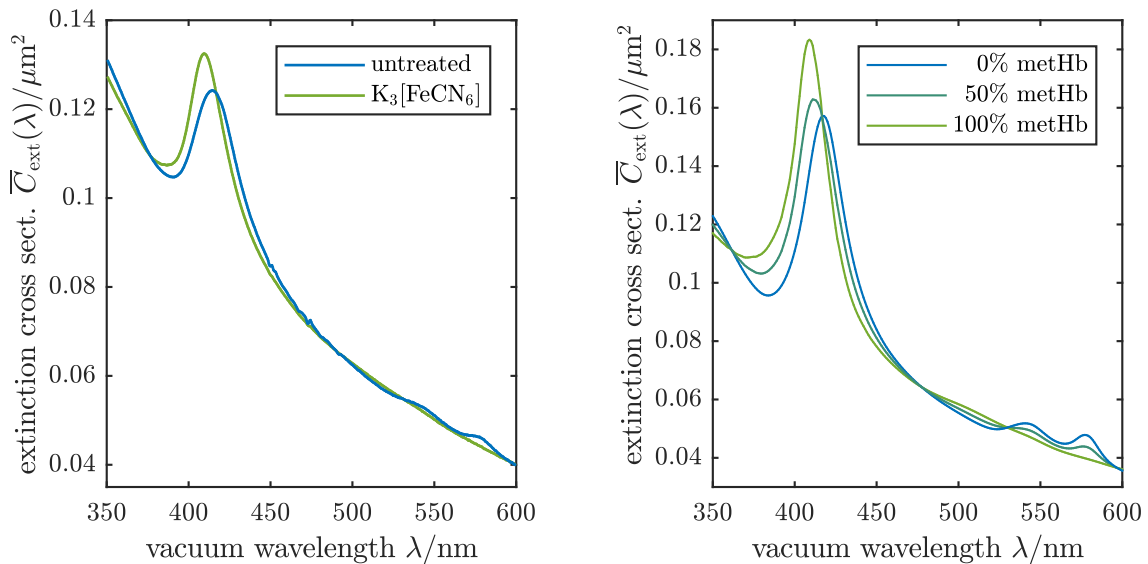


Figure 5.8: Left: Measurements of HbMP, untreated and treated with potassium ferricyanide ($\text{K}_3[\text{FeCN}_6]$) to generate metHb. Samples were in contact with air. Right: Simulation for varying metHb levels with otherwise oxyHb.

presence of particle agglomerates in the suspension, a polydispersity of the HbMP with respect to intra-particle Hb concentration or Hb composition, or the presence of albumin or other non-functional Hb variants in the particles, neither of which was taken into account in the simulations. Hence, no fully quantitative comparison, or even the solution of an inverse problem, is possible with the present model, like it was the case for spheroid RBCS and PS beads discussed in chapter 4. One can, however, compare the *positions* of spectral features relatively well, even if the peak heights are not the same. For a higher resolution, intermediate compositions were simulated, that are not shown in Fig. 5.8. The peak of the $\text{K}_3[\text{FeCN}_6]$ -treated particles is at 409.7 nm, which in the simulation corresponds to a metHb level between 80% (410 nm) and 90% (409.3 nm). Hence, given the remaining discrepancies between simulation and measurement discussed above, the assumption of particles converted completely to metHb seems to be reasonable. If, on the other hand, the peak of the untreated particles, which sits at 414.3 nm is compared to simulations, this suggests that the metHb level is between 30% (414.5 nm) and 40% (413.3 nm) rather than the desired value near 0% (417.5 nm).

Fig. 5.9 shows two measurements of the same sample of (untreated) HbMP, where in one case the sample was first in contact with air and then the suspension was bubbled with argon (Ar) for 15 min in order to wash out any oxygen. If the particles are able to reversibly bind oxygen, they should be deoxygenated by this procedure. The argon flow was turned off before the measurement, because otherwise gas bubbles in the sample would cause an additional light scattering background that complicates analysis of the spectra. We have seen before that there is a considerable metHb level in the particles. Hence, this experiment was simulated by setting $\phi^{\text{met}} = 1/3$ and then varying ϕ^{oxy} between 0 and $2/3$ with $\phi^{\text{deoxy}} = 2/3 - \phi^{\text{oxy}}$ in Eq. (5.4), which is shown in the right panel of Fig. 5.9. As can be seen the shift of the extinction cross section during deoxygenation of the sample corresponds well to the effect observed in the simulation. However the measurement for the argon-purged sample rather corresponds to the simulation for an incomplete deoxygenation, i. e., $\phi^{\text{deoxy}} \approx 1/3$. This may in part be due to the fact that the spectrum could not be recorded while

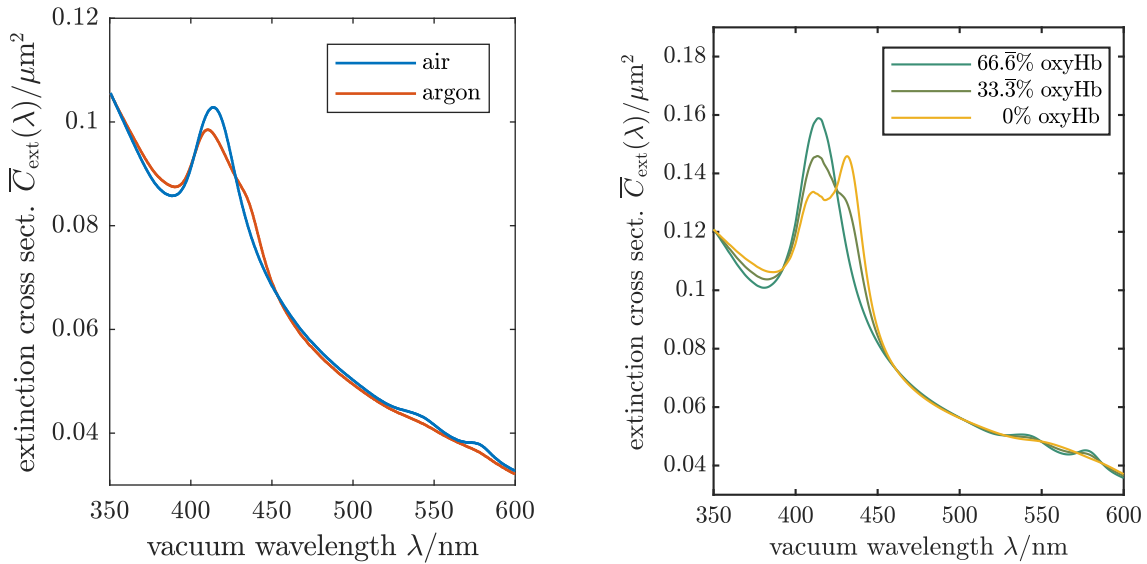


Figure 5.9: Left: Measurements of HbMP in contact with air (for oxygenation) and after bubbling with argon (for deoxygenation). Right: Simulation for varying oxygenation at 33.3% metHb level.

the argon was bubbling through the suspension, i. e., when the oxygen concentration was lowest. Thus the sample might have been partly re-oxygenated. If the same kind of simulation is repeated for metHb-free particles ($\phi^{\text{met}} = 0$, $\phi^{\text{deoxy}} = 1 - \phi^{\text{oxy}}$), which is shown in Fig. 5.10, the agreement is much poorer than with higher metHb levels of $\phi^{\text{met}} = 30\% \dots 50\%$, indicating again that there is a significant percentage of metHb in the HbMP.

5.4 Summary and outlook

In this chapter, results for the optical properties of different Hb variants that were determined in the preceding two chapters and simulations of particle extinction spectra were applied to assess the composition of artificial Hb microparticles. By comparison of spherical and spheroidal shape models for the HbMP, it was shown that the deviation of the particle shape from a sphere has only a minor effect on the measured extinction spectra. In contrast, the particle concentration and particle size (or volume) distribution have a much stronger influence. We compared measurements of extinction spectra of HbMP that were subject to different treatments with simulation results for varying Hb composition. This comparison reveals that a chemical conversion of almost all the Hb molecules in the particles to metHb is possible and results in a significant change of their optical properties. Judging from the position of the main peak around 415 nm in the extinction spectra, the metHb level in the untreated particles is between 30% and 40%. These levels may be too high for the intended use as an oxygen carrier. Regardless of the outcome of this analysis, this demonstrates that such a comparison between measurements and simulation allows to assess the particle composition and may thus give guidance for the fabrication process in order to reduce the metHb content of the particles. Comparison of simulations with a second experiment, where the HbMP were exposed to air (for oxygenation) and argon (for deoxygenation) reveals their ability to bind and release oxygen, while indicating at the same time the presence of a

relatively high level of non-functional Hb.

The measurements discussed here and the mathematical model used for simulations allow to assess the composition of HbMP with an accuracy of the levels of the Hb variants ϕ^x that seems to be about 10 percentage points. However, due to the lack of established methods to compare against, this is hard to quantify. Even if the metHb levels can be decreased by improvements of the production process, this measurement accuracy may not be sufficient for the approval of the HbMP for clinical trials [115]. In the previous chapter, an inverse problem was discussed for extinction measurements of microparticles and cells for a quantitative determination of their optical properties

and sizes. In principle, this approach can be applied to the HbMP, too, but not without some modifications. When analyzing the spectral extinction cross sections of sphered RBCs, the imaginary RI increment of the intracellular Hb was assumed to be known, since the RBCs were fully oxygenated. This assumption was tested by lysis of the cells. For the HbMP which have variable Hb composition, the imaginary RI increment is not a priori known in the general case. For the case, where the particles are (presumably) fully converted to metHb by treatment with potassium ferricyanide, one can fix the imaginary RI increment of the mathematical particle model to that of metHb and attempt to retrieve the real part of the RI increment of metHb as described for oxygenated RBCs in chapter 4. Parameters of the size distribution need to be fixed or constrained, because otherwise no unique solution is found. The reason for this is the lack of specificity of the effect of particle size, particle concentration and particle RI on the extinction spectra of small particles in the absence of Mie resonances or a ripple structure. However, the results thus obtained for the real RI increment do not agree well with the curves computed using Kramers-Kronig relations in chapter 3.

One can also slightly modify the inverse-problem solver of the previous chapter by setting the vector of relative Hb compositions ϕ as a model parameter instead of the expansion coefficients \mathbf{a} of the real RI or real RI increment. The numerical implementation of the forward model needs to be modified accordingly, e.g., by also including the derivatives of the extinction cross section with respect to the imaginary RI, not only the real RI. But this is straight forward. If the measurement data discussed here are analyzed in this way, the quality of the fit is rather poor: about as good as the agreement between measured and simulated curves in Fig. 5.8 and Fig. 5.9. In particular, the peak heights in $\overline{C}_{\text{ext}}$ do not agree well with the measurements. This indicates that the mathematical model for the HbMP is incomplete. One important point to consider could be that other substances than oxyHb, deoxyHb and metHb are present in the particles, but were not accounted for in the model. Hence, one should possibly include the content of HSA (whose RI increment is only known at single wavelengths) into the model. Furthermore, it is not quite clear in how far the optical properties of the considered Hb variants change

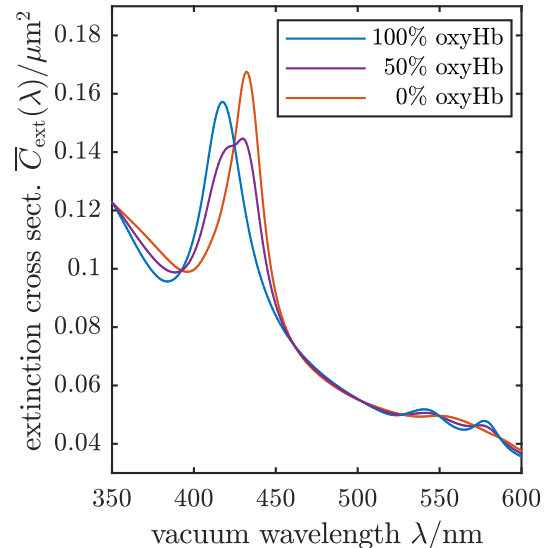


Figure 5.10: Simulation for varying oxygenation at 0% metHb level

due to the cross-linking process, which chemically modifies the protein chains and could change their conformation. In native Hb, conformational changes are known to occur during reversible binding and release of oxygen [76,116]. Subtle changes of the protein chains in the subunits of the Hb molecule due to mutations are known to have a considerable effect on the oxygen affinity [117]. Hence artificially introduced changes in the proteins due to cross linking may affect the oxygen binding capacity and the absorption spectra of the Hb molecules. Thus it is not even clear if the optical properties of the non-cross-linked Hb variants in solution can be used for a quantitative functional analysis of the HbMP. On the other hand a hypothetical increase of the oxygen affinity of the Hb molecules due to cross-linking could be an explanation for what appeared to be an incomplete deoxygenation when the oxygen was purged from the sample with argon.

When discussing the deviations between the extinction cross sections of spheroids and spheres, we also discussed the spectral absorption cross section $C_{\text{abs}}(\lambda)$. The absorption cross section of either shape model is almost identical to the curves computed in the Rayleigh limit for small particles. This could provide a way to increase the sensitivity of optical measurements and simplify the analysis of measured spectra. If one could measure them, the analysis of $C_{\text{abs}}(\lambda)$ spectra of HbMP suspensions would be almost as straight forward as the analysis of the absorption spectra of homogeneous Hb solutions, because in contrast to scattering and extinction cross sections in general, the absorption cross section in the Rayleigh limit is a product of a term depending only on particle size and a term depending only on the complex particle RI. Firstly, this means that C_{abs} in the Rayleigh limit is proportional to the particle volume. In an ensemble measurement, one only has access to the product of the size-averaged cross section and the particle concentration. Hence knowledge of the volume fraction of particles would be sufficient for the analysis of these spectra instead of the (more difficult to access) particle size distribution. Secondly, for the case considered here, where the imaginary RI of the particles is much smaller than their real RI, the RI-dependent factor in C_{abs} basically reproduces the absorption spectrum of the particles' material – the quantity that one would like to measure. Of course, all these considerations only make sense if the absorption cross section of the particles can actually be measured. If one recalls that $C_{\text{ext}} = C_{\text{sca}} + C_{\text{abs}}$, measuring C_{abs} is equivalent to measuring the scattering cross section C_{sca} , since C_{ext} can already be measured from the collimated transmittance. A measurement of $C_{\text{sca}}(\lambda)$ is in principle possible by collecting all the light scattered by the sample in all directions onto a spectrometer. This could be achieved by extending the optical setup for the measurement of C_{ext} considered here (chapter 4) by two *integrating spheres*. These hollow spheres are coated on the inside with a material of high diffuse reflectance. Any light entering the sphere is multiply reflected until an isotropic radiation field is established inside the sphere. Hence a light intensity proportional to the incident total power from different directions can be coupled out through a small opening and measured with a spectrometer. One of these spheres would need to be mounted in the forward-scatter direction of the sample cuvette and one in the backscatter direction in order to collect the light scattered into either hemisphere. Using a suitable calibration due to the spectral reflectance of the integrating spheres, as well as thin sample cuvettes in order to lose as little light to the sides as possible, this would allow to measure the total scattered power of the particle suspension and hence the ensemble-averaged scattering cross section $\overline{C}_{\text{sca}}(\lambda)$. The absorption cross section could then be computed as $\overline{C}_{\text{abs}}(\lambda) = \overline{C}_{\text{ext}}(\lambda) - \overline{C}_{\text{sca}}(\lambda)$. For the application

discussed here, this would mean taking the difference of two signals of similar amplitude, because for most wavelengths $\overline{C}_{\text{abs}}(\lambda)$ is smaller than $\overline{C}_{\text{ext}}(\lambda)$ by a factor of 10 to 1000, making $\overline{C}_{\text{abs}}(\lambda)$ prone to measurement noise.

Chapter 6

Modeling and simulation of light scattering by red blood cells in flow cytometry*

6.1 Introduction

In this chapter, light scattering simulations for red blood cells (RBCs) in the context of optical flow cytometry are discussed. Optical flow cytometry is a widely used tool to count and differentiate cell populations at high throughput of a few thousand cells per second [1,2]. In an optical flow cytometer (Fig. 6.1), a cell suspension is injected through a capillary into a *flow cell* (or *flow-through cuvette*), where it is accelerated by a fast flowing laminar sheath flow of decreasing cross section. This stretches the sample stream and *hydrodynamically focuses* it to the centerline of the flow channel. The sample stream intersects with one or several laser beams and the light scattered or – in the case of fluorescent labeling – emitted from the cells is collected onto one or several detectors. Standard flow cytometers measure the forward light scatter, by collecting light around the direction of the incident beam onto a detector and the side scatter by collecting at 90° to the incident beam. Fluorescent labeling of cells is often applied, in which case the light emitted by the cells is collected in the 90° direction, too. In contrast to fluorescent labeling, forward light scatter and side scatter provide a label-free means for the examination of biological cells. However, the interpretation of these signals is not straightforward.

If native human RBCs (i. e., not stained or fixed) are analyzed in a flow cytometer, one observes a bimodal histogram for the forward scattering cross section (FSC) [118,119]. This can be qualitatively explained by the fact that native RBCs of biconcave disk-like shape (discocytes) align with their figure axis perpendicular to the fluid flow in a channel much wider than themselves ($250\ \mu\text{m}$ channel width in the cytometer discussed here compared to $2\ \mu\text{m}$ – $8\ \mu\text{m}$ RBC size). This leaves them with one angular degree of freedom, the rotation angle β around the flow axis. The FSC of a face-on illuminated RBC ($\beta = 0^\circ$) is very different from

* This chapter is based on

J. Gienger, H. Groß, V. Ost, M. Bär, and J. Neukammer. Assessment of deformation of native red blood cells in flow cytometry: Measurement and simulation of bimodal forward scatter distributions. *in review at Biomed. Opt. Express*, submitted 27 Oct. 2018.

The flow cytometric experiments with RBCs discussed in this chapter were conceived and performed by Volker Ost and Jörg Neukammer (PTB Berlin). The DDA simulations of light scattering by RBCs were performed by Hermann Groß (PTB Berlin) with the author's shape models.

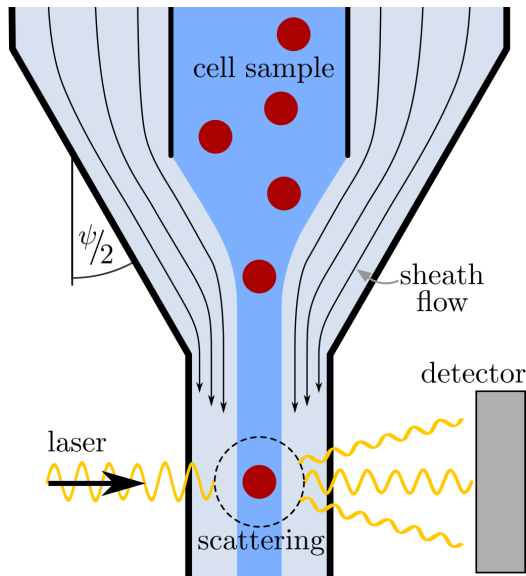


Figure 6.1: Schematic of an optical flow cytometer (not to scale)

the cytometer may deviate significantly from the biconcave shape at rest. Hence, the use of these bimodal histograms as a clinical marker for altered RBC rheology in conditions such as terminal renal failure, diabetes mellitus, sepsis or acute inflammatory state has been proposed [118, 119]. More generally, alterations of mechanical properties of human RBCs have been reported, e. g., for peripheral vascular disease [120], malaria [121, 122] and diabetes mellitus [123]. However, cytometric studies done so far [118, 119] employ empirical criteria to link the forward scatter histograms to the RBC shape or to detect abnormal rheological properties. As a step toward a quantitative analysis, in this chapter a detailed simulation of the scattering of light by native RBCs is performed using the discrete dipole approximation (DDA) and the effect of the distributions of cell orientation, volume and hemoglobin concentration are taken into account by Monte Carlo (MC) sampling. This allows to assess the impact of the RBC shape on the measured histograms of FSCs and thus an indirect evaluation of the deformations occurring in the flow cytometer.

These simulations are compared to measurements of native RBCs with a dedicated flow cytometer that features the simultaneous measurement of FSC with two orthogonal incident lasers with wavevectors \vec{k}_1 and \vec{k}_2 where $\vec{k}_1 \perp \vec{k}_2$, using a helium–neon (HeNe) laser as well as one-direction FSC measurements at different laser wavelengths. The velocity gradients of the fluid flow in the cytometer are estimated and compared to deformations of RBCs reported in the literature. A simple shape model for a stretched RBC is introduced and the deformation in the cytometer is estimated by comparison to light scattering simulations. The assumption that the RBCs align with their long axis in the flow direction, around which they are otherwise free to rotate is put to a test by comparison of measurements where the RBCs are oriented during injection into the flow cell and simulations with non-uniform orientation distributions.

an RBC illuminated from the side ($\beta = 90^\circ$). Depending in the laser wavelength and the solid angle of the detector, the FSC may increase in a “ $\sin(\beta)^2$ fashion” from $\beta = 0^\circ$ to $\beta = 90^\circ$. Since the circular cross section of the injection capillary does not impose any particular cell orientation, all values of β are equally likely and a bimodal histogram is observed in this case with peaks corresponding to the extrema of the FSC as a function of β . The quantitative properties of these histograms, such as inter-peak distance and height depend on the microscopic details of the RBCs, i. e., their shape and the distributions of cell size and intracellular hemoglobin (Hb) concentration. Due to deformation in flow, the shape of RBCs in

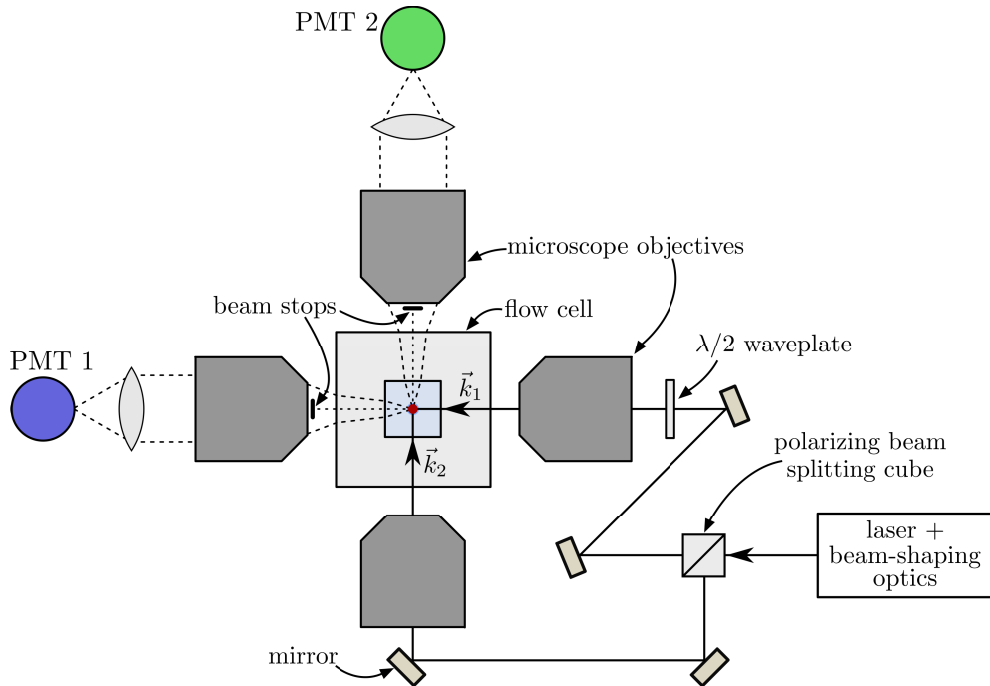


Figure 6.2: Simplified optical layout of the flow cytometer for the simultaneous 2-direction FSC measurement. The beam is divided by a polarizing beam splitting cube and the sample stream in the flow cell is illuminated with two beams of orthogonal wavevectors \vec{k}_1 and \vec{k}_2 . Microscope objectives serve to (1) focus the incident beams and (2) collect the forward-scattered light onto photomultiplier tubes (PMTs).

6.2 Experiment

6.2.1 Optical setup

The measurements of the FSC of native RBCs discussed here were recorded using a dedicated flow cytometer conceived and built by Volker Ost and Jörg Neukammer (PTB Berlin), described in more detail in Refs. 124, 125. The cytometer features the simultaneous measurement of the forward-scattered light with two orthogonal directions of incidence for the laser wavevector \vec{k}_1 and \vec{k}_2 where $\vec{k}_1 \perp \vec{k}_2$ at $\lambda = 632.8$ nm. The corresponding optical layout is shown in Fig. 6.2. The orientations of the RBC and the laser beams relative to each other are illustrated in Fig. 6.3. For the two-direction measurements, the cytometer features two orthogonal optical beam paths for a helium–neon laser (wavelength 632.8 nm). The laser beam is divided using a polarizing beam splitting cube, after which identical optical components are used in both beams paths, whose lengths of approximately 1 m are identical to within about 1 mm. Furthermore,

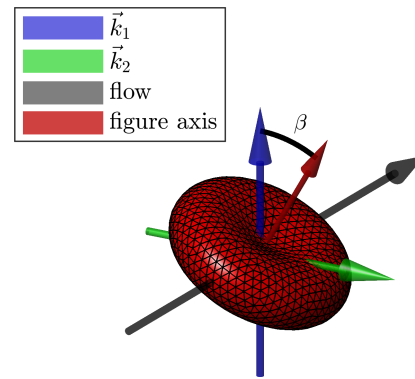


Figure 6.3: Surface triangulation of a discocyte shape model with arrows indicating the orientation of the RBC relative to the flow axis and the two incident lasers with wavevectors \vec{k}_1 and \vec{k}_2

the experimental setup incorporates an Ar⁺-laser with an output wavelength of 413.1 nm and a Kr⁺-laser that was tuned by means of a wavelength selecting prism to $\lambda = 488.0$ nm and 457.9 nm. These lasers were used for FSC measurements with a single direction of incidence (not shown in Fig. 6.2). The output beams of the lasers are shaped individually by spherical and cylindrical telescopes in order to form elliptical beams, which are then superimposed by dichroic beam splitters and focused via a microscope objective to a common spot of approximately the same size $10\ \mu\text{m} \times 42\ \mu\text{m}$ (full width of $1/e^2$ points of intensity) in the flow cell at the intersection point with the blood cells. The minor axis of the elliptical focus and the polarization vectors of the electric field are parallel to the direction of flow.

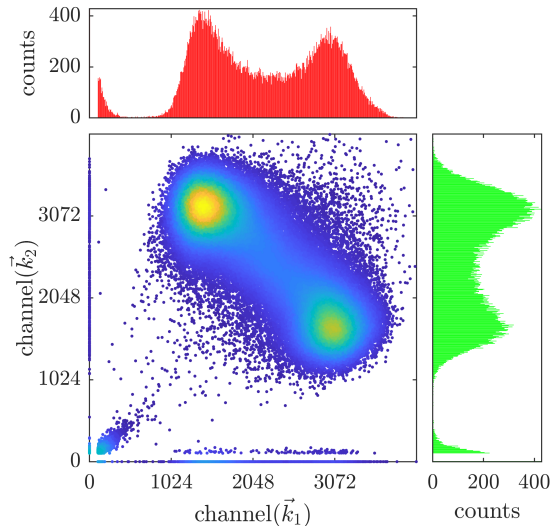


Figure 6.4: Measurements of the 2-direction forward-scattered intensity of a blood sample at 632.8 nm

$2.2^\circ \leq \vartheta \leq \vartheta_4 = 8.2^\circ$. The signal thus measured with the PMTs is proportional to the intensity of light scattered into the detector aperture. Each cell passing the laser beam causes a current pulse in the PMTs, the peak height of which is analyzed in the following. An example for measurement data is shown in Fig. 6.4, where density-colored (bright=high density) scatter plots are shown, created with the `dscatter` function of the FACS Matlab package [126]. Each dot in the 2D plot corresponds to a single cell. The histograms on the top and side are projections of the dot plot to a single axis. The x and y axes of the main plot are the channel number of the analog-to-digital converter (ADC) proportional to the intensity scattered into the microscope objectives, i. e., these measurements are not calibrated to yield an absolute cross section. The calibration procedure is discussed in section 6.4.6.

6.2.2 Flow setup

The flow cell of the cytometer consists of two parts, which are fused together: a cylindrical inlet part and the quadratic cuvette tube with the flow channel. The cylindrical inlet has an inner radius of $R_{\text{max}} = 2$ mm. The conical part, where the inlet diameter reduces to the dimensions of the quadratic flow channel (see Fig. 6.1) has an apex angle of $\psi = 25^\circ$.

The volume flow rate of the sheath flow was adjusted to approximately $\dot{V} =$

The light scattered by the cells is collected with microscope objectives onto photomultiplier tubes (PMTs). In order to block the direct laser beam, the objectives have beam stops mounted in front of them on the optical axis. For the 1-direction FSC measurements the angle of observation $\vartheta_1 = 3.3^\circ \leq \vartheta \leq \vartheta_2 = 17.4^\circ$ is determined by a circular beam stop and the numerical aperture of the light collecting microscope objective $20\times/\text{N.A.} = 0.4$. In the FSC measurements with two orthogonal HeNe laser beams, two identical microscope objectives $7\times/\text{N.A.} = 0.19$ for collimation of the scattered light were used. Stripe-shaped beam-stops parallel to the incident polarization vector were used resulting in an observation angle of $\vartheta_3 =$

$0.8 \text{ L h}^{-1} = 0.22 \text{ mL s}^{-1}$ by applying a driving pressure of 300 hPa. Consequently, the average fluid velocity in the $250 \mu\text{m} \times 250 \mu\text{m}$ channel of cross section $A_{\min} = (1/16) \text{ mm}^2$ amounted to $v_{\text{avg}} = \dot{V}/A_{\min} = 3.56 \text{ m s}^{-1}$. A laminar flow profile is developed downstream in the flow channel of 10 mm length. In order to assess the velocity of cells at the point of measurement, i. e., at the point of intersection with the laser beams, measurements were performed using two laser beams at a known distance ($110 \mu\text{m}$). The measured time delay between the light scattering signals from the lasers corresponds to cell velocities of 7 m s^{-1} .

The stainless steel capillaries used for injection of the diluted blood sample into the sheath flow had a specified inner diameter of $153 \mu\text{m}$. Besides using the standard capillary with circular outlet, a preferential orientation was imposed on the RBCs during injection by using a capillary with a flattened output end. This was achieved by carefully squeezing several capillaries between two polished plates. Subsequent examination of the modified capillaries under a light microscope revealed an oval inner cross section measuring approximately $20 \mu\text{m}$ along the narrow direction. This oriented the RBCs predominantly with their wide axis along the long axis of the flattened capillary.

The end of the sample injection capillaries was positioned in the center of the conical part of the flow cell at a distance of $\Delta z = 4 \text{ mm}$ to the quadratic flow channel. The volume rate of the sample flow typically amounted to $\dot{V}_{\text{sample}} = 85 \text{ nL s}^{-1}$. At the sample velocity of $v = 7 \text{ m s}^{-1}$, determined by the sheath flow, this volume rate corresponds to a cross section of the sample stream of $A_{\text{sample}} = \dot{V}_{\text{sample}}/v = 12.1 \mu\text{m}^2$ or a diameter of $3.9 \mu\text{m}$.

6.2.3 Blood preparation

Human RBCs from one healthy volunteer were analyzed (written informed consent was obtained). The blood was collected by venipuncture and anticoagulant ethylenediaminetetraacetic acid (EDTA), contained in 2.7 mL tubes (Monovette EDTA K, Sarstedt AG & Co., Germany). The blood samples were diluted by a factor of about 100 in phosphate buffered saline (PBS) when investigating native erythrocytes. For testing the device and for calibration, isovolumetric sphering of RBCs was applied using the procedure described by Kim and Ornstein [22, 99]. I. e., the RBCs were suspended in a mixture of isotonic saline, bovine serum albumin (BSA) and sodium dodecyl sulfate (SDS), which causes their lipid membrane to contract while not changing the volume. Hematological parameters of the volunteer were obtained from the complete blood count (CBC) using a hematology analyzer. The relevant parameters of the RBCs are shown in Tab. 6.1. $\text{MCV} = \mathbb{E}(V)$ is the *mean corpuscular volume* and $\text{RDW} = \text{CV}(V)$ is the *red cell distribution width*, where \mathbb{E} denotes the expectation value (or mean) and CV denotes the coefficient of variation, i. e., the relative standard deviation. $\text{MCHC} = \mathbb{E}(c_{\text{Hb}})$ is the *mean corpuscular hemoglobin concentration*, where c_{Hb} is the intracellular Hb concentration. The *hemoglobin distribution width* width $\text{HDW} = \text{CV}(c_{\text{Hb}})$ is not a routinely measured parameter.

Table 6.1: Hematological parameters for the concentration distribution and size distribution of the RBC sample

MCHC/g L ⁻¹	HDW/%	MCV/fL	RDW/%
344	5	92.7	12.4

For the simulations presented in this chapter it was set to a typical value that best fits the measurements of sphered RBCs.

6.3 Hydrodynamics

6.3.1 Estimate of velocity gradients

Let us take a closer look at the hydrodynamic situation in the flow cytometer in order to understand which types of forces are acting on the RBCs before and during measurement. The dimensions of the flow cell and the volume flow rates are described in section 6.2.2. The flow of the sheath fluid in the cytometer in the absence of the blood cells is described by the Navier–Stokes equation for an incompressible fluid

$$\frac{\partial \mathbf{v}}{\partial t} + (\mathbf{v} \cdot \nabla) \mathbf{v} - \frac{\mu}{\rho_0} \Delta \mathbf{v} = -\frac{1}{\rho_0} \nabla p + \mathbf{g}, \quad (6.1)$$

where \mathbf{v} is the velocity field, μ and ρ_0 are the the viscosity and density of the fluid, respectively and p is the pressure. The body accelerations \mathbf{g} , e. g., due to gravity can be set to zero here. No-slip boundary conditions, i. e., $\mathbf{v} = 0$ have to be

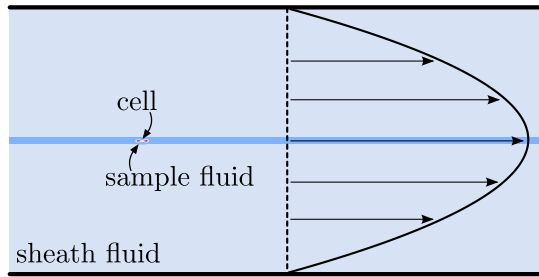


Figure 6.5: RBC in the flow channel of the cytometer (to scale)

fulfilled at the walls of the flow cell of the cytometer. Because the RBCs are much smaller than the cross section of the flow channel (Fig. 6.5), the velocity profile is not expected to change significantly due to the presence of the single RBCs. The question addressed now is: Which viscous forces due to velocity gradients in the fluid flow are experienced by a RBC while passing through the cytometer? There are two kinds of velocity gradients in the cytometer: (1) Transverse gradients occur due to the flow profile in the channel, which is a (mostly) developed laminar *Poiseuille flow* at the point of measurement. (2) Longitudinal gradients occur at the conical part of the flow cell, where its cross section decreases from the rather wide inlet to the narrow flow channel, i. e., the velocity increases downstream and one has *extensional flow*.

Transverse gradients

Analytical solutions of the Navier–Stokes equation exist for certain cases of pipe flow, and these can be used to estimate the transverse gradients at the point of measurement as well as to validate the assumption of a developed flow profile. Let x denote the direction of the flow channel. Then a flow that is fully developed ($\partial \mathbf{v} / \partial x = 0$), stationary ($\partial v / \partial t = 0$) and swirl-free ($v_y = v_z = 0$) has a velocity field $\mathbf{v} = v_x(y, z) \mathbf{e}_x$. Consequently, the term $(\mathbf{v} \cdot \nabla) \mathbf{v}$ in the Navier–Stokes equation vanishes. It follows that the y and z components of the pressure gradient ∇p vanish and the equation reduces to a two-dimensional *Poisson problem*

$$-\Delta_{yz} v_x(y, z) = -\frac{1}{\mu} \frac{dp}{dx} = \text{const} \quad (y, z) \text{ in } \Omega, \quad (6.2)$$

$$v_x(y, z) = 0 \quad (y, z) \text{ on } \partial\Omega, \quad (6.3)$$

where Ω denotes the cross section of the pipe and $\Delta_{yz} = \partial^2/\partial y^2 + \partial^2/\partial z^2$ denotes the two-dimensional Laplace operator. Since the pressure drops along the pipe, one has $dp/dx < 0$. The solutions to this equation, describing laminar flow, are known as *Poiseuille flow*. For a circular pipe of radius R the solution (in cylindrical coordinates) is particularly simple

$$v_x(\rho, \varphi) = -\frac{1}{4\mu} \frac{dp}{dx} (R^2 - \rho^2) \stackrel{\text{def. } v_{\max}}{=} v_{\max} \left(1 - \frac{\rho^2}{R^2}\right) \quad \text{for } \rho \leq R, \quad (6.4)$$

i. e., a parabolic velocity profile, where $\rho = \sqrt{y^2 + z^2}$. The volume flow rate through the pipe is given by

$$\dot{V} = \int_0^{2\pi} \int_0^R v_x(\rho, \varphi) \rho \, d\rho \, d\varphi = -\frac{\pi R^4}{8\mu} \frac{dp}{dx} = \frac{1}{2} v_{\max} \pi R^2. \quad (6.5)$$

Hence the average velocity of the Poiseuille flow in a circular pipe is half the maximum velocity $v_{\text{avg}} = \dot{V}/A = \frac{1}{2} v_{\max}$, where $A = \pi R^2$ is the cross-sectional area of the pipe. In the experiments considered here, where the volume rate \dot{V} is known and the maximum velocity v_{\max} can be measured using tracer particles or cells, this property can be used to check whether the flow profile is really fully developed at the point of measurement. However, since the flow channel is quadratic, not circular, this solution can not be applied in the strict sense. Like for a circular domain Ω , there exists an analytical solution for the Poisson problem Eq. (6.2), (6.3) on a rectangle that describes the velocity profile of a fully developed laminar flow in a rectangular pipe. In the special case of a quadratic pipe, i. e., $\Omega = [-a, a]^2$, the velocity is given by

$$v_x(y, z) = -\frac{a^2}{\mu} \frac{dp}{dx} \left\{ \frac{1}{2}(1 - \eta^2) - \frac{16}{\pi^3} \sum_{\substack{j=1 \\ j \text{ odd}}}^{\infty} \frac{1}{j^3 \sinh(j\pi)} \sin\left(\frac{j\pi(1 + \eta)}{2}\right) \right. \\ \left. \times \left[\sinh\left(\frac{j\pi(1 + \zeta)}{2}\right) + \sinh\left(\frac{j\pi(1 - \zeta)}{2}\right) \right] \right\} \quad (6.6)$$

with rescaled dimensionless coordinates $\eta = y/a$ and $\zeta = z/a$, i. e., $(\eta, \zeta) \in [-1, 1]^2$. This flow profile has a maximum velocity of

$$v_{\max} = v_x(0, 0) = -\frac{a^2}{\mu} \frac{dp}{dx} \underbrace{\left\{ \frac{1}{2} - \frac{32}{\pi^3} \sum_{\substack{j=1 \\ j \text{ odd}}}^{\infty} \frac{(-1)^{(j-1)/2} \sinh\left(\frac{j\pi}{2}\right)}{j^3 \sinh(j\pi)} \right\}}_{=0.2946\dots} \quad (6.7)$$

and an average velocity of

$$v_{\text{avg}} = \frac{1}{4a^2} \int_{-a}^a \int_{-a}^a v_x(y, z) \, dy \, dz = -\frac{a^2}{\mu} \frac{dp}{dx} \underbrace{\left\{ \frac{1}{3} - \frac{64}{\pi^5} \sum_{\substack{j=1 \\ j \text{ odd}}}^{\infty} \frac{1}{j^5} \frac{\cosh(j\pi) - 1}{\sinh(j\pi)} \right\}}_{=0.1405\dots} \quad (6.8)$$

Hence the ratio of maximum to average velocity is $v_{\max}/v_{\text{avg}} = 2.096\dots$ for a quadratic pipe. Like in a circular pipe, the tip of the profile can be approximated by a paraboloid

$$v_x(z, y) = v_x(0, 0) + \frac{1}{4\mu} \frac{dp}{dx} (y^2 + z^2) \stackrel{\text{def. } R_{\text{eff}}}{=} v_{\max} \left(1 - \frac{\rho^2}{R_{\text{eff}}^2}\right) \quad \text{for } |y|, |z| \ll a \quad (6.9)$$

with an effective radius of $R_{\text{eff}} = 1.085 \dots \times a$.

In the experiment, the average fluid velocity in the quadratic flow channel was $v_{\text{avg}} = \dot{V}/A = 3.56 \text{ m s}^{-1}$, determined by the volume rate of the sheath flow. Hence for a fully developed Poiseuille flow in a circular flow channel the maximum that should be achieved in the center of a parabolic velocity profile would be $v_{\text{max}} = 2v_{\text{avg}} = 7.1 \text{ m s}^{-1}$. For the quadratic cross section that was used one expects a higher velocity of $v_{\text{max}} = 7.45 \text{ m s}^{-1}$. Velocity measurements of cells traveling along the centerline of the quadratic channel yielded 7 m s^{-1} , which agrees reasonably well with the theoretical value for a circular pipe, but is somewhat smaller than the expectation for a quadratic cross section. This indicates that at the point of measurement, the flow profile is mostly developed, but not fully. Hence, at this point, the velocity gradients are mostly transverse and longitudinal gradients are weak.

The transverse gradients in the flow channel experienced by a RBC moving along the channel's centerline can now be estimated using the approximation of the flow profile in the $250 \mu\text{m} \times 250 \mu\text{m}$ quadratic channel, Eq. (6.9), with effective pipe radius $R_{\text{eff}} = 136 \mu\text{m}$. Since $v_{\text{max}} = 7 \text{ m s}^{-1}$ was measured, a typical transverse velocity gradient (shear rate) for a (deformed) RBC measuring $2\Delta\rho = 5 \mu\text{m}$ across is

$$\dot{\gamma}_{\text{typ}} = \frac{v_x(0) - v_x(\Delta\rho)}{\Delta\rho} = v_{\text{max}} \frac{\Delta\rho}{R_{\text{eff}}^2} = 950 \text{ s}^{-1}. \quad (6.10)$$

Longitudinal gradients

We now consider the longitudinal velocity gradients in the conical part of the flow cell where the RBC suspension is injected (Fig. 6.1). To obtain a quantitative result for the velocity field would require a numerical solution of the Navier–Stokes equation in this non-trivial geometry, at least for a stationary flow, which goes beyond the scope of this thesis. In order to obtain an estimate of the order of magnitude of these gradients, we assume a flat flow profile with $v(x, y, z) = v_{\text{avg}}(x) = \dot{V}/A(x)$ at every cross section of the cone, which has an apex angle $\psi = 25^\circ$. Furthermore, we assume that the circular cone transitions smoothly into the quadratic flow channel of area $A_{\text{min}} = (1/16) \text{ mm}^2$, thus defining the minimal effective radius $R_{\text{min}} = \sqrt{A_{\text{min}}/\pi} = 140 \mu\text{m}$. The radius R reduces linearly with x starting from $R_{\text{max}} = 2 \text{ mm}$ at the inlet ($x = -L = -8.4 \text{ mm}$) and ending in the flow channel at $x = 0$, i. e.,

$$R(x) = R_{\text{min}} - x \tan(\psi/2), \quad \text{for } x < 0. \quad (6.11)$$

Hence, the area $A(x)$ is a quadratic polynomial of x and

$$v_{\text{avg}}(x) = \frac{\dot{V}}{A(x)} = \frac{\dot{V}}{\pi [R_{\text{min}} - x \tan(\psi/2)]^2}. \quad (6.12)$$

The longitudinal gradient of this extensional flow is given by

$$\dot{\epsilon} = \frac{dv_{\text{avg}}(x)}{dx} = \frac{2\dot{V} \tan(\psi/2)}{\pi R(x)^3}, \quad (6.13)$$

which is highest at the narrowest part of the cone ($x = 0$) where it amounts to $\dot{\epsilon}_{\text{max}} = 11.2 \times 10^3 \text{ s}^{-1}$. Besides the velocity and gradients, one can further estimate the time it takes the RBC to get from the point of injection into the flow channel of

constant cross section. This time of passage corresponds to the time during which the RBC is subject to extensional stress. Since the sample injection capillary is placed $\Delta x_{\text{inj}} = 4 \text{ mm}$ upstream from the flow channel, this time is

$$\Delta t = \int_{-\Delta x_{\text{inj}}}^0 \frac{1}{v_{\text{avg}}(x)} dx = \frac{\pi}{3V \tan(\psi/2)} [R(-\Delta x_{\text{inj}})^3 - R_{\text{min}}^3] = 23 \text{ ms}. \quad (6.14)$$

Even when inside the flow channel where $A(x) = \text{const}$, the RBC still experiences stress due to longitudinal velocity gradients, because the flow profile is just developing. These gradients are, however, much weaker than in the conical part. To get an estimate, we note that between the beginning of the flow channel and the point of measurement, some 10 mm downstream, the velocity at the centerline of the channel increases from at least $v = v_{\text{avg}} \approx 3.6 \text{ ms}^{-1}$ to $v_{\text{max}}^{\text{meas}} = 7 \text{ ms}^{-1}$. Hence, a typical time-averaged value for the corresponding extensional strain $\dot{\epsilon}$ is $(7 - 3.6) \text{ ms}^{-1} / 10 \text{ mm} = 340 \text{ s}^{-1}$, which is much less than the estimated $\dot{\epsilon}_{\text{max}} = 11.2 \times 10^3 \text{ s}^{-1}$ at the narrowest part of the cone.

6.3.2 Comparison to microfluidic flows

We now have an estimate of the velocity gradients occurring in the flow cytometer, from which the magnitudes of the resulting viscous forces acting on the RBC can be determined. In the optical simulations presented in the next section the deformations resulting from these forces shall be accounted for by a suitable shape model. Detailed quantitative mathematical models exist for the viscoelastic behavior of RBCs in fluid flows [19, 127, 128] that could be applied to the problem at hand. However, the numerical simulation of these models is a challenging topic on its own that goes beyond the scope of this thesis. Nevertheless, one can at least compare the hydrodynamic situation estimated above to theoretical and experimental results for RBC deformation presented in the literature. To the author's knowledge, detailed quantitative simulations of the deformation of RBCs in a flow cytometer have been described only in one case in the literature: Gibaud [129] discusses the deformation, alignment and lateral migration of RBCs in an impedance flow cytometer. While some qualitative effects can be compared between this study and the optical flow cytometer used here, the geometry of the flow cells of the two devices are quite different. For example the impedance flow cytometer considered by Gibaud does not feature a narrow flow channel but an orifice for electrical impedance measurements. Hence no quantitative shape models for optical simulations can be derived from these results. But they suggest that alignment of the RBCs with their long axis in the flow direction and elongation along this axis are typical effects of the hydrodynamic focusing.

Due to the interesting modes of RBC motion one can observe, a lot of studies of RBC deformation focused on simple shear flows [130, 131], which is not applicable to the situation at hand. Furthermore, microcapillary flow and mesoscale blood dynamics are topics of apparent biomedical importance and have thus been studied extensively in recent years, see Ref. 19 and references therein. The deformation of single RBCs in pipe flow has been studied for microcapillaries of a few μm width, i. e., comparable to the RBC's size and much narrower than the cytometer's flow channel. Flow velocities in these experiments typically are in the $\mu\text{m s}^{-1}$ to cm s^{-1} range [132, 133], i. e., much smaller than in the flow cytometer considered here. In such a stationary microcapillary flow the deformation of the RBC is caused by transverse velocity gradients and the proximity to the capillary walls.

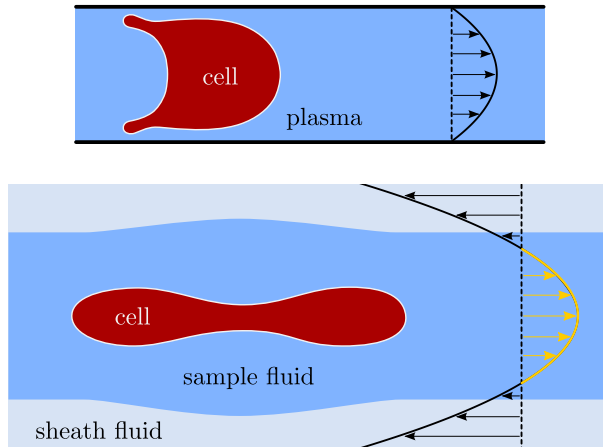


Figure 6.6: Shape of a RBC in a microcapillary [132] (top) compared to the shape and orientation expected in the flow channel of the cytometer (bottom). Developed flow profiles in the absence of the cell are indicated by arrows.

are macroscopically far away. Due to the much higher flow velocity, the transverse gradients and the curvature of the flow profile at the center (in absence of the RBC) are still comparable to microcapillary flows [132, 133]. However, due to the long distance to the walls the RBC is not “squeezed through” the channel like in a microcapillary and the transverse gradients alone might not cause as strong deformations of RBCs in the flow cytometer as depicted in Fig. 6.6.

As discussed above, extensional flow occurs at the conical part of the flow cell of the cytometer, where the sample fluid is injected. The deformation of RBCs in homogeneous extensional flows has been studied by Lee et al. [138] and Yaginuma et al. [139] using hyperbolically converging microfluidic channels. The observation of flowing RBCs with medium-resolution light microscopy in these studies revealed a stretching of the RBCs with an elliptical deformation of the discocyte shape. The extensional stresses ranged from $\sigma_e = 0.1 \text{ Pa}$ to 13 Pa [138] and $\sigma_e = 0.4 \text{ Pa}$ to 16.5 Pa [139], respectively. We estimated the longitudinal gradient (or extensional strain rate) in the flow cytometer to be as high as $\dot{\epsilon}_{\max} = 11 \times 10^3 \text{ s}^{-1}$, i. e., one order of magnitude higher than a typical shear rate due to the curvature of the Poiseuille profile. The sheath fluid is assumed to have the shear viscosity of water $\mu_s \approx 1 \text{ mPa}\cdot\text{s}$. Consequently its extensional viscosity is [138] $\mu_e = 3\mu_s \approx 3 \text{ mPa}\cdot\text{s}$ and the extensional stress upon injection peaks at about $\sigma_{e,\max} = \dot{\epsilon}_{\max} \mu_e \approx 33 \text{ Pa}$. This is of the same order of magnitude as the highest extensional stresses applied to RBCs in Ref. 138, 139, hence similar deformations are expected here, too.

As estimated above, the RBCs in the cytometer take about 23 ms to get through the converging part of the flow cell. During this time, they are exposed to increasing extensional stress $\sigma_e(t) \leq \sigma_{e,\max} \approx 33 \text{ Pa}$. The optical measurement, i. e., the intersection with the laser beams happens downstream in the flow channel, where mostly transverse gradients occur. I. e., the RBCs are measured some time *after* they were exposed to the extensional stress and might have had time to relax from the deformation. The viscoelastic relaxation time constants of stretched RBCs are known to be about 100 ms – 250 ms [140, 141]. In this time a RBC flowing in the flow channel at 7 m s^{-1} covers a distance $\geq 700 \text{ mm}$, i. e., has long passed the laser

The resulting RBC shapes and orientations include “bullet” or “parachute” modes, where the symmetry axis of the RBC is oriented along the flow direction [128, 132–134], which is depicted in the top panel of Fig. 6.6, as well as a “slipper” mode where this symmetry is broken to some extent [134–137]. In experiments with narrow rectangular flow channels a “croissant” shape [137] can be observed, similar to a parachute but without rotational symmetry around the flow axis. In contrast, the (almost) developed laminar flow profile in the flow cell of the cytometer considered here rather corresponds to an *infinite Poiseuille flow* since the walls

a few mm downstream. Hence the effect of the extensional stress is still well visible in the RBC shape at the point of measurement. On the other hand, compared to the relaxation time constants, the exposure time to the extensional stress of around 23 ms seems long enough to expect a noticeable deformation.

6.4 Optical modeling and simulation

6.4.1 Scattering problem and FSC

As already discussed in chapter 1 and detailed in chapter 2, a RBC can be modeled as a homogeneous dielectric particle because it has minimal internal structure (if any at all) and its membrane is very thin [21]. Hence the scattering of a laser beam by a single RBC embedded in a quasi-infinite host medium (the sheath fluid) is described by the Helmholtz equation for the electric field \mathbf{E}

$$\Delta \mathbf{E} + \mathbf{n}^2 k^2 \mathbf{E} = 0, \quad (6.15)$$

where $\mathbf{n} = n + i\kappa$ is the complex refractive index (RI), and $k = \omega/c_0 = 2\pi/\lambda$ is the vacuum wavevector of the electric field of the laser operating at vacuum wavelength λ . For a homogeneous dielectric scatterer with RI \mathbf{n}_s in a non-absorbing host medium with RI n_m , one has

$$\mathbf{n}(\mathbf{r}) = \begin{cases} \mathbf{n}_s & \text{for } \mathbf{r} \text{ inside the scatterer} \\ n_m & \text{outside} \end{cases}. \quad (6.16)$$

The total electric field is the sum of the incident and scattered fields

$$\mathbf{E} = \mathbf{E}^i + \mathbf{E}^s. \quad (6.17)$$

Together with radiation conditions for \mathbf{E}^s at $r \rightarrow \infty$ and continuity conditions for the tangential field components on the particle boundary this defines the scattering problem.

We have already made use of the analytical solution for a spherical scatterer (Mie theory/Mie scattering) in the previous chapters. To solve this problem for more general shapes the scattering problem has to be solved numerically. One possible method, which is employed here is the *discrete dipole approximation* (DDA), where the volume of the scatterer is discretized into a cubic grid. Using the Green's function of the Helmholtz operator, Eq. (6.15) can be re-written as a volume integral equation. Using the volume discretization, this integral equation is then approximated by a system of algebraic equations that can be solved by methods of numerical linear algebra. For numerical reasons, the variable for which this system of equations is written is not the total electric field \mathbf{E} , but rather an "exciting field" \mathbf{E}^{exc} or the polarization \mathbf{P} , from which the total electric field can then be easily computed. An outline of the DDA is given in section 2.2.2 of chapter 2. The DDA method is characterized by requiring a volume discretization only of the scatterer, but not of the surrounding medium. This solution method works for arbitrary incident fields \mathbf{E}^i given on the grid points defining the scatterer. The ADDA 1.2 implementation of the DDA was used. The details of the method and implementation are given in Ref. 66.

The incident beam is assumed to be a plane wave propagating along the z axis, i. e., with wavevector (in the host medium) $\vec{k}_m = 2\pi n_m/\lambda \mathbf{e}_z$. The DDA yields the

total electric field \mathbf{E} inside the scatterer, from which the outside field and far field can be computed, again using the Green's function of the Helmholtz operator and its far-field limit. Among others this allows to compute the *Mueller matrix* of the scattered far field. In general, a Mueller matrix, which is a 4×4 real-valued matrix describes the transformation of the Stokes vector $(I, Q, U, V)^T$ in a linear optical process, such as scattering. Here I is the total intensity of an incident beam, Q and U describe the linearly polarized portion of the light and V describes circular polarization. The scattered far field is transverse and decays like a spherical wave, its Mueller matrix $\mathbf{M}(\vartheta, \varphi)$ describes the direction-dependent intensity in dependence on the polarization state of the incident field. The Stokes vector of the scattered field, relative to the scattering plane [spanned by the unit vectors \mathbf{e}_z and $\mathbf{e}_r(\vartheta, \varphi)$], is given by

$$(I^s, Q^s, U^s, V^s)^T = \frac{1}{k_m^2 r^2} \mathbf{M}(\vartheta, \varphi) (I^i, Q^i, U^i, V^i)^T. \quad (6.18)$$

Since an x -polarized incident beam is used, the Stokes vector in the coordinate system of the laboratory is $I^i (1, 1, 0, 0)^T$. Expressed relative to the scattering plane, this reads

$$(I^i, Q^i, U^i, V^i)^T = I^i (1, \cos 2\varphi, \sin 2\varphi, 0)^T. \quad (6.19)$$

Consequently the total scattered intensity is

$$I^s(\vartheta, \varphi) = \frac{1}{k_m^2 r^2} I^i (M_{11} + M_{12} \cos 2\varphi + M_{13} \sin 2\varphi), \quad (6.20)$$

where the M_{ij} depend on (ϑ, φ) . The forward scattering cross section is computed from this as

$$\text{FSC} = \frac{1}{k_m^2} \iint_{\Omega} (M_{11} + M_{12} \cos 2\varphi + M_{13} \sin 2\varphi) \sin \vartheta \, d\vartheta \, d\varphi, \quad (6.21)$$

where Ω is the detector aperture. The aperture of a microscope objective with on-axis circular beam stop used for the four-wavelength one-direction FSC measurements is given by

$$\Omega_{\text{circle}} = \{\vartheta \in [\vartheta_1, \vartheta_2], \quad \varphi \in [0, 2\pi]\} \quad (6.22)$$

and the aperture with a stripe-shaped beam stop along the x -axis used for the two-direction FSC measurements is given by

$$\Omega_{\text{stripe}} = \{\vartheta \in [\vartheta_3, \vartheta_4], \quad |\sin \varphi| \in [\vartheta_3/\vartheta, 1]\}. \quad (6.23)$$

Here ϑ_2 and ϑ_4 are the outer acceptance angles of the respective microscope objectives, ϑ_1 is the angular radius of the circular beam stop, and ϑ_3 the angular half-width of the stripe-shaped beam stop.

6.4.2 Shape model

Several mathematical models exist to approximately describe the biconcave shape of a native RBC at rest. Here, we use the equation of Yurkin [142], which reads

$$\rho^4 + 2R_4 \rho^2 z^2 + z^4 + R_1 \rho^2 + R_2 z^2 + R_3 = 0. \quad (6.24)$$

This implicit equation describes the surface of the cell in cylindrical coordinates (ρ, φ, z) . As written this shape model is symmetric with respect to rotation around

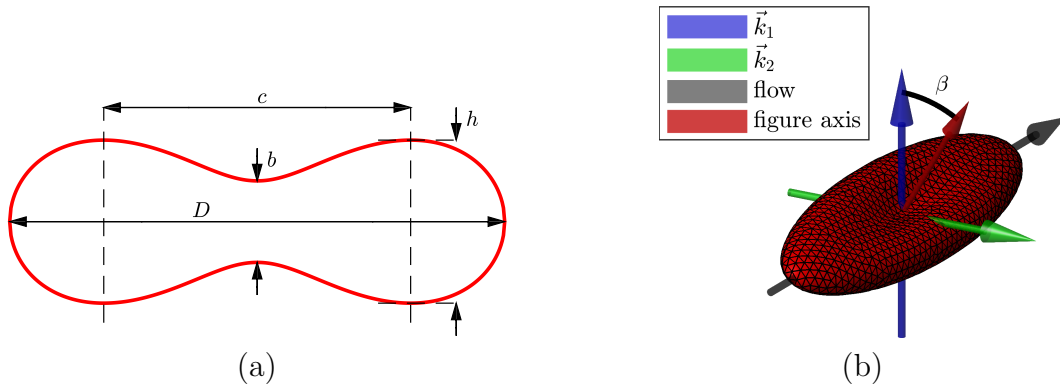


Figure 6.7: (a) Cross section through the center of the shape model defined by Eq. (6.24). (b) Surface triangulation of the stretched model, compare Fig. 6.3. Arrows indicate the orientation of the RBC relative to the flow axis and the two incident lasers with wavevectors \vec{k}_1 and \vec{k}_2 . “Figure axis” denotes the symmetry axis before stretching.

the z -axis, or *axisymmetric*. It further has mirror-symmetry with respect to the xy -plane. Alternatively to the coefficients $R_1 \dots R_4$ of Eq. (6.24), the model can be characterized by the diameter D of the cell, its minimal thickness b and maximal thickness h and the diameter c of the circle of maximal thickness, see Fig. 6.7 (a). This shape model describes RBCs at rest, as they can be observed, e. g., on a glass slide under a light microscope (if one ignores the effects of adhesion to the slide). However, as discussed above in section 6.3, RBCs in the flow cytometer are subject to considerable hydrodynamic forces. Hence, deformation is expected to occur as a response to both, transverse and longitudinal velocity gradients of the sheath fluid. Since the latter are much higher than the former and motivated by the elliptical shapes observed for RBCs in pure extensional flows [138, 139], the above axisymmetric model is extended by a non-uniform linear scaling. In Cartesian coordinates this is expressed by the mapping

$$(x, y, z) \mapsto (f_x x, f_y y, f_z z). \quad (6.25)$$

Since f_x is the direction of fluid flow along which the cell is stretched one has $f_x > 1$.

Table 6.2: Parameters of the shape models used. S is the surface area and V the volume of the cell. The sphericity index (SI) is defined as $SI = \sqrt[3]{36\pi V^2/S}$.

	axisymm.	stretched
f_x	1	9/4
f_y	1	2/3
$D/\mu\text{m}^*$	7.65	7.64
c/D	0.62	0.62
$h/\mu\text{m}$	2.5	2.55
$b/\mu\text{m}$	1.25	0.8
$S/\mu\text{m}^2^*$	125	169
SI*	0.795	0.587

* Values for a RBC with $V = 92.7 \text{ fL} = \text{MCV}$.

Along the other two directions, we expect a compression of the cell $f_y, f_z < 1$. We chose $f_y = f_z = 1/\sqrt{f_x}$. This way, the stretching is described by a single parameter f_x and conserves the cell’s volume, since the determinant of the transformation matrix is then $f_x f_y f_z = 1$.

The result is a shape model whose top-view is an ellipse of major axis $f_x D$ and minor axis $D/\sqrt{f_x}$. The minimum and maximum thickness are $b/\sqrt{f_x}$ and $h/\sqrt{f_x}$, respectively. For the stretched model $f_x = 9/4 = 2.25$ was used. The parameters of the stretched and unstretched shape models are given in

Tab. 6.2 and the corresponding shapes are depicted in Fig. 6.3 and Fig. 6.7 (b), respectively. The parameters of the unstretched model in Tab. 6.2 describe a typical RBC at rest [143]. The parameters of the stretched model were tuned by hand in order to match the 1D and 2D FSC measurements. A variable RBC volume was accounted for by varying the diameter D , while keeping h , b and the ratio c/D constant. Furthermore, the RBC shape model is allowed to rotate around its long axis, i. e., the direction of flow. The Euler angle β is a free parameter of the model, compare Fig. 6.7 (b).

6.4.3 Refractive index

For the optical properties of the fluid, in which the RBCs are suspended during measurement we assume those of water [41], since the sheath fluid is made up mostly of water. For the complex RI of the RBCs we assume wavelength- and concentration-dependent values

$$\mathbf{n}(\lambda; c_{\text{Hb}}) = n_{\text{H}_2\text{O}} + c_{\text{Hb}} [\alpha(\lambda) + i\gamma(\lambda)] \quad (6.26)$$

determined from Kramers-Kronig (KK) relations in chapter 3.¹ Numerical values for the four laser wavelengths used and the mean cellular hemoglobin concentration $\text{MCHC} = 344 \text{ g L}^{-1}$ are given in Tab. 6.3. Note, however, that the complex RI of the RBCs is subject to biological variation due to the variation of the Hb concentration c_{Hb} within the blood sample. This is accounted for in the simulation by sampling a range of values for c_{Hb} .

6.4.4 DDA simulations

It should be noted that the surface triangulations of the RBC shape models in Figs. 6.3 and 6.7 serve only to illustrate the shape. They were not used for scattering simulations, where a volume discretization with 45 nm cubes was employed. The size of the cubes corresponds to 6.9 dipoles per wavelength at the shortest wavelength $\lambda = 413.1 \text{ nm}$ ($\lambda/n_{\text{H}_2\text{O}} = 307.7 \text{ nm}$) and 10.6 dipoles per wavelength at the longest wavelength $\lambda = 632.8 \text{ nm}$ ($\lambda/n_{\text{H}_2\text{O}} = 475.0 \text{ nm}$). Mueller matrices were computed in ADDA 1.2 for $\vartheta = 0.0^\circ : 0.2^\circ : 28.0^\circ$ and $\varphi = 0^\circ : 1^\circ : 360^\circ$, from which the FSC was computed for the respective apertures [Eqs. (6.21) to (6.23)] by numerical integration. In the $a : b : c$ expression a and c are the start and end values, respectively and b is the step width of a uniform grid. An example for the far-field

¹ The values used here for DDA simulations represent the fit of the the deep-UV KK model to the measurement data of Friebel and Meinke [38] for the real RI increment of Hb solutions. The results of chapter 4 of this thesis were not used, because the extinction measurement data used in that chapter to determine the optical properties of RBCs became available only after the computationally expensive DDA simulations of the present chapter had already been performed.

Table 6.3: RI of water and RBCs (at $c_{\text{Hb}} = 344 \text{ g L}^{-1} = \text{MCHC}$) assumed for simulation. $\mathbf{m} = \mathbf{n}/n_{\text{H}_2\text{O}}$ is the relative RI of the RBCs.

λ/nm	413.1	457.9	488	632.8
$n_{\text{H}_2\text{O}}$	1.3424	1.3391	1.3374	1.3321
\mathbf{n}	$1.4316 + 0.0200i$	$1.4343 + 0.0020i$	$1.4299 + 0.0011i$	$1.4230 + 6.2i \times 10^{-5}$
\mathbf{m}	$1.0665 + 0.0149i$	$1.0711 + 0.0015i$	$1.0691 + 8.2i \times 10^{-4}$	$1.0682 + 4.7i \times 10^{-5}$

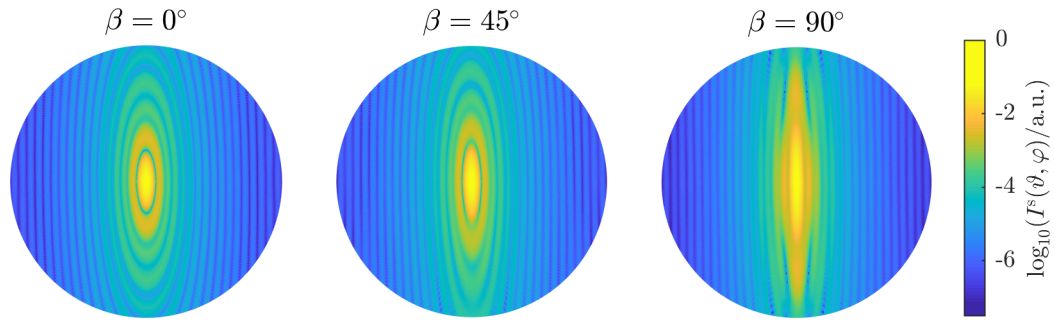


Figure 6.8: Far-field intensity distributions $I^s(\vartheta, \varphi)$ [Eq. (6.20)] on a logarithmic scale at $\lambda = 632.8$ nm for the stretched RBC shape model with $f_x = 2.25$, size $D = 7.8 \mu\text{m}$ and $c_{\text{Hb}} = 335 \text{ g L}^{-1}$. The solid angle is $0^\circ \leq \vartheta \leq 28^\circ$. The long axis of the stretched RBC is oriented horizontally. Three different rotations around this axis are shown. For $\beta = 0^\circ$ the cell is parallel to the image plane.

intensities that were integrated over in order to obtain the FSC is shown in Fig. 6.8. A database of FSC values was thus computed for parameters

$$\begin{aligned} \beta &= 0^\circ : 5^\circ : 90^\circ, \\ c_{\text{Hb}} &= (290 : 15 : 395) \text{ g L}^{-1}, \\ D &= (5.4 : 0.4 : 10.2) \mu\text{m}. \end{aligned}$$

The latter corresponds to RBC volumes V between 49 fL and 169 fL. A wider range for the orientation angle β is not necessary due to the mirror symmetries of the shape model. The density of these grid points was chosen such that intermediate values of the FSC can be quickly computed by cubic spline interpolation. We denote this interpolant by the function $g(V, \beta, c_{\text{Hb}})$.

For a fixed size ($D = 7.6 \mu\text{m}$ or $V = 91.5$ fL) and concentration ($c_{\text{Hb}} = 335 \text{ g L}^{-1}$), the angular dependence of the FSC $g(\beta)$ was computed for elongation factors $f_x = 1.75 : 0.25 : 3$. The result is shown in Fig. 6.9. Histograms were sampled by generating pseudorandom uniformly distributed orientations β as described below. The best agreement between simulation and experiment was found for $f_x = 2.25$. Hence the full database, accounting for polydispersity, was computed for $g(V, \beta, c_{\text{Hb}})$ with $f_x = 2.25$.

6.4.5 Propagation of probability distributions

While the optical simulations yield a function for the FSC in dependence on the model parameters, the observable in the experiment is a (one- or two-dimensional) histogram of FSC values. The corresponding quantity in the theoretical model is the probability distribution function (pdf) of the FSC. In order to compute it, the pdfs of the input parameters V, β, c_{Hb} need to be propagated through the nonlinear function g . If one is dealing with scalar random variables, where the pdf p_x of the random variable x is given and one wants to know the pdf p_y of $y = g(x)$, this change of variables can be done analytically using the expression

$$p_y(y) = \left| \frac{d}{dy} g^{-1}(y) \right| p_x(g^{-1}(y)) \quad (6.27)$$

for functions $g(x)$ that are monotonic and can be uniquely inverted, or the corresponding expression for non-monotonous functions, where the right hand side of

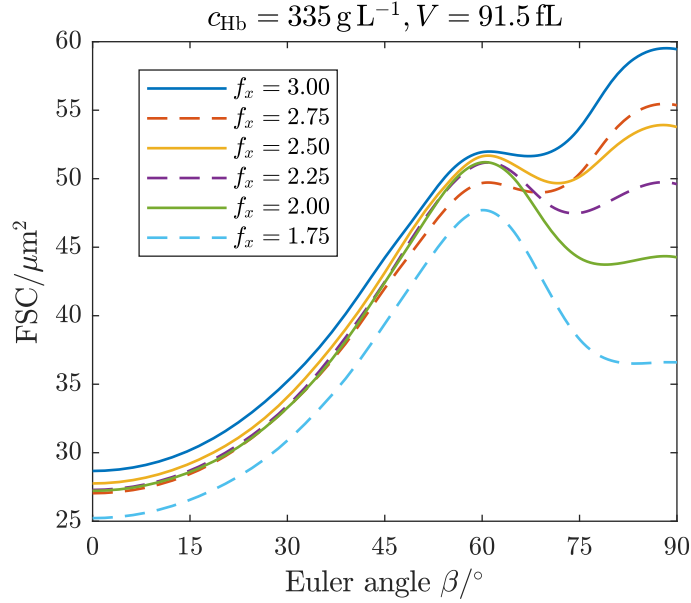


Figure 6.9: Dependence of the simulated FSC on orientation angle β and elongation factor f_x for fixed volume and Hb concentration

the above equation is summed over all solutions fulfilling $g(x) = y$. However, this method can not be easily transferred to higher dimensions. Hence the change of variables for the pdfs was achieved by a direct sampling Monte Carlo (MC) technique. $N_{\text{MC}} = 10^5$ triples of pseudorandom numbers were drawn for $(V, \beta, c_{\text{Hb}})$ from their respective distributions. A uniform distribution was assumed for β , a normal one for c_{Hb} and a log-normal distribution for V , compare section 4.4.1 of chapter 4. The distribution parameters for c_{Hb} and V are given in Tab. 6.1. The FSC was computed for each of the N_{MC} triples, i. e., $y^j = g(V^j, \beta^j, c_{\text{Hb}}^j)$, $j = 1, \dots, N_{\text{MC}}$. The pdf $p_y(y)$ for discrete values $y = y_\nu$, $\nu = 1, \dots, N_{\text{bins}}$ is then approximated by a histogram of the MC samples $\{y^j\}_{j=1}^{N_{\text{MC}}}$, with appropriate normalization. If the number of grid points is chosen appropriately (e. g., $N_{\text{bins}} = 60$ was used for calibration, see below), then the pdf $p_y(y)$ at intermediate values can be computed by interpolation. The pdfs thus computed were used for calibration of the FSC-axes (see next subsection).

To model the 2-direction FSC measurements, one sets

$$\text{FSC}(\vec{k}_1) = x^j = g(V^j, \beta^j, c_{\text{Hb}}^j) \quad \text{and} \quad \text{FSC}(\vec{k}_2) = y^j = g(V^j, 90^\circ - \beta^j, c_{\text{Hb}}^j) \quad (6.28)$$

for each random parameter triple and the pdfs of x and y follow accordingly. The joint pdf $p_{xy}(x, y)$ could be computed in the same manner, but this function is actually not required here since the comparison with measurements will be made based on 2D dot plots. In this case, instead of computing a smooth pdf, detector noise was mimicked by adding independent normally distributed pseudorandom numbers of zero mean and $0.5 \mu\text{m}^2$ standard deviation to the MC samples for the FSC. This yields a list of data that can be treated and plotted just like experimental data. Density-colored scatter plots were created with the `dscatter` function of the FACS Matlab package [126].

6.4.6 Axes calibration

Calibration of the FSC-axes to obtain absolute values in μm^2 was performed by comparing measurements of the forward-scattered intensity of isovolumetrically sphered

RBCs (see section 6.2.3) to forward scattering cross sections according to Mie scattering computations. Plane wave incidence was assumed. The RIs, hematological parameters (see Tab. 6.1) and the MC sampling method for extracting probability distributions were the same as used for the DDA simulations described above. The conversion factor between the channel number of the ADC, which records the (linearly-amplified) signal of the PMTs, proportional to scattered intensity, and absolute cross section is set by numerical optimization such that the scalar product between the measured and simulated frequency/probability distributions becomes maximal.

For Mie scattering, the Mueller matrix elements read [61]

$$M_{11} = \frac{1}{2} (|S_2|^2 + |S_1|^2), \quad (6.29)$$

$$M_{12} = \frac{1}{2} (|S_2|^2 - |S_1|^2), \quad (6.30)$$

$$M_{13} = 0, \quad (6.31)$$

where S_2 and S_1 are the diagonal elements of the (2×2 complex) amplitude scattering matrix that depend only on ϑ , compare section 2.2.1 of chapter 2. Hence one obtains for the circular beam stop used in the 1-direction FSC measurements

$$\begin{aligned} \text{FSC}_{\text{circle}}^{\text{Mie}} &= \frac{1}{k_m^2} \int_{\vartheta_1}^{\vartheta_2} \int_0^{2\pi} [M_{11}(\vartheta) + M_{12}(\vartheta) \cos 2\varphi] d\varphi \sin \vartheta d\vartheta \\ &= \frac{2\pi}{k_m^2} \int_{\vartheta_1}^{\vartheta_2} M_{11}(\vartheta) \sin \vartheta d\vartheta. \end{aligned} \quad (6.32)$$

For the stripe-shaped beam stop along the x -direction used in the 2-direction measurements, one obtains

$$\text{FSC}_{\text{stripe}}^{\text{Mie}} = \frac{2}{k_m^2} \int_{\vartheta_3}^{\vartheta_4} \{M_{11}(\vartheta) [\pi - 2\Phi(\vartheta)] - M_{12}(\vartheta) \sin[\Phi(\vartheta)]\} \sin \vartheta d\vartheta, \quad (6.33)$$

where $\Phi(\vartheta) := \arcsin(\vartheta_3/\vartheta)$. For both cases, the ϑ integration can be carried out numerically.

In the following, the random variable y denotes the forward scattering cross section. The above Eq. (6.32) and Eq. (6.33) allow to compute the FSC of sphered RBCs as a function of cell volume V and Hb concentration c_{Hb} , which is denoted by $y = g(V, c_{\text{Hb}})$. As described above, by MC sampling of V and c_{Hb} , one can compute the corresponding pdf of the cross sections $p_y^{\text{Mie}}(y)$. The corresponding measured signal is a histogram for the channels $j = 0, 1, \dots, N-1$ of the ADC with counts $h_0, \dots, h_{N-1} \in \mathbb{N}_0$. The channel numbers linearly correspond to intensities or scattering cross sections, i. e.,

$$y_j = q j, \quad (6.34)$$

however the calibration factor q is unknown. If there are M total events in the measurement, the normalized histogram that can be compared to the simulated pdf to determine the calibration factor q is

$$p_y^{\text{exp}}(y_j) = \frac{1}{M q} h_j. \quad (6.35)$$

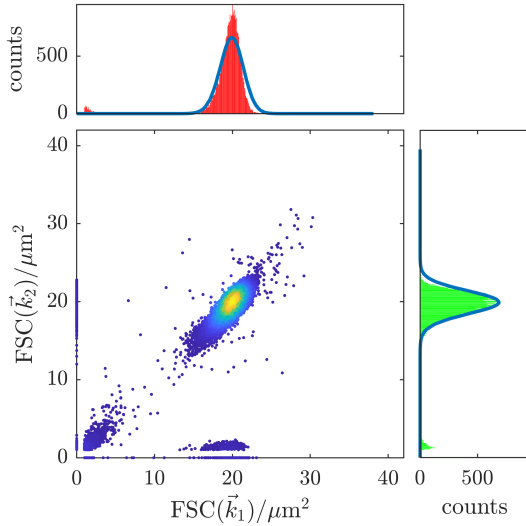


Figure 6.10: Calibration of FSC axes using sphered RBCs and Mie theory. The solid lines indicate the simulated probability distributions (normalized to the number of counts). Both axes were calibrated independently.

632.8 nm used different apertures and beams stops, the calibration was performed for both cases separately. An example of this calibration procedure is shown in Fig. 6.10.

6.5 Results

6.5.1 Comparison between measurements and simulations

Results for the simulated dependence of the FSC on β for varying stretching factor $f_x = 1.75, \dots, 3$ of monodisperse samples (i. e., constant RBC volume V and Hb concentration c_{Hb}) were already shown in Fig. 6.9. While such curves are computed relatively easily from simulation data, the dependence of the FSC on β cannot be obtained from the experiment since the orientation of an individual cell is not known. However, these simulated curves may help to understand why and under which conditions a bimodal distribution is observed in the FSC histograms. Since all angles β are equally likely, i. e., the pdf of β is a constant, according to the rule for change of (scalar) variables in probability densities, Eq. (6.27), a maximum in the pdf of $\text{FSC} = g(\beta)$, or equivalently in the FSC histograms (1D or 2D), occurs whenever the derivative $dg(\beta)/d\beta$ is low, i. e., near the extrema of the curves in Fig. 6.9. As can be seen, all curves have a minimum at $\beta = 0$ and at least one maximum at higher angles. For high stretching factors f_x , the curves are almost monotonically increasing, which then effectively leads to a bimodal distributions for the FSC – one peak for the minimum of $g(\beta)$ and one peak for the maximum (or several maxima of similar height). For lower stretching f_x , a pronounced intermediate maximum at $\beta \approx 60^\circ$ is developed, which then results in multimodal histograms for the FSC, and possibly very intricate shapes for the 2D FSC histograms. However, the curves in Fig. 6.9 do not give the full picture, for which polydispersity

The conversion factor q between channel number of the ADC and absolute cross section is now determined by numerical optimization such that the scalar product between the normalized pdfs of measurement and simulation becomes maximal

$$\begin{aligned} & \int_0^\infty p_y^{\text{Mie}}(y) p_y^{\text{exp}}(y) dy \\ & \approx \sum_{j=0}^{N-1} p_y^{\text{Mie}}(y_j) p_y^{\text{exp}}(y_j) q \\ & = \frac{1}{M} \sum_{j=0}^{N-1} p_y^{\text{Mie}}(q j) h_j \rightarrow \max. \end{aligned} \quad (6.36)$$

Numerically, this was done using `fminsearch` in Matlab (Matlab R2018a, The MathWorks, Inc.).

This axis calibration was performed for each of the four laser wavelengths separately. Since the 1-direction and 2-direction FSC measurements at $\lambda =$

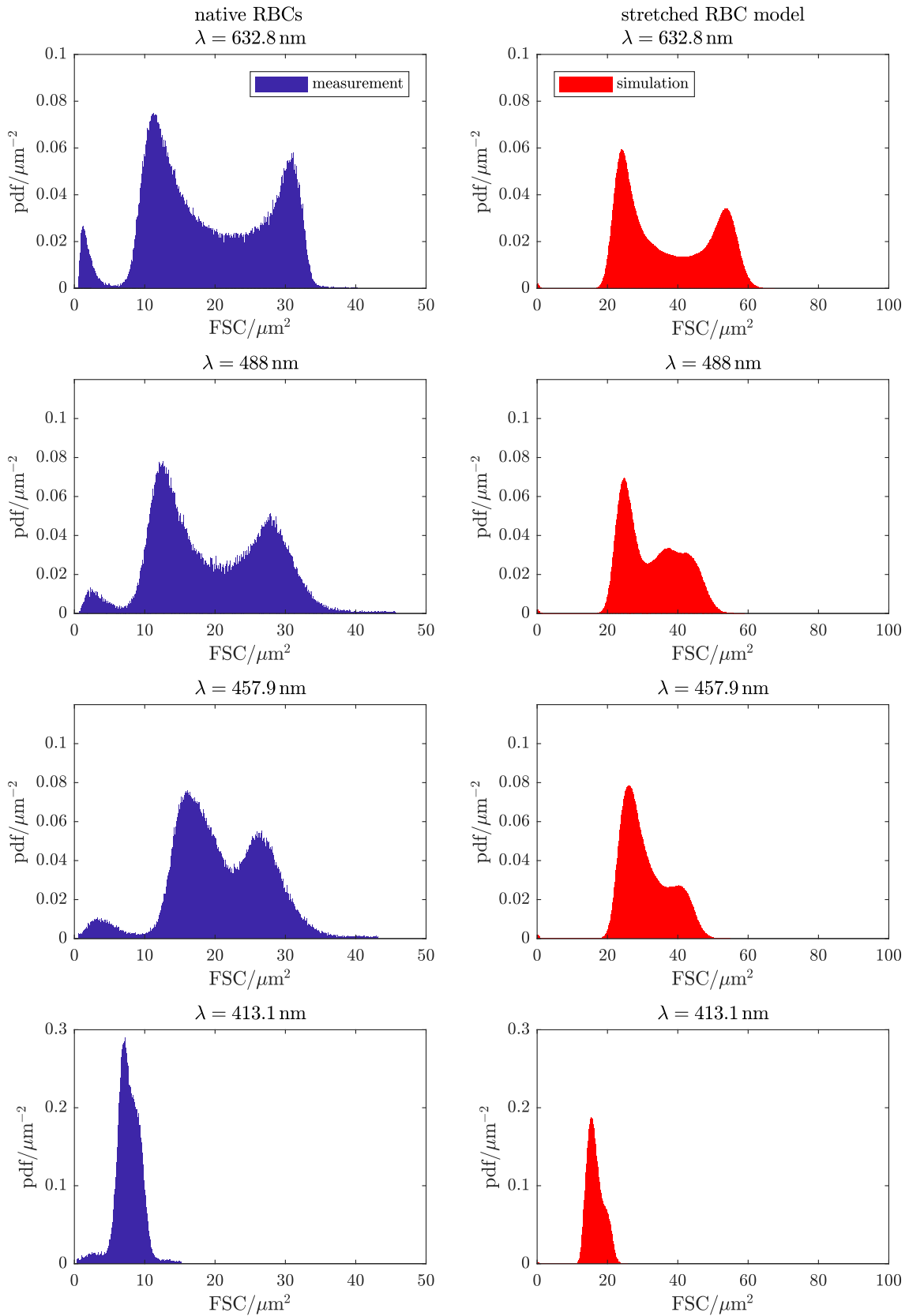


Figure 6.11: Comparison between measurements and simulations of the FSC ($3.3^\circ \leq \vartheta \leq 17.4^\circ$) at four different laser vacuum wavelengths λ . The y -axes show the probability density function. The simulated pdfs were smoothed using the $0.5 \mu\text{m}^2$ Gaussian noise that was also applied to the simulated 2D histograms.

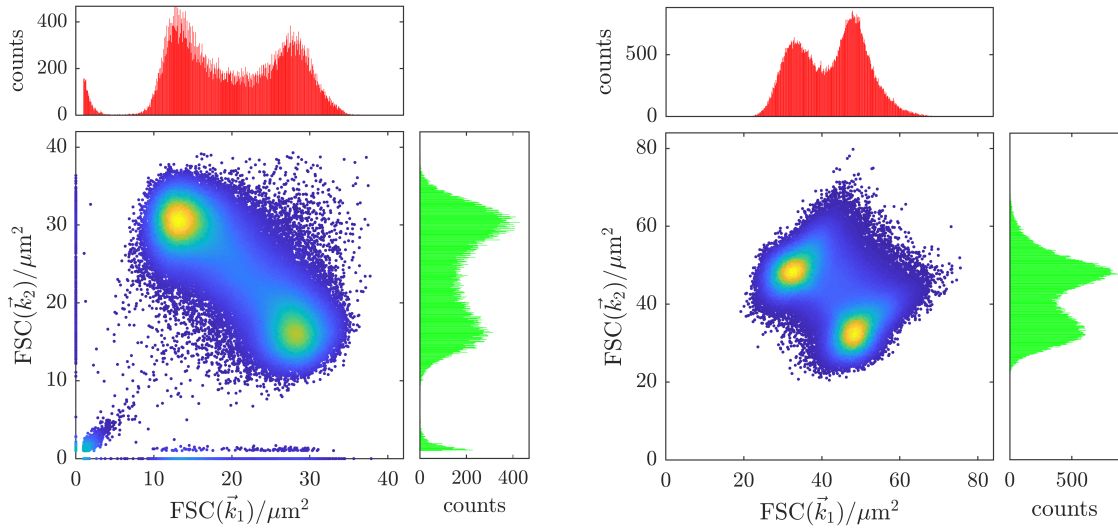


Figure 6.12: Measurement data (left) and simulation (right) of the 2-direction FSC for native RBCs. The simulation was performed using the stretched shape model and the hematological parameters from the CBC (Tab. 6.1). The orientation angle β is uniformly distributed, i. e., $\beta \in \mathcal{U}(-90^\circ, 90^\circ)$.

needs to be considered. If simulations of the 2-direction FSC histograms are performed with monodisperse ensembles, in the 2D plots one sees clearly drawn lines instead of point clouds and sharp peaks instead of broad ones in the corresponding 1D histograms. The effects of variable cell size and variable intracellular Hb concentration (i. e., variable RI) turn out to have effects of similar magnitude in “smearing out” these curves. These distributions were taken into account in the following and a fixed stretching factor $f_x = 2.25$ was used.

Fig. 6.11 shows measurements of FSC histograms with one incident laser beam at vacuum wavelengths $\lambda = 413.1$ nm, 457.9 nm, 488 nm and 632.8 nm in comparison with simulation data obtained with the stretched shape model. At $\lambda = 632.8$ nm, bimodal histograms occur in both, experiment² and simulation and qualitatively, the agreement between the two is good. However, even though the FSC axis was calibrated using measurements of sphered RBCs and Mie scattering computations, there is a significant deviation of the absolute FSC scales, by about a factor two. However, this deviation can be explained by the model assumptions made. This will be discussed in detail in section 6.5.2. As the laser wavelength is decreased from 632.8 nm down to 413.1 nm, the imaginary part of the RI of the RBCs increases, i. e., they become

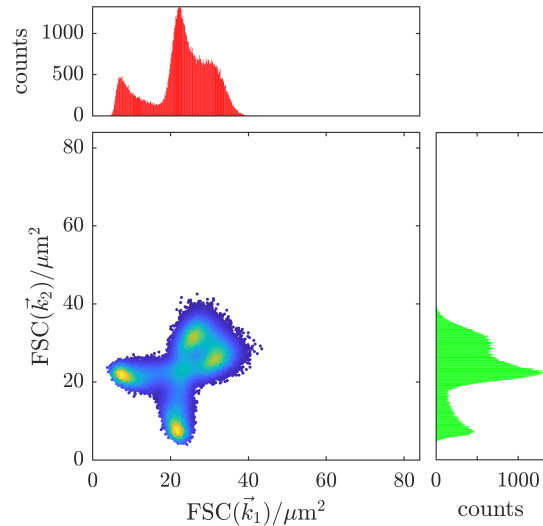


Figure 6.13: Simulation of the 2-direction FSC in Fig. 6.12 using the undeformed, axisymmetric shape model and the hematological parameters from the CBC

² The peak at very low FSC in the experimental data is due to blood platelets in the sample.

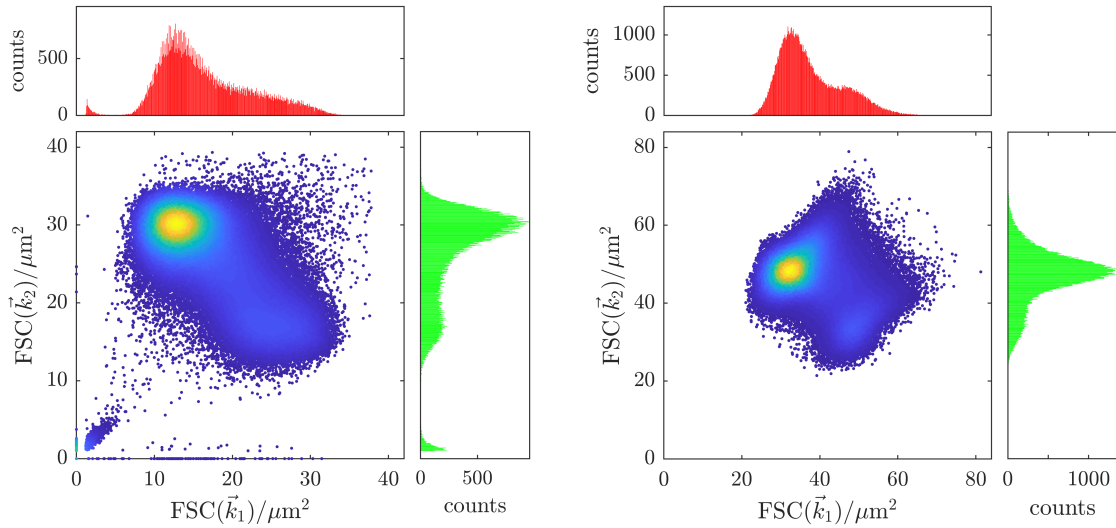


Figure 6.14: Measurement data (left) and simulation (right) of the 2-direction FSC for native RBCs injected through a flattened capillary resulting in preferential orientation face-on to \vec{k}_1 . Simulation as in Fig. 6.12, but with β normally distributed around \vec{k}_1 , i. e., $\beta \in \mathcal{N}(0, 36^\circ)$.

significantly absorbing. The result is a decrease of both, the inter-peak distance and the height of the high-FSC peak. At 413.1 nm the distribution is very narrow and unimodal with only a slight shoulder remaining of the high-FSC peak. These tendencies are reproduced in the simulations, however, quantitative agreement is not achieved. Note that the same shape model was used for all wavelengths. The parameters of the shape model were tuned by hand until the simulations agreed qualitatively with the measurement data at 632.8 nm, but no attempt was made for mathematical optimization. The RBC volume and intracellular Hb concentration was sampled according to the hematological parameters of the blood sample and the Hb concentration-dependent RI dispersion of RBCs was considered according to the results of chapter 3.

The 1D histograms contain no direct evidence to support the assumption that the RBCs are oriented with their symmetry axis (before deformation) perpendicular to the flow. This assumption can be tested using the 2D histograms for FSC measurements with two perpendicular laser beams at 632.8 nm. Fig. 6.12 shows scatter plots of $x = FSC(\vec{k}_1)$ vs. $y = FSC(\vec{k}_2)$ with marginal histograms of x and y individually. Calibrated measurement data is compared to simulations. The measurement data exhibit a bimodal distribution, which (in 2D) lies on a cross diagonal ($y = \text{const} - x$) of the plot. The latter indicates that the RBCs are oriented in a way, where they are asymmetric with respect to the direction of flow. If the RBCs were oriented with their rotational axis aligned to the flow, as it occurs, e. g., in microfluidic flows [128, 132, 133], or in any other way symmetric around the flow axis, they would “look the same” from both directions \vec{k}_1 and \vec{k}_2 . This would result in a 2D histogram located on the main diagonal ($y = x$) of the plot as observed for spheroid RBCs (Fig. 6.10). The symmetry between the upper and lower triangle of the plot is, however, not perfect, indicating a slight preference for cell orientation face-on to \vec{k}_1 . This may be caused by imperfections or asymmetries of the flow cell or the sample injection capillary of the flow cytometer. Another possible explanation are slight differences in the detector apertures of the two laser beam paths, e. g., caused by

variation of the beam stop's position. Similar to the 1D case, the simulated scatter plot reproduces the qualitative features of the experiment (cross-diagonal, bimodal 2D distribution) well, but the absolute FSC values deviate significantly.³ If, on the other hand, the non-stretched, axisymmetric shape model is used in the simulation, the results look very different from the experiment, even qualitatively. This is shown in Fig. 6.13. Rather than describing a bimodal distribution, the maxima of the 2D FSC plot form a “loop”. Projected to the 1D histograms this results in a trimodal distribution.

The cross-diagonal character of the 2D measurements already indicates that bimodality is a result of random orientation of the cells, described by angle β . Experimentally, this was investigated further by measurements where the steel capillary used for injecting the RBCs into the cytometer was flattened to an oval cross section measuring 20 μm along the narrow direction. This results in predominant orientation of the cells along $\beta = 0^\circ$, or face on to \vec{k}_1 . The corresponding measurement data and simulations are shown in Fig. 6.14. A pronounced asymmetry occurs now between the formerly symmetric peaks: The peak with low FSC(\vec{k}_1) and high FSC(\vec{k}_2) remains almost unaffected whereas the high-FSC(\vec{k}_1)/low-FSC(\vec{k}_2) peak is suppressed. In the simulations, this effect is reproduced if the orientation angle β is sampled from a normal distribution $\beta \in \mathcal{N}(0, 36^\circ)$ instead of a uniform distribution $\beta \in \mathcal{U}(-90^\circ, 90^\circ)$.

6.5.2 Influence of laser beam shape

As mentioned before, the most significant difference between simulated and measured FSCs is a deviation by about a factor 2, with otherwise qualitative agreement of the histograms. This deviation can be explained by the assumption made in the simulations of the incident laser beam being a plane wave. In the cytometric setup, the incident beam is shaped to an elliptical focus with semi-axes (e^{-2} points of intensity) $w_{0\perp} = 21 \mu\text{m}$ perpendicular to the flow direction and $w_{0\parallel} = 5 \mu\text{m}$ along the flow direction. The hydrodynamic focusing ensures that the sample stream is centered in the focal ellipse along the long axis. The RBCs can be assumed to be centered in the light focus also in the other direction, because the measurement signals are proportional to the pulse heights of the scattered intensities, corresponding to the moment when the RBC is right at the center of the focal ellipse. For the sphered RBCs of approximately 5.6 μm diameter for which the calibration of the FSC-axis was performed, and which are smaller than the elliptical beam focus, this causes only little variation of the incident electric field \mathbf{E}^i : it varies across the sphered cell between $e^{-(2.8 \mu\text{m}/5 \mu\text{m})^2} = 69\%$ and 100% of the maximum. With the stretching factor $f_x = 2.25$, the deformed cells on the other hand reach lengths of around 17 μm such that the incident electric field at the tips is only $e^{-(8.5 \mu\text{m}/5 \mu\text{m})^2} = 5\%$ of the amplitude at the center. In other words: Much less cell mass is in the beam focus for stretched RBCs than for sphered ones. The result is a lower scattering cross section for the former when an elliptical beam is used instead of a plane wave. The impact on the FSC was estimated performing additional simulations with circular Gaussian laser beams (as readily available in ADDA 1.2) of waist radii $w_0 \in [5, 30] \mu\text{m}$ at a fixed $c_{\text{Hb}} = 335 \text{ g L}^{-1}$. Results of these computations are shown in Fig. 6.15

³ The microscope objectives in the 2-direction forward scatter measurements have a lower numerical aperture than the ones in the 1-direction measurements and the beam stops are different. Hence, the absolute FSC values differ from the measurements at $\lambda = 632.8 \text{ nm}$ discussed above.

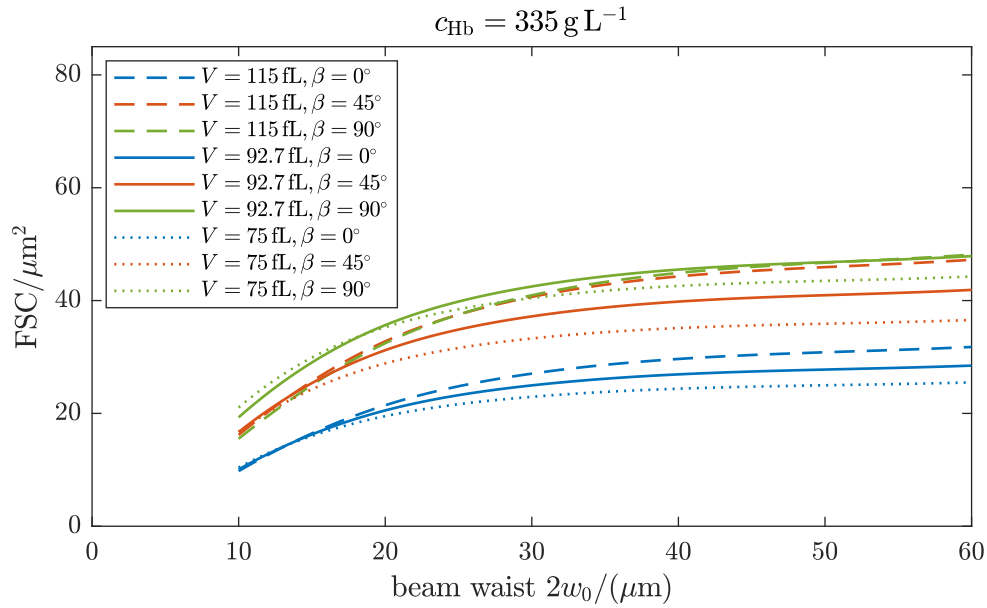


Figure 6.15: Dependence of the FSC of the stretched shape model on the waist diameter $2w_0$ of a Gaussian beam for three different RBC volumes and orientations at fixed Hb concentration. A plane wave corresponds to $w_0 \rightarrow \infty$.

for selected RBC volumes V and orientations β . As expected, the main effect of the Gaussian beam compared to the plane wave is to reduce the FSC in total with decreasing beam waist. Apart from this, the general shape of the function $g(V, \beta)$ does not change drastically with beam waist. An elliptical Gaussian beam [144], that could also be used for \mathbf{E}^i in the DDA simulations, is expected to have a similar effect with a magnitude somewhere in between the cases of $w_0 = w_{0\parallel} = 5 \mu\text{m}$ and $w_0 = w_{0\perp} = 21 \mu\text{m}$. Hence simulations with a realistic Gaussian beam are expected to yield very similar qualitative agreement with the measurements, while at the same time providing better quantitative agreement for the absolute values of the FSC.

6.6 Summary and Discussion

In this chapter, the distribution of forward light scattering cross sections of native RBCs in a flow cytometer were modeled and simulated. The experimentally measured bimodal distributions of the FSC were explained by a combination of random orientation of the RBCs around the flow axis and deformation due to sheath fluid velocity gradients. The velocity gradients in the cytometer were estimated using analytical solutions for fully developed pipe flow and a consideration of the average velocity in the conical part of the flow cell. It was found that the longitudinal gradients right after sample injection are much higher than the transverse gradients in the flow channel of constant cross section $250 \mu\text{m} \times 250 \mu\text{m}$, where cell velocities are about 7m s^{-1} . A comparison to hydrodynamic deformation of RBCs in the literature was made.

The discrete dipole approximation was applied to calculate the Mueller matrix and the FSC of the RBCs in dependence on different shapes, orientations and Hb concentrations. A simple extension of an existing RBC shape model [142] was proposed, in which the axisymmetric equilibrium shape (with figure axis perpendicular

to the flow) is linearly stretched along the flow direction and compressed perpendicular to it. Furthermore, we accounted for the fact that intracellular Hb concentration c_{Hb} varies within the RBC population even of a single person by several percent (HDW = 5% for the blood sample examined) and consequently the RI varies from cell to cell, depending linearly on c_{Hb} . Even though not perfect, FSC histograms computed with the proposed shape model and using independently measured hematological parameters (MCV, RDW and MCHC) are in good qualitative agreement with measurements of the 1D and 2D FSC. The remaining deviation of the absolute FSC values can be explained by the laser beams in the experiment having a finite, elliptical focus, in contrast to the plane waves assumed in the simulation. No such agreement between simulation and experiment is obtained with the unstretched, axisymmetric shape model for RBCs at rest. This indicates that significant deformation of native human RBCs occurs during measurement in the flow cytometer which can be attributed to the hydrodynamic forces present in the cytometer's flow cell. As a side note, axisymmetric shape models have been used in many simulation studies in the context of RBCs in flow cytometry [27, 145–147]. Depending on the hydrodynamic parameters in the particular cytometers used, deformations may need to be included in the corresponding optical modeling.

Since the estimated extensional strain of the fluid flow is higher than the shear strain, the deformation of the RBCs was attributed to the former. The extensional stress upon injection of the RBC sample into flow channel was estimated to peak at about $\sigma_{e,\text{max}} \approx 33$ Pa. This is of the same order of magnitude as the highest extensional stresses applied to RBCs in experiments by Lee et al. [138] ($\sigma_e \in [0.1, 13]$ Pa) and Yaginuma et al. [139] ($\sigma_e \in [0.4, 16.5]$ Pa), which can thus serve for a plausibility check of the ad hoc shape model for deformed RBCs proposed here.

Firstly, this shape model is consistent with the elliptical deformation of RBCs in homogeneous extensional flow reported in Refs. 138, 139. In the analysis of those experiments, a *deformation index* $\text{DI} = (X - Y)/(X + Y)$ was employed, where X and Y are the long and short axis of the RBC, respectively, as seen in a light microscope. The relation to the stretching parameter f_x in the present shape model is

$$\text{DI} = \frac{f_x - 1/\sqrt{f_x}}{f_x + 1/\sqrt{f_x}}. \quad (6.37)$$

Lee et al. [138] reported $\text{DI} \approx 0.6$ for stresses $\sigma_e = 10$ Pa which corresponds to $f_x = 2.52$. This deformation is comparable to the value of $f_x = 2.25$ (or $\text{DI} = 0.54$) for which best agreement of simulation and FSC measurement was found here, however at a higher maximum stress. Hence, one could expect a stronger deformation. On the other hand, Yaginuma et al. reported lower deformation $\text{DI} \approx 0.35$ (corresponding to $f_x = 1.63$) for higher stresses than Lee et al. of $\sigma_e = 16.5$ Pa.

The different deformation indices might be explained by the different passage times of the RBCs through the converging part of the flow cell or flow channel. In the cytometer considered here, the RBCs take an estimated 23 ms to get through the conical part of the flow cell and the extensional stress $\sigma_e(t) \leq \sigma_{e,\text{max}}$ increases as they flow. In the two previously mentioned experiments, the RBCs took about 200 ms [138] and 2.5 ms [139] to go through the hyperbolic converging channels, at the respective highest reported extensional stresses, experiencing constant extensional stress. Since the viscoelastic relaxation times of stretched RBCs (100 ms–250 ms [140, 141]) are comparable or longer than these times, the measured deformation may not be fully developed and the DI's reported can only be compared to

limited extent. Considering this, the stretching factor f_x required here to explain the experimental data appears consistent (or at least not in contradiction) to the directly measured deformations of RBCs in homogeneous extensional flows [138, 139]. Hence, we conclude that the measured RBC shape in the optical flow cytometer is an impression of the extensional stresses occurring further upstream during hydrodynamic focusing and not so much a steady state shape caused by the laminar flow profile in the narrow flow channel.

By comparison between measurements and simulations, it was demonstrated that the occurrence of bimodal FSC histograms in optical flow cytometry is a combined effect of random orientation angle β of the RBCs relative to the laser and their deformed shape due to hydrodynamic forces. It was also demonstrated that a preferential orientation can be imposed by using flattened injection capillary with an oval inner cross section instead of a circular one. From the simulations for varying stretching factor (Fig. 6.9) it is evident that selecting the appropriate observation angle β allows to measure FSC signals that are either very sensitive ($\beta \approx 90^\circ$) or insensitive ($|\beta| < 60^\circ$) to hydrodynamic stretching. Hence, this kind of simulation can serve to guide future experimental designs, e. g., for finding empirical measures of RBC shapes and pathologies from FSC histograms [118, 119].

Even though a quasi-exact numerical solver for the electromagnetic scattering problem was employed, the agreement between simulation and measurement remains only qualitative. In order to quantitatively analyze FSC histograms of native RBCs, the mathematical model would need to be refined: Firstly, the use of elliptical Gaussian beams [144] is expected to bring the absolute FSC values of experiment and simulation into agreement. More importantly, a shape model that reflects the actual mechanical processes in the cell is required, particularly if elastic parameters of the cells are to be determined by standard flow cytometry. The proposed *ad hoc* shape model for deformed RBCs has some unrealistic properties. For example, it is known that the RBC volume and surface area remain quasi-constant during deformation of the cell [127]. While the distribution of RBC volumes was measured independently in a CBC and sampled accordingly in the simulations, the surface areas of the RBCs in the blood sample are unknown. However, the correlation between volume and surface area reported in the literature suggest that an average RBC in the blood sample considered here (92.7 fL volume) should have a surface area of about $125 \mu\text{m}^2$ [148]. The deformed shape model predicts a surface area of $169 \mu\text{m}^2$, which is not plausible. A more realistic description of the shape could possibly be found by simulations using mathematical models for the viscoelastic behavior of RBCs in fluid flows [19, 127, 128]. A combined approach involving both, accurate optical and cell mechanical simulations could allow to extract quantitative elastic information about cells using high throughput flow cytometers that are already present in many laboratories.

Summary

In this thesis, we considered problems related to the quantitative modeling of light scattering by human red blood cells (RBCs) and analyzed measurements of RBCs and artificial microparticles with extinction spectroscopy as well as flow cytometry, which shall now be summarized.

Chapter 1

In chapter 1, an introduction was given to RBCs, regarding their structure and them routinely being measured with optical flow cytometry in laboratory medicine. We further discussed how their complex refractive index (RI) provides the contrast in light scattering measurements. The complex RI of the liquid cytoplasm of RBCs, making up the vast majority of the cell volume, is linearly dependent on the intracellular concentration c_{Hb} of hemoglobin (Hb) according to

$$\mathbf{n}(\lambda) = n_{\text{H}_2\text{O}}(\lambda) + c_{\text{Hb}}[\alpha(\lambda) + i\gamma(\lambda)].$$

While the imaginary RI increment $\gamma(\lambda)$ is well known, strong discrepancies are present in the literature values for the real part of the RI increment $\alpha(\lambda)$. These hamper a true quantitative analysis of RBC light scattering measurements. Hence, one important problem tackled in this thesis was the accurate determination of the RI increment of RBCs.

Chapter 2

In chapter 2, we considered the theoretical foundations of light scattering problems as well as the numerical solution methods employed in this thesis. The scalar and vector Helmholtz equations for the electric and magnetic field were derived from the Maxwell equations for time-harmonic fields. The Helmholtz equation $\Delta\mathbf{E} + \mathbf{n}^2 k^2 \mathbf{E} = 0$ is the governing equation for the light scattering by RBCs, which – due to their particularly simple structure – can be modeled as optically homogeneous dielectric particles. We introduced vector spherical wavefunctions (VSWFs), which can be used for solving the Helmholtz equation for homogeneous scatterers by separation of variables. The basics of the T -matrix method for the numerical solution of scattering problems, which consists in a representation of the incident and scattered fields in VSWFs were briefly outlined. Afterwards, we went through the most important steps in the derivation of the Mie solution for a spherical scatterer. For more general scatterers, we discussed the concept of the discrete dipole approximation (DDA), which is based on the volume-integral formulation of the vector Helmholtz equation $-\nabla \times \nabla \times \mathbf{E} + \mathbf{n}^2 k^2 \mathbf{E} = 0$. By volume discretization of the scatterer, approximation of the field inside the grid cells and careful treatment of the singularities for the Green's function of the differential operator $\nabla \times \nabla \times \mathbb{1} - k_{\text{m}}^2$, the integral equation

is converted to a system of linear equations with three equations for every grid cell. Typically, for scattering of visible light by RBCs, the number of grid cells are in the hundred thousands to over a million.

Chapter 3

In chapter 3, the real RI increment $\alpha(\lambda)$ of different Hb variants in aqueous solutions was computed from literature spectra of the imaginary RI increment $\gamma(\lambda)$ for the wavelength range $\lambda \in [228, 1100]$ nm using Kramers-Kronig (KK) relations. We discussed that KK relations arise for any linear response function under the only requirement of a causal behavior of the system. Furthermore we discussed the symmetry implications of the commonly used form of these relation for the complex RI. Analytical transformations for three exemplary absorption spectra were calculated – a δ -peak, a rectangle peak and a Lorentzian peak – to give an impression of the implications of the KK relations for the complex RI.

For an application of the KK relations to Hb solutions, we formally separated the imaginary RI into a water and a Hb part, of which the former results in the well-known real RI of water after KK transformation. Hence, only the Hb part needs to be transformed numerically to obtain the real RI increment $\alpha(\lambda)$. The literature absorption spectra [37, 39, 72] do not resolve the strong deep UV absorbance of Hb's peptide-backbone, which was thus supplemented by a Lorentzian line of unknown amplitude, located at 187 nm [74]. In addition, a δ -peak at zero wavelength was introduced that accounts for extreme UV absorbance. The amplitudes of these peaks are free parameters of the model. They were determined by a linear least-squares fit to an independently measured reference curve for the real RI increment $\alpha_{\text{meas}}(\lambda)$. Hence, an analysis using KK relations cannot resolve the discrepancies between the existing measurement data for the real RI increment of Hb and RBCs with respect to their absolute value, but it can serve as a consistency check. Two different datasets were considered for this parameter fitting: (1) The real RI increment data measured by Friebel and Meinke [38] using reflectance spectroscopy on extracted RBC cytoplasm and (2) the real RI increment data determined in chapter 4 of this thesis from the extinction spectra of suspensions of intact sphered RBCs. Both datasets are for oxygenated Hb (oxyHb). The fit to the data of Friebel and Meinke [38] results in significant discrepancies, indicating that these data may be incorrect. In contrast, the independent measurement results of chapter 4 were found to be in very good agreement with the KK analysis and were used in the following KK analysis of different Hb variants.

We then discussed the improvements of the present analysis method over KK approaches previously discussed in the literature by other authors [68, 69]. Afterwards, the KK analysis was applied to spectra of deoxygenated Hb (deoxyHb) and the non-functional methemoglobin (metHb) variant to yield their real RI increments. To this end, we employed the deep UV model parameters obtained from the analysis of oxyHb. Since, in contrast to oxyHb, no measurements of the real RI increment exist for deoxyHb and metHb, the KK analysis provides an important tool to make such information available with relatively easily.

Chapter 4

Chapter 4 dealt with the analysis of extinction spectra of spherical microparticles and cells in order to determine their RI by solving an inverse problem. The aim

was to determine the real RI increment of isovolumetrically sphered, intact RBCs. But first, the method was evaluated using synthetic polystyrene (PS) microbeads. We briefly discussed the concept of the extinction cross section of a light-scattering particle, describing the combined effects of scattering and absorption, as well as the corresponding mathematical expression for the Mie solution for a spherical scatterer. It was further explained how a spectrum of the ensemble-averaged extinction cross section $\overline{C}_{\text{ext}}(\lambda)$ can be determined from collimated transmittance measurements of dilute cell or particle suspensions. A mathematical model for this measurement quantity was formulated based on a numerical implementation of Mie scattering, averages over the distributions of size and – in the case of RBCs – intracellular Hb concentration of the polydisperse ensemble of microparticles or cells. The sensitivity of this forward model to the size and optical properties was discussed.

We then turned to the problem of inferring the particle RI (or RI increment) from such measurement data. For PS microbeads as an example, we discussed that a pointwise inference for all wavelengths separately under the assumption of a known size distribution is problematic due to instabilities with respect to errors of the particle size. To overcome these issues and reduce the number of parameters representing the ensemble of scatterers, an expression of the real particle RI $n(\lambda)$ or the real RI increment of the RBCs $\alpha(\lambda)$ with a relatively small set of suitable basis functions was discussed, namely Lorentz-type resonances (LTRs) and third-order cardinal splines. This was used to implement a mathematical forward model for the measured cross sections which can furthermore compensate errors of the particle or cell concentration in the suspensions. The data analysis method then consists in applying nonlinear least-squares optimization to fit the L model parameters to the N measurement data points. For the cases discussed, we had $N \approx 1800$ data points and between $L = 23$ (for PS using LTRs) and $L = 89$ (for RBCs using splines) model parameters. Uncertainties of the results can be estimated using linearized propagation of covariance matrices of the measurement data.

For the benchmark case of PS beads suspended in water, the retrieved particle RI agreed to within about 3×10^{-3} with literature values for bulk PS [79]. However, it was found that the estimated uncertainties of the RI result thus obtained were too small and could not explain the differences to the literature values quantitatively. As we discussed, this is most likely an indicator of an insufficient model for the uncertainties of the measured spectra, rather than for actual deviations between the RIs of PS in the form of microbeads and of bulk material. The mean diameter of the 2.5 μm PS beads determined from their extinction spectra was well within the uncertainty specified by the manufacturer of the material used. On the other hand, the width of the size distribution, expressed by the coefficient of variation of the diameter, was found to be about 0.5%, which is significantly lower than the specification of 1.4%. It follows that the particles are closer to monodispersity than declared, presumably since the specified distribution widths are estimates of the corresponding upper limit during production.

We then discussed the possibility to determine the RI of an unknown fluid matrix by using particles with known properties as a probe. As a demonstration, the RIs of D-glucose solutions of different concentrations were determined from extinction spectra by suspending in them the same PS particles analyzed before. The accuracy of this kind of RI determination was found to be similar to the determination of the particle RI. The method was also applied to determine the RI increment of the spherizing reagent in which RBCs have to be suspended during measurement. Unfor-

tunately the accuracy was insufficient to resolve the (weak) wavelength dependence of the RI increment of the sphering reagent, hence a wavelength-independent value with appropriate uncertainty was used in the following analysis.

Eventually, the real RI increment $\alpha(\lambda)$ of sphered RBCs was determined from extinction measurements. Due to contact of the samples with air, the RBCs were oxygenated. Blood samples from three different volunteers were analyzed which exhibited strongly different mean corpuscular volumes (MCV) and were selected on purpose to provide some variability in the measurement data. In contrast to the quasi-monodisperse PS beads, which furthermore have a higher RI contrast, the extinction spectra of RBCs did not exhibit a characteristic ripple structure. This made accurate simultaneous determination of size, intracellular Hb concentration and RI increment quasi impossible. As a remedy, the hematological parameters MCHC, MCV and RDW of the blood samples obtained from complete blood counts (CBCs) with hematology analyzers were used for regularization of the least-squares optimization problem. The three curves for $\alpha(\lambda)$ obtained from the three different blood samples agree relatively well, with deviations on the 0.01 mL g^{-1} scale. In contrast to the KK analysis of absorption spectra of Hb solutions, the nonlinear analysis of extinction spectra of sphered RBCs yields absolute values for the real RI increment of Hb solutions and RBCs. The results found in chapter 4 speak in favor of this quantity being around $\alpha \approx 0.22 \text{ mL g}^{-1}$, which is in good agreement with some of the values reported in the literature (having, however, higher uncertainties) [48, 49]. As discussed above, these results are furthermore in very good agreement with the Kramers-Kronig analysis of chapter 3. However, because literature data range from about $\alpha \approx 0.15 \text{ mL g}^{-1}$ to $\alpha \approx 0.27 \text{ mL g}^{-1}$, disagreement of the results presented here is necessarily found with many other sources. Possible explanations for these deviations and the advantages of the method employed in this chapter were discussed. In combination with KK relations (chapter 3), the results of chapter 4 provide accurate values for the RI increment of RBCs and different Hb variants over a wide wavelength range.

Chapter 5

As an application of the results of the previous two chapters, chapter 5 was about the analysis of extinction spectra of hemoglobin microparticles (HbMP). Firstly, we assessed the influence of the non-spherical “peanut shape” of these artificial HbMP on the measured spectra by comparison of spherical and spheroidal shape models. The non-spherical particle shape has only minor effect on the extinction spectra and hence the Mie solution was used for further analysis. We compared measured extinction spectra of HbMP to simulations in order to assess the levels of different Hb variants in the particles. In particular, this allowed to assess the levels of the non-functional metHb variant in untreated particles (30%–40%) and particles whose Hb molecules were converted to metHb by chemical treatment (80%–90%). By comparison between simulations and measurement data for HbMP exposed to air (for oxygenation) and argon (for deoxygenation) reveals their ability to bind and release oxygen ($\text{oxyHb} \leftrightarrow \text{deoxyHb}$), while indicating at the same time the presence of a relatively high level of non-functional Hb.

For a perspective higher accuracy of the determination of the levels of different Hb variants, we discussed possible improvements of the data analysis, including the use of numerical optimization like in chapter 4 and issues with such an approach, which are linked to the simplistic forward model. For a more complete model of

the particle RI it would be necessary to consider a variety of other substances, such as the serum albumin present in the particles, whose optical properties would, however, first need to be determined accurately. Lastly we discussed why the optical properties of Hb molecules in solution might be unsuitable to accurately describe the cross-linked HbMP, in which the protein chains are chemically altered. As a possibility for experimental improvements, measuring the spectral absorption cross section $C_{\text{abs}}(\lambda)$ of the particle suspension was discussed. In principle, the absorption cross section is experimentally accessible by extending the current optical setup with two integrating spheres. In contrast to the extinction cross section $C_{\text{ext}}(\lambda)$, the absorption cross section $C_{\text{abs}}(\lambda)$ of the HbMP could be shown to be accurately modeled by the Rayleigh limit for small particles. In this limit the mathematical expressions for the cross sections simplify significantly. We discussed the possibility to exploit this for a straightforward data analysis that could yield the absorption spectrum of the particles' material.

Chapter 6

In chapter 6, we modeled and simulated the light scattering by native RBCs in an optical flow cytometer. In particular, histograms of the forward light scattering cross sections (FSCs) of native RBCs were considered, which in the experiment exhibit a pronounced bimodality at certain wavelengths. We estimated the velocity gradients in the flow chamber of the cytometer, which comprises longitudinal gradients during hydrodynamic focusing and transverse gradients in the $250\ \mu\text{m} \times 250\ \mu\text{m}$ flow channel, where cells reach velocities of $7\ \text{m s}^{-1}$. By comparison to the shapes of RBCs reported for different flow conditions in the literature, a simple shape model was proposed that accounts for the expected deformation in the cytometer. In particular, the estimated longitudinal (extensional) velocity gradients of the sheath flow exceed the transverse (shear) gradients by one order of magnitude. Shapes reported for RBCs in homogeneous extensional flows at extensional stresses comparable to the cytometer [138, 139] motivate an elliptical RBC shape. Hence, an existing model [142] for the axisymmetric biconcave resting shape of RBCs was extended by a linear stretching along the flow direction and compression perpendicular to it. The DDA was applied to calculate the Mueller matrix of the RBCs for different volumes, intracellular Hb concentrations and orientations. The FSC was computed from the Mueller matrix by integration over the detector aperture. The random orientation of the RBCs around the flow direction as well as their distributions of size and intracellular Hb concentration were simulated by direct Monte Carlo sampling.

By comparison between measurements and simulations, it was demonstrated that the occurrence of bimodal FSC histograms in optical flow cytometry is a combined effect of the random orientation angle β of the RBCs relative to the laser and their deformed shape due to hydrodynamic forces. A comparison between FSC measurements for different laser wavelengths and simulations reveals that the proposed elliptically elongated shape model reproduces the qualitative features of the experiment very well when the independently measured hematological parameters MCV, RDW and MCHC are used, i. e., these are not free parameters of the model. Comparison with two-direction FSC measurements using orthogonal lasers allows to assess the hypothesis of an alignment of the RBCs with their narrowest cross section perpendicular to the flow direction and a random orientation around this axis. This is confirmed by the symmetry properties of the 2D histograms as well as the breaking of this symmetry when RBCs are actively oriented during injection in

the cytometer, which could be reproduced by the simulation. No such agreement between simulation and experiment was obtained with the unstretched, axisymmetric shape model for RBCs at rest. This indicates that significant deformation of native human RBCs occurs during measurement in the flow cytometer which can be attributed to the hydrodynamic forces present in the cytometer, most notably the extensional flow during hydrodynamic focusing. Due to the good qualitative agreement with the experiments, such simulations could be used as a guidance for future cytometer designs and cytometric studies of RBC rheology, because, in contrast to the experiment, quantities like the far-field intensity distribution of single cells or the dependence of the FSC on cell size, orientation and shape are directly available in the simulation. Lastly, we discussed that by a combination with detailed mathematical modeling of the hydrodynamics and cell mechanics, an assessment of mechanical properties of RBCs might be possible from measurements and simulations of light scattering.

Own Publications

Journal Publications

- [a] J. Gienger, H. Groß, J. Neukammer, and M. Bär. Determining the refractive index of human hemoglobin solutions by Kramers–Kronig relations with an improved absorption model. *Appl. Opt.*, 55(31):8951–8961, 2016.
- [b] J. Gienger, M. Bär, and J. Neukammer. Extinction spectra of suspensions of microspheres: determination of the spectral refractive index and particle size distribution with nanometer accuracy. *Appl. Opt.*, 57(2):344–355, 2018.
- [c] J. Gienger, K. Smuda, R. Müller, M. Bär, and J. Neukammer. Refractive index of human red blood cells between 290 nm and 1100 nm determined by optical extinction measurements. *Sci. Reports*, 9(1):4623, 2019.
- [d] J. Gienger, H. Groß, V. Ost, M. Bär, and J. Neukammer. Assessment of deformation of native red blood cells in flow cytometry: Measurement and simulation of bimodal forward scatter distributions. *in review at Biomed. Opt. Express*, submitted 27 Oct. 2018.

Conference Papers

- [e] J. Gienger, H. Groß, and J. Neukammer. Improved result for the refractive index of human hemoglobin solutions by Kramers-Kronig relations. *EMTS 2016 proc., IEEE Xplore*, 2016.

References

- [1] G. C. Salzman. Light scattering analysis of single cells. In *Cell analysis*, pages 111–143. Springer, 1982.
- [2] H. M. Shapiro. *Practical flow cytometry*. John Wiley & Sons, fourth edition, 2003.
- [3] A. Wax, M. G. Giacomelli, T. E. Matthews, M. T. Rinehart, F. E. Robles, and Y. Zhu. Optical spectroscopy of biological cells. *Adv. Opt. Photon.*, 4(3):322–378, 2012.
- [4] K. Ramser and D. Hanstorp. Optical manipulation for single-cell studies. *J. Biophotonics*, 3(4):187–206.
- [5] B. O. Leung and K. C. Chou. Review of super-resolution fluorescence microscopy for biology. *Appl. Spectrosc.*, 65(9):967–980, 2011. PMID: 21929850.
- [6] A. G. Godin, B. Lounis, and L. Cognet. Super-resolution microscopy approaches for live cell imaging. *Biophys. journal*, 107(8):1777–1784, 2014.
- [7] I. W. Schie and T. Huser. Methods and applications of Raman microspectroscopy to single-cell analysis. *Appl. Spectrosc.*, 67(8):813–828, 2013.
- [8] B. Rappaz, A. Barbul, Y. Emery, R. Korenstein, C. Depeursinge, P. J. Magistretti, and P. Marquet. Comparative study of human erythrocytes by digital holographic microscopy, confocal microscopy, and impedance volume analyzer. *Cytom. Part A*, 73A(10):895–903, 2008.
- [9] Y. Sung, N. Lue, B. Hamza, J. Martel, D. Irimia, R. R. Dasari, W. Choi, Z. Yaqoob, and P. So. Three-dimensional holographic refractive-index measurement of continuously flowing cells in a microfluidic channel. *Phys. Rev. Appl.*, 1:014002, 2014.
- [10] J. Jung, L. E. Matemba, K. Lee, P. E. Kazyoba, J. Yoon, J. J. Massaga, K. Kim, D.-J. Kim, and Y. Park. Optical characterization of red blood cells from individuals with sickle cell trait and disease in Tanzania using quantitative phase imaging. *Sci. Reports*, 6:31698, 2016.
- [11] G. Dardikman, Y. N. Nygate, I. Barnea, N. A. Turko, G. Singh, B. Javidi, and N. T. Shaked. Integral refractive index imaging of flowing cell nuclei using quantitative phase microscopy combined with fluorescence microscopy. *Biomed. Opt. Express*, 9(3):1177–1189, 2018.

- [12] P. Müller, M. Schürmann, S. Girardo, G. Cojoc, and J. Guck. Accurate evaluation of size and refractive index for spherical objects in quantitative phase imaging. *Opt. Express*, 26(8):10729–10743, 2018.
- [13] Y. Park, M. Diez-Silva, G. Popescu, G. Lykotrafitis, W. Choi, M. S. Feld, and S. Suresh. Refractive index maps and membrane dynamics of human red blood cells parasitized by *Plasmodium falciparum*. *Proc. Natl. Acad. Sci.*, 105(37):13730–13735, 2008.
- [14] K. Kim, H. Yoon, M. Diez-Silva, M. Dao, R. R. Dasari, and Y. Park. High-resolution three-dimensional imaging of red blood cells parasitized by *Plasmodium falciparum* and in situ hemozoin crystals using optical diffraction tomography. *J. Biomed. Opt.*, 19(1):011005, 2013.
- [15] J. Jung, K. Kim, J. Yoon, and Y. Park. Hyperspectral optical diffraction tomography. *Opt. Express*, 24(3):2006–2012, 2016.
- [16] K. van de Graaff. *Human Anatomy*. McGraw-Hill, sixth edition, 2001.
- [17] K. Kaushansky, M. A. Lichtman, J. T. Prchal, M. Levi, O. W. Press, L. J. Burns, and M. A. Caligiuri. *Williams hematology*. McGraw-Hill Education, 9th edition, 2016.
- [18] H. J. Deuling and W. Helfrich. Red blood cell shapes as explained on the basis of curvature elasticity. *Biophys. J.*, 16(8):861, 1976.
- [19] J. B. Freund. Numerical simulation of flowing blood cells. *Annu. review fluid mechanics*, 46:67–95, 2014.
- [20] V. Heinrich, K. Ritchie, N. Mohandas, and E. Evans. Elastic thickness compressibility of the red cell membrane. *Biophys. J.*, 81(3):1452–1463, 2001.
- [21] R. Barer. Refractometry and interferometry of living cells. *J. Opt. Soc. Am.*, 47(6):545–556, 1957.
- [22] D. H. Tycko, M. H. Metz, E. A. Epstein, and A. Grinbaum. Flow-cytometric light scattering measurement of red blood cell volume and hemoglobin concentration. *Appl. Opt.*, 24(9):1355–1365, 1985.
- [23] N. Mohandas, Y. R. Kim, D. H. Tycko, J. Orlik, J. Wyatt, and W. Groner. Accurate and independent measurement of volume and hemoglobin concentration of individual red-cells by laser-light scattering. *Blood*, 68(2):506–513, 1986.
- [24] S. V. Tsinopoulos and D. Polyzos. Scattering of He–Ne laser light by an average-sized red blood cell. *Appl. Opt.*, 38(25):5499–5510, 1999.
- [25] L. Bi and P. Yang. Modeling of light scattering by biconcave and deformed red blood cells with the invariant imbedding T-matrix method. *J. Biomed. Opt.*, 18(5):055001, 2013.
- [26] R. Liu, G. Spicer, S. Chen, H. F. Zhang, J. Yi, and V. Backman. Theoretical model for optical oximetry at the capillary level: exploring hemoglobin oxygen saturation through backscattering of single red blood cells. *J. Biomed. Opt.*, 22(2):025002, 2017.

- [27] M. A. Yurkin, K. A. Semyanov, P. A. Tarasov, A. V. Chernyshev, A. G. Hoekstra, and V. P. Maltsev. Experimental and theoretical study of light scattering by individual mature red blood cells by use of scanning flow cytometry and a discrete dipole approximation. *Appl. Opt.*, 44(25):5249–5256, 2005.
- [28] N. Ghosh, P. Buddhiwant, A. Uppal, S. K. Majumder, H. S. Patel, and P. K. Gupta. Simultaneous determination of size and refractive index of red blood cells by light scattering measurements. *Appl. physics letters*, 88(8):084101, 2006.
- [29] L. Tong, J. Kauer, S. Wachsmann-Hogiu, K. Chu, H. Dou, and Z. J. Smith. A new red cell index and portable RBC analyzer for screening of iron deficiency and Thalassemia minor in a Chinese population. *Sci. Reports*, 7(1):10510, 2017.
- [30] K. G. Phillips, S. L. Jacques, and O. J. T. McCarty. Measurement of single cell refractive index, dry mass, volume, and density using a transillumination microscope. *Phys. Rev. Lett.*, 109:118105, 2012.
- [31] Y. Jang, J. Jang, and Y. Park. Dynamic spectroscopic phase microscopy for quantifying hemoglobin concentration and dynamic membrane fluctuation in red blood cells. *Opt. Express*, 20(9):9673–9681, 2012.
- [32] M. Friebel, A. Roggan, G. Müller, and M. Meinke. Determination of optical properties of human blood in the spectral range 250 to 1100 nm using Monte Carlo simulations with hematocrit-dependent effective scattering phase functions. *J. Biomed. Opt.*, 11(3):034021, 2006.
- [33] M. Meinke, G. Müller, J. Helfmann, and M. Friebel. Empirical model functions to calculate hematocrit-dependent optical properties of human blood. *Appl. Opt.*, 46(10):1742–1753, 2007.
- [34] D. Yim, G. Baranoski, B. Kimmel, T. Chen, and E. Miranda. A cell-based light interaction model for human blood. *Comput. Graph. Forum*, 31(2pt4):845–854, 2012.
- [35] Schott AG. TIE-29 Refractive index and dispersion, 2016.
- [36] R. Barer and S. Joseph. Refractometry of living cells: Part I. Basic principles. *Q. J. Microsc. Sci.*, s3-95(32):399–423, 1954.
- [37] M. Friebel and M. Meinke. Determination of the complex refractive index of highly concentrated hemoglobin solutions using transmittance and reflectance measurements. *J. Biomed. Opt.*, 10(6):064019, 2005.
- [38] M. Friebel and M. Meinke. Model function to calculate the refractive index of native hemoglobin in the wavelength range of 250-1100 nm dependent on concentration. *Appl. Opt.*, 45(12):2838–2842, 2006.
- [39] W. G. Zijlstra, A. Buursma, and O. W. van Assendelft. *Visible and near infrared absorption spectra of human and animal haemoglobin: determination and application*. VSP, 2000.

- [40] D. J. Segelstein. *The complex refractive index of water*. PhD thesis, University of Missouri – Kansas City, 1981.
- [41] M. Daimon and A. Masumura. Measurement of the refractive index of distilled water from the near-infrared region to the ultraviolet region. *Appl. Opt.*, 46(18):3811–3820, 2007.
- [42] R. Barer. Interference microscopy and mass determination. *Nature*, 169(4296):366, 1952.
- [43] K. Gilev, E. Yastrebova, D. Strokotov, M. Yurkin, N. Karmadonova, A. Chernyshev, V. Lomivorotov, and V. Maltsev. Advanced consumable-free morphological analysis of intact red blood cells by a compact scanning flow cytometer. *Cytom. Part A*, 91(9):867–873, 2017.
- [44] E. N. Lazareva and V. V. Tuchin. Measurement of refractive index of hemoglobin in the visible/NIR spectral range. *J. Biomed. Opt.*, 23(3):035004, 2018.
- [45] O. Zhernovaya, O. Sydoruk, V. Tuchin, and A. Douplik. The refractive index of human hemoglobin in the visible range. *Phys. Medicine Biol.*, 56(13):4013, 2011.
- [46] J. Wang, Z. Deng, X. Wang, Q. Ye, W. Zhou, J. Mei, C. Zhang, and J. Tian. Measurement of the refractive index of hemoglobin solutions for a continuous spectral region. *Biomed. Opt. Express*, 6(7):2536–2541, 2015.
- [47] J. Gienger, H. Groß, J. Neukammer, and M. Bär. Determining the refractive index of human hemoglobin solutions by Kramers–Kronig relations with an improved absorption model. *Appl. Opt.*, 55(31):8951–8961, 2016.
- [48] Y. Park, T. Yamauchi, W. Choi, R. Dasari, and M. S. Feld. Spectroscopic phase microscopy for quantifying hemoglobin concentrations in intact red blood cells. *Opt. Lett.*, 34(23):3668–3670, 2009.
- [49] A. Ojaghi, M. E. Fay, W. A. Lam, and F. E. Robles. Ultraviolet hyperspectral interferometric microscopy. *Sci. Reports*, 8(1):9913, 2018.
- [50] Y. Kim, H. Shim, K. Kim, H. Park, S. Jang, and Y. Park. Profiling individual human red blood cells using common-path diffraction optical tomography. *Sci. Reports*, 4, 2014.
- [51] Y. Xiong, A. Steffen, K. Andreas, S. Müller, N. Sternberg, R. Georgieva, and H. Bäumlner. Hemoglobin-based oxygen carrier microparticles: Synthesis, properties, and in vitro and in vivo investigations. *Biomacromolecules*, 13(10):3292–3300, 2012. PMID: 22978797.
- [52] Y. Xiong, Z. Z. Liu, R. Georgieva, K. Smuda, A. Steffen, M. Sendeski, A. Voigt, A. Patzak, and H. Bäumlner. Nonvasoconstrictive hemoglobin particles as oxygen carriers. *ACS Nano*, 7(9):7454–7461, 2013. PMID: 23915101.
- [53] H. Bäumlner, Y. Xiong, Z. Z. Liu, A. Patzak, and R. Georgieva. Novel hemoglobin particles – promising new-generation hemoglobin-based oxygen carriers. *Artif. Organs*, 38(8):708–714, 2014.

- [54] Y. Kim, H. Shim, K. Kim, H. Park, J. H. Heo, J. Yoon, C. Choi, S. Jang, and Y. Park. Common-path diffraction optical tomography for investigation of three-dimensional structures and dynamics of biological cells. *Opt. Express*, 22(9):10398–10407, 2014.
- [55] J. Lim, K. Lee, K. H. Jin, S. Shin, S. Lee, Y. Park, and J. C. Ye. Comparative study of iterative reconstruction algorithms for missing cone problems in optical diffraction tomography. *Opt. express*, 23(13):16933–16948, 2015.
- [56] S. Asano and G. Yamamoto. Light scattering by a spheroidal particle. *Appl. Opt.*, 14(1):29–49, 1975.
- [57] S. Asano. Light scattering properties of spheroidal particles. *Appl. Opt.*, 18(5):712–723, 1979.
- [58] G. Mie. Beiträge zur Optik trüber Medien, speziell kolloidaler Metallösungen <ger.> [Contributions to the optics of turbid media, particularly of colloidal metal solutions]. *Annalen der Physik*, 330(3):377–445, 1908.
- [59] L. Lorenz. Lysbevægelsen i og uden for en af plane Lysbølger belyst Kugle <dan.> [Light movement inside and outside of a sphere illuminated by a plane light wave]. *Vidensk. Selsk. Skr.*, 6:1–62, 1890.
- [60] M. Kerker. *The scattering of light, and other electromagnetic radiation*. Academic Press, 1969.
- [61] C. F. Bohren and D. R. Huffman. *Absorption and Scattering of Light by Small Particles*. Wiley, 1983.
- [62] F. M. Kahnert. Numerical methods in electromagnetic scattering theory. *J. Quant. Spectrosc. Radiat. Transf.*, 79–80:775–824, 2003. Electromagnetic and Light Scattering by Non-Spherical Particles.
- [63] M. I. Mishchenko, L. D. Travis, and A. A. Lacis. *Scattering, absorption, and emission of light by small particles*. Cambridge University Press, 2002.
- [64] T. Wriedt. Light scattering theories and computer codes. *J. Quant. Spectrosc. Radiat. Transf.*, 110(11):833 – 843, 2009. Light scattering: Mie and more – Commemorating 100 years of Mie’s 1908 publication.
- [65] M. A. Yurkin and A. G. Hoekstra. The discrete dipole approximation: an overview and recent developments. *J. Quant. Spectrosc. Radiat. Transf.*, 106(1):558–589, 2007.
- [66] M. A. Yurkin and A. G. Hoekstra. The discrete-dipole-approximation code ADDA: Capabilities and known limitations. *J. Quant. Spectrosc. Radiat. Transf.*, 112(13):2234 – 2247, 2011.
- [67] C. F. Bohren. What did Kramers and Kronig do and how did they do it? *Eur. J. Phys.*, 31(3):573, 2010.
- [68] D. J. Faber, M. C. G. Aalders, E. G. Mik, B. A. Hooper, M. J. C. van Gemert, and T. G. van Leeuwen. Oxygen saturation-dependent absorption and scattering of blood. *Phys. Rev. Lett.*, 93(2):028102, 2004.

- [69] O. Sydoruk, O. Zhernovaya, V. Tuchin, and A. Douplik. Refractive index of solutions of human hemoglobin from the near-infrared to the ultraviolet range: Kramers-Kronig analysis. *J. Biomed. Opt.*, 17(11):115002, 2012.
- [70] G. S. Adair, F. R. S., and M. E. Adair. The density increments of proteins. *Proc. Royal Soc. Lond. A: Math. Phys. Eng. Sci.*, 190(1022):341–356, 1947.
- [71] H. Arwin. Optical properties of thin layers of bovine serum albumin, γ -globulin, and hemoglobin. *Appl. Spectrosc.*, 40(3):313–318, 1986.
- [72] Y. Sugita, M. Nagai, and Y. Yoneyama. Circular dichroism of hemoglobin in relation to the structure surrounding the heme. *J. Biol. Chem.*, 246(2):383–388, 1971.
- [73] A. R. Goldfarb, L. J. Saidel, and E. Mosovich. The ultraviolet absorption spectra of proteins. *J. Biol. Chem.*, 193(1):397–404, 1951.
- [74] A. H. Woods and P. R. O’Bar. Absorption of proteins and peptides in the far ultraviolet. *Science*, 167(3915):179–181, 1970.
- [75] C. A. Emeis, L. J. Oosterhoff, and G. de Vries. Numerical evaluation of Kramers-Kronig relations. *Proc. Royal Soc. London. Ser. A, Math. Phys. Sci.*, 297(1448):54–65, 1967.
- [76] M. F. Perutz. Hemoglobin structure and respiratory transport. *Sci. Am.*, 239(6):92–125, 1978.
- [77] M. Frankowski, P. Simon, N. Bock, A. El-Hasni, U. Schnakenberg, and J. Neukammer. Simultaneous optical and impedance analysis of single cells: A comparison of two microfluidic sensors with sheath flow focusing. *Eng. Life Sci.*, 15(3):286–296, 2015.
- [78] K. Svoboda and S. M. Block. Biological applications of optical forces. *Annu. Rev. Biophys. Biomol. Struct.*, 23(1):247–285, 1994. PMID: 7919782.
- [79] I. D. Nikolov and C. D. Ivanov. Optical plastic refractive measurements in the visible and the near-infrared regions. *Appl. Opt.*, 39(13):2067–2070, 2000.
- [80] T. Inagaki, E. T. Arakawa, R. N. Hamm, and M. W. Williams. Optical properties of polystyrene from the near-infrared to the x-ray region and convergence of optical sum rules. *Phys. Rev. B*, 15:3243–3253, 1977.
- [81] E. K. Naumenko, T. V. Oleinik, and A. Y. Khairullina. Determination of the real part of relative refractive-index of spherical particles using scattering-matrix components. *Opt. Spectrosc.*, 53:288–290, 1982.
- [82] J. D. Felske and J. C. Ku. A technique for determining the spectral refractive indices, size, and number density of soot particles from light scattering and spectral extinction measurements in flames. *Combust. Flame*, 91(1):1 – 20, 1992.
- [83] M. R. Jones, B. P. Curry, M. Q. Brewster, and K. H. Leong. Inversion of light-scattering measurements for particle size and optical constants: theoretical study. *Appl. Opt.*, 33(18):4025–4034, 1994.

- [84] M. R. Jones, K. H. Leong, M. Q. Brewster, and B. P. Curry. Inversion of light-scattering measurements for particle size and optical constants: experimental study. *Appl. Opt.*, 33(18):4035–4041, 1994.
- [85] A. P. Nefedov, O. F. Petrov, and O. S. Vaulina. Analysis of particle sizes, concentration, and refractive index in measurement of light transmittance in the forward-scattering-angle range. *Appl. Opt.*, 36(6):1357–1366, 1997.
- [86] X. Ma, J. Q. Lu, R. S. Brock, K. M. Jacobs, P. Yang, and X.-H. Hu. Determination of complex refractive index of polystyrene microspheres from 370 to 1610 nm. *Phys. Medicine Biol.*, 48(24):4165, 2003.
- [87] G. E. Thomas, S. F. Bass, R. G. Grainger, and A. Lambert. Retrieval of aerosol refractive index from extinction spectra with a damped harmonic-oscillator band model. *Appl. Opt.*, 44(7):1332–1341, 2005.
- [88] B. N. Khlebtsov, V. A. Khanadeev, and N. G. Khlebtsov. Determination of the size, concentration, and refractive index of silica nanoparticles from turbidity spectra. *Langmuir*, 24(16):8964–8970, 2008. PMID: 18590302.
- [89] Y. Zhang, Y. Zhang, X. Han, P. Tuersun, and K. F. Ren. Influence of refractive index in particle sizing by light extinction spectrum. *Procedia Eng.*, 102:315 – 321, 2015. New Paradigm of Particle Science and Technology Proceedings of The 7th World Congress on Particle Technology.
- [90] R. Blümel, M. Bağcıoğlu, R. Lukacs, and A. Kohler. Infrared refractive index dispersion of polymethyl methacrylate spheres from Mie ripples in Fourier-transform infrared microscopy extinction spectra. *J. Opt. Soc. Am. A*, 33(9):1687–1696, 2016.
- [91] G. Crawley, M. Cournil, and D. D. Benedetto. Size analysis of fine particle suspensions by spectral turbidimetry: potential and limits. *Powder Technol.*, 91(3):197 – 208, 1997.
- [92] H. Sobral and M. Peña-Gomar. Determination of the refractive index of glucose-ethanol-water mixtures using spectroscopic refractometry near the critical angle. *Appl. Opt.*, 54(28):8453–8458, 2015.
- [93] For highly efficient numerical Mie computations the Fortran 77 code by W. J. Wiscombe (wiscombe@climate.gsfc.nasa.gov), NASA Goddard Space Flight Center was used, wrapped in Matlab.
- [94] J. Schäfer. MatScat. <https://www.mathworks.com/matlabcentral/fileexchange/36831-matscat>, 2012.
- [95] T. R. Lettieri, A. W. Hartman, G. G. Hembree, and E. Marx. Certification of SRM1960: Nominal 10 μm diameter polystyrene spheres (‘space beads’). *J. research Natl. Inst. Standards Technol.*, 96(6):669, 1991.
- [96] A. Ratnani and E. Sonnendrücker. B-splines and isogeometric analysis. https://www-m16.ma.tum.de/foswiki/pub/M16/Allgemeines/AdvFE16/bsplines_Ahmed.pdf, 2016.

- [97] G. V. Milovanović and Z. Udovičić. Calculation of coefficients of a cardinal B-spline. *Appl. Math. Lett.*, 23(11):1346 – 1350, 2010.
- [98] W. M. bin Mat Yunus and A. bin Abdul Rahman. Refractive index of solutions at high concentrations. *Appl. Opt.*, 27(16):3341–3343, 1988.
- [99] Y. R. Kim and L. Ornstein. Isovolumetric spherizing of erythrocytes for more accurate and precise cell volume measurement by flow cytometry. *Cytometry*, 3(6):419–427, 1983.
- [100] J. Gienger, M. Bär, and J. Neukammer. Extinction spectra of suspensions of microspheres: determination of the spectral refractive index and particle size distribution with nanometer accuracy. *Appl. Opt.*, 57(2):344–355, 2018.
- [101] R. Schiffer. Light scattering by perfectly conducting statistically irregular particles. *J. Opt. Soc. Am. A*, 6(3):385–402, 1989.
- [102] R. Schiffer. Perturbation approach for light scattering by an ensemble of irregular particles of arbitrary material. *Appl. Opt.*, 29(10):1536–1550, 1990.
- [103] O. S. Zhernovaya, V. V. Tuchin, and I. V. Meglinski. Monitoring of blood proteins glycation by refractive index and spectral measurements. *Laser Phys. Lett.*, 5(6):460, 2008.
- [104] R. E. Green, H. M. Sosik, R. J. Olson, and M. D. DuRand. Flow cytometric determination of size and complex refractive index for marine particles: comparison with independent and bulk estimates. *Appl. Opt.*, 42(3):526–541, 2003.
- [105] W. Somerville, B. Auguié, and E. L. Ru. SMARTIES: User-friendly codes for fast and accurate calculations of light scattering by spheroids. *J. Quant. Spectrosc. Radiat. Transf.*, 174:39 – 55, 2016.
- [106] W. C. Mundy, J. A. Roux, and A. M. Smith. Mie scattering by spheres in an absorbing medium. *J. Opt. Soc. Am.*, 64(12):1593–1597, 1974.
- [107] P. Chýlek. Light scattering by small particles in an absorbing medium. *J. Opt. Soc. Am.*, 67(4):561–563, 1977.
- [108] C. F. Bohren and D. P. Gilra. Extinction by a spherical particle in an absorbing medium. *J. Colloid Interface Sci.*, 72(2):215 – 221, 1979.
- [109] G. Videen and W. Sun. Yet another look at light scattering from particles in absorbing media. *Appl. Opt.*, 42(33):6724–6727, 2003.
- [110] M. I. Mishchenko. Electromagnetic scattering by a fixed finite object embedded in an absorbing medium. *Opt. Express*, 15(20):13188–13202, 2007.
- [111] The MathWorks, Inc. Matlab documentation: Unconstrained non-linear optimization algorithms. <https://mathworks.com/help/optim/ug/unconstrained-nonlinear-optimization-algorithms.html>. Accessed Sept. 2018.

- [112] The MathWorks, Inc. Matlab documentation: Least-squares (model fitting) algorithms. <https://mathworks.com/help/optim/ug/least-squares-model-fitting-algorithms.html>. Accessed Sept. 2018.
- [113] H. Bäumler and R. Georgieva. Coupled enzyme reactions in multicompartement microparticles. *Biomacromolecules*, 11(6):1480–1487, 2010. PMID: 20486658.
- [114] K. P. Jensen and U. Ryde. How O₂ binds to heme: Reasons for rapid binding and spin inversion. *J. Biol. Chem.*, 279(15):14561–14569, 2004.
- [115] R. Linberg, C. D. Conover, and K. L. Shum. Hemoglobin based oxygen carriers: How much methemoglobin is too much? *Artif. Cells, Blood Substitutes, Biotechnol.*, 26(2):133–148, 1998.
- [116] M. Bringas, A. A. Petruk, D. A. Estrin, L. Capece, and M. A. Martí. Tertiary and quaternary structural basis of oxygen affinity in human hemoglobin as revealed by multiscale simulations. *Sci. Reports*, 7(1):10926, 2017.
- [117] S. E. Jorge, M. Bringas, A. A. Petruk, M. Arrar, M. A. Marti, M. S. Skaf, F. F. Costa, L. Capece, M. F. Sonati, and D. Estrin. Understanding the molecular basis of the high oxygen affinity variant human hemoglobin Coimbra. *Arch. Biochem. Biophys.*, 637:73 – 78, 2018.
- [118] M. Piagnerelli, K. Zouaoui Boudjeltia, D. Brohee, A. Vereerstraeten, P. Piro, J.-L. Vincent, and M. Vanhaeverbeek. Assessment of erythrocyte shape by flow cytometry techniques. *J. Clin. Pathol.*, 60(5):549–554, 2007.
- [119] C. Ahlgrim, T. Pottgiesser, T. Sander, Y. O. Schumacher, and M. W. Baumstark. Flow cytometric assessment of erythrocyte shape through analysis of FSC histograms: Use of kurtosis and implications for longitudinal evaluation. *PLOS ONE*, 8(3):1–6, 2013.
- [120] H. L. Reid, J. A. Dormandy, A. J. Barnes, P. J. Lock, and T. L. Dormandy. Impaired red cell deformability in peripheral vascular disease. *The Lancet*, 307(7961):666 – 668, 1976. Originally published as Volume 1, Issue 7961.
- [121] H. A. Cranston, C. W. Boylan, G. L. Carroll, S. P. Sutera, J. R. Williamson, I. Y. Gluzman, and D. J. Krogstad. Plasmodium falciparum maturation abolishes physiologic red cell deformability. *Science*, 223(4634):400–403, 1984.
- [122] J. P. Mills, M. Diez-Silva, D. J. Quinn, M. Dao, M. J. Lang, K. S. W. Tan, C. T. Lim, G. Milon, P. H. David, O. Mercereau-Puijalon, S. Bonnefoy, and S. Suresh. Effect of plasmodial RESA protein on deformability of human red blood cells harboring Plasmodium falciparum. *Proc. Natl. Acad. Sci.*, 104(22):9213–9217, 2007.
- [123] H. Schmid-Schönbein, J. Weiss, and H. Ludwig. A simple method for measuring red cell deformability in models of the microcirculation. *Blut*, 26(6):369–379, 1973.
- [124] V. Ost. *Aufbau und Charakterisierung eines Laser-Durchflusszytometers zur Zählung und Differenzierung von Blutzellen* <ger.> [Setup and characterization of a laser flow cytometer for counting and differentiation of blood cells]. PhD thesis, Freie Universität Berlin, Germany, 1993.

- [125] V. Ost, J. Neukammer, and H. Rinneberg. Flow cytometric differentiation of erythrocytes and leukocytes in dilute whole blood by light scattering. *Cytometry*, 32(3):191–197, 1998.
- [126] R. Henson. Flow cytometry data reader and visualization. <https://mathworks.com/matlabcentral/fileexchange/8430-flow-cytometry-data-reader-and-visualization>.
- [127] R. Skalak, A. Tozeren, R. Zarda, and S. Chien. Strain energy function of red blood cell membranes. *Biophys. J.*, 13(3):245 – 264, 1973.
- [128] C. Pozrikidis. Axisymmetric motion of a file of red blood cells through capillaries. *Phys. Fluids*, 17(3):031503, 2005.
- [129] E. Gibaud. *Numerical simulation of red blood cells flowing in a cytometer*. PhD thesis, Université de Montpellier, France, 2015.
- [130] C. Pozrikidis. Numerical simulation of the flow-induced deformation of red blood cells. *Annals Biomed. Eng.*, 31(10):1194–1205, 2003.
- [131] J. M. Skotheim and T. W. Secomb. Red blood cells and other nonspherical capsules in shear flow: Oscillatory dynamics and the tank-treading-to-tumbling transition. *Phys. Rev. Lett.*, 98:078301, 2007.
- [132] T. W. Secomb, R. Skalak, N. Özkaya, and J. F. Gross. Flow of axisymmetric red blood cells in narrow capillaries. *J. Fluid Mech.*, 163:405–423, 1986.
- [133] G. Tomaiuolo, M. Simeone, V. Martinelli, B. Rotoli, and S. Guido. Red blood cell deformation in microconfined flow. *Soft Matter*, 5:3736–3740, 2009.
- [134] R. Skalak and P.-I. Branemark. Deformation of red blood cells in capillaries. *Science*, 164(3880):717–719, 1969.
- [135] C. Pozrikidis. Numerical simulation of cell motion in tube flow. *Annals Biomed. Eng.*, 33(2):165–178, 2005.
- [136] H. Noguchi and G. Gompper. Shape transitions of fluid vesicles and red blood cells in capillary flows. *Proc. Natl. Acad. Sci.*, 102(40):14159–14164, 2005.
- [137] S. Quint, A. F. Christ, A. Guckenberger, S. Himbert, L. Kaestner, S. Gekle, and C. Wagner. 3D tomography of cells in micro-channels. *Appl. Phys. Lett.*, 111(10):103701, 2017.
- [138] S. S. Lee, Y. Yim, K. H. Ahn, and S. J. Lee. Extensional flow-based assessment of red blood cell deformability using hyperbolic converging microchannel. *Biomed. Microdevices*, 11(5):1021, 2009.
- [139] T. Yaginuma, M. S. N. Oliveira, R. Lima, T. Ishikawa, and T. Yamaguchi. Human red blood cell behavior under homogeneous extensional flow in a hyperbolic-shaped microchannel. *Biomicrofluidics*, 7(5):054110, 2013.
- [140] R. M. Hochmuth, P. R. Worthy, and E. A. Evans. Red cell extensional recovery and the determination of membrane viscosity. *Biophys. J.*, 26(1):101–114, 1979.

- [141] J. P. Mills, L. Qie, M. Dao, C. T. Lim, and S. Suresh. Nonlinear elastic and viscoelastic deformation of the human red blood cell with optical tweezers. *Mech. & chemistry biosystems : MCB*, 1(3):169–180, 2004.
- [142] M. A. Yurkin. *Discrete dipole simulations of light scattering by blood cells*. PhD thesis, University of Amsterdam, 2007.
- [143] Y. C. Fung, W. C. O. Tsang, and P. Patitucci. High-resolution data on the geometry of red blood cells. *Biorheology*, 18(3-6):369–385, 1981.
- [144] W. H. Carter. Electromagnetic field of a Gaussian beam with an elliptical cross section. *J. Opt. Soc. Am.*, 62(10):1195–1201, 1972.
- [145] O. Ergül, A. Arslan-Ergül, and L. Gürel. Computational study of scattering from healthy and diseased red blood cells. *J. Biomed. Opt.*, 15(4):045004, 2010.
- [146] D. Dannhauser, D. Rossi, F. Causa, P. Memmolo, A. Finizio, T. Wriedt, J. Hellmers, Y. Eremin, P. Ferraro, and P. A. Netti. Optical signature of erythrocytes by light scattering in microfluidic flows. *Lab on a Chip*, 15:3278–3285, 2015.
- [147] K. V. Gilev, M. A. Yurkin, E. S. Chernyshova, D. I. Strokotov, A. V. Chernyshev, and V. P. Maltsev. Mature red blood cells: from optical model to inverse light-scattering problem. *Biomed. Opt. Express*, 7(4):1305–1310, 2016.
- [148] P. B. Canham and A. C. Burton. Distribution of size and shape in populations of normal human red cells. *Circ. research*, 22(3):405–422, 1968.

Abbreviations

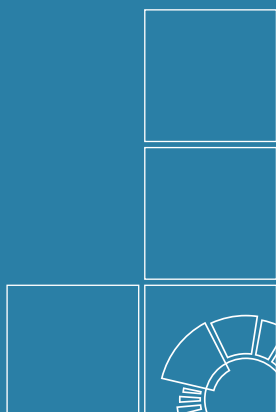
abbreviation	explanation
i. e.	<i>id est</i> (lat.) – that is
cf.	<i>confer</i> (lat.) – “compare”
et al.	<i>et alii</i> (lat.) – “and others”
e. g.	<i>exempli gratia</i> (lat.) – “for the sake of example”, “for example”
etc.	<i>et cetera</i> (lat.) – “and so on”
vs.	<i>versus</i> (lat.) – “against”, “compared with”
ADC	analog-to-digital converter
AR	Abbe refractometer
BSA	bovine serum albumin (protein)
CBC	complete blood count (hematological measurement)
deoxyHb	deoxygenated hemoglobin
EDTA	ethylene-diaminetetraacetic acid
FSC	forward scattering cross section
Hb	hemoglobin
HbMP	hemoglobin microparticle
HCT	hematocrit (volume fraction of RBCs in blood; hematological parameter)
HDW	hemoglobin distribution width (coefficient of variation of intra-RBC Hb concentration; hematological parameter)
HGB	hemoglobin concentration in blood (hematological parameter)
HSA	human serum albumin (protein)
IR	infrared
KK	Kramers-Kronig (relations/transformation)
LTR	Lorentz-type resonance
MC	Monte Carlo
MCH	mean corpuscular hemoglobin content (hematological parameter)
MCHC	mean corpuscular hemoglobin concentration (mean of intra-RBC Hb concentration; hematological parameter)
MCV	mean corpuscular volume (mean of RBC volume; hematological parameter)

abbreviation	explanation
metHb	methemoglobin (non-functional hemoglobin variant)
N.A.	numerical aperture
oxyHb	oxygenated hemoglobin
PBS	phosphate buffered saline
pdf	probability density function
PMT	photomultiplier tube
PS	polystyrene
RBC	red blood cell, erythrocyte
RDW	red cell distribution width (coefficient of variation of RBC volume; hematological parameter)
RI	refractive index
SDS	sodium dodecyl sulfate (a surfactant)
SEM	scanning electron microscopy
UV	ultraviolet
VSWF	vector spherical wavefunction
w/v	weight in volume (concentration; 1%w/v equals 10 g L ⁻¹)
WBC	white blood cell, leukocyte

Danksagung

Zuallererst möchte ich meiner Familie für die fortwährende Unterstützung während meines Studiums und meiner Doktorandenzeit danken. Insbesondere danke ich meiner Partnerin Mara Oßwald dafür, dass sie mir in den letzten Wochen und Monaten vor Abgabe dieser Arbeit den Rücken freigehalten hat.

Ich danke Kathrin Smuda für die großartige und fruchtbare Zusammenarbeit im Themenfeld der Extinktionsspektren von Partikeln und Zellen. Hermann Groß möchte ich für seinen engagierten Beitrag zu einem angenehmen Arbeitsumfeld an der PTB, anerkennende Worte und interessante Diskussionen danken. Außerdem danke ich ihm für gründliches Korrekturlesen eines Großteils dieser Dissertation. Weiterhin danke ich Jörg Neukammer dafür, dass er mich mit einigen der in dieser Arbeit behandelten zentralen Fragestellungen bekannt gemacht hat. Markus Bär danke ich dafür, dass er mich zur Publikation meiner Ergebnisse motiviert und diese vorangetrieben hat und mich dabei mit seiner Erfahrung als Wissenschaftler unterstützt hat. Abschließend danke ich Hans Bäumler, Andreas Kummrow und Martin Hussels für anregende Diskussionen.



Herausgeber:

Physikalisch-Technische Bundesanstalt
ISNI: 0000 0001 2186 1887

Presse und Öffentlichkeitsarbeit

Bundesallee 100
38116 Braunschweig

Telefon: (05 31) 592-93 21
Telefax: (05 31) 592-92 92
www.ptb.de

Vertrieb:

Fachverlag NW in der
Carl Schünemann Verlag GmbH

Zweite Schlachtpforte 7
28195 Bremen

Telefon: (04 21) 369 03-0
Telefax: (04 21) 369 03-63
www.schuenemann-verlag.de